
Cold-Atom Loading of Hollow-Core Photonic Crystal Fibre for Quantum Technologies

By

ASHBY PAUL HILTON



THE UNIVERSITY
of ADELAIDE

Institute of Photonics and Advanced Sensing
&
School of Physical Sciences
UNIVERSITY OF ADELAIDE

A dissertation submitted to the University of Adelaide in
accordance with the requirements of the degree of
DOCTOR OF PHILOSOPHY
Primary supervisor: PHILIP LIGHT
Co-supervisors: CHRISTOPHER PERRELLA and ANDRE LUITEN.

MARCH 3, 2020

TABLE OF CONTENTS

| | Page |
|--|-------------|
| Abstract | vii |
| Dedication | ix |
| Declaration of Authorship | xi |
| List of Tables | xi |
| List of Figures | xiii |
| Glossary | xvii |
| | |
| I Background | 1 |
| | |
| 1 Introduction | 3 |
| 1.1 Atomic Species | 4 |
| 1.2 Thesis Outline | 5 |
| 1.3 Publications, Conference Attendance, and awards | 8 |
| | |
| 2 A History of the Field | 11 |
| 2.1 Overview | 11 |
| 2.2 Early Theoretical work | 12 |
| 2.3 Hot Atomic Transport Through Glass Capillaries | 14 |
| 2.4 Transportation of Laser Cooled Atoms Through Glass Capillaries | 17 |
| 2.5 Development of Photonic Crystal Fibre | 19 |
| 2.5.1 Solid Core Fibre | 19 |
| 2.5.2 Bandgap Fibre | 21 |
| 2.5.3 Kagome-Lattice Fibre | 23 |
| 2.6 Application of Thermal Vapours in Hollow-Core Fibre | 26 |
| 2.6.1 Spectroscopy of Atomic Vapour in Hollow-Core Fibre | 27 |

| | | |
|--|--|-----------|
| 2.6.2 | Inline Fibre Microcells | 29 |
| 2.6.3 | High Optical Depth Generation (LIAD) | 30 |
| 2.6.4 | Efficient Nonlinear Optics | 32 |
| 2.6.5 | High Bandwidth Quantum Memories | 37 |
| 2.6.6 | Summary: Application of thermal vapours in hollow-core fibre | 40 |
| 2.7 | Loading of Cold atoms into hollow-core fibre | 40 |
| 2.8 | Contemporary Work in the Field | 45 |
| 2.9 | Summary | 50 |
| II Cold Atom Loading Experiment | | 51 |
| 3 Experimental Apparatus | | 53 |
| 3.1 | Overview | 53 |
| 3.2 | Hollow-Core Fibre | 54 |
| 3.2.1 | Fundamental Mode | 55 |
| 3.2.2 | Higher Order Modes | 57 |
| 3.2.3 | Fibre Coupling | 59 |
| 3.2.4 | Fibre Preparation and Installation | 62 |
| 3.3 | Vacuum System | 63 |
| 3.3.1 | Chamber | 63 |
| 3.3.2 | Pump Down Protocol | 65 |
| 3.3.3 | Vacuum Break Protocol | 66 |
| 3.4 | Atomic Source | 67 |
| 3.4.1 | Implementation | 68 |
| 3.4.2 | Dispenser Cleaning Protocol | 69 |
| 3.5 | Laser Systems & Stabilisation | 70 |
| 3.5.1 | Probe Laser | 70 |
| 3.5.2 | Cooling Laser | 72 |
| 3.5.3 | Repump Laser | 75 |
| 3.5.4 | EIT Control Laser | 76 |
| 3.5.5 | Guide Laser | 79 |
| 3.5.6 | Optical Switching | 80 |
| 3.6 | Magneto Optical Trap | 81 |
| 3.6.1 | Laser System | 83 |
| 3.6.2 | Anti-Helmholtz Coils | 85 |
| 3.6.3 | Compensation Coils | 86 |
| 3.6.4 | Timing | 88 |

| | | |
|------------|--|------------|
| 3.6.5 | MOT Optimisation | 90 |
| 3.6.6 | MOT Performance | 91 |
| 3.7 | Computer Oversight | 92 |
| 3.7.1 | PC User Interface | 92 |
| 3.7.2 | Arduino Due | 95 |
| 3.8 | Summary | 97 |
| 4 | Interrogation Techniques | 99 |
| 4.1 | Fluorescence Counting | 100 |
| 4.1.1 | Theory – Isotropic Scattering of Light | 100 |
| 4.1.2 | Implementation | 101 |
| 4.2 | MOT Loading Time | 102 |
| 4.3 | Shadow Imaging | 104 |
| 4.3.1 | Implementation | 105 |
| 4.3.2 | Image Processing | 107 |
| 4.4 | Temperature Calculation | 109 |
| 4.5 | Absorption spectroscopy | 110 |
| 4.5.1 | Pulse Train Generation | 112 |
| 4.5.2 | Broadband DC Absorption Spectroscopy | 115 |
| 4.5.2.1 | Implementation | 116 |
| 4.5.2.2 | Data Processing | 117 |
| 4.5.3 | Heterodyne Detection Absorption Spectroscopy | 121 |
| 4.5.3.1 | Implementation | 122 |
| 4.5.3.2 | Data Processing | 125 |
| 4.6 | Summary | 128 |
| 5 | Monte-Carlo Modelling | 129 |
| 5.1 | Overview | 129 |
| 5.2 | Included Physics | 130 |
| 5.3 | Starting Conditions | 133 |
| 5.4 | Solving the Equations of Motion | 134 |
| 5.5 | Processing Results | 135 |
| 5.6 | Summary | 137 |
| III | Publications | 139 |
| 6 | High-efficiency cold-atom transport into a waveguide trap | 141 |
| | Publication: High-efficiency cold-atom transport into a waveguide trap | 144 |

| | |
|---|------------|
| 7 Dual-Color Magic-Wavelength Trap for Suppression of Light Shifts in Atoms | 155 |
| Publication: Dual-Color Magic-Wavelength Trap for Suppression of Light Shifts in Atoms | 158 |
| 8 Light-shift spectroscopy of optically trapped atomic ensembles | 167 |
| Publication: Light-shift spectroscopy of optically trapped atomic ensembles . . . | 171 |
| 9 Optimal design for spectral narrowing and fast frequency sweep of an interferometer-stabilized laser | 191 |
| Publication: Optimal design for spectral narrowing and fast frequency sweep of an interferometer-stabilized laser | 194 |
| IV Conclusion and Outlook | 201 |
| 10 Conclusion and Future Work | 203 |
| 10.1 Summary | 203 |
| 10.2 Future Work | 206 |
| 10.2.1 Hollow-Mode Optical Guide | 206 |
| 10.2.2 Raman EIT Coherent Phenomena | 209 |
| 10.3 Concluding Remarks | 212 |
| V Appendices | 215 |
| A Code Snippets | 217 |
| A.1 Data Processing | 217 |
| A.1.1 Heterodyne Absorption Spectroscopy | 217 |
| A.1.2 DC Absorption Spectroscopy | 222 |
| A.2 Monte-Carlo Simulation | 230 |
| B Low-Noise Analog Lock Box Manual | 241 |
| Low-Noise Analog Lockbox Manual | 241 |
| Bibliography | 261 |

ABSTRACT

Ultra-strong light-atom interaction is a key resource for numerous applications in quantum-information processing, nonlinear optics, and quantum sensing. Maximising the strength of the interaction requires optimising the combination of light-atom coherent interaction time, spatial overlap between the optical mode and the atomic cross section, and the number of participating atoms.

An exciting approach to achieving these goals is to use a collection of laser-cooled atoms inside a hollow-core photonic crystal fibre. Here the tight transverse confinement provided by fibre guarantees overlap between the atomic sample and guided optical modes over an arbitrarily long distance. Laser cooling improves the effective atom number of the sample by increasing the fraction that participate in the interaction and significantly improves the coherent interaction time by reducing the spatial decoherence rate of the ensemble.

This project focuses around the development of an apparatus that realises the laser-cooling, trapping, and loading of atoms into a kagome-lattice hollow-core fibre. In this thesis we describe the development of the elements required to realise this task, including the vacuum system, laser sources, computer oversight, and theoretical models employed. The resulting platform is capable of achieving the ultra-high optical depths required for exciting quantum-optics applications such as long-lived coherent optical pulse storage.

We have demonstrated high-efficiency transport of cold rubidium atoms from a magneto-optical trap into a hollow-core fibre, measuring a peak optical depth of 600 with only 3×10^6 atoms. These experiments were guided by a Monte-Carlo simulation that has been shown to have excellent agreement with the physical system. The results show that this platform is in an excellent position to investigate coherent optical phenomena at the few-photon level.

Along the way we investigated the application of light-shift engineering to both measure and compensate for the perturbative effects the strong light fields present in the experiment have on atomic states. We extend the ‘magic-wavelength’ technique used in the atomic lattice clock community to nullify the lineshape broadening of the

target ensemble by introducing an additional light field. This allows the technique to be implemented in a broad range of atomic species and transitions, where the original technique was only accessible for limited species with specific energy-level structures.

We also take advantage of light-shift engineering to extract a detailed model of the spatial distribution of an optically-trapped ensemble through a simple spectroscopic technique. We use this model to infer the temperature, coherence time, and number of atoms in the trap in addition to the depth of the trap itself. Experimentally we demonstrate this on our cold-atom-filled fibre platform, showing that this information can be extracted from a system with limited optical access and where conventional techniques cannot be applied.

The apparatus and experimental techniques we have developed place this project in an excellent position to perform cutting-edge research in the fields of quantum information processing and nonlinear optics.

DEDICATION AND ACKNOWLEDGEMENTS

There are many people who have contributed to this experience over the five long years it has taken, and I would not have made it in one piece without you all. Here is a small collection of thanks I would like to give.

First of all I would like to thank my supervisor Phil Light for the enormous amount of support he has provided. I have learned so much through your guidance, and I could not have asked for a better mentor. Thank you for the long hours you spent in lab banging your head against the wall with me, and for putting up with my stupider moments. I owe you a ride sometime, with coffee and a cake.

Next I would thank Andre Luiten for his support of my work, and for dragging me out to Adelaide in the first place. The opportunities and experiences I have had here have been life changing, and I have never regretted that decision. Your insight and quick wit has been an inspiration.

To Christopher Perrella and the post-docs that have come and gone over the years, thank you for the influence you have had on my education. "It takes a village to raise a child" as the saying goes, and it has been a privilege to member of this one.

To my fellow students and comrades in arms, thank you all for the network of support you provided me. I will fondly remember the beers in the pub, picnics, and movies dinners. Nate, Sarah, Ka, Ada, and all the rest of you - I wish you all the best. It's also surprising the bonds we make in three days at conference, how long they last, and how far they reach. To Daniel, Mateusz, Sean, Stuart, Cera, Kenneth, Sab, James, and David, I wish you all the best, and I'll see you next time.

To my emotional support crew, or 'friends', thanks for dragging me out of the lab to go climbing, play games, see movies, and all the rest. Physics is a full time job, and it gets very easy to spend every second of every day thinking and talking about how to solve the most recent problem, and how to make the next exciting experiment work. It is incredibly important to surround yourself with people who are not physicists, and who are perfectly

TABLE OF CONTENTS

happy to pick you up and take you on a hiking or climbing trip for a few days with no internet, or even just sit down and play games until midnight. These moments have made a world of difference, so thanks Matt and Rachael, Brendan and Pinky, and all the rest of you.

To family, close and extended, you have been an amazing support over the years. Thank you Mum and Dad, Lintilla and Murray for caring for me in every way. You made this possible. To Lynne and Mark, Josh and Verity, thank you for accepting me into your family - it as been a wonderful experience.

Finally, to my wonderful Cat. You are my everything, and it would be impossible to put into words the effect your have had on my life. You have been by my side through this whole adventure, and I would not have made it without you.

DECLARATION OF AUTHORSHIP

I certify that this work contains no material which has been accepted for the award of any other degree or diploma in any university or other tertiary institution and, to the best of my knowledge and belief, contains no material previously published or written by another person, except where due reference has been made in the text.

In addition, I certify that no part of this work will, in the future, be used in a submission for any other degree or diploma in any university or other tertiary institution without the prior approval of the University of Adelaide and where applicable, any partner institution responsible for the joint-award of this degree.

I give consent to this copy of my thesis when deposited in the University Library, being made available for loan and photocopying, subject to the provisions of the Copyright Act 1968.

The author acknowledges that copyright of published works contained within this thesis resides with the copyright holder(s) of those works. I also give permission for the digital version of my thesis to be made available on the web, via the University's digital research repository, the Library catalogue and also through web search engines, unless permission has been granted by the University to restrict access for a period of time.

I acknowledge the support I have received for my research through the provision of an Australian Government Research Training Program Scholarship.

Signed:

_____, Date: 22 / 01 / 20

Ashby Hilton

LIST OF TABLES

| TABLE | Page |
|--|-------------|
| 3.1 Cylindrical vector vortex mode parameters | 58 |
| 3.2 Table of power split across the cooling arms | 74 |
| 3.3 Compensation coil parameters | 87 |
| 10.1 EIT spectrum fit parameters | 211 |

LIST OF FIGURES

| FIGURE | Page |
|---|------|
| 2.1 Confinement of atoms to a capillary: red and blue detuned dipole traps | 13 |
| 2.2 Diagram of hot atom transport experiments | 15 |
| 2.3 Guidance mechanism in solid core photonic crystal fibre | 20 |
| 2.4 Theory of Bragg reflection | 22 |
| 2.5 Guidance in photonic bandgap fibre | 23 |
| 2.6 Guidance in kagome-lattice fibre | 24 |
| 2.7 Kagome lattice core geometries | 25 |
| 2.8 Diagram of HC-PCF gas flow apparatus | 28 |
| 2.9 Inline fibre microcell | 29 |
| 2.10 The LIAD process | 31 |
| 2.11 Diagram of nonlinear process mediated by atomic transitions | 34 |
| 2.12 Multiphoton synchronisation protocol | 37 |
| 2.13 Lambda Raman quantum memory protocol | 38 |
| 2.14 ORCA quantum memory protocol | 39 |
| 2.15 Typical cold-atom loading system | 41 |
| 2.16 Light storage pulse sequence diagram | 43 |
| 2.17 Excitation of Rydberg atoms | 46 |
| 2.18 Magic wavelength technique | 49 |
| | |
| 3.1 Microscope image of kagome-lattice fibre end-face | 55 |
| 3.2 Fundamental fibre mode | 56 |
| 3.3 Calculated electric field profiles for the $l = \pm 1$ LG ₀₁ CVVBs | 57 |
| 3.4 Finite element analysis solution for fibre-guided hollow mode | 59 |
| 3.5 Images of the hollow mode before and after the kagome-lattice fibre | 60 |
| 3.6 Hollow-core fibre coupling assembly | 61 |
| 3.7 Hollow-core fibre bake-out assembly | 62 |
| 3.8 Model of complete vacuum assembly | 64 |
| 3.9 Setup used to perform vacuum breaks and pump downs | 65 |
| 3.10 Rubidium dispenser | 68 |

| | |
|---|-----|
| 3.11 Rubidium dispenser current response | 69 |
| 3.12 Diagram of the probe laser setup | 71 |
| 3.13 Probe laser spectroscopy | 72 |
| 3.14 Diagram of the cooling laser setup | 73 |
| 3.15 Cooling laser phase lock | 74 |
| 3.16 Diagram of the repump laser setup | 75 |
| 3.17 Repump laser spectroscopy | 77 |
| 3.18 Diagram of the EIT control laser setup | 78 |
| 3.19 Measurement of the EIT control laser phase lock performance | 78 |
| 3.20 EIT control laser spectroscopy | 79 |
| 3.21 Diagram of the guide laser setup | 80 |
| 3.22 Diagram of the timing for the fast optical switch | 82 |
| 3.23 Diagram of the cooling beam geometry | 83 |
| 3.24 Model of a MOT cooling arm assembly | 84 |
| 3.25 Diagram of the anti-Helmholtz coil configuration | 85 |
| 3.26 Model of one of the MOT coils | 86 |
| 3.27 Diagram of the compensation coil setup | 87 |
| 3.28 MOT loading and experimental timing chart | 89 |
| 3.29 Schematic of the communication between elements of the lab control system | 93 |
| 3.30 Snapshot of the control system interface – diagnostics and cameras | 94 |
| 3.31 Snapshot of the control system interface – parameters and programs | 94 |
| | |
| 4.1 Fluorescence capture setup | 102 |
| 4.2 MOT loading rate | 103 |
| 4.3 Shadow imaging double-passed AOM setup | 105 |
| 4.4 Shadow imaging diagram | 106 |
| 4.5 Shadow imaging setup | 107 |
| 4.6 Shadow image processing | 108 |
| 4.7 Atom cloud temperature calculation | 111 |
| 4.8 Gaussian pulse sequence for absorption spectroscopy | 112 |
| 4.9 Generating the AOM pulse sequence | 113 |
| 4.10 AOM efficiency calibration map | 114 |
| 4.11 Testing Gaussian pulse production | 115 |
| 4.12 DC spectroscopy fibre interrogation setup | 117 |
| 4.13 Processing broadband spectroscopy data | 118 |
| 4.14 DC spectroscopy pulse mask calibration | 119 |
| 4.15 Heterodyne spectroscopy diagram | 123 |
| 4.16 Heterodyne probe and LO setup | 123 |

| | |
|---|-----|
| 4.17 Heterodyne spectroscopy fibre interrogation scheme | 124 |
| 4.18 Raw heterodyne spectroscopy data | 126 |
| 4.19 Processed heterodyne spectroscopy data | 127 |
| 5.1 A demonstration of the trajectories produced by the Monte-Carlo model | 136 |
| 5.2 Juxtaposition of experimental results and the Monte-Carlo model | 138 |
| 10.1 Demonstration of hollow-mode guidance of atoms | 207 |
| 10.2 Transmission EIT measurement in blue-mode guided atoms | 209 |
| 10.3 Heterodyne spectroscopy of an EIT feature | 210 |
| 10.4 Demonstration of optical pulse storage | 212 |

GLOSSARY

- OD** optical depth.
- AMO** atomic, molecular, and optical physics.
- AOM** acousto-optic modulator.
- APD** avalanche photodiode.
- BEC** Bose-Einstein condensate.
- BPD** balanced photodiode.
- CAD** computer-aided design.
- CCD** charge-coupled device.
- CSV** comma-separated values.
- CVVB** cylindrical vector vortex beam.
- CW** continuous-wave.
- ECDL** external-cavity diode laser.
- EIT** electromagnetically-induced transparency.
- EOM** electro-optic modulator.
- FFT** fast Fourier transform.
- FWHM** full-width at half-maximum.
- FWM** four-wave mixing.
- GPIB** IEEE-488 general purpose interface bus.

- GUI** graphical user interface.
- HC-PBF** hollow-core photonic bandgap fibre.
- HC-PCF** hollow-core photonic crystal fibre.
- HWP** half-wave plate.
- LIAD** light-induced atomic desorption.
- LO** local oscillator.
- LVIS** low velocity intense source.
- M-TIR** modified total internal reflection.
- MOT** magneto optical trap.
- MTS** modulation transfer spectroscopy.
- NPBS** non-polarising beam splitter.
- OAM** orbital angular momentum.
- ODT** optical dipole trap.
- ORCA** off-resonance cascaded absorption.
- PBS** polarising beam splitter.
- PCF** photonic crystal fibre.
- PGC** polarisation gradient cooling.
- PM** polarisation maintaining.
- QWP** quarter-wave plate.
- RGA** residual gas analyser.
- SAS** saturated absorption spectroscopy.
- SHG** second harmonic generation.
- SMF** single-mode optical fibre.

SNR signal-to-noise ratio.

SPST single-pole single-throw.

SRS stimulated Raman scattering.

TIR total internal reflection.

UHV ultra-high vacuum.

USB universal serial bus.

XPM cross-phase modulation.

Part I

Background

INTRODUCTION

Since the early demonstrations of laser cooling of neutral atoms in the 80s by Chu, Cohen-Tannoudji, and Phillips [22, 23, 89] cold atomic ensembles have exploded in use, and can now be found in virtually every [atomic, molecular, and optical physics \(AMO\)](#) laboratory in the world. These systems are particularly well known for the high densities and low velocities that make them near-perfect platforms for applications such as investigating quantum phenomena [20, 108], developing ultra-high accuracy clocks [44], and implementing cutting-edge sensors [115, 133].

One extremely exciting avenue of research in this field is the interfacing of cold-atom ensembles with complex geometries and materials. The platform investigated here is the controllable loading of cold rubidium atoms into the core of a [hollow-core photonic crystal fibre \(HC-PCF\)](#). These innovative fibres are exciting in their own right, with much research going into the fabrication of fibre with lower losses and wider guidance bands [9, 104, 105]. One of their defining features is the ability to guide light without a solid core, allowing for the introduction of atoms or molecules, which in turn, strongly interact with light guided through the core.

Using powerful optical dipole traps it is possible to funnel a cloud of laser-cooled atoms down into the fibre, resulting in an extremely high aspect ratio system. The well defined guided modes of the fibre result in near-perfect overlap between the guided atoms and any interrogating fields over the entirety of the quasi-one-dimensional system, which

could be many centimetres long. The tight transverse confinement of both light and the atomic medium leads to extremely strong light-atom interaction, resulting in a platform capable of exploring quantum optics at the few-photon level [87].

This is a rapidly evolving field, with great improvements being found in the use of new hollow-core fibres with better guidance properties such as the kagome-lattice fibre [24]. Similarly, improvements in the atom-loading efficiency are leading to compact systems with exceptionally large **optical depths (ODs)** [15]. One of the current limitations of these systems is the strongly perturbative effect the optical guide has on the trapped atoms. To avoid this, most experiments are performed in short intervals in which the guide has been switched off. This limits the lifetime of the atomic ensemble to the time the atoms take to hit the walls of the core. Potential solutions to this problem, explored in this thesis, include the use of magic-wavelength optical traps as in the atomic lattice clock field [53, 135].

The goal of this project was to build a cold-atom-in-fibre platform for exploring quantum optics phenomena at the few-photon level, with particular interest in coherent optical pulse storage and retrieval. Long term plans include the investigation of hollow-mode optical guides for extending the lifetime of coherent optical states in the trapped atoms, and implementing the gradient echo memory protocol for efficient, high bandwidth storage of coherent optical states.

1.1 Atomic Species

The atom of choice for this experiment is rubidium, specifically the isotope ^{85}Rb . The reason for using this element is predominantly convenience, as rubidium is widely considered one of the easiest atoms to laser cool, and is commonly used in **AMO** labs around the world.

Rubidium is an alkali metal with atomic number of 37 and only two common isotopes, of which ^{85}Rb has a natural abundance of 72%. Chemically, the single valence electron lies in an $5S$ orbital making the element highly reactive with a low melting point and high vapour pressure at room temperature. This is useful for vacuum systems and vapour cells, where significant number densities can be present at room temperature.

The atomic structure is relatively easy to understand and predict due to the lack of

strong multi-electron interaction or relativistic contributions. Rubidium possesses an extremely accessible collection of strong optical transitions between the $5^2S_{1/2}$ ground states and the fine-structure split $5^2P_{1/2}$ and $5^2P_{3/2}$ first excited states, labelled the D_1 and D_2 lines respectively. The D_2 line is particularly useful due to the presence of a closed transition on the $|F = 3\rangle \rightarrow |F' = 4\rangle$ hyperfine transition that is separated from the next closest transition by $20\times$ the natural linewidth of $2\pi \cdot 6.07$ MHz. This allows for efficient laser cooling which, combined with a convenient transition wavelength of 780 nm, makes a cold rubidium experiment both cheap and easy to build.

In terms of quantum-optics applicability, the two long-lived hyperfine-split ground states provide an excellent platform for performing Raman transitions and investigating Λ -[electromagnetically-induced transparency \(EIT\)](#). In addition, the D_1 transition frequency lies conveniently at twice the erbium gain band at 1560 nm. The development of highly efficient second harmonic generation techniques has allowed for use of cheap and high quality telecommunication lasers and modulators in lab-based rubidium experiments.

To summarise, rubidium is one of the easiest atomic species to work with in an atomic physics lab, and is an excellent match to the hollow-core fibre experiment. For more information regarding its specific values and properties I highly recommend the detailed compilation *Rubidium 85 D Line Data* by the legendary Daniel A. Steck [[114](#)].

1.2 Thesis Outline

This thesis is broken into five parts, each of which is described below.

[Part I](#) contains the introduction, an overview of the work, and a detailed review of the history and context of this project. The literature review also contains descriptions of various relevant physical phenomena as well as specific experimental techniques that are commonly employed in the field.

[Part II](#) contains detailed descriptions of the experimental apparatus and techniques developed throughout the project. This includes full descriptions of the interrogation protocols and data analysis software written, as well as an overview of the Monte-Carlo model built to simulate the experiment.

This thesis is primarily presented by publication, and [Part III](#) contains the four scientific journal articles written during the duration of the PhD program.

The first of these, [High-efficiency cold-atom transport into a waveguide trap](#), is the direct result of majority of the experimental work done during the project. This article describes the apparatus, mathematical models, and interrogation techniques used generate the cold atoms and load them into the hollow-core fibre. The results we attained in this work show the highest number of cold atoms loaded in fibre as well as a the highest loading efficiency.

The second article, [Dual-color magic-wavelength trap for suppression of light shifts in atoms](#), describes a light-shift engineering experiment performed in which we demonstrate the to ability to compensate for the ac-Stark shift experienced by a trapped atomic ensemble. This was the first demonstration of a technique that had been long theorised in the literature, and included comparison with a detailed mathematical model, and analysis of the ultimate performance of the technique.

The third article, [Light-shift spectroscopy of optically trapped atomic ensembles](#), is a strongly mathematical work in which we present a model for the effect of the spatially varying light-shift present in a dipole trap on the atomic absorption spectrum. We show that this model can be used to extract useful physical parameters of the atomic system in-situ, with minimal perturbative effect on the ensemble.

The final article presented here, [Optimal design for spectral narrowing and fast frequency sweep of an interferometer-stabilized laser](#), is an outcome from concurrent project. The project required a narrow, highly-tunable laser source for accurate determination of the Boltzmann constant using optical Doppler broadening thermometry. The article details the insight we developed regarding the optimal design of the fibre-based laser stabilisation system, and demonstrates the effectiveness of this technique for stabilisation and sweeping of the frequency of a diode laser.

Each of these articles is presented along with context for the work and a formal statement of authorship detailing the contribution made by each author.

[Part IV](#) contains a summary of the thesis, and the project as a whole. This includes a discussion of the contribution this work has made to the field, a map for the future of this

experiment with preliminary results, and a brief outlook on the field in general.

Finally, [Part V](#) consist of a collection of short appendices containing details such as code snippets for the data processing protocols, and a detailed manual of the schematics and operation of the low-noise analog lock box developed over the course of the project.

I thank for your interest in the work of myself and my colleagues, and wish you the best of luck should you continue reading.

1.3 Publications, Conference Attendance, and awards

The following is a list of the publications, conference attendance, and awards received during the period of this PhD.

Publications

- A. P. HILTON, P. S. LIGHT, L. TALBOT, AND A. N. LUITEN, *Optimal design for spectral narrowing and fast frequency sweep of an interferometer-stabilized laser*, Opt. Lett. **45**, 45 (2020). doi: [10.1364/OL.45.000045](https://doi.org/10.1364/OL.45.000045)
- A. P. HILTON, C. PERRELLA, A. N. LUITEN, AND P. S. LIGHT, *Dual-Color Magic-Wavelength Trap for Suppression of Light Shifts in Atoms*, Phys. Rev. Appl. **11**, 024065 (2019). doi: [10.1103/PhysRevApplied.11.024065](https://doi.org/10.1103/PhysRevApplied.11.024065)
- A. P. HILTON, C. PERRELLA, F. BENABID, B. M. SPARKES, A. N. LUITEN, AND P. S. LIGHT, *High-efficiency cold-atom transport into a waveguide trap*, Phys. Rev. Appl. **10**, 044034 (2018). doi: [10.1103/PhysRevApplied.10.044034](https://doi.org/10.1103/PhysRevApplied.10.044034)
- S. LEE, M. S. HEO, T. Y. KWON, H. G. HONG, S. B. LEE, A. P. HILTON, A. N. LUITEN, J. G. HARTNETT, AND S. E. PARK, *Operating atomic fountain clock using robust DBR laser: Short-term stability analysis*, IEEE Trans. Instrum. Meas. **66**, 1349 (2017). doi: [10.1109/TIM.2016.2637559](https://doi.org/10.1109/TIM.2016.2637559)
- W. A. AL-ASHWAL, A. HILTON, A. N. LUITEN, AND J. G. HARTNETT, *Low Phase Noise Frequency Synthesis for Ultrastable x-Band Oscillators*, IEEE Microw. Wirel. Components Lett. **27**, 392 (2017). doi: [10.1109/LMWC.2017.2678400](https://doi.org/10.1109/LMWC.2017.2678400)
- M. S. HEO, S. E. PARK, W. K. LEE, S. B. LEE, H. G. HONG, T. Y. KWON, C. Y. PARK, D. H. YU, G. SANTARELLI, A. P. HILTON, A. N. LUITEN, AND J. G. HARTNETT, *Drift-Compensated Low-Noise Frequency Synthesis Based on a cryoCSO for the KRISS-F1*, IEEE Trans. Instrum. Meas. **66**, 1343 (2016). doi: [10.1109/TIM.2016.2620187](https://doi.org/10.1109/TIM.2016.2620187)
- P. S. LIGHT, A. P. HILTON, R. T. WHITE, C. PERRELLA, J. D. ANSTIE, J. G. HARTNETT, G. SANTARELLI, AND A. N. LUITEN, *Bidirectional microwave and optical signal dissemination*, Opt. Lett. **41**, 1014 (2016). doi: [10.1364/OL.41.001014](https://doi.org/10.1364/OL.41.001014)

Conference Attendance

- A. P. HILTON, C. PERRELLA, F. BENABID, B. M. SPARKES, A. N. LUITEN, AND P. S. LIGHT,
Engineering Ultra-Strong Light-Atom Interaction Using Cold Atom Filled Hollow Core Fibre,
(Poster) ICAP 2018 Summer School, Barcelona, Spain.
- A. P. HILTON, C. PERRELLA, F. BENABID, B. M. SPARKES, A. N. LUITEN, AND P. S. LIGHT,
High-Efficiency Cold-Atom Transport into a Waveguide Trap,
(Poster) ICAP 2018, Barcelona, Spain.
- A. P. HILTON, C. PERRELLA, B. M. SPARKES, A. N. LUITEN, AND P. S. LIGHT,
Exploring the Limits of Ultra-Strong Light Atom Interaction in a Waveguide-trapped Cold Atoms,
(Oral Presentation) ANZCOP 2017, Queenstown, New Zealand.
- A. P. HILTON, A. N. LUITEN, AND P. S. LIGHT,
Loading of Magneto-Optically Cooled Rubidium Atoms into Hollow-Core Photonic-Crystal Fibre,
(Oral Presentation) AIP Congress 2016, Brisbane, Australia.
- A. P. HILTON, C. PERRELLA, P. S. LIGHT, G. SANTARELLI, J. ANSTIE, AND A. N. LUITEN,
Bidirectional microwave and optical signal dissemination,
(Oral Presentation) ANZCOP 2015, Adelaide, Australia.

Awards

- IPAS BEST PAPER AWARD 2019 — OUTREACH CATEGORY
Won the award for best paper in 2019 for the outreach category based on the media coverage and international attention received for my paper titled *High-efficiency cold-atom transport into a waveguide trap*.

A HISTORY OF THE FIELD

"We investigate the theory of atomic waveguides made from hollow optical fibers and find no fundamental obstacles to their practical realization."

*Atomic Waveguides and Cavities from Hollow Optical
Fibers*

Savage *et al.* 1993

2.1 Overview

Cold atoms have been used in state-of-the-art quantum optics experiments since the first theoretical [4, 41, 128, 129] and experimental [90, 91, 93, 94] demonstrations of laser cooling in the 1970s and 1980s. While interesting on their own right, the ability to interface strongly interacting particles with microstructured materials holds great interest. The geometry of the material can be tailored to strengthen certain attributes, suppress others, or produce entirely new behaviours. This thesis involves the loading of cold rubidium atoms into one example of a microstructured material, a hollow-core optical fibre, which enhances the interaction between atoms and guided light pulses in a long quasi-one-dimensional medium.

Here I present an overview of the historical development of this field, providing context for the thesis as a whole. This is written chiefly in chronological order, so as

to best highlight the stepwise development of the technology and methodology. It is important to also mention the work done by contemporary researchers, much of which has been discussed in person at various conferences or remote communication. I also detail other work that is relevant for specific reasons such as shared methodology or an alternative technology seeking to achieve the same goals.

2.2 Early Theoretical work

Driven by preliminary work in the transport of atoms using coherent optical fields [4, 14, 61], and the development of optical fibres for guiding light, Ol'Shanii *et al.* discussed combining these concepts to transport atoms along a hollow-core fibre for several meters [80]. The proposed setup involved a high power (1 W) laser source coupled into the fundamental Gaussian mode of a 100 μm diameter hollow optical fibre. Tuning the laser lower in frequency than a strong optical transition, referred to as 'red detuning', produces a force on the atoms towards the highest optical intensity, spatially trapping the atoms. This technique is referred to as an [optical dipole trap \(ODT\)](#), and an excellent review of this concept and implementations can be found at [38]. Implementing this technique, the trapped atoms would be prevented from interacting with the walls of the fibre. The authors showed that the flow of atoms along such a fibre could follow bends in the fibre up to a reasonable radius of curvature, and suggested the use of this method for precise delivery of atoms to a microscopic target. The publication noted that, as the guiding potential is dependent on coupling to atomic transitions, there is the ability to strongly select which atoms, isotopes, and even quantum states survive the transport process.

An alternative approach to guiding atoms through a confined geometry was proposed soon after that uses a blue detuned light field coupled into the walls of a small glass capillary or hollow fibre [70, 107]. If the transverse scale length of the guiding structure is of similar magnitude to the optical wavelength then guided modes can exist with significant intensity outside the bulk material, referred to as the evanescent field. This phenomenon, successfully used to reflect slow moving atoms from surfaces [7, 39], could be employed to repel atoms from the walls of a hollow fibre. Savage *et al.* suggest this as method for building miniature atomic waveguides and cavities.

Further work on this approach was done by Ito *et al.*, who calculated the guided modes of a cylindrical core hollow-core fibre [48]. The evanescent field of these modes decay exponentially outside the glass, becoming insignificant less than 50 nm from the inner wall. Despite this, the authors suggest that 1 mW of light detuned by only a few times

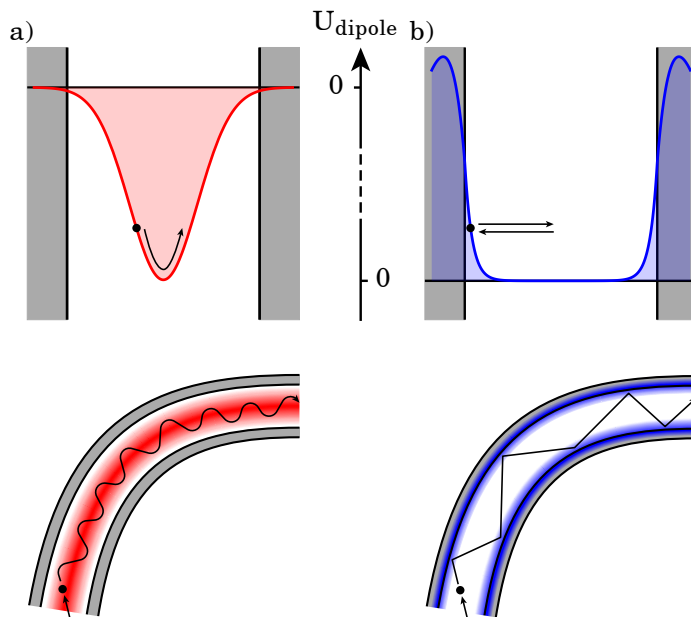


Figure 2.1: The two atomic guidance mechanisms proposed: a) tight confinement within the fibre by a red-detuned fundamental mode, and b) reflection off the walls of the fibre by a rapidly decaying blue-detuned evanescent field.

the natural linewidth above the D_2 transition in rubidium could produce a sufficiently deep guide to transport hot atoms with a temperature up to 1 mK.

These two approaches are common throughout the atom trapping community, each with its own pros and cons. Red detuned attractive traps are easy to implement: a simple Gaussian beam possesses the necessary intensity profile to strongly trap atoms, as shown in Figure 2.1 a). This beam profile is easy to generate, and is typically well matched to the guided modes of hollow waveguides. Unfortunately these traps hold the atomic sample at the location of highest optical intensity, and as such, the location of highest guide photon scattering rate. This can limit the useful time one can store a delicate quantum state without perturbation.

On the other hand, blue detuned repulsive traps hold the atoms in the region of lowest optical intensity, seen in Figure 2.1 b), resulting in weak spontaneous scattering and longer atomic lifetimes. This comes at the cost of lower trap depths for the same optical power, and significantly increased experimental complexity due to the shape of the spatial potentials required. Additionally it is difficult to manufacture waveguides capable of supporting these modes with low loss, and even more difficult to couple to these modes

exclusively. The larger core size, enforced by the need to accept higher order transverse modes, typically allows for a large number of other undesired modes that strongly overlap and complicate its use.

2.3 Hot Atomic Transport Through Glass Capillaries

Early experimental work on guiding atoms was done using glass capillaries rather than hollow-core fibre. Glass capillaries are formed from large-diameter hollow glass rods that are heated to the point of plasticity, and drawn down to small diameter, thin walled tubing. Unlike conventional optical fibre, bare capillaries are not able to guide light through the core by means total internal reflection. It is possible however to couple light through a capillary by exploiting grazing incidence reflection off the walls [103]. These are not generally considered to be true guided modes and are highly lossy – typically > 10 dB/m, and are highly sensitive to imperfections in the walls or even slight bending of the capillary. The walls of a capillary are however able to support guided modes through total internal reflection, and can be used to propagate appropriate cylindrically-symmetric modes over long distances.

The focus of much of this early work was the desire to transport hot atoms from a high-pressure source chamber to a low-pressure detection chamber, with the intent to deliver a clean, high-flux source of atoms to a specific location. A typical setup for these experiments is shown in [Figure 2.2 a](#)). The first demonstration of this technique was made by Renn *et al.* [99], in which hot rubidium atoms were transported through a 40 μm diameter, 3.1 cm long glass capillary. The optical guide consisted of tens of milliwatts of light, detuned several gigahertz red of the D_2 transition and coupled into the core of the glass capillary. There was no preparation of a specific sample in this, and the guide selects atoms that happen to be travelling towards to the core of the fibre with a sufficiently low transverse velocity. The atoms that survived the transport were directed at a hot wire and the resulting ions detected using an electron multiplier.

This technique showed a continuous flux of order 10^3 rubidium atoms per second arriving in the detection chamber, and was sensitive to the detuning of the optical guide around the atomic transition, a clear sign of optical transport. The authors were also able to show that the guide was able to function even with a bent capillary, with high optical powers permitting tighter bends.

Shortly afterwards, the same team demonstrated an atomic flux through a 20 μm -

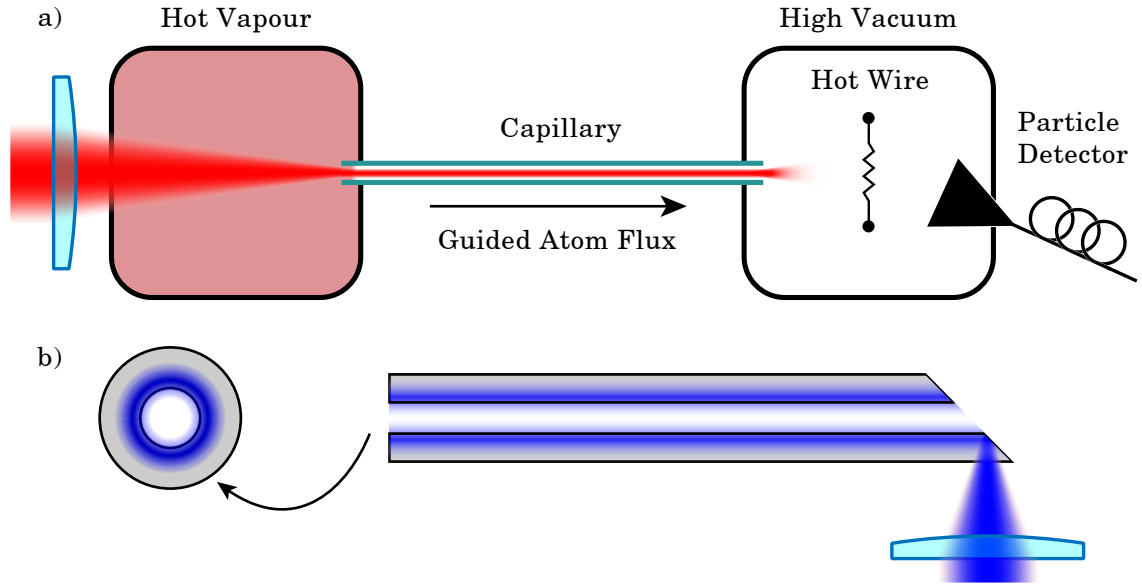


Figure 2.2: Typical implementation of a hot-atom transport experiment using a) a co-propagating red-detuned guide and b) a counter propagating blue-detuned guide coupled into a LP01 mode from the side.

diameter-core capillary using the repulsive evanescent field of a laser guided in the glass wall [98]. In this demonstration, they used an order of magnitude more optical power than their previous work, but were able to reduce the loss of atoms to the wall during transport. Due to the large core size, and the multi-mode nature of both the glass wall and the hollow core, a small amount of blue detuned light couples into the core. This interacts with the atoms in transport, producing force towards the lossy wall of the core. This was overcome by including a weak attractive optical guide coupled into the core to counterbalance the residual repulsive field. The authors note they intended to move to very small core capillaries ($1.4\ \mu\text{m}$), which would allow the transportation of atoms over long distances using only the evanescent guide.

The same year, a purely repulsive evanescent field guide was presented by Ito *et al.* [46], using very narrow capillaries with diameters of $2\ \mu\text{m}$ and $7\ \mu\text{m}$. In this work, the guide laser transports the output of a collimated thermal beam of rubidium atoms through a 3 cm long capillary. The atoms were detected using two-step photo-ionisation, allowing both isotopes and both hyperfine ground states to be resolved. The authors further developed the method for coupling the optical guide beam into the capillary walls by introducing a 45° cut to the end of the capillary [47]. The beam entered the chamber

perpendicular the axis of the capillary and was focused into the external wall opposite the cut, undergoing total internal reflection and coupling strongly into guided modes of the capillary wall, as illustrated in [Figure 2.2 b](#)). The authors reported 38 % coupling efficiency of the guide beam, and are able to selectively excite the desired guided mode.

In 1997 a detailed paper was published by Renn *et al.* [100]. This work developed a strong theoretical model for the transport of hot atoms through hollow glass capillaries using the red detuned grazing incidence reflection guide technique. The result of this model was a set of power law dependencies of the transport efficiency in the high- and low- intensity limits. The authors also describe a heating mechanism expected to limit the effectiveness at high guide intensities. In brief, this mechanism dominates when spontaneous absorption is high, resulting in significant likelihood of the atom being excited. This excited state experiences the same magnitude of trapping potential as the ground state, but with opposite sign, becoming repulsive. As absorption is mostly likely at the peak optical intensity, excited atoms are likely to be repelled strongly outwards before relaxing to the ground state, arriving at a higher transverse radius than where they started, and hence with a larger trapping potential. Over multiple cycles of this process the atom gains not only significant energy in the direction of the guide laser field, but also in the transverse plane, resulting in heating. This is recognisable as the inverse of the Sisyphus cooling process, used to cool atoms below the Doppler limit.

Renn *et al.* compared their model to a detailed experimental study of the transport efficiency for a wide range of guide powers, detunings, and fibre bend radii, qualitatively identifying the predicted heating process. The authors show that even a small bend in the capillary is able to strongly mitigate heating and suggest that in blue repulsive traps the same mechanism may present as transverse cooling.

This marks the end of early investigation into the use of [ODTs](#) for transporting hot atomic samples through thin glass capillaries. During this period both the red attractive traps and blue repulsive evanescent-field traps suggested in the original theoretical works were demonstrated to good effect by a number of research groups. Key limitations identified by the community were the strong optical losses in grazing incidence reflection guidance experiments, and difficulty coupling to the necessary modes used in evanescent field guidance experiments. These problems limited the useful distance of atom transportation to a few centimetres. No experiments were performed on atoms during transport, and results were primarily collected using various ionisation techniques, limiting the resolution to the isotope, or perhaps the specific hyperfine ground state.

Never-the-less, this era set the foundation for the use of micrometer-diameter glass capillaries as atomic waveguides.

2.4 Transportation of Laser Cooled Atoms Through Glass Capillaries

A natural extension of the work with hot atoms, given the parallel development of laser cooled atomic systems, were attempts to transport cold atoms through hollow glass capillaries. A key motivation for this work was the ability to have extremely low background gas pressure vacuum chambers to store and manipulate cold atom ensembles. The main source of atom loss in such a system is due to collisions with stray hot atoms of the same species. The lower the pressure one can achieve in the chamber, the longer the atomic sample will survive. This is however at odds with the need for an abundance of atoms to catch and cool in order to build a large cold atom ensemble in the first place. An obvious solution is to use one high pressure chamber to catch and cool atoms, before funnelling them through a narrow aperture into an ultra high vacuum science chamber. A nice solution to this would be an [ODT](#) guide coupled through a glass capillary.

The chief difference between transporting hot and cold atoms is the significant difference in velocity along the longitudinal direction, which may be many orders of magnitude lower for the cold atoms. Hot atoms transported through a capillary may only interact with the walls a few times (18 reflections by Renn *et al.* [99]), while cold atoms will spend a relatively long time in transit. This makes cold atoms more sensitive to both loss and heating mechanisms present inside the fibre.

The first demonstration of transporting cold atoms through capillaries was presented in 1998 by Wokurka *et al.* in a series of conference papers [130, 131]. The authors described a laser cooled beam of metastable neon coupled from a 2-D [magneto optical trap \(MOT\)](#) into a range of glass capillaries with cores between 20 μm and 250 μm , using both red detuned attractive and blue detuned repulsive guides. They used tens of milliwatts of optical power and successfully transported the atoms through the capillaries with varying levels of efficiency. A key limitation appeared to be problematic heating effects at high intensities that lead to loss of atoms.

Following this work, Dall *et al.* demonstrated the transport of cold metastable helium through a variety of square and circular capillary geometries and sizes [30]. The authors

used tens of milliwatts of guide power coupled into the walls of the glass capillaries, and show clear detection of atoms at the output of the capillary using a *Channeltron* particle incidence detector. The key source of atom loss in the system was identified to be the difficulty in coupling to a single, low order optical mode. As a result, the interplay between many higher-order modes produces an optical intensity that is highly speckled with areas where there is no trapping potential. It is suggested that careful design and fabrication of the capillaries could lead to single mode guidance in the glass wall and a significant improvement in efficiency.

Finally for this era, Müller *et al.* were able to transport a [low velocity intense source \(LVIS\)](#) beam of rubidium atoms from a [MOT](#) through a glass capillary [75]. In this work the authors used a pinhole-bored mirror as a retroreflector for one of the [MOT](#) beams, with a 23 cm long, 100 μm inner-diameter capillary located in the bore hole. The other end of the fibre was directed into a secondary vacuum chamber with a standard hot wire and particle detection system. Cold atoms are pushed towards the hole in the mirror due to the unbalanced optical forces, and are guided through the capillary by several tens of milliwatts of blue-detuned laser light coupled into walls of the capillary. The authors noted that the geometry of the coupling optics resulted in highly multi-mode guidance of light in the walls, producing a strongly speckled trap. Nonetheless a flux of $\sim 6 \times 10^5/\text{s}$ was generated using this technique, and the use of a push on the $|F = 2\rangle \rightarrow |F' = 3\rangle$ cycling transition before the hot wire allowed for the distinction between atoms transported in each of the ground states.

This work is specifically noteworthy as it was the first demonstration of interrogation of the atoms while in transport – a key step towards the use of these waveguides as platforms for application rather than transportation. The authors used a microwave delivery antenna to apply a π -pulse to the atom flux, coherently driving population on $|F = 1, mF = 0\rangle \rightarrow |F' = 2, mF' = 0\rangle$ while in the capillary. The populations were read out after the fibre, and the narrow microwave transition was found to have an inhomogeneous broadening of several kilohertz above the Fourier-limited width of 100 Hz measured for the free-space [LVIS](#) beam. This broadening was stated to be due to AC-Stark shift of the internal states by the presence of the guide beam, a recurring problem with future work. Despite residual broadening, the authors clearly demonstrate the ability to preserve the internal states of atoms transported through a narrow waveguide and over relatively long distances using an optical guides, a vital stepping stone on the path towards a useful platform for quantum optics.

Save for one or two other papers, the interest in hollow glass capillaries for atom transport ends here. The work done in this period showed a strong improvement in experimental techniques, with detection schemes becoming more specific and allowing for analysis of the evolution of internal states during the transport process. The predominant mindset of the time was the use of these capillaries as delivery mechanisms with which one could load an extremely low background pressure ensemble for further experiment. The development of true hollow-core optical fibre in the early 2000s changed this by allowing a low-loss optical mode to exist in the same physical space as the atomic sample.

2.5 Development of Photonic Crystal Fibre

A new type of optical fibre was developed in the 1990s at the Universities of Southampton and Bath and was coined [photonic crystal fibre \(PCF\)](#) due to the periodic microstructure it employed to guide light. The seminal publication in this field is taken to be "Single-Mode Photonic Band Gap Guidance of Light in Air" by Cregan *et al.* [28], in which the authors describe two new processes by which light can be confined to the core of a fibre. The new guidance mechanisms allowed for the creation of optical fibre in which the core has a lower refractive index than the cladding, and could even be empty. The clear advantage of this fibre was the ability to functionalise it – to turn the fibre into a physics package by coating the inside surface, filling it with liquids or gases, or even atomic samples. Here I briefly describe several relevant types of [PCF](#), and the physics behind how they guide light. For a more detailed description, I recommend one of the many excellent reviews of the field, such as by Russell [105], Poletti *et al.* [92], or Markos *et al.* [69].

2.5.1 Solid Core Fibre

The most commonly used optical fibre is step-index fibre which can be found strewn across every [AMO](#) lab in the world, and in large bundles between telecommunication hubs. The physics behind this technology is very simple: by using a high refractive index core (n_2) and a low refractive index cladding (n_1), light incident at a sufficiently small angle is perfectly reflected from the interface between n_2 and n_1 due to [total internal reflection \(TIR\)](#). Using a core material with sufficiently low loss allows the light to propagate over long distances and around tight corners via many interactions with the walls. This is illustrated in [Figure 2.3 a\)](#) and [c\)](#), where the critical angle (θ_c) that is necessary to produce [TIR](#) is given by

$$\theta_c = \arcsin(n_1/n_2). \tag{2.1}$$

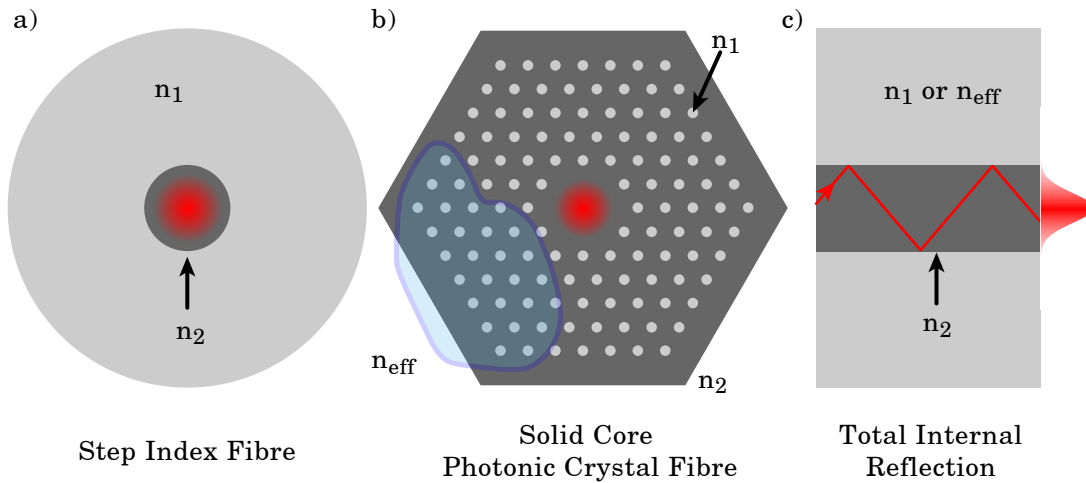


Figure 2.3: a) Conventional step-index fibre with $n_1 < n_2$, b) solid-core [photonic crystal fibre \(PCF\)](#) with an effective cladding index of $n_{\text{eff}} < n_2$, and c) the relevant guidance mechanism: total internal reflection.

In typical [single-mode optical fibre \(SMF\)](#) the cladding is a single layer outside the core, and the difference in refractive indices is produced via careful introduction of dopants. An alternative design was presented by Cregan *et al.* in which the cladding is formed from a periodic array of low index rods or hollow tubes, with the core defined by one or several missing elements, as depicted in [Figure 2.3 b\)](#). Fabrication of this design is more complicated, as the structure is assembled by hand using long glass rods approximately 1 mm across [56]. The rods are stacked in the desired geometry with high or low index material used as required. Alternatively, hollow capillaries can be introduced when a hole is desired in the final design. This assembly, named the stack, is then heated in a fibre draw tower and drawn down from a few centimetres across into canes roughly 3 mm to 4 mm in diameter. These canes are once again heated and drawn into optical fibre, with final diameter of typically around 300 μm . This fabrication process is known as ‘stack and draw’, as opposed to other methods for making microstructured optical fibres such as die extrusion, and preform milling.

The guidance mechanism in solid core [PCF](#) can be thought of as predominantly determined by the interaction between the bulk material core and the effective bulk properties of the cladding. Using this simplification, the guidance mechanism is described as [modified total internal reflection \(M-TIR\)](#), where the refractive index of the cladding n_1 has been replaced by n_{eff} , the effective refractive index. As this term is a function

of the geometry of the cladding rods, in addition to both refractive indices and optical wavelength, it provides additional degrees of freedom that can be manipulated to modify the guidance properties of the fibre.

Fibres of this design have found use in a range of applications, including the development of endlessly single mode optical fibre [13], super-continuum generation [96], and the generation, manipulation, and propagation of orbital angular momentum modes of light [106]. While these applications are of strong interest to both commercial and academic fields the presence of a solid core prevents the use of these fibres as atom waveguides.

2.5.2 Bandgap Fibre

While TIR and M-TIR are highly effective mechanisms for confining light, they require a cladding with lower refractive index than the core. This limitation prevents their use in the development of hollow-core fibre, as currently no materials exist in the optical domain with a refractive index lower than vacuum. On the other hand, grazing incidence reflection can guide light along the empty core of a capillary, and while Maxwell's equations can be solved to find guided modes [68], in reality these solutions are highly sensitive to stress, bending, and surface quality of the waveguide. These modes typically have attenuation lengths on the order of millimetres, making them inappropriate for use in cold atom guidance systems.

A third approach to prevent propagation of light from the core into the cladding is to use Bragg reflection, the coherent reflection of light off of a periodic structure. The physical process behind this phenomena is the following: light incident on a partially reflective surface, such as the interface between two materials with different refractive indices, is both transmitted and reflected. If the materials are periodically layered, as depicted in Figure 2.4, then the transmitted light will once again partially reflect off a second deeper interface, with this new reflection returning to arrive at the first interface. The returned light from the second interface ($i = 1$) will overlap with the first surface reflection ($i = 0$) and propagate in the same direction, having accumulated some optical phase determined by its wavelength and the path lengths and refractive indices of the layered materials. Should the accumulated phase at the output port be an integer multiple of 2π then there will be constructive interference and the second reflection will efficiently escape the material. This same process can be iteratively mapped out to each interface ($i = 2, 3, 4, \dots$), and if the anti-resonant condition is met, the reflection will be efficient in each case, resulting in a near perfect reflection of the beam off of the surface.

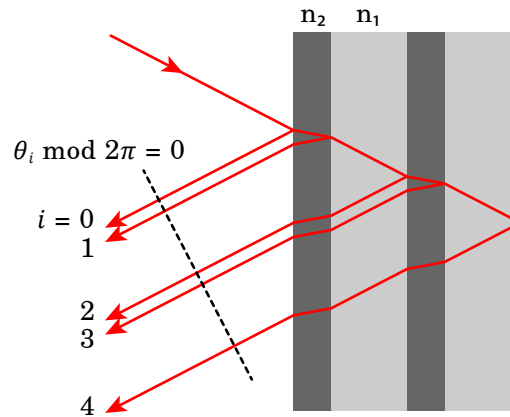


Figure 2.4: Reflection of light from a layered medium by Bragg reflection, in which the paths taken by the reflection from each iterative interface constructively interfere upon returning to input face of the surface, resulting in efficient reflection of the beam.

This concept is used widely in distributed Bragg reflectors such as dielectric mirrors and fibre Bragg cavities. These devices will have some wavelength range over which this process results in high reflectivity, and as such, in which light is forbidden from propagating through the periodic structure. This range is termed the photonic stopband, or, in reference to a similar process in solid state physics, the photonic bandgap. While the example provided was for a one-dimensional case, the same process can be applied to two or three dimensions, in which the periodic structure exists as a surface, or volume. [Hollow-core photonic bandgap fibre \(HC-PBF\)](#) employs a two-dimensional array of high refractive index rods suspended in a thin web to produce this effect in 2-D, as depicted in [Figure 2.5](#). The guided mode exists in a single or multi-cell defect in the photonic crystal where the geometry has been designed to produce a bandgap for all wave vectors in the first Brillouin zone of the reciprocal lattice, and as such, for the entire cladding. The ability to tailor the cladding structure has demonstrated an enormous range of possible geometries that will guide light, each with distinct traits and uses [104].

[HC-PBF](#) can be designed to support a single Gaussian-like mode, and can be tuned to any wavelength range that does not possess additional loss mechanisms, such as absorption by the cladding material. As most of the light propagates in the empty core, the loss in type of fibre can be extremely low. Early work achieved attenuation of 13 dB/m in 2003 [111] followed two years later by Roberts *et al.* demonstrating 1.2 dB/km [101] in a superior fibre design, suggesting that improved fabrication could reduce this value to as low as 0.1 dB/km – better than conventional low-loss step-index fibre. The spectral width of the bandgap is limited by the nature of Bragg reflections, and is typically up to 20 % of

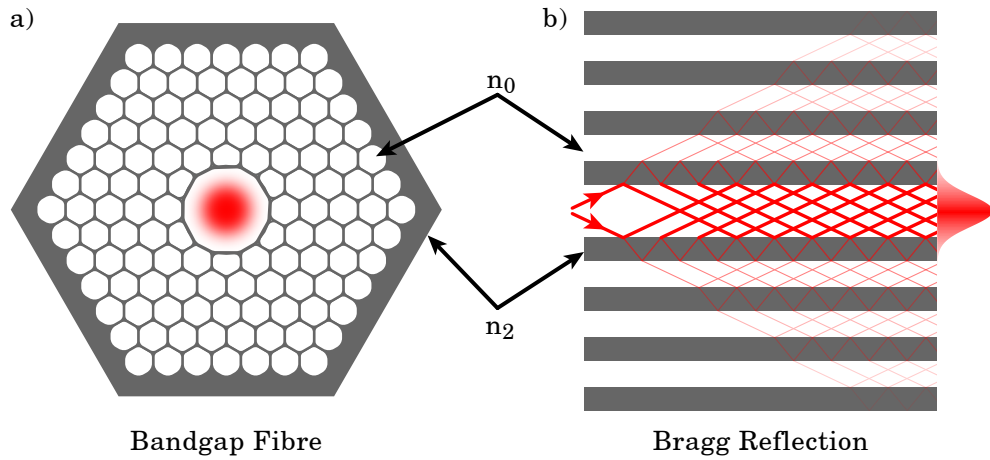


Figure 2.5: a) **Hollow-core photonic bandgap fibre (HC-PBF)** with $n_0 < n_2$, and $n_0 \approx 1$, b) The relevant guidance mechanism: Bragg reflection.

the stopband centre frequency. This roughly matches the calculated fractional bandwidth of a distributed Bragg reflector given by

$$\frac{\Delta f_0}{f_0} = \frac{4}{\pi} \arcsin\left(\frac{n_2 - n_1}{n_2 + n_1}\right) \quad (2.2)$$

from [81]. In the case of an air – silica interface at 780 nm where $n_1 = 1$ and $n_2 = 1.45$, the fractional bandwidth is 24 %.

In summary, **HC-PBF** are devices capable of supporting low-loss optical modes over a moderate spectral window. The key disadvantages of these fibres are the limited spectral bandwidth achievable and the complexity of fabrication. Along these lines, work has been done to produce fibres with multiple bandgaps in order to bridge spectral regions of interest [64]. Another downside is the small amount of light that exists within the walls of the core due to imperfect fabrication of the photonic crystal geometry. This residual surface mode allows for undesired interaction with surface contaminants as well as introducing sensitivity to the quality of the core walls.

2.5.3 Kagome-Lattice Fibre

A significant downside of **HC-PBF** is the complexity of the fabrication process. One attempt at reducing this problem was made by using only hollow capillaries, and not independently pressurising them during drawing of the cane. The resulting fibre had an entirely different structure in the cladding, with the struts forming a trihexagonal tiling pattern as depicted in **Figure 2.6 a)** and is known as kagome-lattice fibre after the

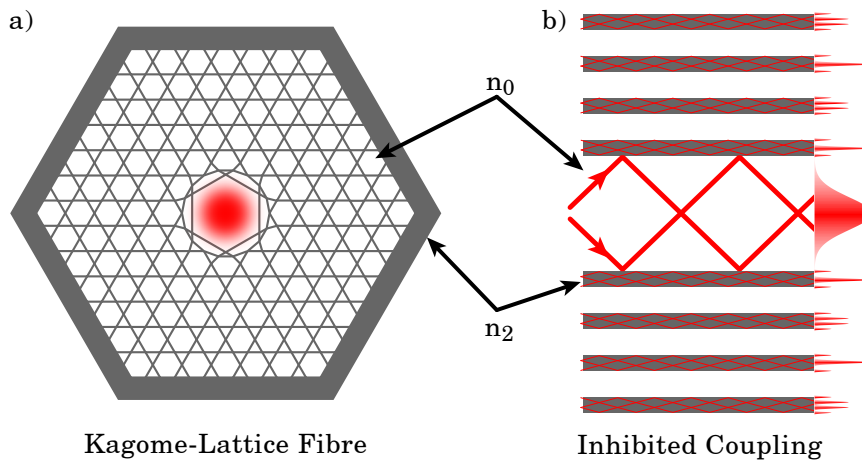


Figure 2.6: a) Kagome lattice fibre with $n_0 < n_2$, and $n_0 \approx 1$, b) the relevant guidance mechanism: Inhibited coupling.

Japanese basket weaving pattern of the same geometry. This fibre does not guide using a photonic bandgap despite some superficial similarities. Unlike HC-PBF, the mechanism by which kagome-lattice fibre guides light is still a contentious topic.

While its fabrication was unintentional, this new fibre showed an extremely wide transmission band, guiding light from below 400 nm to above 1650 nm with less than 3 dB/m. The first mention in the literature of this new fibre was made by Benabid *et al.* in 2002 [11], where the authors use the wide transmission band, low dispersion, and tight optical confinement to reduce the power threshold of [stimulated Raman scattering \(SRS\)](#) in the hydrogen-filled fibre by two orders of magnitude. Notably, the guidance band covers the entire visible spectrum (and then some), allowing the fibre to guide ‘white light’.

This design was further developed with a range of core sizes [24] and materials, consistently demonstrated extremely wide-band guidance with sub dB/m loss [2]. In-depth wave vector analysis of the kagome cladding shows that it does not possess a photonic bandgap [9, 82], and that the density of states in the cladding is low but non-zero in the guidance range. It was also found that the specific kagome lattice pattern is not necessary to demonstrate this process, with square-lattice designs showing similar guidance properties [27]. The current hypothesis for confinement of light to the core of kagome-lattice fibre is ‘inhibited coupling’ guidance.

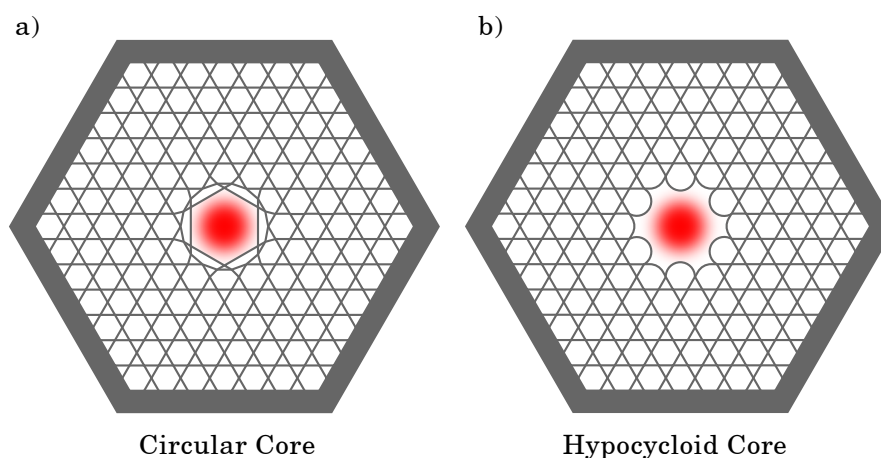


Figure 2.7: Kagome lattice fibres with a) circular core and b) hypocycloid core geometries.

Inhibited coupling can be described by the following argument: for light to couple from one spatial mode to another, there must be a non-zero overlap between the transverse electric field profiles. If all the modes that exist in the cladding have extremely disparate spatial profiles to the modes in the core, then there is no channel for which the light can escape. For kagome-lattice fibre the cladding modes show extremely-high spatial-frequency structure along the longitudinal direction of the walls that are akin to the resonant modes in whispering-gallery mode resonators. This modal mismatch is depicted in [Figure 2.6 b](#)), although a more colourful and realistic demonstration can be found in Figure 1 of *Generation and Photonic Guidance of Multi-Octave Optical-Frequency Combs* by Couny *et al.* [25].

A significant advancement of kagome-lattice fibre was made with the realisation that predominant sources of loss were residual light in the walls of the core, where the lattice has been deformed by the draw method. These losses can be reduced by elongating the interior walls of the cladding, and extending the separation of fundamental mode and the first nodes of the cladding lattice [124]. This design is named ‘hypocycloid-core’ kagome-lattice fibre and the difference between this geometry and the original is shown in [Figure 2.7](#). The result of this work was to push down the attenuation in kagome-lattice fibre from several dB/m down to 0.18 dB/m from 850 nm to 1750 nm, limited by nonuniformity in the stack during the fabrication process.

Significant work has been done on describing the guiding mechanisms of kagome-lattice fibre and attempting to predict the ideal structure and geometry to achieve both

low-loss and wide spectral guidance [18, 19]. Additionally there is much interest in the effects of bending on the performance of the fibre, and how to mitigate these perturbations by modifying the numbers of cladding rings, the pitch of these rings, the curvature of the core walls, and width of the walls [1, 31]. Generally the results show that thinner walls, more cladding rings, and stronger curvature of the interior walls produce the lowest loss and most robust guidance properties, with recent demonstrations showing attenuation of less than 10 dB/km [71, 126] in application relevant wavelength ranges.

Further attempts to simplify the fabrication process produced a subcategory of devices that are broadly labelled as ‘negative-curvature’ fibres, and which typically possess only a single ring of cladding structure. The guidance mechanism present is essentially the same as for hypocycloid-core kagome-lattice fibre – inhibited (or anti-resonant) coupling between the core and cladding modes prevents leakage and hence loss of power from the core. These fibres have excellent attenuation, with <0.1 dB/m over a 650 nm range in the near infrared, albeit with an increased sensitivity to bending, with spectral width dropping rapidly for bend radii below 15 cm [8]. There is much interest in these structures due to their ease of production and the potential for using exotic materials in their construction, opening up hollow-core guidance in otherwise inaccessible areas of the spectrum. An excellent review of this field was done by Wei *et al.* [125].

In summary, kagome-lattice fibre is an alternative to HC-PBF with extremely broad transmission windows that are not limited by the edge of the cladding stopband. This type of fibre has matured quickly and is easier to fabricate than HC-PBF, with better tolerance of bending, excellent mode shapes, and extremely low dispersion. Unfortunately kagome-lattice fibre has yet to reach the extremely low attenuation of certain cutting edge HC-PBF. However, over short lengths such as are used in bench-top lab experiments, there is little difference between losses of 0.1 dB/km, 1 dB/km and 10 dB/km. This fibre is of particular interest for interfacing with cold-atom ensembles due to the very low power fraction at the walls of the core, resulting in minimal interaction of guided light with any of the sample atoms that adhere to the surface.

2.6 Application of Thermal Vapours in Hollow-Core Fibre

While hollow-core fibre is the key to a long, pseudo-one-dimensional confinement of cold atom samples, it also presents an excellent platform for interfacing light with thermal atomic and molecular vapours. The key attributes that make hollow-core fibre interesting in this field are the ability to wrap long path lengths into small physical packages, the

high optical intensities achievable for low powers, and the high damage threshold. One use of these properties is filling a fibre with a sample and sealing the ends, producing an inline fibre micro-cell with minimal physical footprint [10]. Another is the extremely low thresholds required to generate nonlinear phenomena such as SRS [25].

In the previous section I noted specific applications of various PCF geometries as they were relevant to the development of the technology. Here I provide a broad overview of the range of uses of hollow-core fibre, as well as detail into specific cases that are more relevant to fields of AMO, quantum optics, and precision metrology.

2.6.1 Spectroscopy of Atomic Vapour in Hollow-Core Fibre

The measurable transmission of a uniform density sample of length l can be written as

$$T = \exp(-\alpha l) \tag{2.3}$$

where α is the attenuation coefficient of the sample, in units of inverse meters. Weak atomic transitions or low concentration samples both exhibit relatively weak absorption. One way to increase the strength of the light-atom interaction is to simply make l larger, which can be done using a multi-pass cell or a resonant enhancement cavity. In contrast, a very low-tech solution is to make the effective interaction length long simply by indeed making the path length very long.

Optical fibre is inherently one-dimensional and long lengths are easily managed; for example one could potentially have hundreds of meters of optical path wound around a 10 cm cylinder. Using state of the art fibre geometries it is possible to guide light over the hundreds of nanometres of spectrum necessary to fully interrogate the ro-vibrational spectra of complex organic molecules. Such a platform would have an added advantage of requiring a sample volume of significantly less than a millilitre to make such a measurement. The platform is easily filled with gas by introducing a pressure differential across the ends, see Figure 2.8, and optically interrogated using standard spectroscopy techniques. This application has not been missed, and there are many examples of the use of HC-PCF for detailed spectroscopy of weak features [35, 84, 110].

The primary limitation of the frequency resolution achievable in hollow-core fibre for spectroscopy is the greatly increased effect of transit time broadening, in which the size of guided optical mode provides an upper bound on the transverse distance over which an

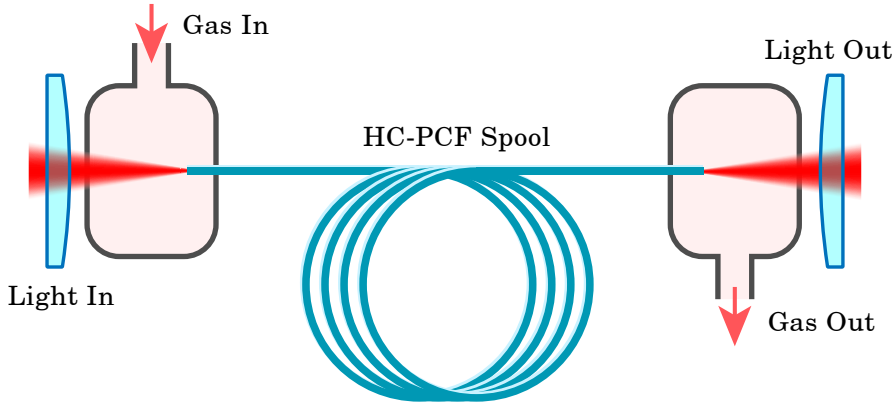


Figure 2.8: Example of a hollow-core fibre gas sensor platform for long interaction lengths.

atom can interact. This effect can be described by a most probable transit time, τ_{tt} :

$$\tau_{tt} = 2 \frac{w}{v} \quad (2.4)$$

where w is the Gaussian spot size of the optical field and v is the most probable velocity of the sample. The **full-width at half-maximum (FWHM)** of the associated inhomogeneous broadening is given by

$$\begin{aligned} \delta\nu_{tt} &= \frac{1}{2\pi} \frac{v}{w} 2\sqrt{2\ln(2)} \\ &\approx 0.4 \frac{v}{w}. \end{aligned} \quad (2.5)$$

In a typical room temperature vapour cell with 1.5 mm waist Gaussian profile laser fields and a most probable velocity of 300 m/s, the transit crossing time is 10 μ s. In comparison, atoms in a hollow-core fibre with 15 μ m waist fundamental mode will cross the field in one hundredth of the time, with a resulting broadening of 7.5 MHz. Early demonstrations of **EIT** in several μ m core, acetylene ($^{12}\text{C}_2\text{H}_2$) filled **HC-PBF** show broadening on the order of 10 MHz, which are attributed to this effect [12, 36, 40, 42, 117]. Similar experiments done with ammonia ($^{14}\text{NH}_3$) in both **HC-PBF** and kagome-lattice fibre showed pressure broadened linewidths of 25 MHz. The presence of pressure broadening was due to the high number density required to achieve a useful transmission signal, as the transition strength for ammonia is significantly weaker than that for acetylene.

One technique that can produce narrower linewidth in certain circumstances is the application of an anti-relaxation coating to the walls of the core [63], which was able

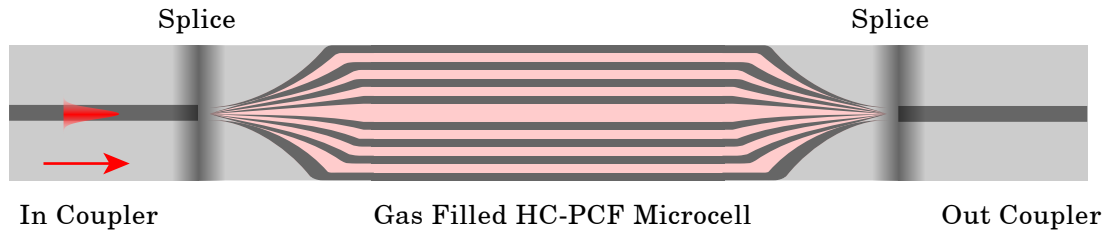


Figure 2.9: An inline fibre microcell consisting of a length of [hollow-core photonic crystal fibre \(HC-PCF\)](#) spliced to [single-mode optical fibre \(SMF\)](#) on both sides.

to reduce the linewidth contribution due to transit time from 7 MHz to 1 MHz. Other approaches include the use of larger fibre core as a trade off to reduce the transit time broadening to a level that is acceptably small [84], or the use of heavy molecules such as $^{127}\text{I}_2$ for which the most probable velocity is reduced by a factor of three over acetylene [62]. In cases where sub-Doppler resolution is not necessary, or even in high resolution applications in which megahertz linewidths are acceptable, this platform is very suitable. To reach sub-megahertz frequency resolution it would be necessary to either cool the atomic sample to reduce the crossing time or develop significantly better anti-relaxing coatings.

2.6.2 Inline Fibre Microcells

An alternative to the open-ended fibre with continuous gas flow described above is the sealed fibre microcell. In this application an atomic or molecular sample is loaded into a segment of [HC-PCF](#) which is then sealed and fused to conventional optical fibre on both ends, as depicted in [Figure 2.9](#). Once sealed the cell becomes a passive device with no vacuum pumps, gas flow, heating or other apparatus required. This platform is very appealing for packaged systems, with fibre connectivity guaranteeing reliable coupling and resilience to external motion.

This design was proposed by Benabid *et al.*, in which the authors demonstrate both a hydrogen filled cell for efficient and low-threshold generation of [SRS](#), and an acetylene filled microcell for use as a compact frequency standard [10]. The [HC-PCF](#) to [SMF](#) join was made with a fusion splicer with typical losses of ~ 1 dB. While far inferior to the sub 0.1 dB splices achieved between two sections of [SMF](#), the loss is low enough to achieve effective delivery and collection of interrogation light. Continued work on this system demonstrated sub-Doppler features in acetylene with a similar microcell design, with the

device being sturdy enough to survive being cooled to 77 K [26].

The use of fibre microcells as compact frequency standards was further investigated by Knabe *et al.* in 2009 [55], and Wang *et al.* in 2013 [123]. The authors undertook an analysis of the dependence of frequency stability on fibre size and type, using a selection of **HC-PBF** and kagome-lattice fibres with cores ranging from 10 μm to 70 μm . The results showed a clear advantage to using larger core diameters to increase τ_{tt} , and a preference for kagome-lattice fibre due to the cleaner fundamental mode, with less optical power transmitted in the walls. This is particularly important from an accuracy standpoint as light in the cladding is more strongly affected by changes in wavelength and temperature variations, introducing sources of frequency drift.

The key downsides to the development of these devices are splice losses and contamination of the microcell during the splicing process. Work done by Light *et al.* showed that while fibre microcells could be filled with even highly corrosive samples such as $^{127}\text{I}_2$, the performance was significantly degraded by contaminants [62]. Recent work done with short, high pressure acetylene filled microcells showed difficulties due to étalon-like features from the sealing splices, and frequency offsets due to residual contamination [45].

2.6.3 High Optical Depth Generation (LIAD)

A constant push in the field of **AMO** is the need for stronger light-atom interaction, and as such, higher **OD**. One technique for generating strong interaction is by dramatically increasing the number density of the atomic absorbers. In systems using alkali metals such as rubidium or caesium this can be achieved by increasing the temperature of the environment, as the vapour pressure scales exponentially with temperature. The downside to this is that higher temperatures result in faster atoms, collisional broadening, and shorter transit times. An alternative was developed in the 1990s by Gozzini *et al.*, in which high number densities can be temporarily produced by a process named **light-induced atomic desorption (LIAD)** [37]. The underlying mechanism behind **LIAD** is not well understood, but I will present a brief description of the process below.

LIAD has typically been demonstrated in macroscopic vapour cells coated in some form of anti-relaxation film such as paraffin; however I focus on the process as it has been applied to rubidium-filled hollow-core fibre, with reference to **Figure 2.10**. Here solvent-based self-assembled coatings such as octadecyldimethylmethoxysilane are used

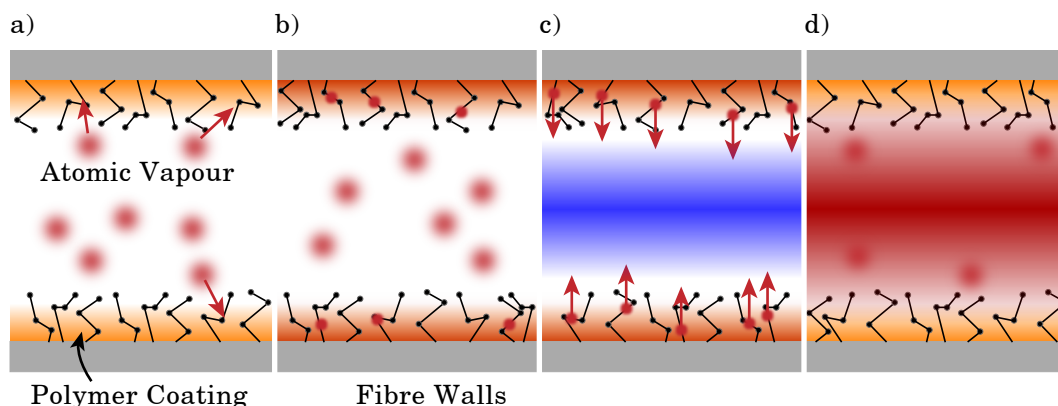


Figure 2.10: The **light-induced atomic desorption (LIAD)** process. a) An atomic vapour (dark-red) is introduced to a polymer-coated glass cell or fibre and begins to adsorb into the coating. b) Over time a steady state is reached with a low pressure of gas-phase atoms in the core and a high density of nanoclusters inside the polymer film. c) A high powered laser (blue) induces desorption of the nanoclusters from the film. d) The resulting vapour pressure is increased far above that for an ideal gas of the same temperature, producing a high number-density environment that will slowly be reabsorbed into nanoclusters, as in a).

as they can be introduced into the fibre, allowed to adhere to the core, and then flushed, resulting in a monolayer. When the fibre is exposed to a rubidium vapour, atoms are adsorbed into the coating layer forming nanoclusters (a) [52]. Over time (potentially many months), the rate of loss of atoms into the coating matches the rate of release of atoms from the coating due to thermal processes, and a steady state pressure is reached (b). A high-power laser is then coupled to the fibre where the residual intensity at the walls expels atoms from the nanoclusters back into the gas phase (c). The vapour pressure in the fibre core rises dramatically, as there can be a large number of atoms sequestered in the polymer film (d). Over time the high density of atoms decreases as they either exit the fibre or are reabsorbed into the coating, eventually returning to a steady state pressure.

This process was first used in a fibre platform by Ghosh *et al.* where the authors demonstrated an increase in atom number by nearly three orders of magnitude to a total *OD* of over 2000 with the application of a 1 mW desorption beam [35]. The very low optical power needed to produce this effect is due to the small core diameter used (6 μm), and a strong advantage to this platform. Further development of this technique came with the discovery that the same process was capable of produce large atom numbers without the need for polymer coatings [109, 110]. The authors suggest that the porosity of the glass walls could allow for adsorption and desorption processes in a similar fashion

to the polymer coating. The ability to effectively switch on and off the number density with a relatively low power optical field is a promising feature for a deployable platform, as it extends the operational lifetime of the device and allows the vacuum systems to be predominantly under high vacuum. This is a significant advantage over high-temperature, high-pressure alkali-metal systems that have severe corrosion problems with any non-inert material inside the chamber.

The use of **LIAD** was extended to large-core kagome-lattice fibre by Sprague *et al.*, where tens of milliwatts of optical power were used to generate extremely high optical depths of 3×10^3 [112], and later 235×10^3 [52]. A point of interest in these experiments is the relatively long-lived nature of the high number-density state, with **ODs** of 1000 for over three hours. A key limitation to this useful time is the escape of atoms from the fibre ends, which the authors note could be addressed by sealing the fibre on both ends, as discussed in [subsection 2.6.2](#). This was also discussed by Donvaskar *et al.* [32] in the concept of building a contained rubidium vapour cell for nonlinear optics that could be run outside a vacuum system.

High **OD** generation in room-temperature vapour-filled hollow-core fibre is an extremely attractive platform for nonlinear optics experiments. These systems offer minimally complicated experimental setups with tight optical confinement and strong interactions, with the main cost being the high relaxation rate of the medium due to hot thermal distributions and small crossing times. However there are many applications for which lifetimes of tens to hundreds of nanoseconds is perfectly acceptable, such as ultra-fast optics, high-bandwidth optical memories, and nonlinear optics. In these cases there is no need to cool the atomic medium.

2.6.4 Efficient Nonlinear Optics

The combination of high the **ODs**, high optical intensities, and low loss offered by thermal-atom filled hollow-core fibres result in an exceptional platform for exploring nonlinear optics.

Many systems are well described by linear optics, in which the material response is linear in the applied field. A material that behaves in this way is known as a linear material, and its response to an oscillating electric field is given by its dielectric polarization density:

$$\mathbf{P} = \epsilon_0 \chi^{(1)} \mathbf{E} \tag{2.6}$$

where $\chi^{(1)}$ is the first order susceptibility of the material. In this case, the response of a system to a set of input fields can be decomposed into the sum of the response for each field independently.

In contrast, a nonlinear material has a higher order susceptibilities $\chi^{(n)}$ which allow for both self-modulation and cross-coupling between electromagnetic fields. This interaction can be given by a Taylor expansion out to the relevant order in \mathbf{E} :

$$\mathbf{P}(t) = \epsilon_0 \left(\chi^{(1)} \mathbf{E} + \chi^{(2)} \mathbf{E}^2 + \chi^{(3)} \mathbf{E}^3 + \dots \right). \quad (2.7)$$

In most cases $\chi^{(n)}$ is very small for $n > 1$, and as such extremely strong electric fields are required to produce a significant nonlinear response. There are two distinct forms of nonlinear behaviour: parametric and non-parametric nonlinearities.

Parametric nonlinearity is typically associated with the susceptibility of a bulk material, and is a property of both its chemical composition and molecular structure. This type of behaviour has only weak wavelength dependence that is typically associated with broadband absorptive losses in the material. It is also distinct in that it occurs instantaneously and is not tied to the lifetime of an energy level. Certain crystals such as lithium niobate (LiNbO_3), β -barium borate (BBO), or potassium titanyl phosphate (KTP), possess a strong $\chi^{(2)}$ as well as the birefringence necessary to achieve stable phase matching. These crystals are commonly used in [second harmonic generation \(SHG\)](#), or ‘frequency doubling’. There are similar processes that can be exploited in gas-phase media.

Non-parametric nonlinearity typically arises in the interaction between electric fields and specific energy levels in atomic or molecular vapours, and is more relevant to this work. In this case, the behaviour of the material is determined by transitions themselves, and is strongly wavelength dependent. There is a wide range of phenomena that fall into this category including common spectroscopy techniques such as [saturated absorption spectroscopy \(SAS\)](#) and [modulation transfer spectroscopy \(MTS\)](#) and even incoherently-driven multi-photon transitions. The typical signs that an optical-atomic process is nonlinear are significant perturbation to the steady-state population, or that multiple photons are required to drive the process.

Two non-parametric nonlinear phenomena that show promise in atomic vapour loaded hollow-core fibre are [four-wave mixing \(FWM\)](#) and [cross-phase modulation \(XPM\)](#). Both of these processes rely on strong $\chi^{(3)}$ nonlinearities, and are driven at wavelengths that correspond to allowed transitions in the atomic medium of choice.

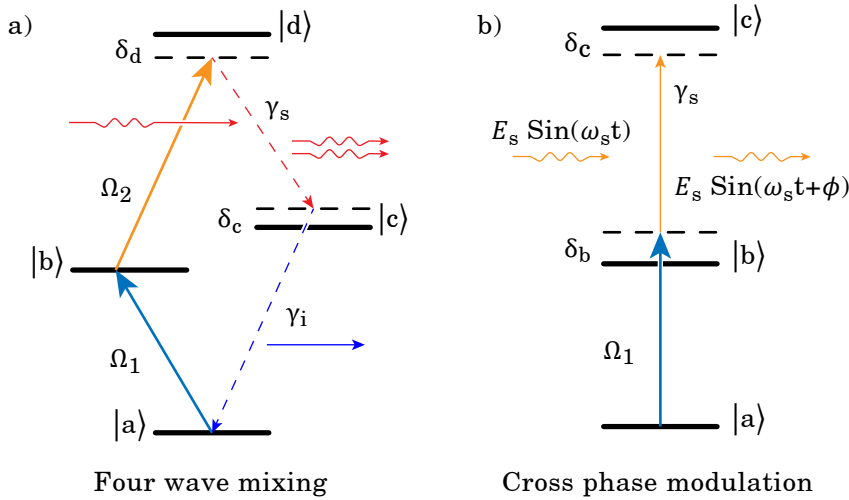


Figure 2.11: Two nonlinear processes mediated by strong atomic transitions. a) **Four-wave mixing (FWM)**, where the strong control fields Ω_1 and Ω_2 are used to amplify a weak input signal γ_s . b) **Cross-phase modulation (XPM)**, in which the control field Ω_1 produces a shift ϕ in the phase of the electric field of the signal photon γ_s .

FWM, as the name suggests, is a process that involves four optical fields. One arrangement, shown in [Figure 2.11 a\)](#), demonstrates direct optical amplification of an extremely weak signal. In this setup two strong pump fields Ω_1 and Ω_2 build coherence between the ground state $|a\rangle$ and the excited state $|d\rangle$. The excited-state detuning δ_d is typically chosen to be large relative to the spectral width of the excited state to prevent undesired generation of spontaneous emission through the $|d\rangle \rightarrow |c\rangle \rightarrow |a\rangle$ pathway. The incidence of a signal photon γ_s stimulates a new photon pair: a second signal photon as well as an idler photon γ_i . This process is mediated by near-resonant interaction with $|c\rangle$, and as such is strongly dependent on the two-photon detuning δ_c , with maximum probability of the process occurring at $\delta_c = 0$. Both the original and newly generated signal photons can continue in the medium to repeat this process, with a possible gain of much greater than unity.

A different nonlinear process with great potential is **XPM**. The ability to non-destructively interact two photons is of great interest in the field of quantum information processing and quantum computing. The ultimate goal of this would be a system that is capable of deterministically generating a π radian phase shift in the electric field of a single signal photon using a single control photon, with negligible attenuation of either photon [120]. This acts as an elementary quantum logic gate, specifically a controlled-phase or C-PHASE gate [17]. Alternatively, this system can be used to perform non-demolition

photon counting by measuring the polarisation rotation of a strong ‘meter’ beam due to the presence of the single signal photon.

In an atomic ensemble these effects can be generated by a three level ladder system, such as the arrangement shown in [Figure 2.11 b](#)). In the C-PHASE example the signal photon γ_s is off resonance from the upper transition $|b\rangle \leftrightarrow |c\rangle$. When there is no control field Ω_1 , the signal photon passes through the medium with no interaction. When the control field is applied it non-resonantly builds coherence between $|a\rangle$ and $|b\rangle$, which mediates the two-photon transition $|a\rangle \leftrightarrow |c\rangle$. Far from the two-photon transition the absorption scales as $1/\delta_c^2$, while the real part of the complex polarizability $\alpha(\omega)$ falls away as $1/\delta_c$. As such, for a strongly mediated transition it is possible to choose a detuning that results in a shift to the phase of the electric field of γ_s without significant absorption.

To effectively drive these processes there are several key design choices that can be made. In order to generate the high intensities required using few- or even single-photons, the optical fields need to be confined to extremely-small transverse mode areas. High on-resonance optical depths are needed to produce the strong light-atom interaction required to mediate the inherently weak coupling between multiple optical fields. The medium must also be capable of supporting the wide range of wavelengths involved in the relevant nonlinear process. All of these aspects can be achieved in a [HC-PCF](#) filled with an appropriate atomic or molecular vapour.

The first demonstration of resonant [FWM](#) in hollow-core fibre was by Londero *et al.* using a relatively long (30 cm) segment of 6 μm core [HC-PBF](#) saturated with atomic rubidium [65]. To produce a large effective non-linearity, the authors used the [LIAD](#) technique discussed in [subsection 2.6.3](#) to produce a peak optical depth of > 20 with a 3 mW desorption beam. The authors used a three-level double- Λ system conceptually similar to the diamond configuration in [Figure 2.11 a](#)) to achieve a small-signal optical gain of > 100 with 3 dB bandwidth of 300 MHz. Of particular note is that only 36 μW of pump power was necessary, orders of magnitude lower than that needed in vapour cells.

An extension of this work showed that the amplification scheme could be modulated via an additional weak optical signal [119]. As the optical gain is strongly dependent on the coherence of the associated energy levels, perturbations to a single state can ‘switch off’ the system. The authors demonstrated this technique by using a weak switching field tuned between one of the double- Λ ground states and an auxiliary excited state

to fully extinguish the optical amplification. While this technique is destructive in its switching, it is a clear demonstration that photon-photon interaction can be achieved in room temperature vapours at the few-photon level.

Moving to a ladder scheme as in [Figure 2.11 b](#)), Venkataraman *et al.* demonstrated all-optical modulation of a weak probe using only one weak control field [[121](#)]. With an optical depth of > 100 the authors were able to achieve 20% modulation of the power of a 600 pW signal beam with only 825 pW of control power. The physical process by which the signal pulse was attenuated is spontaneous absorption through the two-photon transition on the $5S_{1/2} \rightarrow 5D_{5/2}$ line. This process is enhanced through the proximity of the intermediary $5P_{3/2}$ state, the tuning of which must be carefully chosen so as to not weaken the effect through resonant absorption of the control field.

This concept was further developed from optically-induced attenuation to non-destructive phase manipulation. Using the same experimental system as in [[121](#)], Venkataraman *et al.* demonstrated extremely strong phase shifts in a strong meter (or measurement) beam induced by a few-photon signal pulse [[120](#)]. To move from an attenuation based switching to phase manipulation, the authors shifted the optical detunings to avoid both single- and two-photon excitation in the atomic medium. With large enough detunings, the interaction of light and atoms is effectively limited to the cross-Kerr effect. In this demonstration, both single and two-photon detuning were set to 700 MHz, reducing absorption of the signal field to 1% down from the on resonance optical depth of 100. The resulting phase shift of the meter was measured to be 5 mrad for a 5 ns pulse, with a phase-shift per signal photon of 0.3 mrad. Although significantly smaller than π radians of phase modulation, quantum information processing protocols have been developed that require only weak nonlinear interaction on the order of 10^{-5} rad/photon [[76](#)].

Similar work by Perrella *et al.* using fibres with a much larger core diameter (45 μm) demonstrated single-photon phase shifts of 1.3×10^{-6} $\mu\text{rad}/\text{photon}$, [[85](#)]. The authors explore the sensitivity of the process to various experimental parameters such as power in both the signal and meter beam, and detuning from the two-photon transition. It is interesting to note that the phase shift in the meter beam is not sensitive its own optical power, showing that this technique can effectively be used both as a non-demolition photon counting device, or a single photon C-PHASE gate. A continuation of this work investigated the dependence of both the two-photon absorption in general, and XPM specifically, on the fibre core size by including the decoherence due to transit-time broadening [[86](#)]. This analysis presents an excellent guide to designing a hot-atom filled

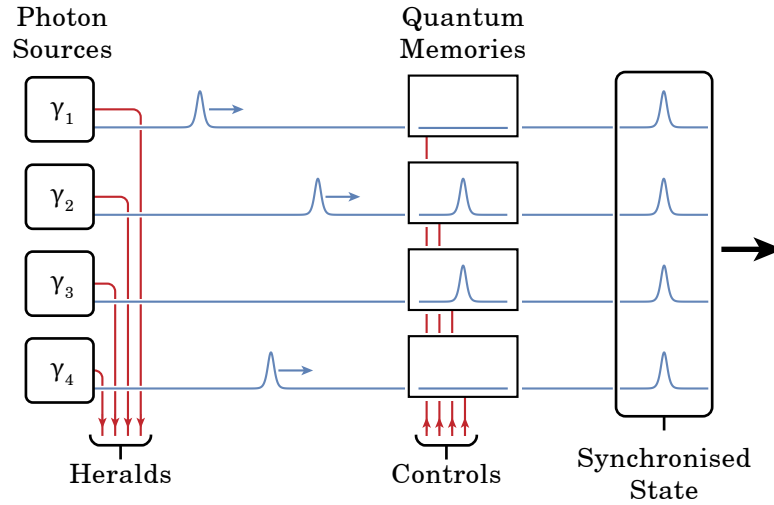


Figure 2.12: Protocol for synchronising probabilistically generated single photons to deterministically generate an arbitrary number multi-photon state using multiplexed quantum memories.

hollow-core fibre platform for engineering photon-photon interaction.

2.6.5 High Bandwidth Quantum Memories

The ability to store quantum information and coherent states is inherently vital to develop complex non-classical technology. While the long-lived storage of quantum states is obviously relevant for implementations such as long-distance quantum key distribution, short-lived high-bandwidth quantum memories also have clear application. One such example is the preparation of deterministic multi-photon states. Constructing a large number state with an array of probabilistic single-photon sources is slow, with the probability of generating N concurrent, heralded photons given by q^N , where q is the probability for any one source to produce a single heralded photon. It has been shown that by using an array of high-bandwidth quantum memories – one for each single-photon source – this likelihood can be increased dramatically [78].

The method by which this can be done is as follows: each single-photon source is directed into a quantum memory. This protocol is shown in Figure 2.12 for a 4 photon system. On the detection of the herald photon indicative of the generation of a single photon from the source, the memory is activated and the signal photon is stored. This process occurs continuously, with each memory washing the stored photon once a new signal photon has been produced, or once the stored photon decoheres beyond usefulness. Once $N - 1$ memories have successfully stored a viable photon, if the final empty channel

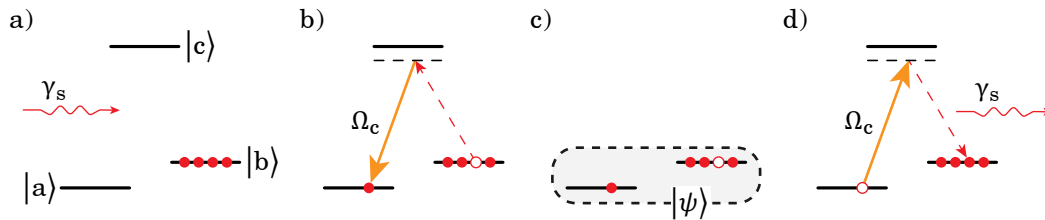


Figure 2.13: A Raman Λ scheme for storage and retrieval of optical pulses, consisting of two long-lived ground states $|a\rangle$ and $|b\rangle$, with an upper state $|c\rangle$ that has strong interaction with both ground states. a) The three-level system is prepared initially in state $|b\rangle$, when a signal photon γ_s approaches. b) A strong control field Ω_c is switched on with detuning such that the single photon transition is avoided, but the two-photon Raman transition is on resonance. c) The signal photon is written into a coherent excitation of both ground states given by $|\psi\rangle$, which can exist for as long as the ground state coherence permits. d) Retrieval is achieved by switching on of the control field which reads out the stored coherence onto the original signal photon through a second Raman transition.

detects a herald (γ_1 in the example), it triggers the release of all other stored photons, which are delayed such that the final state is the N desired concurrent single photons.

This protocol dramatically improves the efficiency of the system, with the new probability of generating the desired multi-photon state given by $(q\eta B)^N$, where η and B are the efficiency and time-bandwidth product of the memory, respectively. In the example given by Nunn et al., the waiting time for a 12-photon state is reduced from 12 years to 100 μs using an array of 1 GHz repetition rate, 50 % heralding efficiency, unsynchronised sources with a matched set of 56 % efficient, 1000 time-bandwidth product quantum memories. This demonstration is a clear indication of the power of easily multiplexed, high-speed quantum memories.

As we have noted already, the key limitation to hot-atom filled hollow-core fibre platforms is the short lifetime of all atomic states due to the short interaction times. This limitation is not so detrimental if one limits their scope to high-speed interaction protocols and high bandwidth applications, such as the synchronisation scheme detailed above. In this case, key requirements for the memory platform will be a) scalability to high N , b) memory efficiency η , and c) high-bandwidth operation. The first demonstration of a system such as this in fibre was made by Sprague *et al.*, who used 20 cm of caesium-vapour filled kagome-lattice fibre with core diameter of 26 μm [113]. The authors used a LIAD pulse to controllably generate optical depths of between 500 and 3500, and a ground state Λ scheme to perform storage and retrieval of light, as described in Figure 2.13.

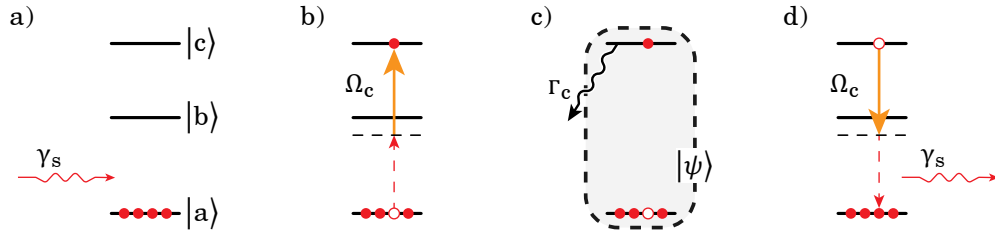


Figure 2.14: The three-level ladder scheme **off-resonance cascaded absorption (ORCA)** behaves much the same as the Raman Λ scheme described in Figure 2.13. The major difference is that in this protocol the storage state (in this case $|c\rangle$) is a doubly-excited state rather than a second ground state. This prevents thermal population of the the storage state, removing the need to prepare the memory and preventing the generation of noise photons. The price for this is that the storage state is susceptible to decoherence via spontaneous emission (Γ_c), putting an upper limit on the effective lifetime of the system.

The results were extremely promising, showing a time-bandwidth product of 100, with total efficiency of 27%. While the storage time was limited by experimental difficulties producing undesired decoherence, this result was not far from the expected transit time limit of 100 ns. The authors were able to achieve a large B in this regime by exploiting the extremely-high bandwidth of the far-detuned Λ scheme, and the synchronisation gain of this system is 30^N , a considerable advantage for many-photon state generation.

While as-of-yet unpublished, there is work being done at the University of Adelaide to implement a similar high-bandwidth scheme named **off-resonance cascaded absorption (ORCA)** in fibre. This protocol, originally developed by Kaczmarek *et al.* in a vapour cell [51], is depicted in Figure 2.14. The primary difference between **ORCA** and the Raman Λ scheme described above is the use of a second higher-lying state as the storage state, rather than a second ground state. There is only minimal difference conceptually to the two techniques, most of which are determined by the properties of the storage state. The key advantage of the ladder scheme is its intrinsically noise-free performance, as there is no thermally driven population in either the intermediary or storage stages. In addition, in commonly used alkali metals (caesium, rubidium, etc..) the control and probe transitions are far enough separated in colour so as to prevent stray scattering between fields. At this moment this project is capable of storing weak classical pulses for several nanoseconds, while the full bandwidth is still being investigated.

2.6.6 Summary: Application of thermal vapours in hollow-core fibre

Small core [HC-PCF](#) has shown a great range of applications, ranging from compact optical frequency reference cells to single-photon source synchronisation arrays. The common advantages seen from these devices are their compact physical footprint, the strong interaction between coupled light and the atomic sample, and the ability to drive high-intensity processes with relatively low optical powers. There is however still room for further development, specifically in the ability to consistently apply anti-relaxing coatings, and the sealing and splicing of fibre loaded with volatile atomic samples. In terms of fundamental limitations, the harshest is the limit to coherent interaction time which is set by both the transit time across the fibre core, and the broad Doppler profile due to the thermal distribution. These properties make hot atomic vapour loaded [HC-PCF](#) a powerful platform in the realm of high-speed atomic physics and miniaturisation.

2.7 Loading of Cold atoms into hollow-core fibre

Following the work done with cold atoms in capillaries in the 1990s, the development of [PCF](#) led shortly after to their use in conjunction with cold atoms. The benefits are clear: whereas before the attenuation of a core-guided mode was measured in dB/mm, now light could be coupled through 10 cm of fibre with negligible loss. In addition, the wide spectral guidance of these fibres made it feasible to perform experiments on the atoms while inside the fibre, as has been discussed in [section 2.6](#). The following is a description of the work that was undertaken in this field leading up to the commencement of this project.

The first demonstration of interfacing cold atomic ensembles and true hollow-core fibre was by Christensen *et al.* in 2008 [21]. The authors initially prepared a sodium [Bose-Einstein condensate \(BEC\)](#) in an [translatable-focus ODT](#). The centre of the trap was then shifted to move the atoms to within a millimetre of the tip of a 2 cm length of 10 μm core [HC-PBF](#). A second trap laser was coupled through fibre from the opposite end, and by careful adjustment of the power in the two traps the atomic ensemble was transferred into the fibre. After some time (typically 5 ms to 30 ms) the initial [ODT](#) was ramped back on and the atoms were retrieved. The efficiency of this scheme was found to be 5%, a number that the authors suggested to be a lower bound limited by experimental difficulties.

Work done at the same time (and referenced by Christensen *et al.* as unpublished) by Bajcsy *et al.* showed dramatically more exciting results [5]. This represents the first use of a cold-atom-in-fibre system as a physics platform. The authors used a short (3 cm)

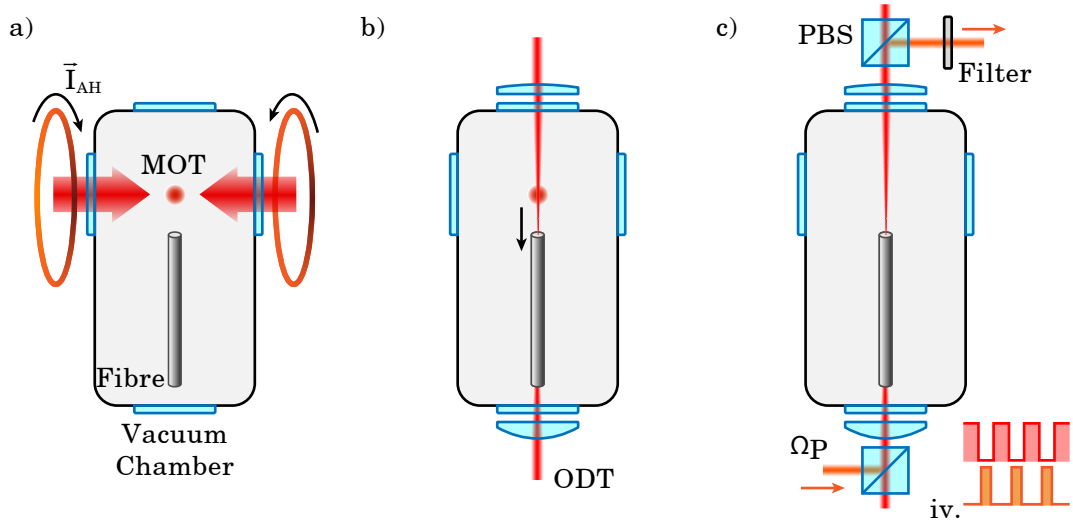


Figure 2.15: A typical setup for performing cold-atom in fibre experiments. a) A MOT produces an ensemble of cold atoms a short distance away from the tip of a short length of HC-PCF, inside a vacuum chamber. b) Once the atomic cloud has formed, the cooling and trapping field are switched off and a high-power, far-detuned laser coupled through the fibre is switched on (Ω_T). This field produces a strong ODT, guiding the atomic ensemble into the fibre. c) Once inside the fibre the atoms are interrogated using a weak probe field (Ω_P). This beam is combined with the trap laser on one side of the chamber, and separated on the other, using a combination of polarisation (PBS) and spectral filtering. iv) To avoid perturbation of the probe transition by the dipole trap, the two beams are modulated 180° out of phase.

length of $7\ \mu\text{m}$ core HC-PBF mounted vertically inside a vacuum chamber, above which was situated the necessary equipment to form a MOT of rubidium-87. Once cooled the atomic sample was moved to the tip of the fibre using both gravity and a magnetic trap generated by four wires that surrounded the initial cloud and approached the end of the fibre, producing a focusing force. Atoms were transferred from this trap into an ODT that was coupled through the fibre core from below, preventing the cold ensemble from interacting with the walls of the fibre. This apparatus was capable of coupling 3000 atoms into the fibre core which, due to the tight confinement of the fibre, resulted in an optical depth of 30, later improved to 180. Later analysis of various loading schemes including the magnetic guide, a blue-detuned funnel and light sheet, and simply allowing the atoms to fall, showed little dependence on the technique used [6]. The authors concluded that without additional cooling during the loading process there was little advantage to any particular adiabatic coupling scheme.

The authors demonstrated the application of this platform by investigating EIT

in a 3-level Λ scheme, in which only 4500 control photons were required to produce a transparency window with 50 % transmission. Using a strong control and a third switching field as in [119], the full EIT transmission was reduced to half using only 700 switch photons [88]. The extremely low energies required to perform these fully optical operations is astounding, and a clear demonstration of this platform's applicability in quantum information processing fields.

In a return to the use of fibre as a transport mechanism for cold atoms, Vorrath *et al.* demonstrated a direct transport of microkelvin temperature atoms through a horizontally-mounted hollow-core fibre [122]. The authors used a dipole beam coupled through the fibre to convey atoms from a three-dimensional MOT into an 88 mm length of 12 μm core HC-PBF, and successfully imaged the resulting spray of atoms out the far end. The peak atom flux achieved was 1×10^5 atoms/s, and the use of a second reservoir trap on the entrance side of the fibre allowed the authors to maintain a constant flux of 1×10^4 atoms/s over 150 ms. While this work did not perform specific experiments on the atoms in the fibre, the demonstration of an effective fibre-based matter-waveguide was a significant step towards implementing fibre-guided matter-wave interferometry.

The most dramatic results of this period in time were by Blatt *et al.* in a pair of publications in 2014 and 2016 [15, 16]. Using a very carefully designed MOT system, the authors were able to guide 2.5×10^5 rubidium-87 atoms into a 7 μm core HC-PBF, producing an optical depth of 1000 on the $|F = 1\rangle \rightarrow |F' = 1, 2\rangle$ transitions. Technically this was achieved through a combination of magnetic compression of the MOT, and the use of a specifically tailored three-dimensional dark-spot [54], resulting in both a high number density and large atom number ensemble. Not only was this work an impressive show of light-atom interaction strength, but these optical depths were also measured on non-cycling transitions capable of performing interesting quantum optics protocols. The authors tested their cold-atom filled fibre platform by exploring slow light, light storage, and stationary light phenomena using a 3-level Λ EIT configuration.

Limiting the optical depth to ~ 200 to avoid excessive absorption from the nearby $|F = 1\rangle \rightarrow |F' = 0\rangle$ transition, Blatt *et al.* demonstrated an EIT-driven optical delay of 500 ns on the $|F = 1\rangle \rightarrow |F' = 1\rangle$ transition. By adiabatically switching off the control field, the optical pulse is stored as a collective excitation of the atomic medium, as previously described in Figure 2.13, and shown in Figure 2.16. The high optical depth and relatively long-lived ground states provided by the confined cold ensemble allowed the authors to store an optical pulse for 0.6 μs with 23 % efficiency, where the lifetime was dominated

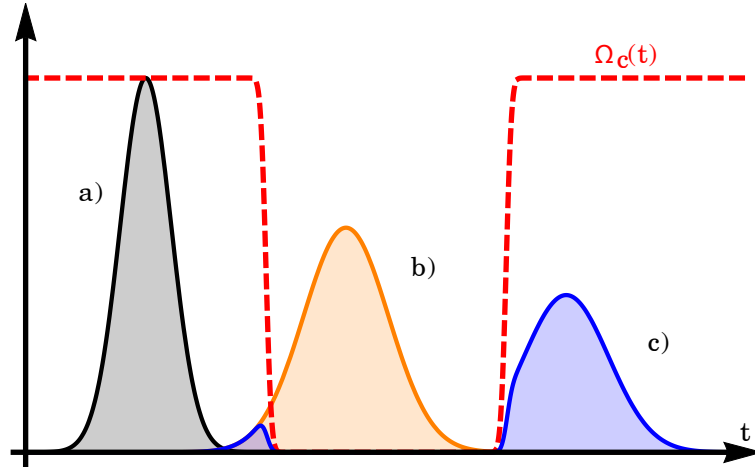


Figure 2.16: Pulse sequence demonstrating [EIT](#) based storage of an optical pulse. a) The signal pulse with no atomic medium. b) In the presence of a strong [EIT](#) feature the input pulse is delay and broadened due to the reduced group velocity. c) The control field $\Omega_c(t)$ is adiabatically reduced to zero while the pulse is inside the medium, storing the signal as a collective excitation. When the control field is turned back on at a later time, the transparency window is restored and the pulse is read out of the medium, with some loss of signal due to absorption or dephasing processes.

by transit relaxation of the atomic ensemble at a rate of 0.009Γ . The authors noted that the use of μ -metal shields around the fibre in addition to external compensation of the background magnetic fields in the lab was necessary to achieve this level of coherence, as any DC field or gradient along the ensemble produces dephasing among the Zeeman sub-states. Replacing the single control field with a counter-propagating pair, the authors demonstrated stationary light phenomena with efficiency of 2.8%, limited by the modest optical depth and transit-time decoherence.

A final example of the use of cold atoms in hollow-core fibre aims at their use as an active frequency standard. The alkaline-earth metals possess an electronic structure that is extremely desirable as the basis for cutting-edge optical atomic clocks. Specifically, the closed outer S-orbital results in a long-lived metastable $|^3P_0\rangle$ state with an extremely weak transition to the $|^1S_0\rangle$ ground state that lies in the optical regime (and for some member of the group, the visible spectrum). For strontium, this transition is approximately 1 MHz wide, and as such makes for an exceptional clock. Indeed, large experimental systems have been developed that use strontium to push the down the uncertainties on various physical parameters and test our models of fundamental physics to increasingly stringent levels [59, 137].

Reducing these clocks and experiments to small physical footprints is a ongoing challenge due to the extreme complexity involved. Towards this goal, a test-of-principle experiment by Okaba *et al.* measured the effects of confinement in a hollow-core fibre on a 1-D strontium lattice using the reasonably narrow $|^1S_0\rangle \rightarrow |^3P_1\rangle$ transition [79]. The authors used a 32 mm length of $34 \times 44 \mu\text{m}$ hypocycloid-core kagome-lattice fibre as their test geometry. The wide guidance band of kagome-lattice fibre is necessary in this case due to the wide range of optical wavelengths needed to perform the experiment, with the intercombination line at 689 nm, the true clock transition at 698 nm, and the trapping lattice magic-wavelengths at 813 nm and 913 nm.

The experiment involved the filling a one-dimensional lattice of cold strontium-88 from a three-dimensional MOT located just outside the tip of the HC-PCF. By adjusting the lattice detuning, the atoms were transported adiabatically into fibre. Once inside, one of the lattice beams was switched off to allow the ensemble diffuse over the whole length of the fibre, then reapplied to achieve a mean lattice site occupation of ~ 0.45 . The combination of the tight spatial confinement, large lattice site spacing, and magic-wavelength trapping produced an extremely perturbation-free sample perfect for a test of high-resolution spectroscopy.

The authors found the atomic lifetime inside the fibre to be 350 ms, limited by the collision of trapped atoms with out-gassed particles from the fibre wall. Lamb-Dicke spectroscopy of the $|^1S_0\rangle \rightarrow |^3P_1\rangle$ transition produced a linewidth of 7.8(4) kHz, which is in agreement of the natural linewidth of the transition, showing no increased dephasing effects from the presence of the fibre at the kilohertz level. While this is still far from the millihertz level lifetimes achieved in state-of-the-art atomic clocks, it is still a promising step towards the use of HC-PCF as a platform for packaging long coherence time AMO experiments.

This was the state of the field at the beginning of my project. Cold-atom in fibre systems had shown high optical depths of 1000 and lifetimes of 1 μs with preliminary experiments demonstrating the delay and storage of optical pulses. In terms of competition (or cooperation), we were aware of two research groups that were actively working in this field: the NLO/QO (Nichtlineare Optik/Quantenoptik) team, lead by Dr. Peters and Prof. Halfmann at Technische Universität Darmstadt, and the EQOQI, QUANTUM (Forschungsgruppe Experimentelle Quantenoptik und Quanteninformation, Arbeitsgruppe Quanten-, Atom- und Neutronenphysik) group lead by Prof. Windpassinger at the Institute of Physics, Johannes Gutenberg-University. Later we would become aware

of the team led by Prof. Lan at the Division of Physics and Applied Physics at Nanyang Technological University, Singapore, and the new team led by Prof. Bajcsy at the Institute for Quantum Computing at the University of Waterloo, who had previously worked in the field at Harvard-MIT.

2.8 Contemporary Work in the Field

So far I have detailed the long history of the field and context that led up to this project at start of my involvement. Over the years since, there has been significant work in the field by both ourselves and other researchers. While our contribution is described in detail in the rest of this manuscript, the results and ideas presented by other researchers have had a considerable impact on the direction of the project throughout. This work is detailed here in brief.

In a continuation of the early work by Vorrath *et al.*, the quantum optics & quantum communication team at Johannes Gutenberg-University further developed their cold-atom in fibre system to explore Rydberg excitation and photon-photon interaction through Rydberg EIT. This process is similar to the Λ or ladder schemes discussed already, where there is a strong control field that is used to perturb a probe signal through a mutually connected intermediary state, shown in Figure 2.17 a). In the case of a Rydberg system, the control field connects the upper level of the probe transition to a very high-lying state that is only just below the ionisation threshold, Figure 2.17 b). This weakly bound atom-electron system is termed a Rydberg atom, and possess a range of properties that make of it interest to quantum optics and nonlinear optics, such as the Rydberg blockage effect Figure 2.17 c).

In experimental work by Langbecker *et al.*, a one-dimensional lattice of cold rubidium-87 was translated into a section of 60 μm hypocycloid-core kagome-lattice fibre using a frequency shift of one of the lattice beams [57]. A Rydberg EIT scheme was implemented using the a control field tuned to the $|5P_{3/2}\rangle \rightarrow |29S_{1/2}\rangle$ transition at 480 nm, which was interrogated using a probe signal tuned across the $|5S_{1/2}\rangle \rightarrow |5P_{3/2}\rangle$ transition. Using this scheme the authors clearly demonstrated EIT behaviour inside the fibre and found that there was little effect of the fibre on the behaviour of Rydberg system over the relevant timescales.

Further theoretical analysis of the conveyor belt loading scheme was undertaken to optimise the final temperature and atom number of the atomic sample [58]. This work

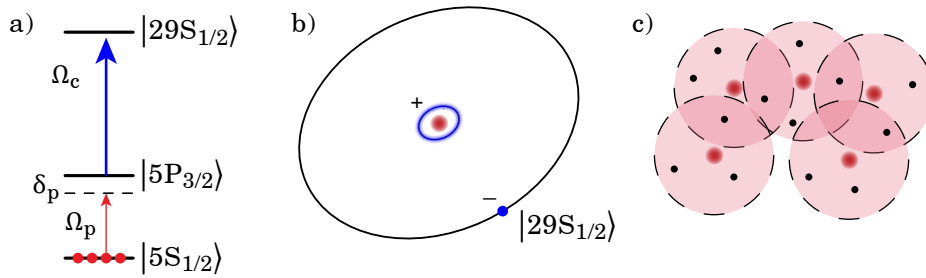


Figure 2.17: Excitation of high lying-Rydberg atoms in rubidium. a) Energy level structure for EIT in Rydberg atoms. The control field Ω_c drives coherence between the $5P_{3/2}$ state and a high-lying Rydberg state with, in this case, $n = 29$. This is probed as usual on the D_2 line. b) Electronic states with such a high principle quantum number have a very large electron radius, resulting in a strong sensitivity to external electric fields. These states also tend to have long lifetimes ($21.7 \mu\text{s}$ for the $29S_{1/2}$ level). c) One interesting phenomena specific to these types of atoms in the Rydberg blockage effect: the strong sensitivity of large n states to external electric fields results in a minimum separation of Rydberg atoms, as the far-from-nucleus electric field from an excited atom will perturb the energy levels of nearby atoms enough to prevent their own excitation by the same optical field.

involved a detailed numerical simulation of the effect of lattice power and frequency shift on the loading performance, and a comparison of these results with experimental data. The conclusion of this investigation was that the lattice power should be adiabatically decreased during the loading process. This counteracts the heating that occurs from spatial compression of the ensemble as it enters the tight confinement of the fibre. The results showed that although this slightly reduced the number of trapped atoms retained, the resulting temperature of the ensemble was decreased by a factor of six relative to the constant-power transport – a significant improvement.

A separate line of theoretical work done by the same group was of particular relevance to our own, being the investigation into line-shape perturbations of fibre-confined cold-atom samples. The problem is as follows: the conventional way of investigating the properties of an atomic ensemble is by absorption spectroscopy, in which a strong atomic transition is probed by a near-resonant optical field. By measuring the absorption of the probe beam over a large frequency range relative to the transition linewidth, it is possible to extract the optical depth as well as other physical properties such as ensemble velocity in the direction of the probe beam, and temperature. However, while the atomic absorption generated by the imaginary part of the susceptibility, $\text{Im}[\chi]$, the probe beam also experiences the real part of the susceptibility, $\text{Re}[\chi]$. This part leads to a refractive

index given by $n_r = 1 + \frac{1}{2} \text{Re}[\chi(x, y)]$. As one can expect, if $\text{Re}[\chi(x, y)]$ is both large and changes quickly in space it can lead to strong lensing of the interrogating optical field. This effect was first seen in cold atomic samples by Roof *et al.*, who had some success modelling the effect of the ensemble on a probe beam as a thin spherical lens [102].

Work by Noaman *et al.* showed that this micro-lensing phenomena is especially detrimental when the atomic ensemble is in close proximity to, or inside, a hollow-core fibre due to the mode selectivity of the fibre itself [77]. The result of this process is that for large *OD* atomic samples, light tuned near to the atomic resonance can be lensed by the ensemble into spatial modes that are not guided by the optical fibre, producing an apparent increase in the absorption of the probe light. This effect is strongly sensitive to the detuning of the probe from the atomic transition, and produces both general asymmetry and narrow nonphysical dips in the measured spectrum. The authors developed a model for the propagation of a Gaussian beam through an inhomogeneous density atomic cloud that included the mode selectivity of the optical fibre. This model was capable of predicting both the experimentally measured asymmetry and increased attenuation for standard 2-level absorption spectroscopy and the Rydberg *EIT* scheme described above. This work was particularly exciting to see published as we had experienced similar lensing problems in our own cold-atom-in-fibre system, and had communicated with the authors regarding our own investigation of this process.

In a similar vein, a detailed theoretical paper by Sulzbach *et al.* investigated the effect of micro-lensing on pulse propagation in an inhomogeneous medium [116]. In this work, the authors investigated the interaction between a spatially varying control Rabi frequency and non-uniform atomic media. The particular test-case for this model was that of Λ *EIT* in a cold-atom filled hollow-core fibre as in [16]. By solving Maxwell's equations for this complex system, the authors investigated the effect of in-fibre micro-lensing on both the time-domain pulse shape and the frequency-domain spectral response of the medium. As in the work by Noaman *et al.*, the authors found a strong asymmetry to the expected transmission spectra due to the sign inversion in $\text{Re}[\chi]$ as the detuning relative to the atomic transition crosses zero. Possible mitigation techniques are suggested, including the use of higher-order transverse spatial modes for the optical field, moving to small-core diameters with lower atomic densities, and careful selection of the single-photon detuning as per the article. As this effect scales detrimentally with fibre core size, the reasonably large 45 μm core used in our experiment is particularly susceptible to this process.

The use of hollow-core fibre as a platform for atom interferometry has been an ongoing suggestion since the first development of capillary-based atom guides. In 2018 the first demonstration of this was made by Xin *et al.*, using Raman pulses to transfer population between ground states in rubidium-85 [132]. The authors used a conventional single dipole-trap setup to load 10^4 atoms into a 4 cm length of 63 μm hypocycloid-core kagome-lattice fibre, and implemented a Mach-Zehnder interferometer protocol. This protocol consisted of a $\pi/2 - \pi - \pi/2$ Raman pulse sequence with inter-pulse separation of T , which is inertially sensitive and has a final closed-path phase of

$$\Delta\phi = -(\boldsymbol{\beta}_1 - \boldsymbol{\beta}_2) \cdot \mathbf{g} T^2 + \phi_1 - 2\phi_2 + \phi_3 \quad (2.8)$$

where $\boldsymbol{\beta}_{1,2}$ are the Raman field propagation constants, \mathbf{g} is the local acceleration due to gravity, and ϕ_i are the initial phases of the Raman fields for the i 'th pulse. The contrast of the interferometer output was found by varying the phase of the final beam-splitter pulse (ϕ_3) and measuring the amplitude of the ground-state population fluctuations, demonstrating the expected sinusoidal dependence.

The authors show a contrast of 0.16, with decoherence time of $\sim 80 \mu\text{s}$, which decreases to less than $20 \mu\text{s}$ when the weak dipole trap is left on during measurement, due to AC-Stark shift dephasing. Xin *et al.* suggested that similar platforms may be able to achieve inertial sensitivity of 60 ppm with similar optical depth and a longer coherence time of 1 ms, providing a highly compact, low power usage, atomic inertial sensor.

A key limitation to the earlier work by Blatt *et al.* was dephasing due to transit-time relaxation, placing an upper limit on the memory lifetime. One solution to this problem is to maintain the ODT during the interrogation sequence, preventing the atoms from hitting the fibre walls. The reason that this is not commonly done is that the presence of the dipole trap, by its nature, perturbs the atoms' energy levels through the AC-Stark effect, producing a new source of decoherence. The effect of this was seen in [132] in which the interferometer contrast decayed at a rate many times faster when the dipole trap was left on (see Figure 2.18 a)).

The precision metrology community experienced a similar hurdle to the development of ultra-accurate optical clocks in which a solution was devised entitled the 'magic wavelength trap' [53, 73, 134]. For this technique, one finds a wavelength for which the both the lower- and upper-levels of the desired transition experience the same AC-Stark shift, or equivalently, trap depth. This process is described in Figure 2.18 b)).

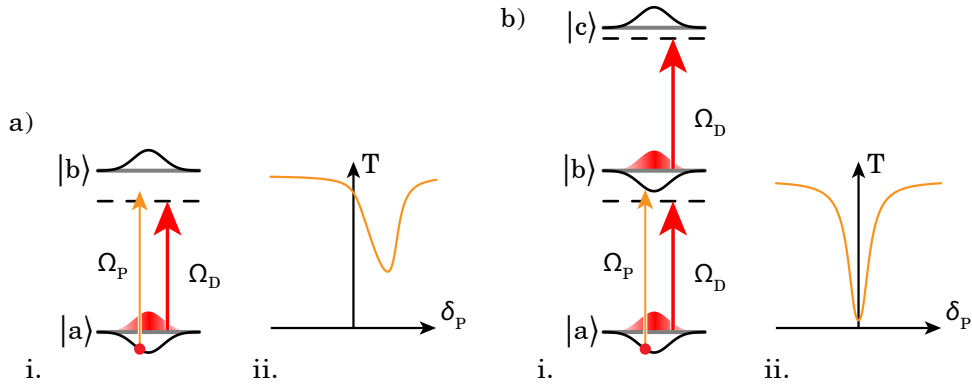


Figure 2.18: The effect of AC-Stark broadening and the magic wavelength technique. a) i) A far red-detuned laser (Ω_D) is used to trap atoms by producing a spatial variation in the energy of the ground state $|a\rangle$, which in turn perturbs the transmission spectra seen by the interrogation laser Ω_P as in ii). b) When turned to the magic wavelength the trapping laser interacts with multiple transitions (simplified here to a single additional transition $|b\rangle \rightarrow |c\rangle$), resulting in matched potentials for states $|a\rangle$ and $|b\rangle$. This removes the inhomogeneous broadening, resulting in a symmetric, narrow feature, as in ii).

Unfortunately, not every atomic species will have a technologically accessible magic wavelength solution – either because of the required wavelength or power.

With this in mind, the University of Waterloo team lead by Prof. Bajcsy moved from rubidium to caesium as the atomic species for their cold-atom-in-fibre experiments. Caesium’s 852 nm D_2 line possess a magic wavelength at 935 nm, a conventionally accessible wavelength suitable for use in dipole trapping. While the combination of a magic-wavelength trap and hollow-core fibre had already been utilised by Okaba *et al.* to perform Lamb-Dicke spectroscopy of strontium [79], this was the first demonstration of such a technique in an alkali atom with transitions useful for quantum logic operations. The authors used a short segment of 7 μm core [HC-PBF](#) to achieve strong-light atom interaction, and were able to suppress the shifts and broadening of the probe transition during measurement by operating the dipole trap in the magic wavelength configuration. Guiding 1.7×10^4 atoms in the fibre, the authors generated an optical depth of ~ 80 , with a single-photon single-atom interaction probability of 0.5%. Using this platform, Yoon *et al.* developed a scheme for monitoring coherent multi-photon processes by interrogating the ground state populations. This technique was tested on spontaneous Raman emission, with the hope to eventually explore super-radiance phenomena [136].

2.9 Summary

This concludes a comprehensive review of the context and history of the use of cold-atom filled hollow-core fibre as a platform for investigating quantum optics and other non-linear phenomena. Common trends in the field are a push for HC-PCF with wider transmission bands, lower losses, and better integration prospects. On the atomic front, experiments have developed to maximise the light-atom interaction strength possible inside the fibre by using higher atomic densities and stronger coupling protocols. While hot-atom filled fibre devices show great promise as compact systems they are limited by transit time and Doppler broadening phenomena, and are primarily being developed for high-speed non-linear applications. Cold-atom systems are still very experimental, with bulky vacuum chambers and complex optical systems, although the development of chip-based cold atom sources may revolutionise this aspect. The biggest current challenge to the performance of cold-atom-in-fibre systems is transit time broadening, limiting coherence times to the order of microseconds. Work is underway to address this setback using either in-fibre cooling protocols to reduce atomic velocities, or using magic-wavelength techniques to allow for interrogation of the atoms while continuously trapped.

Excitingly, in the last few years this field has achieved a few of the great predictions made decades earlier including atom interferometry in fibre, few-photon switching, and efficient storage of optical pulses. This trend will only continue, as this technology has shown to be an exceptional platform for performing a wide range of cutting-edge experiments, and those working in the field have demonstrated that the technical know-how and expertise exists. The rest of this thesis pertains to the development of our cold-atom-in-fibre system and our contribution to this exciting field.

Part II

Cold Atom Loading Experiment

EXPERIMENTAL APPARATUS

Cold atom experiments are incredibly involved systems that tend to grow organically in size and complexity. Despite this, the underlying elements are reasonably standard: these experiments consist of a vacuum chamber, an atomic source, several lasers – the frequency of each stabilised in some fashion to an atomic transition, a cooling/trapping protocol, an interrogation and detection scheme, computer oversight, and finally data analysis. Each laboratory and research group has their own spin on each of these elements, and this project is no different. In this chapter I present a very brief overview of the specific experimental design developed in this work.

3.1 Overview

The heart of the experiment is the fibre – a short length of kagome-lattice [HC-PCF](#) mounted inside the vacuum chamber. The chamber itself sits on one end of an optical table, raised by approximately 20 cm to allow for optical access from below. The chamber supports both the multi-turn copper coils and the six, fibre coupled laser delivery arms necessary for cooling and trapping rubidium. All other optical fields that are used in the experiment are either coupled through the kagome-lattice fibre from viewports in the top or bottom of the chamber, or are directed through other viewports as needed.

The rest of the optical table is dedicated to the free-space optics used to tailor the various optical fields in preparation for their eventual coupling into the vacuum chamber,

performing amplification, frequency modulation, power control, and fast switching. Four of the five laser systems used in the experiment are diode lasers that are carefully frequency stabilised either to various atomic transitions, or to each other, and provide the light necessary for cooling, repumping, and interrogating the atoms. These lasers are housed with the relevant spectroscopy and coupling optics in acoustic isolation (cardboard) boxes resting on slide-out trays in a rack next to the optical table. The necessary light fields are fibre coupled from the rack to the table, allowing us to work on the table without risking unlocking the lasers. The final laser is a [continuous-wave \(CW\)](#) titanium-sapphire laser from company *M Squared*, which is mounted directly to the table as frequency stabilisation is not required in its role as the dipole-trap laser.

All the electronics required to operate the experiment are housed on a metal shelf at head height above the optical table. Any device that can be remotely configured is connected to the computer oversight system via [IEEE-488 general purpose interface bus \(GPIB\)](#), allowing for maximum remote control of the experiment. Similarly, all devices capable of being externally referenced are synced to a 10 MHz signal provided by a commercial caesium clock. The computer oversight system itself is an Arduino Due mounted in a custom input/output breakout board, which connects to the lab computer by [universal serial bus \(USB\)](#). The lab computer (labelled Cold Atoms) runs a home made [graphical user interface \(GUI\)](#) that allows for both simple control over active devices (such as ‘open the cooling shutter’) as well as high-level control of pre-programmed experimental runs (such as ‘take shadow image at times 5 through 50 milliseconds in 5 ms steps’).

Data is typically either cross-chamber absorption images captured on a scientific [charge-coupled device \(CCD\)](#) camera or in-fibre atomic absorption spectra captured on a photodetector and recorded using an oscilloscope. This data can either be processed in real time and displayed on the lab computer screen for diagnostics and testing, or can be stored and processed in bulk at a later time. All data processing is performed in *Igor Pro* using sophisticated custom analysis code, whereas the simulations and models used to guide experimental work are developed in *Mathematica*.

3.2 Hollow-Core Fibre

The hollow-core fibre used in the experiment is an early design of the kagome-lattice core structure provided by Prof. Benabid from the *GPPMM Group, Xlim Research Institute* at the Université de Limoge. The fibre is 10 cm long, with a single-cell defect core with diameter of 45 μm seen in the microscope images of the end-face shown in

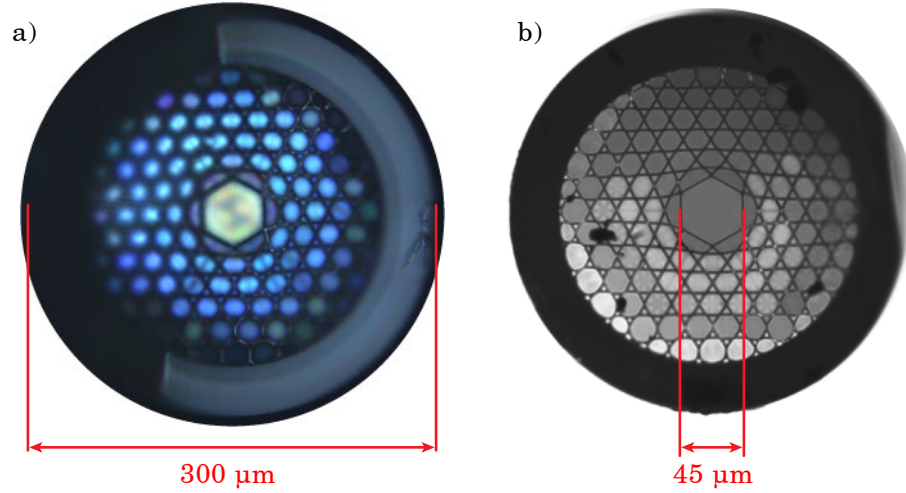


Figure 3.1: Microscope image of the end-face of the 45 μm core kagome-lattice HC-PCF used in the experiment, with a) white light shining through the fibre from opposite end, taken in colour, and b) greyscale, illuminated from above.

Figure 3.1. A description of the guidance mechanism utilised by this type of fibre is given in [subsection 2.5.3](#), where this fibre specifically shows excellent transmission over the 600 nm to 1600 nm spectral band [86]. Most of the losses associated with using a segment of fibre this short are due to the non-AR coated vacuum viewports, with coupling efficiencies into the fundamental mode typically as high as 85 %.

3.2.1 Fundamental Mode

The lowest-order mode guided in the fibre is referred to as the fundamental mode. As the fibre core is reasonably circular, this mode is well approximated by the Laguerre-Gaussian family. These modes are solutions to paraxial Helmholtz equation in cylindrical coordinates and occur in geometries with cylindrical symmetrical – a good approximation for the core of this fibre. These modes are denoted as $\text{LG}_{p,l}$, where the subscripts are the radial and azimuthal indices, respectively.

The spatial relative field strength for these modes is given by

$$u(r, \phi, z) = \sqrt{\frac{2p!}{\pi(p+|l|)!}} \frac{1}{w(z)} \left(\frac{\sqrt{2}r}{w(z)}\right)^{|l|} L_p^{|l|} \left(\frac{2r^2}{w^2(z)}\right) \exp\left(-\frac{r^2}{w^2(z)}\right) \times \exp\left(-ik\frac{r^2}{2R(z)}\right) \exp(-il\phi) \exp(i\psi(z)) \quad (3.1)$$

where $w(z) = w_0 \sqrt{1 + (z/z_R)^2}$ is the spot size at location z , given the beam waist w_0

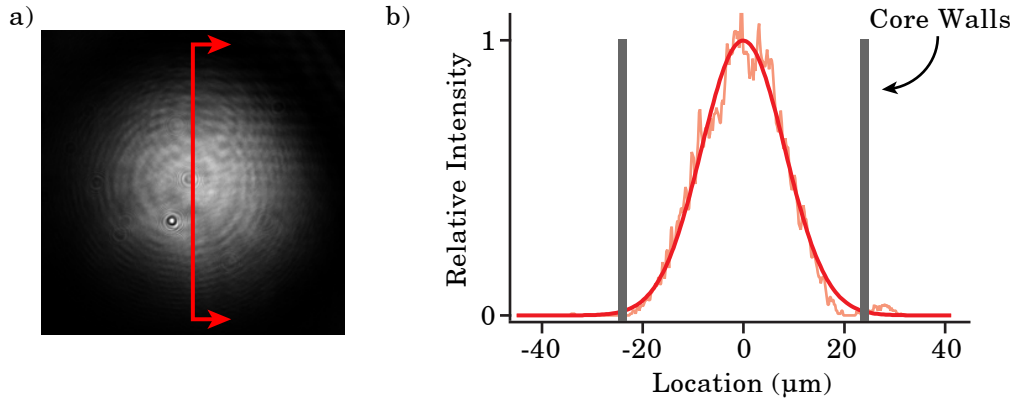


Figure 3.2: a) Image of the fundamental mode in the fibre with 1D slice axis shown, b) analysis of the slice from a) with location axis referred back to the scale of the fibre itself. The measured relative intensity is shown in pink, and Gaussian fit in Red.

and Rayleigh range $z_R = \pi w_0^2/\lambda$ for wavelength λ , $L_p^{||}$ are the generalised Laguerre polynomials, k is the wave number, $R(z) = z[1 + (z_R/z)^2]$ is the radius of curvature, and $\phi(z) = \arctan(z/z_R)$ is the Gouy phase. The intensity of the fundamental LG_{00} mode is much more easily written as

$$I(r, z) = \frac{2P}{\pi w^2(z)} \exp\left(-\frac{2r^2}{w^2(z)}\right) \quad (3.2)$$

where P is the total optical power. This intensity profile is commonly referred to as the Gaussian profile. Technically the guided mode of the fibre falls away faster than a Gaussian, reaching zero intensity before the walls of the core [24]. However this effect is only visible in the low intensity wings of the beam profile, and is ignored for our purposes.

An image of the guided mode can be taken by coupling light into one end of a segment of fibre, and allowing it to diverge from the opposite end. Placing an appropriate lens one focal distance from the output end of the fibre recollimates the beam, which is then incident upon a camera. The result of this is shown in Figure 3.2 where, aside from dust and diffraction artefacts, a nice circularly symmetric intensity profile is displayed. Taking a cross section through the centre of the beam produces a 1D profile of the beam intensity, which is well fit by a Gaussian. The mode $1/e^2$ diameter for this fibre was calculated to be $32.9(6) \mu\text{m}$ using finite-element analysis of the fibre geometry [86].

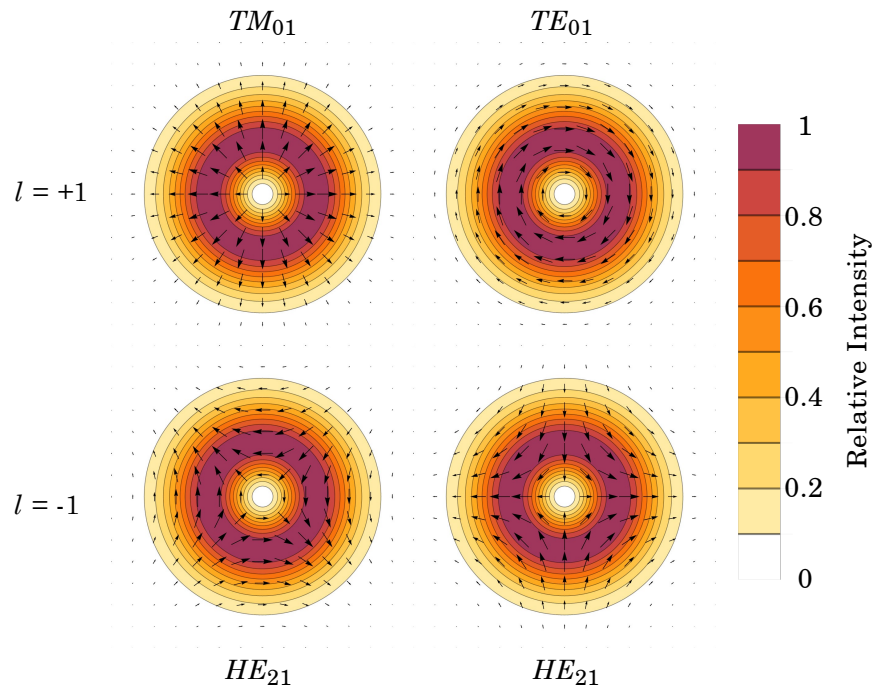


Figure 3.3: The TM_{01} , TE_{01} , and two degenerate HE_{21} modes that form an orthogonal basis for the first set of higher order modes supported by a hollow dielectric waveguide

3.2.2 Higher Order Modes

One of the primary reasons for using such a large core-diameter fibre is its ability to support higher order modes. While this can be frustrating for the user who is trying to couple only to the fundamental, it opens the door to a new dimension of light-atom interaction. The following is a brief description of the useful modes supported by the $45\ \mu\text{m}$ core kagome-lattice fibre and techniques used to couple into these modes.

The geometry of a hollow-core fibre imposes boundary conditions that must be satisfied for a mode to be supported over any useful distance. The cylindrical symmetry and dielectric walls of fibre core restrict the first family of higher order modes to the TM_{01} , TE_{01} , and the two degenerate HE_{21} cylindrical vector vortex beams (CVVBs) [95]. These modes are named this way due to the electric field polarisation vortex that produces a zero in the intensity of the beam on axis, as shown in Figure 3.3. These are similar in nature to the phase-vortex orbital angular momentum (OAM) beams that are more well known, and in fact the two mode families are linear combinations of each other.

| l | ϕ | Mode |
|-----|---------|-----------|
| 1 | 0 | TM_{01} |
| 1 | $\pi/2$ | TE_{01} |
| -1 | 0 | HE_{21} |
| -1 | $\pi/2$ | HE_{21} |

Table 3.1: List of the topological phase l and polarisation orientation ϕ that produce each of the first higher-order modes.

The electric fields of these modes can be described in cylindrical coordinates as

$$A(r) \cdot \left(\cos(\theta(1-l) + \phi) \hat{e}_r - \sin(\theta(1-l) + \phi) \hat{e}_\theta \right) \quad (3.3)$$

where \hat{e}_r and \hat{e}_θ are the polarisation unit vectors in the radial and azimuthal directions, l is the topological charge, ϕ is an arbitrary choice in polarisation orientation, and the radial amplitude function is given by

$$A(r) = \frac{\sqrt{2}r}{w} \exp\left(\frac{-2r^2}{w^2}\right) \quad (3.4)$$

with waist w . The modes shown in [Figure 3.3](#) can all be described by various combinations of l and ϕ , as shown in [Table 3.1](#).

Finite element analysis of the exact structure of the fibre confirms this guidance model, with the predicted eigenmodes matching the expected mathematical models. A comparison between one of the finite element solutions and the TE_{01} is shown in [Figure 3.4](#). Although the structure of the fibre core breaks the degeneracy of the two HE_{21} modes, this effect is very small and all the modes in this family possess effective indices very close to 1. The intensity profile of this mode family is well approximated by the LG_{01} profile given by the square of [Equation 3.1](#) with radial index of 0 and azimuthal index of 1.

Free-space generation of a [CVVB](#) from a Gaussian beam can be achieved in a number of ways. The most robust and reliable method is the use of q -plate, which is a half-wave retarder where the fast axis rotates in orientation azimuthally across the optic. For an $m = 1$ q -plate, the orientation of the fast axis performs a continuous 180° rotation across the device. A linearly-polarised Gaussian beam input on this device will, in the far field, form a [CVVB](#), where the exact mode generated depends on the relative alignment of the input polarisation and orientation of the q -plate. Moving between TM_{01} a TE_{01} output modes is as simple as rotating the input polarisation by 90° .

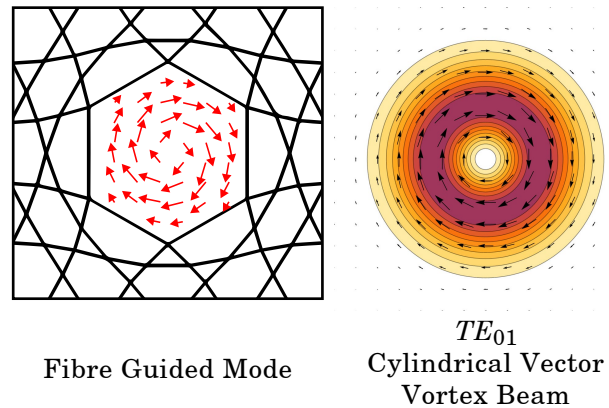


Figure 3.4: Comparison of the electric field vectors a hollow mode guided by the fibre and the TE_{01} cylindrical vector vortex beam.

The quality on a **CVVB** can be confirmed by using a **polarising beam splitter (PBS)** and imaging the horizontally and vertically projected components of the beam. A scalar **OAM** beam generate the same intensity profile in each port with relative powers determined by the polarisation state and angle of the beam. On the other hand a true **CVVB** will separate into a pair of orthogonal, two-lobed spatial modes, where the electric field is 180° out of phase between the two lobes of each.

We use a *Thorlabs* $m = 1$ q -plate (WPV10L-780) to generate the **CVVB** required to excite the hollow mode for the kagome-lattice fibre. When we test the generated mode as discussed above the results show an excellent polarisation state with no obvious overlap between projections, as seen in [Figure 3.5](#). The q -plate produces very little perturbation to the divergence or path of the beam. As such, once the fundamental mode has been coupled into the kagome-lattice fibre, guidance of the hollow mode can be achieved with only minor corrections. When the fibre output is projected into linear components we see no change in the quality of the polarisation state. This confirms that the fibre truly supports this mode and that the coupling processes are minimally damaging to the beam.

3.2.3 Fibre Coupling

Coupling light into the fibre is relatively easy, as the large core results in a low divergence angle of 0.86° . As such it is possible to use conventional lenses and beam sizes, without needing to resort to microscope objectives, as is sometimes needed for small core fibre. In addition, this low divergence allows the coupling lenses to be located far from the end of

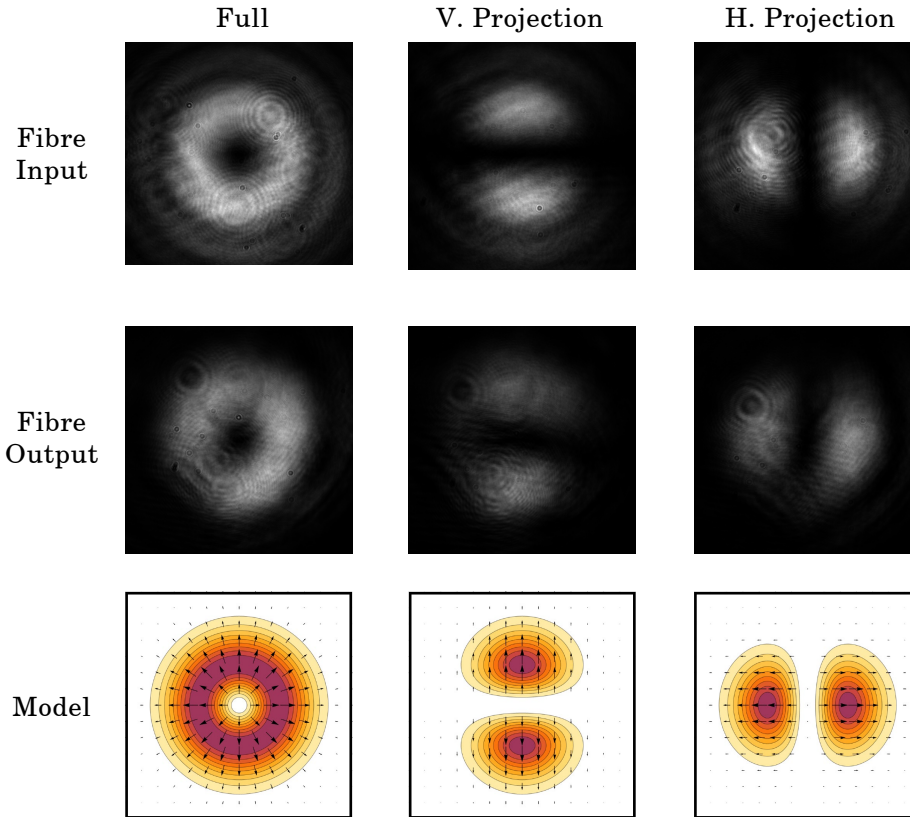


Figure 3.5: Comparison of the experimentally generated CVVB (top row), the mode after coupling through the kagome-lattice fibre (middle row), and the matching model (bottom row). The columns show the full intensity profile (left), and the projection into vertical (middle) and horizontal (right) polarisations.

the fibre, removing the requirement for in-chamber lens assemblies.

The experimental setup used to couple light into and out of the in-vacuum fibre is as follows, and is shown in Figure 3.6. The fibre itself is lightly clamped to a steel post that is bolted to a groove-grabber assembly at the lower flange. The post has a v-groove along its length that holds the fibre along the central axis of the chamber, with one end of the fibre situated a few millimetres from the lower vacuum viewport, and the top of the fibre roughly 25 mm from the centre of the chamber.

Light is coupled into the fibre through the lower viewport using a $\varnothing 50.8$ mm plano-convex lens with $f = 75$ mm, which is rigidly attached to the lower vacuum flange using a Thorlabs flange-grabber and cage-mount assembly. Tuning of the in-coupling lens is

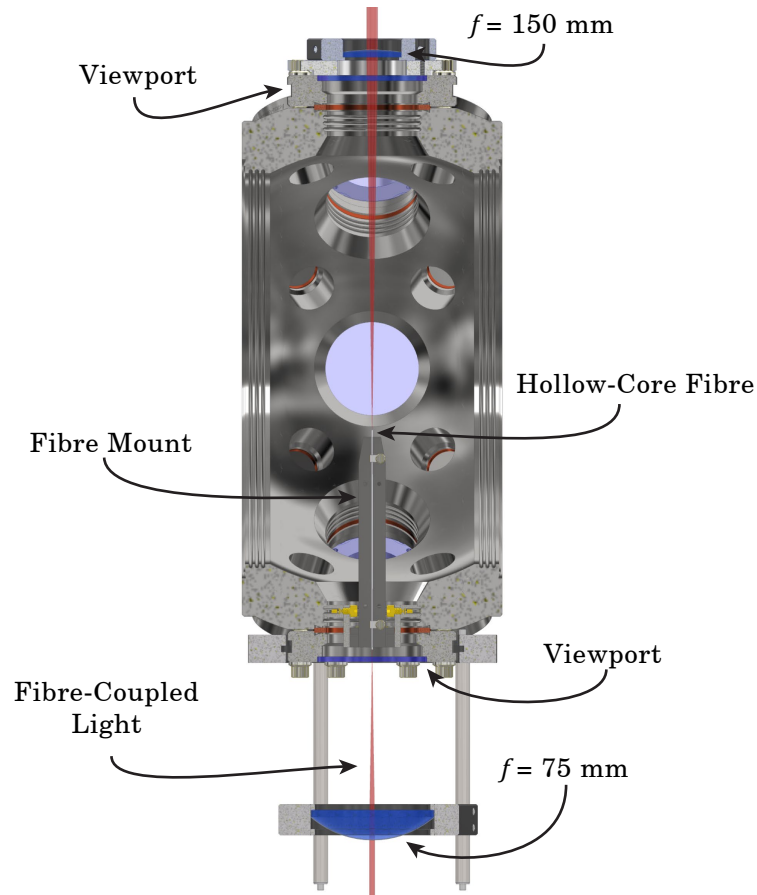


Figure 3.6: Model of the vacuum chamber components relevant to the coupling of light into and out-of the hollow-core fibre.

done by physically sliding the cage-plate up and down the cage-mount rods before locking them in place. This lens does not need fine adjustment, as fine tuning is done using 1 : 1 telescopes in the beam paths of each beam, allowing independent correction of the coupling. The optimum beam size before the lens is $\varnothing 1.5$ mm.

Light leaving through the upper end of the fibre exits the chamber via the upper viewport, and is roughly collimated by a $\varnothing 1$ " plano-convex lens with $f = 150$ mm, located as close to the viewport as possible. The resulting beam is nearly collimated (typically slightly converging) with a beam size of $\varnothing 4.6$ mm – luckily as there is little room between the top of the chamber and the over-table shelf. This beam size is large enough to propagate across the optics table without much change in shape, while small enough to comfortably clear the limiting aperture on standard 1" optics.

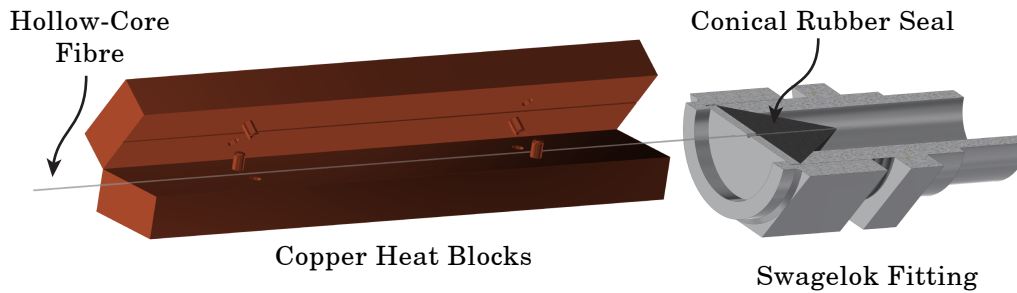


Figure 3.7: Model of the apparatus used to purge and bake the fibre before installation. A conical rubber seal is used in the *Swagelok* fitting to gently purge the fibre with a constant flow of clean nitrogen, while the paired copper-block assembly is used to evenly heat the fibre.

3.2.4 Fibre Preparation and Installation

Hollow-core fibre has the possibility of acting as a powerful virtual leak when used in a [ultra-high vacuum \(UHV\)](#) system due to the extreme aspect ratio, and the enormous surface area of the internal geometry. It is necessary to clean the exterior and interior of the fibre before installation to prevent this from limiting both the laser cooling performance and the in-fibre atom lifetime. The following process has been developed to thoroughly prepare a new segment of fibre for installation.

First the fibre's polymer coating is carefully removed using a scalpel to reduce out-gassing and prevent damage by the bake-out process as the polymer used becomes brittle above $80\text{ }^{\circ}\text{C}$. One end of the fibre is then inserted into a rubber cone with narrow bore hole, which is gently clamped in a standard *Swagelok* fitting, as shown in [Figure 3.7](#). This fitting is used to continuously pass clean nitrogen gas through the fibre during bake-out. The seal is checked by dipping the free end of the fibre into a beaker of isopropanol to confirm the presence of small bubbles caused by the gas flow.

The fibre is then placed into a segmented copper block with appropriately milled groove along its length, forming a complete copper oven for the fibre. The copper block is then raised to over $100\text{ }^{\circ}\text{C}$ for several hours, removing residual volatile surface contaminants. Once complete, the fibre is cooled down and removed from the gas fitting, and the ends are cleaved with a ceramic tile. Now prepared, the fibre is lightly clamped into the v-groove of the in-vacuum mount. Before being bolted into the chamber the fibre is tested on the table in its final mounting state to ensure that no damage has been done during the process.

3.3 Vacuum System

A vacuum chamber is vital for cold-atom experiments, as not only is rubidium highly chemically reactive, but laser cooling itself relies on an extremely low rate of collisions between the atomic sample and any background gas. These chambers are typically operated below 10^{-8} Torr and are carefully cleaned of any organic or otherwise volatile compounds such as rubber or grease. The pressure in a UHV chambers is typically maintained by constant use of an ion pump or other similar device, which is required due to the constant low-level outgassing of trace gasses from every surface. Once sealed, all efforts are made to avoid having to break the vacuum and return the chamber to atmospheric pressures. This is again due to both the susceptibility to contamination, and the low-level rubidium contamination of every surface in the chamber from the source.

3.3.1 Chamber

The setup used in this experiment is an 8" extended spherical octagon from *Kimball Physics* which provides both the internal volume and mounting points to hold the hollow-core fibre, as well as the flanges and external geometry necessary for a three-axis MOT. The chamber, shown in [Figure 3.8](#), is crafted from a single piece of 316L stainless steel and has highly polished UHV compatible surfaces. It is fitted with two 8" CF flanges, eight 2.75" CF flanges, and sixteen 1.33" CF flanges, all of which are aligned to centre of the chamber with a precision of better than 0.1° . All but the smallest size ports have internal grooves compatible with *Kimball Physics* groove-grabber assemblies, although there are no dedicated external mounting points aside from the CF flanges themselves.

The chamber is oriented such that the two large flanges are aligned to the x axis in the horizontal plane with one of the pairs of identical 2.75" flanges aligned vertically in the z axis. This forces a second pair of medium-sized flanges to be in the horizontal plane in the y axis, while the remaining two pairs form a cross at 45° in the $y-z$ plane. This coordinate system is chosen such that the cylindrical axis of the hollow-core fibre defines the z axis of the system, with the central axis of the MOT coils defining the x axis.

All the large and medium CF flanges are fitted with flat, uncoated, fused-silica viewports, save for the one 2.75" flange that connects to the ion pump and UHV valve. Most of these windows are used for laser cooling ($\pm x$ direction and both diagonal pairs), while the vertically aligned windows provide optical access to the hollow-core fibre, and the pair along the $\pm y$ axis provide the optical access necessary for alignment of the MOT and fluorescence detection measurements.

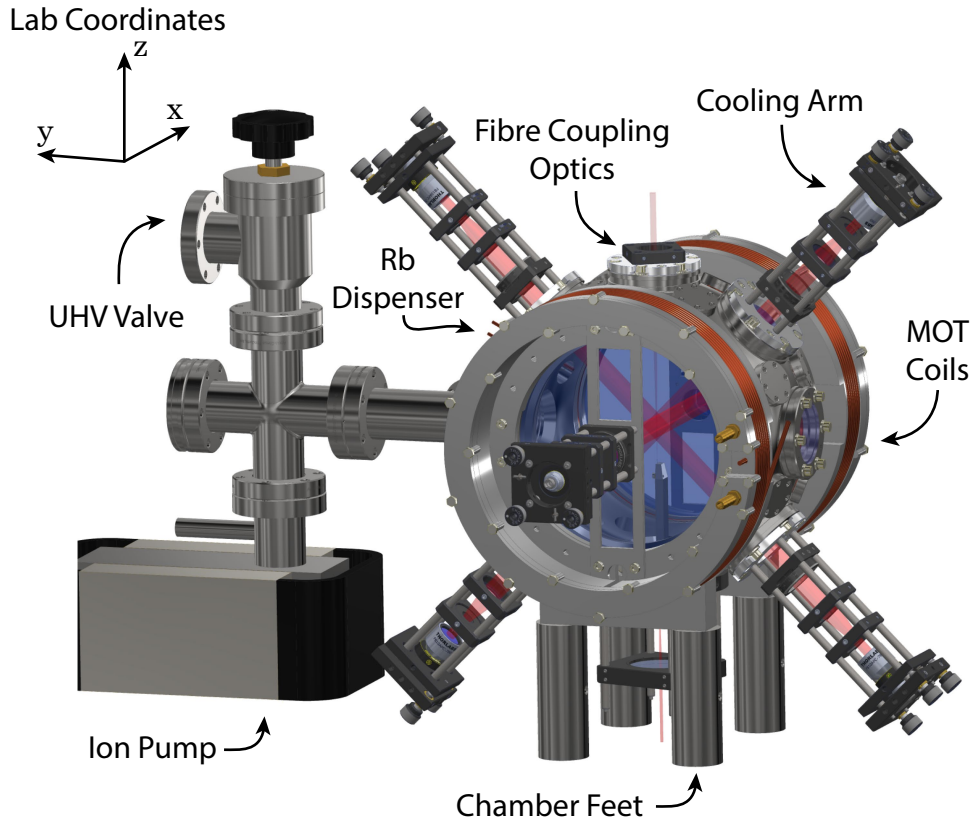


Figure 3.8: A CAD model of the vacuum chamber, including the external fittings and optical fields used for cooling and trapping atoms.

The vacuum pump is a 20 l/s *Varian* diode ion pump that runs constantly. The controller for the device supplies just under 5 kV and in operation reads a current across the element of less than 10 μA , which is the bottom of the gauge. This current is associated with a pressure at the pump of below 10^{-8} Torr, however the pressure in the chamber itself has been estimated to be at most 2×10^{-8} Torr using the loading rate technique described in [3].

The only access to the chamber interior is through a UHV grade manual angle valve located on the four-way cross above the ion pump. This valve is used to attach a turbomolecular pump to perform roughing of the chamber vacuum during pump down and is closed during the final stage of preparation. Once sealed the valve is only used on rare occasions to break the vacuum for maintenance or other work on the chamber interior.

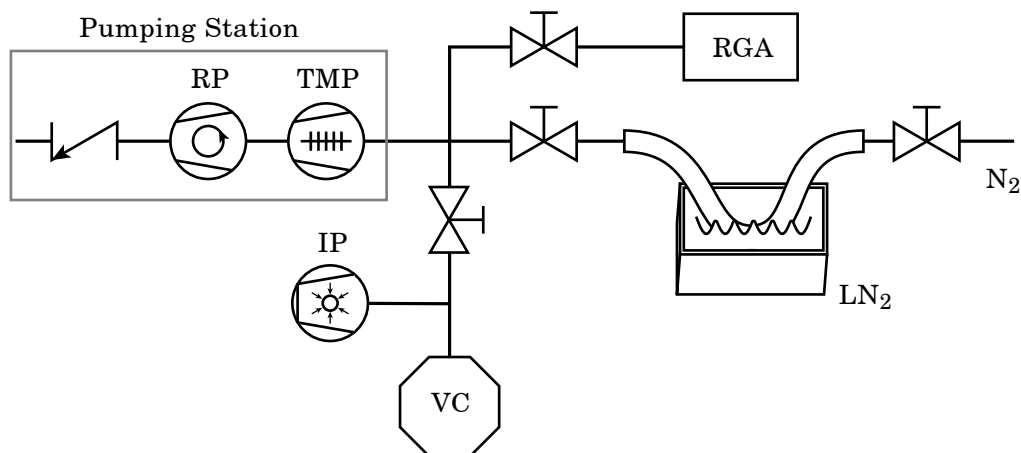


Figure 3.9: Schematic of the setup used to break the vacuum and perform pump downs. Here RP is a roughing pump, TMP is a turbomolecular pump, IP is an ion pump, N₂ is nitrogen gas, LN₂ is a reservoir of liquid nitrogen, RGA is a residual gas analyser, and VC is the vacuum chamber. The nitrogen source is only used during vacuum-break procedures.

3.3.2 Pump Down Protocol

The following is the protocol to prepare and achieve vacuum operation.

First the interior of the chamber is cleaned of surface contaminants using *Kimtech* delicate task wipes and methanol. Any CF flanges that were removed are cleaned and sealed using fresh copper gaskets and standard bolt tightening procedures. Once the chamber is prepared, a four-way cross is attached to the UHV valve on which a combined roughing and turbomolecular pumping station and an residual gas analyser (RGA) are mounted, as shown in Figure 3.9.

To begin, the chamber valve is opened and the pumping station is engaged. Once the pressure has been reduced to the operation range of the turbomolecular pump it is automatically spun up. The RGA is kept under vacuum, and the valve is slowly opened once the turbomolecular pump reaches maximum speed. At this level the device can be turned on, providing a measure of the pressures of gases with various molecular weights. It is typical to see large pressures of water vapour indicative of outgassing from the interior surfaces of the chamber and pump assembly. While this will slowly decrease over time, it is typical to speed up the process by baking out the vacuum chamber in a way similar to that used in subsection 3.2.4. This is done by loosely wrapping a length of heater tape around the chamber and passing current through it to slowly raising the

temperature several tens of degrees.

Once the chamber has reached temperature it is left pumping for several hours, after which the pressure due to water vapour has typically dropped down to the background level of that for nitrogen or other trace gases. At this point the ion pump is switched on, and a short burst of background gas is seen on [RGA](#) as the filament engages. Again the system is left until the trace gases have reached a steady state, then the valve on the chamber is sealed and the system is left to reach [UHV](#) levels. Once sealed, the pressure gauge in ion pump controller is used to diagnose the state of the chamber, and the [RGA](#) can be turned off and resealed. Finally the pumping station can be turned off and the turbomolecular pump is allowed to spin down before the assembly is dismantled.

The chamber is left to continue pumping on the ion pump until the pressure is sufficiently low, at which point the current through the heater tape is slowly reduced and the system reaches its final state, ready for use.

3.3.3 Vacuum Break Protocol

The primary goal of the vacuum break protocol is to return an atmosphere of pressure to the chamber while preventing the introduction of contaminants into the system, allowing for a rapid return to vacuum as soon as possible. This is achieved by refilling the chamber with a clean source of buffer gas, ideally free of water vapour. The setup used to perform this protocol is shown in [Figure 3.9](#).

To begin, the pumping station and [RGA](#) system are attached to the vacuum chamber via a four-way cross, with the last port connected to a clean nitrogen gas outlet via a thick rubber hose with manual valves on each end. This closed system is then roughed and pumped down, while the rubber hose is rested in an insulated container half-filled with liquid nitrogen. When the external vacuum system has been evacuated, the turbomolecular pump is allowed to spin down, but the roughing pump is kept on.

At this point the nitrogen valve is cracked slightly open, allowing a small flow of nitrogen to pass through the cold bath and fill the external system, which is then pumped out by the roughing pump. The liquid nitrogen cold bath serves to freeze out any remaining water vapour onto the walls of the hose, drying the nitrogen source. Once the nitrogen has been run for a minute or so to purge the line, the roughing pump is switched off and the [UHV](#) valve is carefully unsealed, filling the chamber with dry source of clean

nitrogen gas.

The chamber is allowed to reach slightly above atmospheric pressure, at which point the desired maintenance or modifications can be made. It is important to keep the chamber at positive pressure by continuing to flow nitrogen gas through the system, preventing contaminants in the lab from adhering to the walls. Once the chamber is ready to be pumped down again, it is sealed and the nitrogen line is shut off. At this point the protocol described above is followed to return the system to an operational UHV state. We find that following this method allows system to be operational for experiments less than 48 h after the chamber was opened.

3.4 Atomic Source

There are three commonly used types of atomic source used to produce the atomic flux necessary for cooling and trapping. These are: a raw elemental source, a directed oven, and an activated dispenser. Raw elemental sources are typically found in low-complexity vapour cell systems, while directed ovens are used in complex, multi-stage cooling experiments. In this experiment we have used current-activated alkali metal dispensers (also known as ‘getter’ sources) as we do not require the extremely low background pressures necessary for the production of BECs [97]. These devices are available for a range of elements (caesium, potassium, lithium, rubidium, and sodium) and are able to produce an ultra-pure source of atomic flux on command

A rubidium dispenser is a thin strip of a metal with an embedded rubidium-salt compound which is inert at room temperature. When heated above a threshold temperature (typically several hundred degrees Celsius), pure rubidium is released from the compound in a large solid angle. When under vacuum this temperature is easily achieved by passing several A through the strip. Similarly, allowing the the dispenser to cool below the threshold temperature ceases the production of free rubidium atoms, quenching the loading of the MOT in a matter of seconds.

A downside to these devices is that the produced atomic flux typically needs to be pointed directly at the MOT cooling region to effectively loading the trap. As such the large number of atoms with velocities above the capture range of the trap serve only to eject cold atoms from the ensemble, limiting the lifetime and maximum atom number achievable. This is an unfortunate trade off for the convenience of this type of atom source.

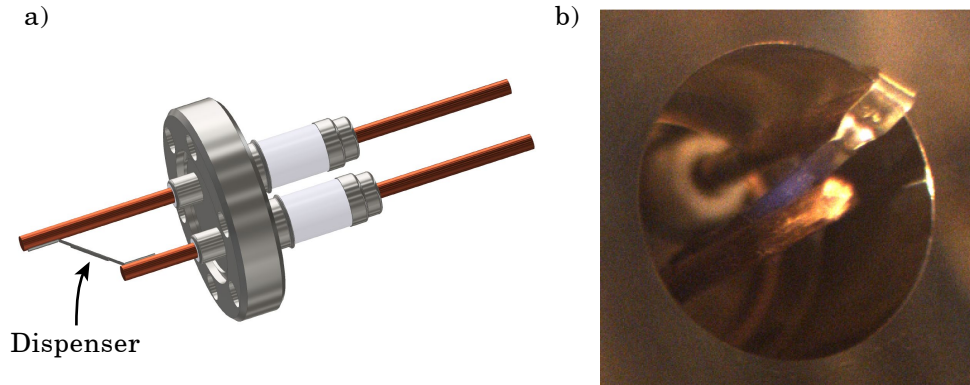


Figure 3.10: a) Model of the dispenser attached to a two-port high-current 1.33" CF feedthrough. b) Camera image of the in-vacuum side of the dispenser while operating at a relatively high current. The rubidium-salt compound region shows a light blue glow.

3.4.1 Implementation

The dispensers used are *SAES* rubidium getters. These devices have an active region roughly $15\text{ mm} \times 3\text{ mm} \times 1\text{ mm}$ in dimension with thin metal pads on each end, and can release several milligrams of pure metal. The experiment has three dispensers installed in the chamber, each mounted on two-port high current 1.33" CF feedthroughs, as shown in [Figure 3.10](#). The thin conductive pads of the dispenser are spot welded to the each of the copper rods of the feedthrough to provide a low-resistance join that does not use soldering agents that susceptible to attack by the rubidium vapour.

The current response of the dispenser is mapped out by using the fluorescence counting technique described in [section 4.1](#) to measure the number of atoms in the [MOT](#) with typical laser-cooling parameters (23 mW per arm with -18 MHz detuning and 6.5 G/cm magnetic field gradient). The current through the dispenser is stepped in small increments with several seconds between each to allow the dispenser to stabilise, with the resulting calibration measurement is shown in [Figure 3.11](#). A curve of the form $y(x) = y_0 + A \exp\left(\frac{x-x_0}{\tau}\right)$ is fit to data points above the threshold at $x_0 = 4.4\text{ A}$, returning values of $y_0 = -2.4(3)$, $A = 2.7(2)$, and $\tau = 0.50(2)\text{ A}$.

While a large atom number is desired for the end-use of the experiment, in typical operation the dispenser is run at $\sim 4.5\text{ A}$. The resulting atom number of 10^8 is high enough for day-to-day use, and choosing to run at low current extends the life of the dispenser significantly.

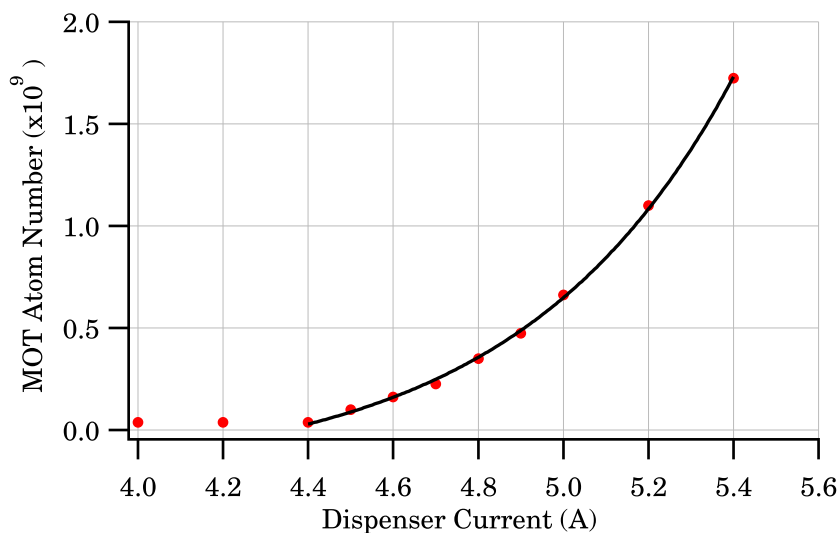


Figure 3.11: Measured number of atoms in the MOT as a function of rubidium dispenser drive current (red circles). An exponential fit is shown to agree well with the data above the threshold current of 4.4 A (black line).

3.4.2 Dispenser Cleaning Protocol

Occasionally the supply of rubidium will run out, typically identified by the steadily increasing dispenser current required to produce the typical number of atoms in the trap. This is a slow process which is likely to be more related to accidental over-current events than typical use. On these occasions it is necessary to switch to an auxiliary dispenser already installed, or to replace the depleted strip with a replacement.

We have found that in both cases the new dispenser does not initially perform as expected. This is a phenomena that has been identified in the literature [97] and is suggested to be due to build up of a conductive micro-layer over the rubidium compound. The solution to this problem is to ‘burn in’ the new device by momentarily supplying a significantly higher current, baking the device and providing a clean surface.

Our particular method for this is to supply $\sim 10\text{A}$ to the device while carefully watching the in-vacuum pressure gauge. A few seconds after switching on the current source a dramatic rise in background pressure is observed, at which point the source is switched off and the ion pump is given several minutes to return the pressure levels to normal. This is repeated three or four times.

Although we have not rigorously tested this method, we find that dispenser behaves as normal after the process, and once the chamber has pumped back down the MOT loads as normal.

3.5 Laser Systems & Stabilisation

Coherent optical fields are vital to the manipulation and interrogation of the atomic ensemble in this project. These light sources perform a range of tasks, including laser cooling, population repumping, optical dipole trapping, and atomic interrogation. Most of these optical fields are generated by home-made [external-cavity diode lasers \(ECDLs\)](#) which have their optical frequencies stabilised to atomic transitions, either via some form of spectroscopic interrogation or through direct comparison with another laser. These laser sources are cheap, user-maintainable, operate on a single longitudinal mode, and typically have a relatively narrow linewidth (typically less than 300 kHz). Below is a short description of each laser used in the experiment, its purpose, and how its frequency is stabilised.

3.5.1 Probe Laser

The probe laser is an [ECDL](#) operated at 780 nm used to interrogate the cold atom system. This laser is tuned to the $|F = 3\rangle \rightarrow |F' = 4\rangle$ cycling transition on the rubidium-85 D_2 line, and is locked directly to resonance using [MTS](#), a frequency-modulated sub-Doppler spectroscopy technique [72]. This laser light is used for two purposes: first it provides a stationary reference with which to stabilise the cooling laser, described in [subsection 3.5.2](#), and second it is used to perform both shadow imaging and absorption spectroscopy, as described in [chapter 4](#).

A diagrammatic representation of the beam path for the laser as well as relevant optics and electronics is shown in [Figure 3.12](#). The laser produces roughly 20 mW of light in an elliptical beam with linear polarisation. The beam ellipticity is corrected with a pair of cylindrical lenses, and an isolator is used to protect the laser from back reflections. The beam is then split into two: one arm with most of the power is split off and coupled into fibre, after which it is sent to both the probe [acousto-optic modulator \(AOM\)](#) setup described in [subsection 4.3.1](#) and to the cooling laser setup as the stable reference for the phase lock.

The remaining free-space light is further split and passed through a room-temperature rubidium vapour cell in both directions to perform the pump-probe spectroscopy [MTS](#).

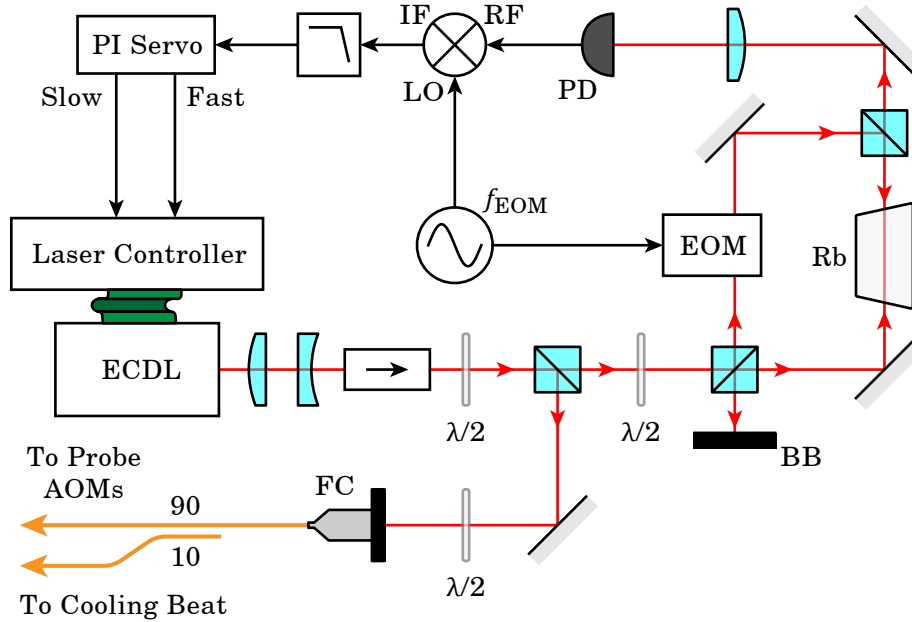


Figure 3.12: Block diagram of the probe laser setup, including the optical and RF components, where PD is photodetector, FC is fibre coupler, BB is beam block, and EOM is electro-optic modulator.

Here the strong pump beam is frequency modulated at a rate of $f_{\text{EOM}} = 9$ MHz and sent counter propagating through the vapour cell to overlap with the weak probe beam. The probe is collected onto a photodetector with both DC and AC coupled outputs. The DC signal is used as a diagnostic to interrogate the Doppler broadened transition manifold, while the AC output is amplified and mixed with an [local oscillator](#) (LO) at the same frequency as the modulation. The demodulated signal is used as an error signal and amplified by our home-made analog lock box and fed back into the fast current and slow piezo modulation ports of the laser. The DC transmission spectrum and demodulated error signal are both shown in [Figure 3.13](#), where the individual hyperfine-split transitions and cross-over transitions are labelled.

A frequency comparison between the probe laser and a frequency comb with stability better than 10^{-14} from 1 s to 1000 s shows a fractional frequency stability of 10^{-11} at thousands of seconds, dominated by slow environmental effects. The fast linewidth of the laser is measured to be 180 kHz. This level of stability is sufficient for the interrogation of the rubidium $5P_{3/2}$ excited state which has a linewidth of 6.07 MHz.

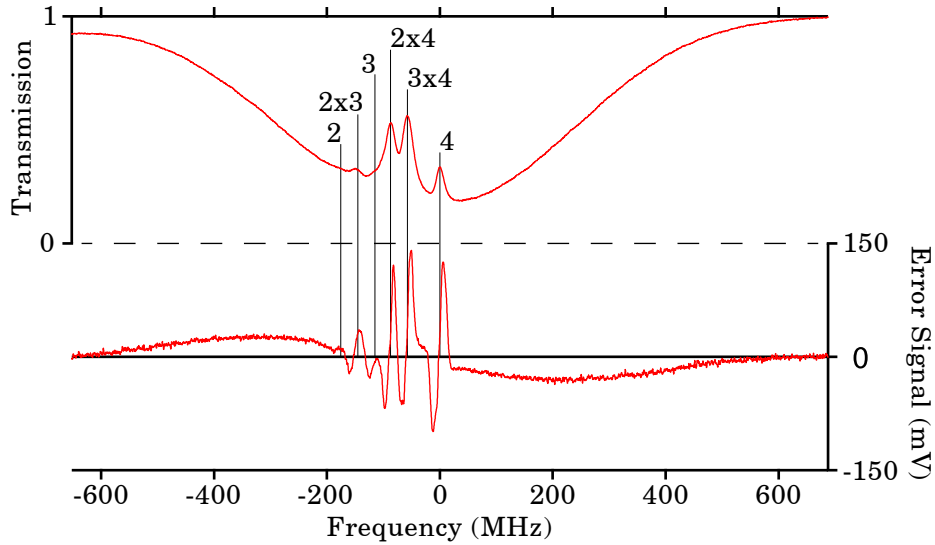


Figure 3.13: Sweep over a saturated absorption spectrum of the $|F = 3\rangle \rightarrow |F'\rangle$ manifold of the D_2 line (top) and the corresponding error signal for the [modulation transfer spectroscopy \(MTS\)](#) lock of the probe laser (bottom). The resolved hyperfine transitions and their cross-over transitions are shown and labelled with the corresponding F' number.

3.5.2 Cooling Laser

The cooling laser is essentially identical to the probe laser described above: it is a home made [ECDL](#) operated at 780 nm. This laser is phase locked to the probe laser well-defined offset frequency, providing the fast, broadband tunability that is needed to transition between the near-resonance detuning used for Doppler cooling and far off-resonance detuning used for [polarisation gradient cooling \(PGC\)](#). The single purpose of this laser is to seed the semiconductor gain module that is used to provide the high optical power necessary for laser cooling of the atomic ensemble.

The output of the diode laser is corrected for astigmatism and passes through two isolation stages for a total of 90 dB of isolation. This is necessary due to the possibility of high power reflections from the optical gain stage that follows. The prepared light is then coupled into fibre and split 90 : 10, where the 10 % goes to the frequency stabilisation scheme and the remaining 90 % goes directly to fibre input of the tapered amplifier.

The tapered amplifier is a *Thorlabs* semiconductor amplifier in a butterfly package with fibre input and free-space output designed to operate at 780 nm (TPA2780P20). We typically achieve 1.5 W of output power with a 10 mW seed, although the mode shape out

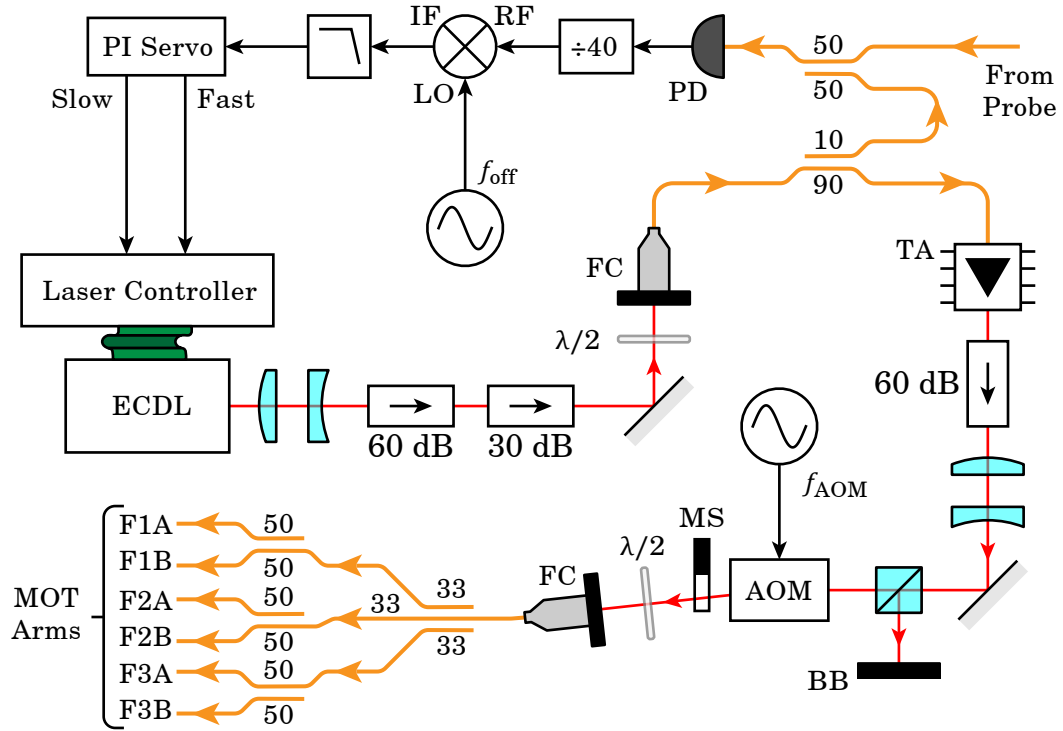


Figure 3.14: Block diagram of the cooling laser setup, including the optical and RF components, where PD is photodetector, FC is fibre coupler, TA is tapered amplifier, BB is beam block, and MS is mechanical shutter.

of the amplifier is poor, limiting the useful output. The amplified light is circularised as best as possible with a cylindrical telescope and passed through an AOM driven at $f_{\text{AOM}} = 80 \text{ MHz}$ as well as a mechanical shutter. This combination provides for fast switching with high isolation.

The amplified and frequency shifted laser light is coupled into optical fibre, and separated into three pairs of matched-power arms using a series of polarisation maintaining (PM) fibre splitters. The input is first split three-ways with an ideal split ratio of 33 : 33 : 33, each arm of which is spliced to a 50 : 50 splitter. Each of these arms provides the light for one of the MOT cooling beams, and they are labelled F(1,2,3)(A,B) for identification. The use of high-quality PM components and fibre splicing makes the entire system very robust and easy to maintain, at the cost of individual tunability of the arms. Although there are variances in optical power between the arms the MOT appears to suffer no ill effects. The measured power at each arm is given in Table 3.2

The 10 % fibre tap off of the seed is combined in fibre with several hundred microwatts

| Cooling arm ID | Optical power (mW) |
|----------------|--------------------|
| F1A | 41.0 |
| F1B | 36.0 |
| F2A | 33.8 |
| F2B | 33.5 |
| F3A | 29.0 |
| F3B | 26.5 |
| Total | 199.8 |

Table 3.2: List of the optical powers measured in each cooling arm.

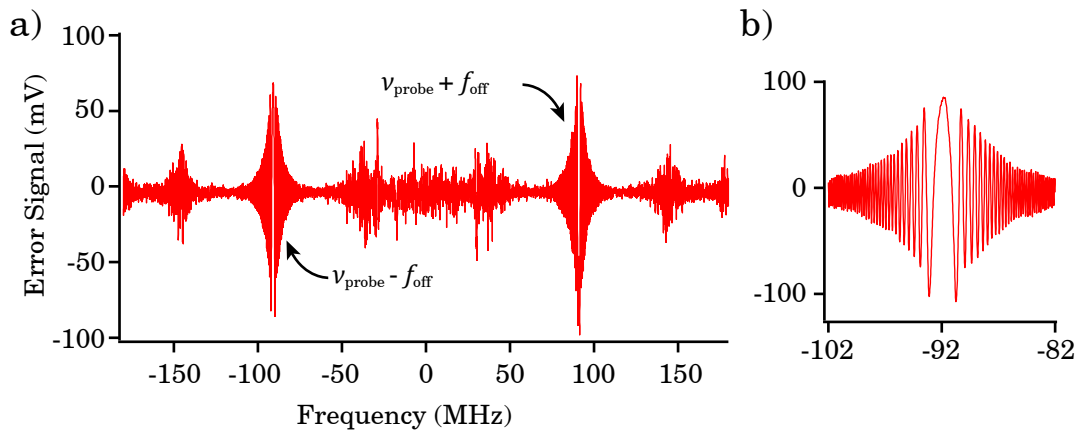


Figure 3.15: The error signal for the frequency-offset lock of the control laser, a) shown over a wide sweep of $> \pm f_{\text{off}}$, and b) a fine sweep around the lock point. The two valid mixing products generated using the technique are shown.

of probe light and collected on a fast photodetector. This produces a electronic signal at the difference frequency in the optical signals, which is then divided in frequency by a factor of 40 using a clock prescaler chip (MC12080) to improve the locking range. The output of the prescaler is mixed with an LO at f_{off} produced by an arbitrary waveform generator and is low-pass filtered. This technique allows us to lock the cooling seed to the probe laser at a tunable offset frequency determined by the product of the division factor and the demodulation frequency. The error signal for this system is shown in Figure 3.15, where only one of the two available lock points will hold the laser at the desired offset frequency.

Once locked the laser can be tuned by manipulating the demodulation frequency, as

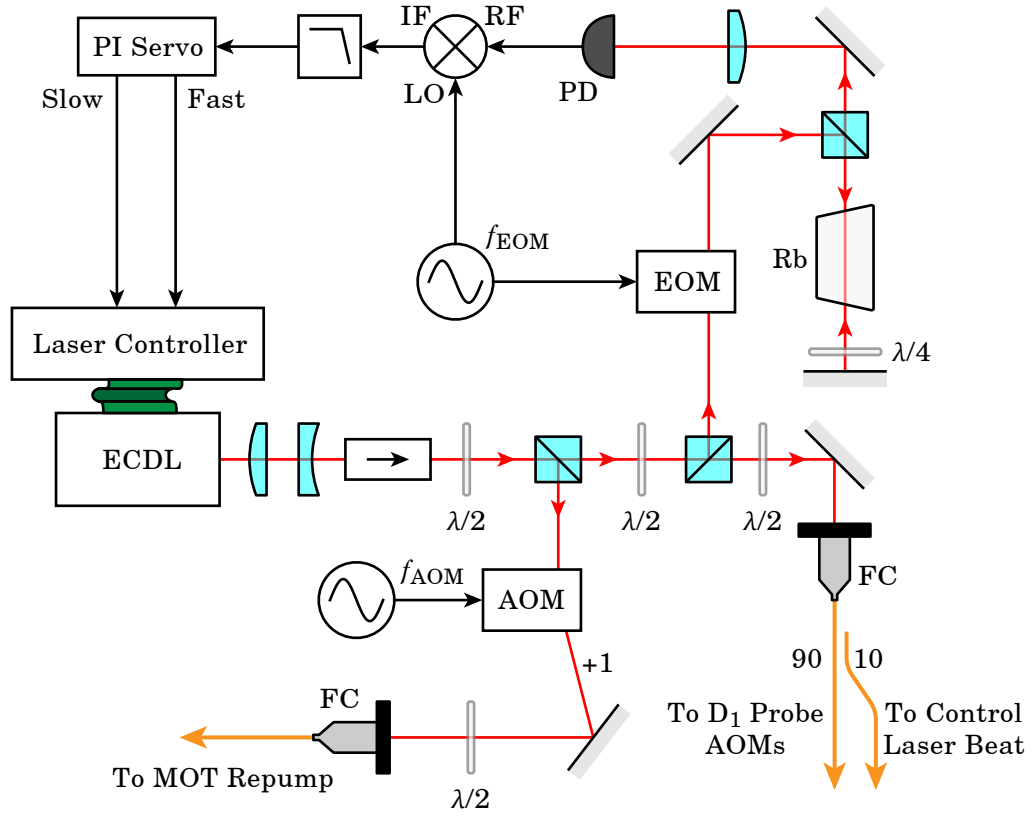


Figure 3.16: Block diagram of the repump laser setup, including the optical and RF components, where PD is photodetector, FC is fibre coupler, and EOM the electro-optic modulator.

long as the change is slow enough to be faithfully mapped onto the laser. By programming a predetermined frequency ramp and return into the arbitrary waveform generator, we are able to perform a wide and fast chirp of the cooling-light detuning using only a trigger from the Arduino (see subsection 3.7.2). When choosing the demodulation frequency to produce the desired optical frequency detuning it is necessary to remember the presence and sign of the frequency shift produced by the switching AOM.

3.5.3 Repump Laser

Unlike the previously described lasers, this homemade ECDL operates at 795 nm, intended to drive transitions on the D_1 line rather than the D_2 line. This laser is primarily used as the repumper during laser cooling, pushing population from the dark $|F = 2\rangle$ ground state up to the $|F' = 3\rangle$ excited state, from which it has a high likelihood of returning to the cooling-active $|F = 3\rangle$ ground state. In more recent experiments this laser is also used as a probe laser to investigate EIT phenomena on the D_1 line.

The repump is locked to the $|F = 2\rangle \rightarrow |F' = 2 \times 3\rangle$ crossover transition. This is a useful feature as it allows the use of a single-passed AOM at 180.8 MHz to shift the laser frequency onto resonance with the $|F = 2\rangle \rightarrow |F' = 3\rangle$ transition, which can also perform fast switching of the beam.

This output of the laser is corrected for astigmatism with a cylindrical telescope and passed through an isolator, as shown in Figure 3.16. The laser is split into three directions in free space, the first goes through an AOM with frequency shift f_{AOM} equal to half the excited-state hyperfine separation of 361.6 MHz, and is coupled into fibre. This light is sent to the vacuum chamber to act at the repump for the MOT.

The second free-space beam is a weak tap that is sent through an electro-optic modulator (EOM), retroreflected through a rubidium vapour cell, and collected on a photodetector. An error signal is produced by taking the AC signal from the photodetector, demodulating it at the EOM drive frequency of $f_{\text{EOM}} = 7$ MHz, and low-pass filtering it. This technique is known as frequency-modulated saturated absorption spectroscopy and is used to achieve high signal-to-noise sub-Doppler laser frequency stabilisation. The error signal, shown in Figure 3.17, is then amplified by our homemade lock box and fed back to both the current and piezo modulation ports on the laser controller.

The final free-space beam is directly coupled into fibre and split 90 : 10. The 90 % arm leads to the D_1 probe AOM setup described in 4.5.3.1, which is used to generate both the stepped-detuning pulses for interrogation and the LO for heterodyne detection. The 10 % arm is sent to the EIT control laser system for phase locking.

3.5.4 EIT Control Laser

The EIT control laser is a relatively recent addition to the experiment, and is used in EIT spectroscopy and pulse storage experiments. Again, this is a homemade ECDL with a high power 795 nm diode. This laser is frequency offset phase locked to the repump laser, allowing it to be located anywhere in the $|F = 3\rangle \rightarrow |F'\rangle$ manifold of the D_1 line.

The configuration of the control laser setup is very similar to that of the cooling laser but without the high-power amplification stage, and is shown in Figure 3.18. The laser output passes through a cylindrical telescope to correct for astigmatism, an isolator, and is coupled directly into fibre. Once in fibre a 90 : 10 splitter is used to tap off light for a frequency offset phase lock against the repump laser. This offset lock behaves similarly to

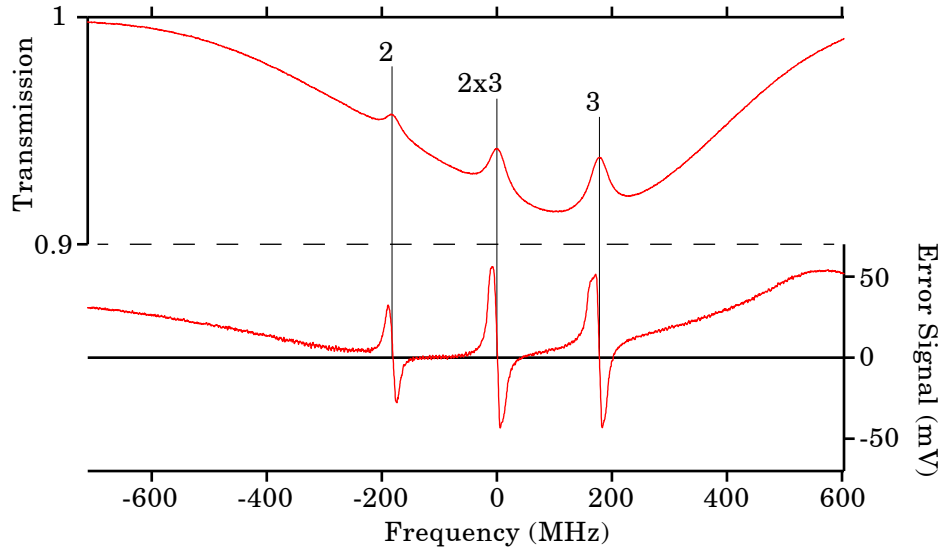


Figure 3.17: Sweep over a saturated absorption spectrum of the $|F = 2\rangle \rightarrow |F'\rangle$ manifold of the D_1 line (top) and the corresponding error signal for the frequency-modulated saturated absorption spectroscopy lock of the repump laser (bottom). The resolved hyperfine transitions and their cross-over transitions are shown and labelled with the corresponding F' number.

the cooling laser offset lock, however the difference in optical frequencies is significantly higher as the repump is locked to the $|F = 2\rangle \rightarrow |F' = 2x3\rangle$ crossover transition while the control needs to interact with the $|F = 3\rangle \rightarrow |F' = 3\rangle$ transition – a difference of 2.8549 GHz.

A high performance microwave divider with a much lower division ratio is used here (*Hitite* HMC365) as the phase coherence between the repump (used as the **EIT** probe) and the control strongly affects the performance of the **EIT** protocol. In addition, the fast lock box output is fed directly into a high-speed current modulation port on the laser headboard, avoiding delays and added noise from passing through the laser controller. This allow us to achieve Hertz-level linewidth on the phase lock between the two lasers, as measured out-of-loop on the unused arm of the 50 : 50 splitter. This measurement is shown in [Figure 3.19](#), where the linewidth is limited at 1 Hz by the resolution bandwidth of the device. The error signal of this phase lock is shown in [Figure 3.20](#), where the **LO** frequency has been chosen to shift the laser lock point to the $|F = 3\rangle \rightarrow |F' = 2\rangle$ transition. The large difference in optical frequencies in the phase lock allows for wide tuning of the lock point over the entire Doppler broadened $|F = 3\rangle \rightarrow |F'\rangle$ manifold.

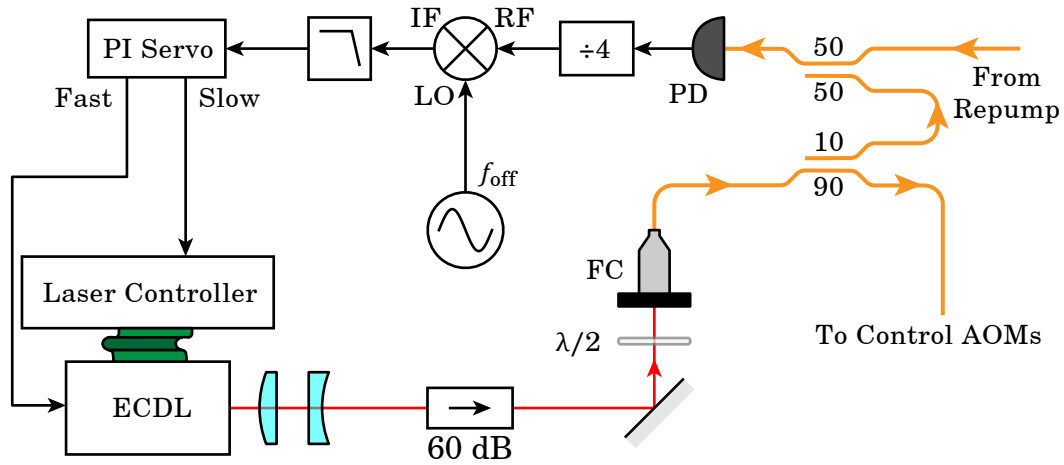


Figure 3.18: Block diagram of the **EIT** control laser setup, including the optical and RF components.

The 90 % port of the fibre splitter is sent to the same **AOM** setup used for shadow imaging and broadband absorption spectroscopy, allowing for fast switching of the control signal around the lock point. The source of light used in the **AOM** switching setup can be switched between the probe and **EIT** control by setting a beam block appropriately, although in the future this will be replaced by a pair of Arduino controlled mechanical shutters.

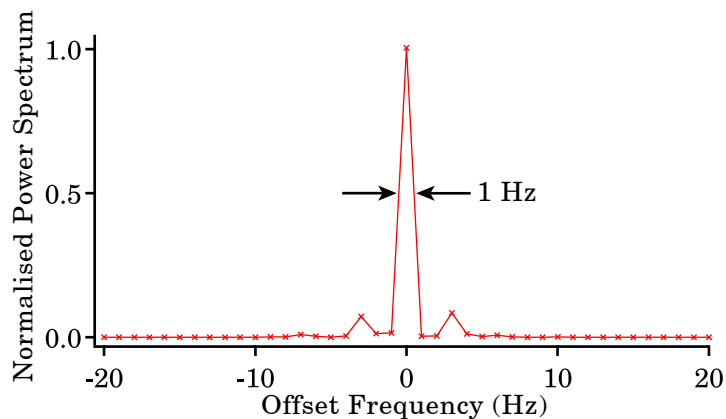


Figure 3.19: Measurement of the phase lock performance **EIT** control laser showing a **FWHM** of 1 Hz limited by the resolution bandwidth of the spectrum analyser.

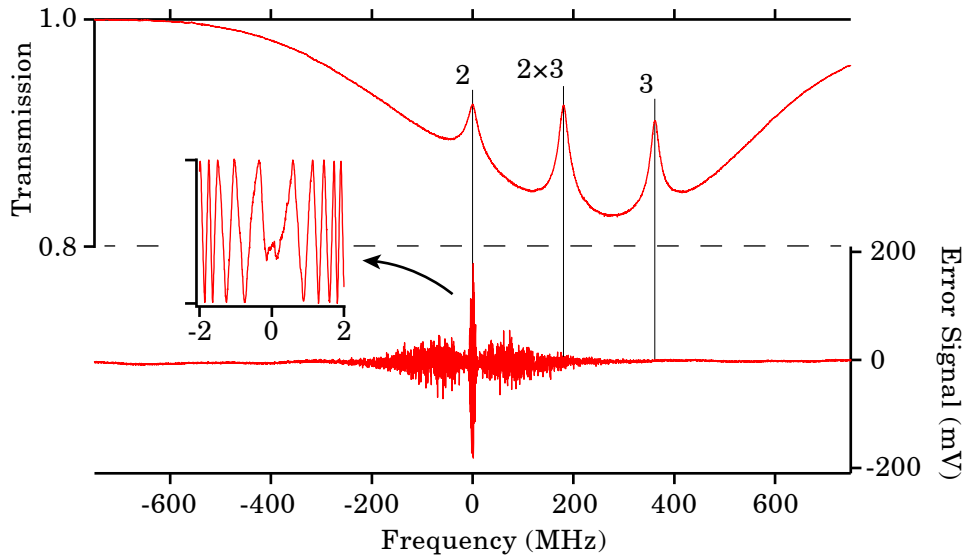


Figure 3.20: Sweep over a saturated absorption spectrum of the $|F = 3\rangle \rightarrow |F'\rangle$ manifold of the D_2 line (top) and the error signal for the frequency-offset lock of the control laser (bottom). The inset shows a fine sweep over the lock point. The resolved hyperfine transitions and their cross-over transitions are shown and labelled with the corresponding F' number.

3.5.5 Guide Laser

Unlike all other lasers used in this experiment, the guide laser is not a diode laser. Although the requirements of high tunability and high power could be satisfied with an [ECDL](#), we currently use an *M squared* CW titanium sapphire laser, known by its model as the SolsTiS. This laser is software tunable over 700 nm to 1000 nm with minimal beam steering, and has an output of 2.8 W in a very good mode shape.

The output of the SolsTiS is passed through an isolator and a small amount of power is tapped off with an [PBS](#) and sent to the wavemeter via fibre as shown in [Figure 3.21](#). The wavemeter is monitored by the lab PC, and when a wavelength (or detuning from the D_1 or D_2 transitions) is desired, the PC sends coarse and fine tuning commands to the SolsTiS controller until the wavelength is within 500 MHz of the set point, at which point the controller is sent the command to enable the coarse frequency lock. Fine control of the laser should be possible, but a broken piezo in the internal reference cavity prevents us from using this feature.

The rest of the power is [AOM](#) shifted, passed through a mechanical shutter, and fibre

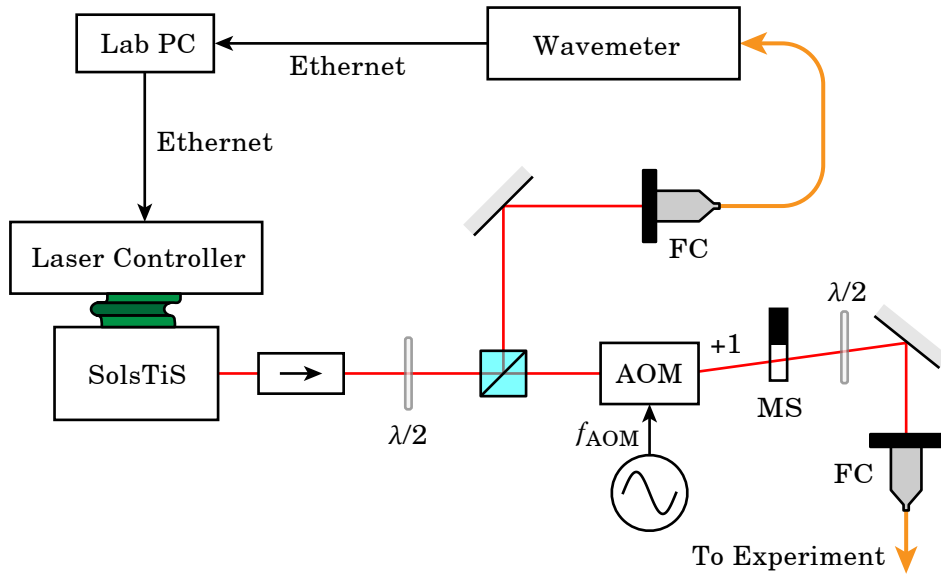


Figure 3.21: Block diagram of the guide laser setup, including the optical and RF components.

coupled for delivery to the experiment. Minimal optics are required as the beam mode out of the laser is circular and well collimated. The order and frequency of the AOM is irrelevant in this case, as the laser is typically detuned between 200 and 1000 GHz from an atomic transition, and as such the +80 MHz AOM shift makes little difference.

3.5.6 Optical Switching

Rapid switching of optical beams is a common element to many of the systems used in the experiment including the cooling, repump, guide, and probe beams. There are two common techniques used to perform switching of an optical beam: direct mechanical shuttering, or acousto-optic modulation.

Mechanical shuttering is as it sounds: a control signal triggers a physical barrier that blocks the optical path. This method provides 100% extinction of the optical beam when in the shut position, but has a long delay (ms) and a slow rise and fall time (100 μ s). A common implementation of such a device uses the read-write head of a spinning-disc hard drive as the actuator [67].

In comparison, an acousto-optic switch exploits the angular deviation through an active AOM to spatially separate the on and off states of the optical beam. By selectively

coupling the frequency shifted beam into optical fibre the on and off states can be very well isolated, with extinctions of > 60 dB. In addition, as these devices rely on the electrostriction of a crystal element by the applied RF signal, the switching speed can be extremely fast. Typical implementations achieve 100 ns rise times, limited by the crossing of the acoustic wave across the beam. The use of extremely small or focused beams through the AOM can improve this further.

A downside to AOM based switches is that the high RF power being applied to the crystal leads to heating and thermal expansion, which in turn produces steering of the optical beam passing through it. When in steady state operation this effect is constant presents no problem. Similarly, when used to produce low duty cycle, short pulse sequences, the slow thermal effect does not play a major role. However in the case of slow, high duty cycle switching, this effect can cause strong modulation of the output beam power.

The solution we use to address this issue is to implement an AOM followed by a mechanical shutter for these systems. The state of the AOM is control by amplitude modulation of the RF drive signal with a fast microwave [single-pole single-throw \(SPST\)](#) switching chip (*Analog Devices* HMC550). In the case of an optical beam that is primarily in the off state, the mechanical shutter is kept shut while the AOM is kept active. This allows the thermally sensitive element of the system to remain in a steady state. When switching is desired, the system is first prepared by switching off the RF drive signal to the AOM and enabling the mechanical shutter control. Several milliseconds later the shutter opens, and the fast RF switch is used for precise, rapid rise time switching on of the optical beam.

To revert the system to an off state the same process is followed in reverse. The AOM is switched off precisely when desired, after which the mechanical shutter control is disabled. Once the shutter has closed the AOM is returned to its active state, allowing it to remain in thermal equilibrium. A measured timing diagram for a full pulse sequence is shown in [Figure 3.22](#) along with a zoom into the falling edge of the optical signal.

3.6 Magneto Optical Trap

The introduction of laser cooling by Chu, Cohen-Tannoudji, and Philips in the 1980s changed the state of play in atomic physics, allowing the preparation of high number-density ensembles of identical, near stationary particles [22, 23, 89–91]. These systems

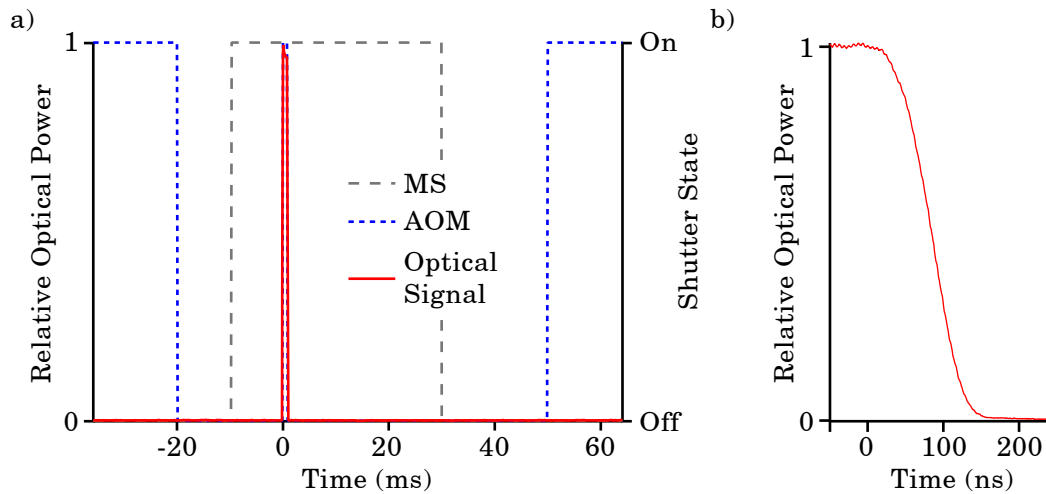


Figure 3.22: Timing diagram of the optical switch system. a) The mechanical shutter (grey, dashed) and AOM (blue, dotted) based switch states are shown along with the resulting optical signal (red). b) The falling edge of the optical signal shows a 90 – 10 fall time of 80 ns.

have become the workhorses of the AMO community, and have expanded into a wide field of techniques used to cool and trap every atomic species and geometry imaginable.

Our implementation of laser cooling consists of a three-axis MOT on the D_2 $|F = 3\rangle \rightarrow |F' = 4\rangle$ cooling transition. Once filled, the atomic ensemble is further cooled with a short $\sigma_+\sigma_-$ PGC phase. The secondary cooling is complemented with a temporal dark-spot, in which the repump power is reduced to allow a larger number density to accumulate in the dark $|F = 2\rangle$ ground state. This approach is capable of capturing 10^8 atoms in a 2 mm diameter cloud with an ensemble temperature of 5 μK .

The field of laser cooling is mature and there are several well respected texts available that provide detailed and nuanced description of the history, theory, and application of these techniques. I recommend the seminal text *Laser Cooling and Trapping* by Metcalf and Straten [74], as well as the detailed mathematical investigation of sub-Doppler cooling *Laser cooling below the Doppler limit by polarization gradients: simple theoretical models* by Dalibard and Cohen-Tannoudji [29]. As such I provide here only a description of the layout and configuration of the MOT used in this experiment. Specific detail is given to the apparatus used in the cooling and repump systems as well as the anti-Helmholtz and compensation coils.

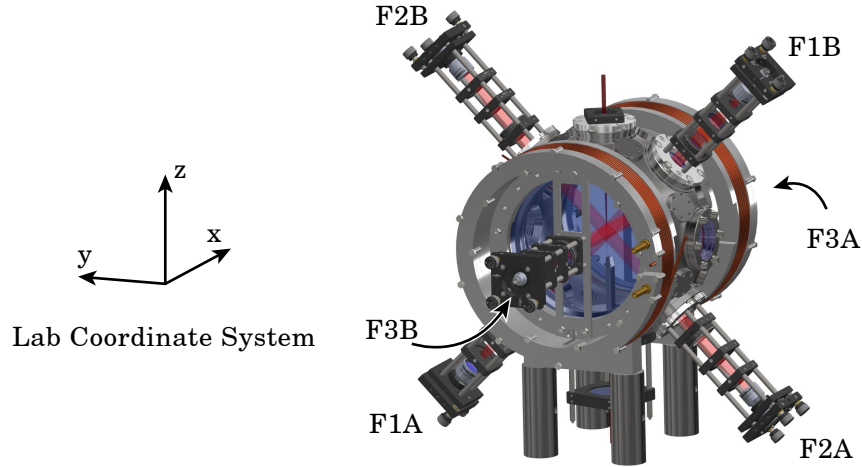


Figure 3.23: The vacuum chamber assembly with the lab reference frame and cooling arm axes shown.

3.6.1 Laser System

The production and stabilisation of the light used for laser cooling and repumping are described in detail in [subsection 3.5.2](#) and [subsection 3.5.3](#) respectively. The switching of the lasers is discussed in [subsection 3.5.6](#), and the computer oversight discussed in [section 3.7](#). Here I describe the physical implementation of the laser fields around the vacuum chamber.

The implementation of laser cooling used here relies on power-matched counter-propagating beams in three orthogonal axes. While it is common to use one input beam and a retroreflection stage in axis, we instead use six independent input beams, each fibre coupled from a 1×6 fibre splitter. These input beam axes are shown in [Figure 3.23](#), where each fibre input is labelled with an axis number (1,2,3) and an end (A,B). This provides us with the flexibility to unplug the chamber for access, as well as providing a very robust light delivery system.

Once at the chamber, the fibres are connected to a *Thorlabs* cage mount assembly that holds a 7.5 mm beam diameter fibre collimator (F810APC-780), a pair of lenses forming a $2\times$ beam expanding telescope ($f = -25\text{mm}$ and $f = 50\text{mm}$), and a [quarter-wave plate \(QWP\)](#). The four radial cooling arms ($F1A$, $F1B$, $F2A$, and $F2B$) are set to have σ_+ circular polarisation with respect to their direction of propagation, while the axial cooling arms ($F3A$ and $F3B$) have σ_- polarisation.

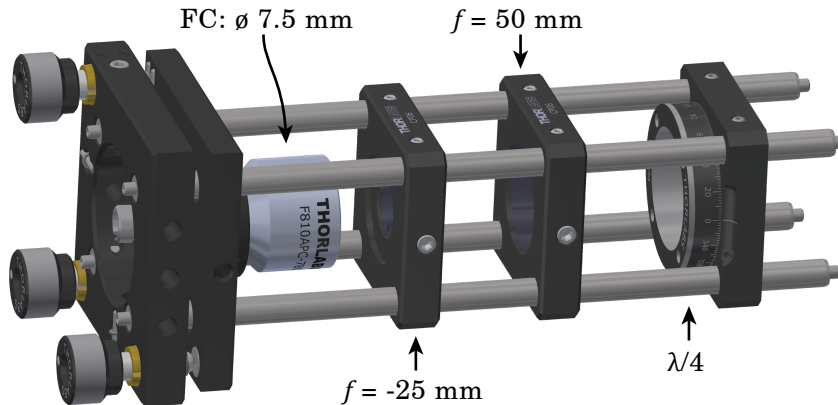


Figure 3.24: Model of one of the **MOT** cooling arm assemblies. Each of these are attached to the vacuum chamber by the four *Thorlabs* rails.

The polarisations are set with the assistance of an *Edmund Optics* polarisation directed flat lens. This specialty optic uses a liquid crystal thin film to act as a polarisation-sensitive Fresnel lens. When incident on the front face of the optic σ_+ light is focused and σ_- light is diverged. This is a helpful tool for diagnostics as there are few other ways of identifying the handedness of a circularly polarised light beam.

The geometry of the chamber and cage mount assemblies provides a coarse alignment of the cooling arms. Fine adjustment can be made using the two-axis tilt control of the kinematic mount holding the fibre collimators. This is typically used to ensure that each cooling beam is aligned well with its pair on the other side of the chamber. It is difficult however to confirm that this has optimised the six-beam overlap volume, or that the overlap is in the correct spot relative to the hollow-core fibre and anti-Helmholtz field zero. As such any final alignment of the cooling arms is done using the **MOT** itself.

The repump field is either combined with the cooling light in free space before the 1×6 way fibre splitter, or is directed through the chamber using its own collimation stage. Both techniques work well and result in similar **MOT** temperature, density, and atom number. The primary advantage of using a separate collimator for the repump is the ability to investigate spatial dark spot techniques. While not presented here, very preliminary results from these tests have shown a factor of 2 improvement in the number atoms coupled into the hollow-core fibre, where the dark-spot mask was simply a 2 mm hex key glued into an optics cage mount. The vertical dark stripe through the repump was aligned to the **MOT** by simply walking the beam until the steady state fluorescence dropped.

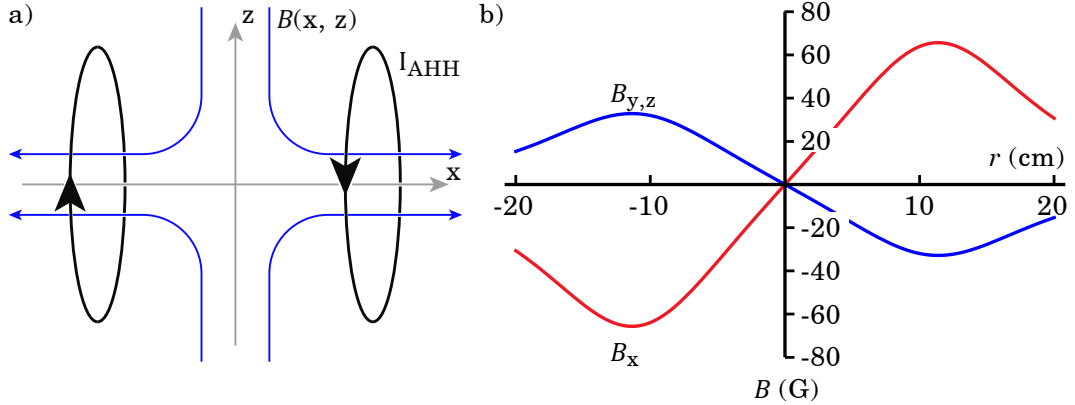


Figure 3.25: a) Anti-Helmholtz coils generate a quadrupole field in which the magnetic field lines diverge from the centre of the coil pair. b) The magnetic fields generated along the x (red) and y, z (blue) axes by the coils used in the experiment for a current of 60 A.

3.6.2 Anti-Helmholtz Coils

A quadrupole magnetic field is used to produce the spatially varying Zeeman shifts necessary to trap laser cooled atoms. This type of field possesses a zero at its centre with uniform field gradient in every direction, and is easily generated by a pair of coils fed current in opposite directions, as shown in [Figure 3.25 a](#)). It is clear that the axial field is opposite in sign to the field in any radial direction, as required to satisfy Maxwell's equations.

The magnetic field inside this geometry can be calculated by modelling the system as a pair of N turn coils of radius r separated by a distance d carrying a current I . The resulting field along the central x -axis is given by

$$B_x(x) = \frac{\mu_0}{4\pi} 2\pi r^2 IN \left(\left((x - d/2)^2 + r^2 \right)^{-3/2} - \left((x + d/2)^2 + r^2 \right)^{-3/2} \right) \quad (3.5)$$

where μ_0 is the permeability of free space. The field along any direction perpendicular to x (here we choose the lab axes y and z) is of opposite sign, and when the distance between the coils is equal to the diameter of the coils themselves, the system gains symmetry in $x - z$ plane. In this case the magnetic field in the z and y directions is $-\frac{1}{2}$ of that along x , as required to satisfy Maxwell's equations.

The choice of parameters and design used in the experiment is as follows. The coils consist of \varnothing 3.5 mm enamelled copper wire, wound around an aluminium former that is designed to bolt directly onto the 4.5" vacuum viewports, as shown in [Figure 3.26](#). Each coil is roughly 22 cm in diameter and has 21 turns total (3 layers of 7 turns each). The

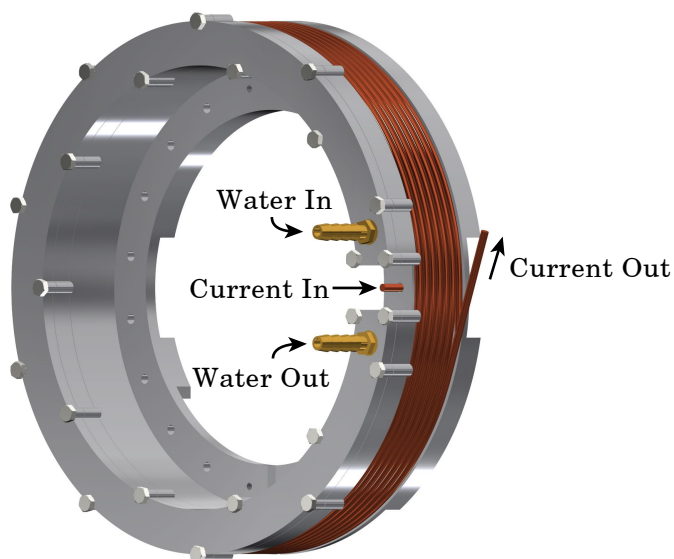


Figure 3.26: Model of one of the MOT coils.

two coils are connected in series with a total electrical resistance of $\sim 0.09 \Omega$. At a typical drive current of 60 A they produce 320 W of heat, and as such each coil is fitted with a C-shaped water cooling plate which is continuously flushed with water at a flow rate of 2l/min. This is enough to allow for continuous operation without noticeable thermal drift in alignment through the vacuum chamber.

This coil design allows us to achieve an axial magnetic field gradient of 0.12 GA/cm. The current supply used to drive the coils is a *Delta Elektronika* SM 15 - 100, and is able to supply 100 A at 15 V, although the experiment is typically operated at 60 A. This current produces a magnetic field gradient on axis of 7 G/cm, which can be switched off with a $1/e$ time constant of 1.5 ms using a digital logic trigger from the Arduino.

3.6.3 Compensation Coils

The presence of stray DC magnetic fields in the lab produces a shift in the zero of quadrupole field. This in turn results in a displacement of the MOT away from the geometric centre of the chamber. As the atomic cloud is only 2 mm across and the diameter of optical guide beam at the centre of the chamber is only 700 μm , it does not take much to misalign the MOT with the guide beam entirely. This can be compensated for by intentionally introducing a correction field, moving the magnetic zero back into the overlap with the guide laser.

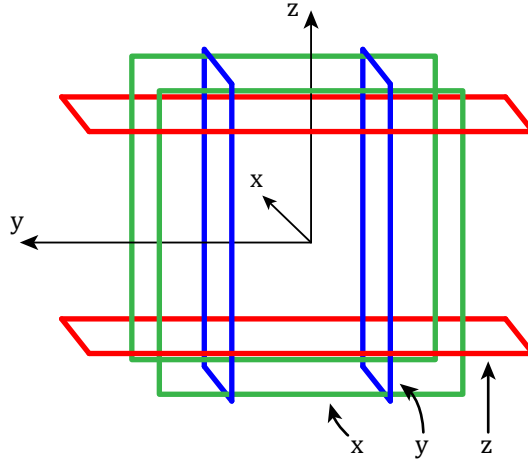


Figure 3.27: Diagram of the compensation coil setup, with each pair of coils shown in a different colour.

| Axis | Side length (cm) | Separation (cm) | Turns | Field Strength (G/A) | Resistance (Ω) |
|------|------------------|-----------------|-------|----------------------|-------------------------|
| x | 66 | 33 | 21 | 0.51 | 3 |
| y | 70 | 39 | 21 | 0.48 | 3 |
| z | 98 | 55 | 42 | 0.69 | 8 |

Table 3.3: List of properties of the compensation coils.

This correction field is produced by three independent pairs of square magnetic coils arranged around the vacuum chamber in each axis. This coil shape is chosen to be easier to mount and provide better access to the chamber. The coils are labelled x -, y -, and z -compensation coils given by the lab reference frame axis they lie in, and their orientation is shown in [Figure 3.27](#).

The spacing between each coil is chosen to be $0.56\times$ the side length, producing a maximally flat field strength across the central region. For the side lengths used, there is ideally less than 0.1% deviation in applied field strength across the central 20 cm of the chamber – which is essentially the entire vacuum volume. All parameters of the compensation coils are listed in [Table 3.3](#).

The coils are driven by a three-channel DC power supply (*Aim TTi* MX100T), where each pair of coils is connected in series with one channel. The device has a [GPIB](#)

connection, allowing it to interface with the Arduino. During testing and configuration of the MOT location the compensation fields are stepped over, and the sign of the fields are inverted by manually swapping the banana plug orientation if need be. The compensation field required is typically very stable over time, however manipulation of the pointing of the cooling beams can shift the MOT enough to require readjustment of the compensation fields. A typical set of compensation fields (driving currents) used are -1.7 G, (-3.4 A), -0.5 G (-0.1 A), and -1.7 G (-2.5 A) in the x , y , and z directions respectively.

3.6.4 Timing

There are roughly five phases to the typical experimental run, including loading of the MOT, a brief second cooling stage, the drop of atoms into the fibre, interrogation of the atomic sample, and a relaxation period. These stages are fairly self explanatory, however a short description of the timing of the cooling processes is given here, and shown diagrammatically in [Figure 3.28](#).

In the default state of the system the cooling, repump, and guide lasers are shuttered, and the compensation and anti-Helmholtz coils are all off. When an experimental run is begun, the first stage is the MOT loading stage. In this stage the cooling and repump lasers are switched on to their full power of 180 mW and 5 mW respectively and the cooling detuning is set to -18 MHz. The compensation coils are set to their initial states and the anti-Helmholtz coils are set to their initial gradient of 6.5 G/cm, triggering the start of MOT formation.

This stage lasts for 1.5 s, after which the PGC stage is performed. This phase is much shorter at only 15 ms, and consists of a ramp in cooling parameters described above. The start and end values used are chosen via the optimisation scheme described in [subsection 3.6.5](#). After the PGC is complete the cooling, repump, and anti-Helmholtz coils are all switched off and the guide beam is switched on, beginning the drop phase.

During the drop phase it is possible to change the current through each pair of compensation coils. This has been tested as a technique to minimise the ground-state dephasing of the ensemble due to DC magnetic fields, however it is not implemented in any of the work presented here.

After the prescribed fall time the interrogation sequence begins. At the start of the interrogation sequence a short repump pulse is sent through the fibre to pump all atoms

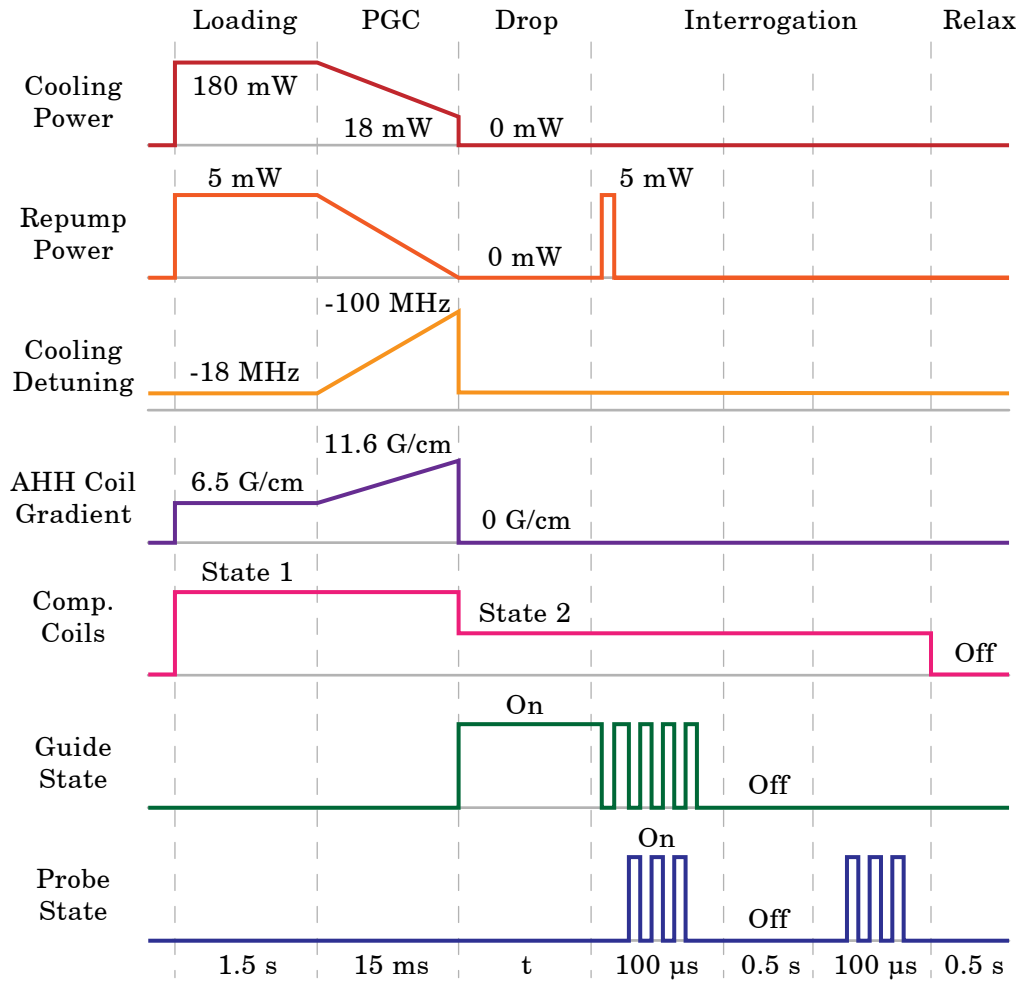


Figure 3.28: Timing diagram of the loading of the MOT, PGC, atom drop, interrogation and relaxation stages. Timing and parameters shown at typical values.

into the appropriate hyperfine ground state. The guide and in-fibre probe beams are then synchronously modulated in counter phase to allow for measurement in the absence of AC-Stark shifts caused by the guide. After the signal data set with an atomic ensemble the guide is switched off for 500 ms allowing the atoms to adhere to the fibre walls or otherwise leave the interrogation region. A second probe sequence is then performed to generate the reference data set.

Finally the entire system is allowed to relax in the off state for 500 ms, allowing for thermal effects to dissipate. The entire sequence can be run again after this delay. It is worth noting that all these times and values can be modified on the spot should it be

necessary.

3.6.5 MOT Optimisation

Performing a human optimisation over the many degrees of freedom available in MOT loading and PGC stages of the experiment is very time consuming. In addition, it is not necessarily obvious what the optimisation goal is. One could choose to maximise the number of atoms in the MOT or the minimise atomic cloud temperature, however in reality these characteristics are not independent. Similarly, choosing the three compensation coil values to zero the background field in the chamber may not be the correct approach, as a mismatch between the geometric centre of anti-Helmholtz coils and the fibre axis is more than likely. As such, the only useful target is to use the desired goal, which is the optical depth achieved in the kagome-lattice fibre. The technique used to maximise the number of atoms in the fibre is a combination of human and machine optimisation.

Once a MOT has been realised at all, careful tuning is done of the tilt in both axes of each cooling beam. With a monitor on the voltage of the fluorescence detector, each axis of each beam is walked a fixed distance in both directions, and the maximum fluorescence is used to choose the final state. This is repeated over all cooling beams two or three full times to correct for poor overlap in the cooling volume.

Next a coarse search is done to find the compensation coil values that align the MOT to the fibre axis. To do this a standard Arduino program is run that makes an in-fibre absorption measurement at 75 ms after release, at which time any atoms caught in the dipole trap will be inside the fibre. This program is run in a sweep over the x - and y -axis compensation coil values. Once any absorption is detected, the coil values with peak optical depth are recorded and used as starting conditions for the machine-learning optimisation package, MLOOP [127].

MLOOP is an open-source algorithm written in python for use in scientific experiments. A configuration file is edited to include the number of parameters to be searched over, the minimum and maximum bound of each, and a starting location. The python script is integrated with the lab control system such that MLOOP generates a text file with the next position in configuration space to try, which is read in by the control system and executed. An experimental run is done to measure the optical depth in the fibre, the results of which are returned to MLOOP, which then processes the accumulated data and generates a new set of parameters to investigate. This process continues until the end

condition is met, which is typically set to search until 100 runs have passed without a new best optical depth.

While the mechanics of the machine learning algorithm are somewhat beyond me, it does work roughly as expected, and typically after an hour the process is complete and the software produces a best guess at the local maximum value and associated parameters. This process is run over several groups of four or fibre related experimental parameters. One such group is the compensation coil values in each direction and anti-Helmholtz coil beginning and end currents. Another is the PGC parameters, including the beginning and end powers of the cooling and repump lasers, the beginning end end cooling laser detuning, and the duration.

Whether or not the end result is a local or global maximum in every parameter is uncertain as we have not attempted to validate the performance of the optimisation algorithm. Nonetheless, this technique does appear to at the very least maximise the *OD* in each parameter independently, and the time saved by automating this process is priceless.

3.6.6 MOT Performance

The performance of a MOT is measured by the number of atoms trapped, the loading rate, the number density (or size) of the cloud and the ensemble temperature. To conclude this section, these parameters are discussed below.

In typical conditions we are able to trap 10^8 atoms at steady state, with a loading rate of 10^8 atoms/s. These values are strongly dependent on the current through the rubidium dispenser, as discussed in subsection 3.4.1. It is well known however that the atomic density in a MOT is limited by photon re-scattering and two-body collisional processes [34, 54]. As such, substantially increasing the atom number results in a larger ensemble with similar density. As the Gaussian $1/e$ diameter of the cloud is 2 mm it is already larger than the guide beam at that height, and there is little to be won by turning up the rubidium dispenser current and over-filling the MOT.

Without additional cooling the MOT temperature is measured to be $150\ \mu\text{K}$ in the horizontal direction perpendicular to the shadow imaging axis. The temperature in the vertical direction is typically measured to be slightly higher, at around $250\ \mu\text{K}$. These values well match the Doppler temperature of $146\ \mu\text{K}$ for the D_2 line [114]. After the

second stage cooling which consists of a short burst of PGC and a temporal dark-spot, the temperature of the atomic cloud is significantly lower. The lowest temperatures we have measured are 3 μK and 5 μK in the horizontal and vertical directions respectively, although as of writing this thesis the currently achievable temperatures are much higher at 25 μK and 40 μK suggesting that the MOT parameters are not currently well optimised.

Although the MOT performance is adequate for the experiments currently being run, colder temperatures and higher densities always directly translate into improved optical depths in the fibre. Improving on μK temperatures is however technically challenging and would require significant additional infrastructure to implement tertiary cooling schemes such as a resolved-sideband Raman cooling [60]. In the future this may well be a path worth exploring.

3.7 Computer Oversight

The experiment is a complex system of scientific instruments, home made electronics, and electro-optics, many of which must be switched or triggered with sub-millisecond precision. In addition, there are many devices with parameters and settings that it is desirable to vary between runs, either for optimisation or for parameter-space data collection. There are commercial solutions available that can perform these tasks such as the *National Instruments* experiment control suites, however these tend to be very expensive.

We use an Arduino Due to perform the direct control of the scientific instruments and digital switching required. The lab PC runs a high-level user interface that communicates with Arduino as well as other pieces of equipment that are connected to the university network including the *M Squared* SolsTiS and the *HighFinesse* wavemeter. The PC also performs direct acquisition of data recorded on the oscilloscope, and is capable of performing real-time analysis of the run-to-run data. A schematic of the communication network between these devices is shown in Figure 3.29, and further detail regarding these systems is given below.

3.7.1 PC User Interface

The PC user interface is Windows sidebar written in C# that communicates with the Arduino via direct serial connection, and other external devices over serial or Ethernet. This allows the user to read and change the currently stored experimental parameters such as laser detuning, coil currents, and the guide laser wavelength.

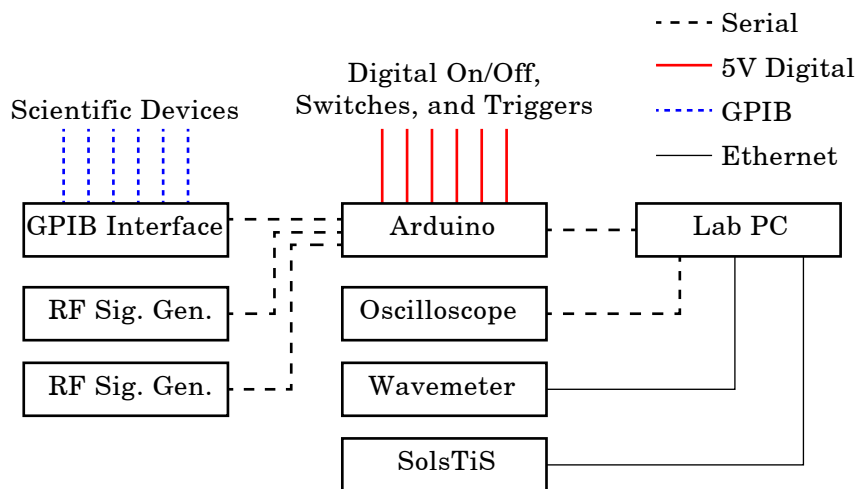


Figure 3.29: Schematic of the communication network between elements of the lab control system.

The control system is the primary platform for performing diagnostics on the Arduino and other connected hardware, as seen in [Figure 3.30 a](#)). Here the state of various cameras and external equipment is displayed, along with the wavelength of any given channel of the wavemeter, and a list of all communication between the PC and the Arduino.

There are several *Point Grey* cameras used to image the atomic cloud in various ways. The control system provides an interface which controls the shutter times, gains, frame rates and other setting of each camera without opening the proprietary software, as shown in [Figure 3.30 b](#)). This is very useful as it allows the system to switch between continuous triggering of the cameras during testing and external triggering during experimental runs in which shadow imaging is performed.

Although all the experimental parameters used are stored on the Arduino, the control system provides an interface with which to read off and edit these values. The full list of parameters available is show in [Figure 3.31 a](#)), along with a set of default values read from the freshly restarted Arduino.

The user interface provides a direct means to execute both low-level and high-level programs on the Arduino. Low-level programs are those that control specific elements on apparatus, such as opening the mechanical shutter for guide laser. This is done by

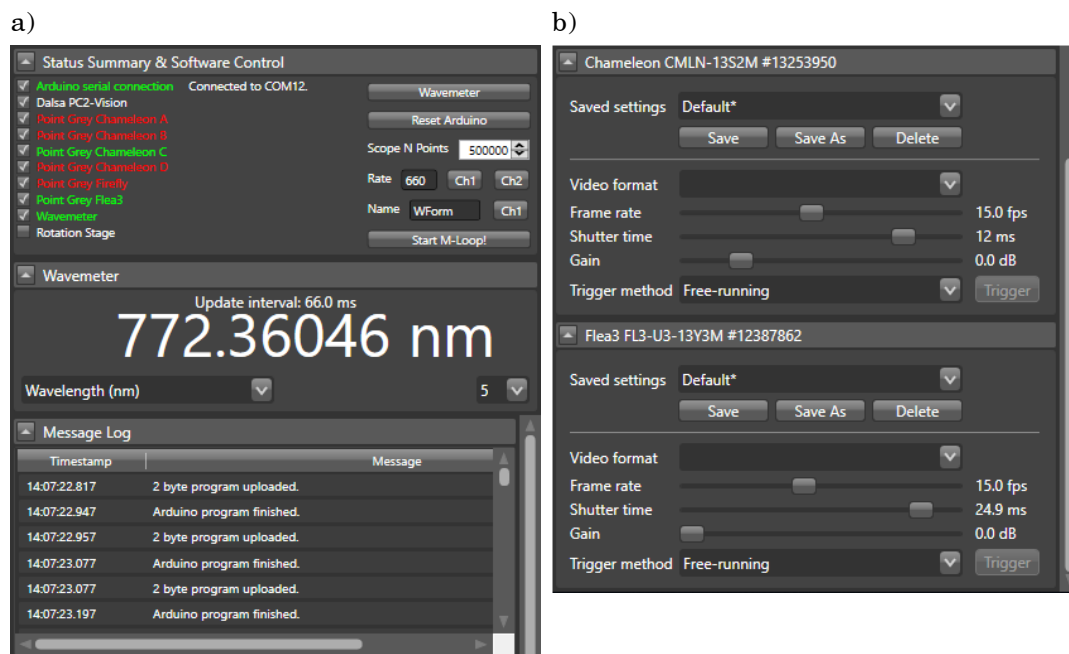


Figure 3.30: Snapshot of the first half of the control system GUI, showing a) the diagnostics overview and b) the camera configuration.

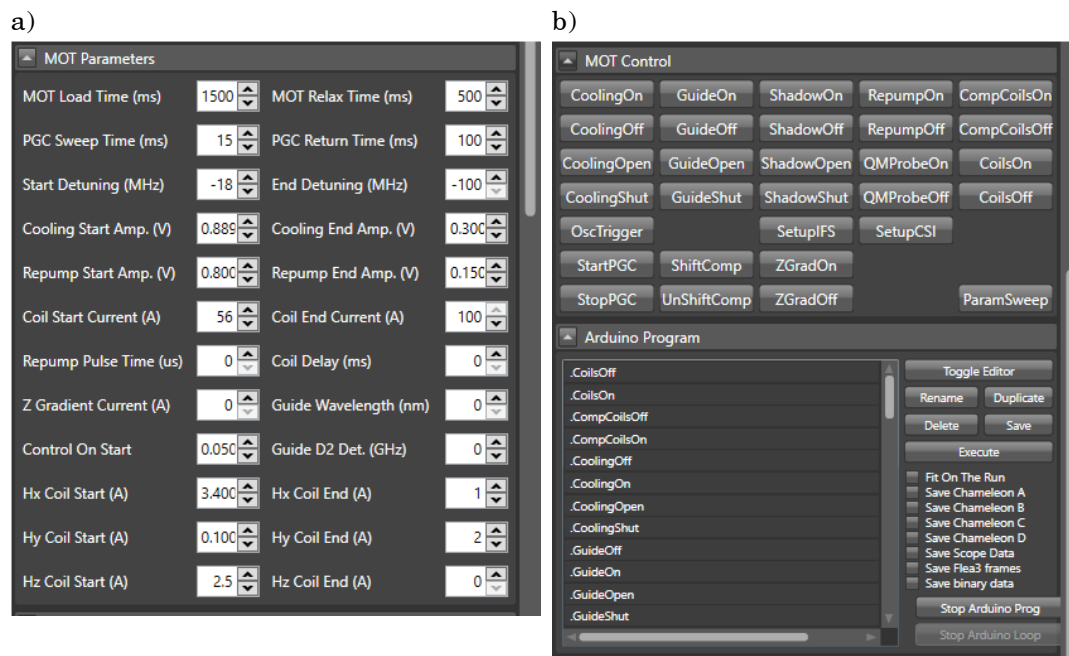


Figure 3.31: Snapshot of the second half of the control system GUI, showing a) the experimental parameter control and b) the Arduino command and program control.

clicking the ‘GuideOpen’ button in the ‘MOT Control’ window, seen in [Figure 3.31 b](#)). This sends the appropriate command byte to the Arduino which sends the allocated digital output high, triggering the mechanical shutter to open.

The relatively small memory available on the Arduino limits any series of commands to less than 3600 bytes. To overcome this barrier the Arduino has high-level programs available that typically only take one user input: the time at which to interrogate the atoms after their release from the trap. This way the large number of commands necessary to reset the experiment, prepare and cool the atomic ensemble, perform the interrogation sequence, and bring the system back to rest, are all abstracted away from the user and onto the Arduino. As an example the `TakeShadowImage(t)` command is available in the user interface. This command performs an entire experimental run and takes a set of shadow imaging data at a time t after release from the MOT, and can easily be iterated or looped over many times without running into the maximum command limit.

There are cases in which this is still inadequate for large scale data collection. In this situation there is a general purpose function available in the user interface that will perform another degree of iteration, sending the currently selected Arduino program and each time saving all the collected data to a separate folder on the local disc. An example of this use is to perform high averaging number measurements of the atom absorption spectrum at many time steps to generate a plot of optical depth against time after release, all of which is then repeated for several different choices of guide laser wavelength.

The PC user interface also serves to acquire data captured on the oscilloscope or CCD camera and write it to disc. In the case of oscilloscope data this can be done as either human-readable [comma-separated values \(CSV\)](#) files or raw binary data, while camera images are saved as bitmaps. All raw data is saved to a solid state drive on the computer, after which it is processed in *Igor Pro* and the treated data is saved to shared lab *Dropbox* account. All data used in publications, reports, or for other formal purposes are additionally stored in raw format.

3.7.2 Arduino Due

The Arduino is the beating heart of the experiment. It holds all the experimental parameters necessary to run the MOT and is connected to every piece of scientific equipment in the lab that needs to be configured, triggered, or otherwise operated during the experiment. The primary reason for using an Arduino Due for this task is that it offers

a fast, dedicated processor, which is of great importance when timing reproducibility is key. The low cost of replacement (\$50 AUD) and ease of use are additional benefits.

The Arduino has a range of inputs and outputs that are used to control the experiment. These include 54 digital input/output pins, 12 analog inputs, 2 analog outputs, and 4 hardware serial ports. As the device runs at 3.3 V and many older pieces of equipment require 5 V signals for triggering we use an array of bidirectional 3.3 V to 5 V logic level converters to prepare the digital input/outputs for use.

The digital outputs pins are either used for triggering or on/off state control. Devices that require triggering include the arbitrary waveform generators used in the probe pulse train generation and fast guide modulation systems, the data collection oscilloscope, and the [PGC](#) cooling detuning ramp. Devices with on/off state control include each of the RF switches and mechanical shutters used to perform optical switching and the output control of anti-Helmholtz coil current supply.

Many other devices are controlled using the hardware serial ports. The first serial port connects to an *ICS* serial to [GPIB](#) interface device, which in turn is connected to every device that is capable of [GPIB](#) control. This includes the waveform generators, the anti-Helmholtz coil current supply, and the three channel current supply for the compensation coils. This interface allows configuration of each device as well as dynamic control between experimental runs.

Two of the remaining hardware serial ports are connected to *Novatech Instruments* four-channel signal generators that supply all RF signals that do not need frequency modulation or fast control. These outputs are typically used to drive constant frequency [AOMs](#) used as shutters or fixed frequency shifters. Once configured these devices can be unplugged from serial communication but this is unnecessary for us at this time.

Finally, one of the two analog outputs is connected to the buffered analog control port of the anti-Helmholtz coil current supply. This control port allows us to set and manipulate the coil current on a much faster timescale than can be achieved through [GPIB](#) communication. This is primarily used to perform the ramp in magnetic field gradient during [PGC](#).

In typical operation the Arduino sits waiting to receive commands from the attached

PC. Upon receiving a command byte stream it will perform each command in order until receiving the ‘finished’ byte, at which point it responds to the PC with a confirmation byte. If the oscilloscope is sent a trigger to collect data the Arduino will return a byte to the PC informing it that there is an oscilloscope trace to be acquired. Upon restart the Arduino connects to each device and resets the state of the device to the default configuration capable of operating the experiment.

One of the nice aspects of this system is that neither the computer nor the Arduino are uniquely important, as each simply runs software that can be backed up conveniently. Should the Arduino fail or be damaged during testing, it can be replaced the same day with an off-the-shelf device at very low cost. In addition, any of the scientific equipment connected to the Arduino can always be returned to a functional state by resetting the Arduino, and further any malfunctioning equipment can be swapped out with a like (or sometimes even similar) device and returned to a working state. At the same time, the operation of the entire system can be easily edited or reconfigured with very low programming knowledge, and by always retaining a working copy of the code the system is always recoverable.

3.8 Summary

In this chapter I have presented an overview of various components of the experimental system. This includes the kagome-lattice hollow-core fibre, the vacuum chamber and surrounds, laser sources, MOT, and computer oversight system. I have also provided detailed descriptions of the protocols used to configure, prepare or operate many of elements presented.

In the next chapter I discuss the interrogation protocols and data processing techniques used to extract information from the cold-atom system.

INTERROGATION TECHNIQUES

Sophisticated interrogation protocols and data analysis techniques are vital to cold-atom experiments. In this project there are broadly three techniques used to interrogate the system, each of which is able to extract different information about the state of the atomic ensemble.

The first, fluorescence counting, is a passive method that uses the rate of photons scattered from the cooling beams by the atomic ensemble to infer the number of atoms present. This is primarily a diagnostic tool, and requires that laser cooling be active.

The second, shadow imaging, is an active technique that relies on the atoms' absorption of a beam of probe light to cast a shadow or silhouette onto a camera. This method requires a path of optical access through the vacuum chamber, and is a destructive measurement. However, the spatial resolution of the technique allows for measurement of the motion of the atomic ensemble when repeated over multiple time steps. This is vital information when attempting to understand the atom-loading process, and can be used to infer the thermodynamic temperature of the ensemble.

The third technique is absorption spectroscopy, in which a probe field is passed through the atoms and collected on a photodetector. By quickly stepping the frequency of probe across an atomic transition, it is possible to map out the atomic absorption feature in time.

Unlike fluorescence capture and shadow imaging this technique can be used to interrogate atoms inside the hollow-core fibre. With careful analysis the resulting data can provide a plethora of information regarding the physical properties of the ensemble including the number of atoms, the ground-state lifetime, and the thermodynamic temperature of the ensemble.

These techniques are briefly described below in the specific context of the experiment.

4.1 Fluorescence Counting

Measuring the cooling light scattered by atoms in the MOT is a common diagnostic tool used in cold-atom experiments. This technique is particularly useful as it is very simple to experimentally implement, and can be used to provide real-time information on the performance of the laser cooling system. The following is a brief overview of the technique, how is it experimentally implemented, and typical data collected for the experiment.

4.1.1 Theory – Isotropic Scattering of Light

Atoms in the MOT reside at the centre of the overlapping cooling beams. In this context we can treat the trapped atoms as being two level particles in the presence of a single monochromatic light field. The effect of the quadrupole magnetic field used to capture cold atoms in the MOT can be ignored here as the atoms are confined to the zero of the field. The light-atom interaction for this system can be described by the optical Bloch equations [66], which for the total steady-state scattering rate of photons from a single light field is given by

$$R_{\text{sc}} = \left(\frac{\Gamma}{2}\right) \frac{I_0/I_{\text{sat}}}{1 + 4(\Delta/\Gamma)^2 + I_0/I_{\text{sat}}} \quad (4.1)$$

(see [114]), where Δ is the angular-frequency detuning of the cooling lasers, Γ is the natural decay rate of the excited state, $I_0 = \frac{2P_0}{\pi w^2}$ is the on-axis intensity for a single cooling beam with power P_0 and waist w , and I_{sat} is the saturation intensity for the transition.

In the high-intensity limit ($I_0 \gg I_{\text{sat}}$) the scattering rate reduces to $\Gamma/2$, however this is typically not true due to the large detunings used in Doppler cooling. When the MOT is active, the atoms are illuminated by three pairs of counter-propagating optical fields with specific choices of σ_- and σ_+ polarisation. For the purposes of this measurement, it is assumed that the combination of directions and polarisation results in an optical field with isotropic polarisation and average intensity $I = 6I_0$. In addition, the effects of sub-Doppler cooling mechanisms and radiation trapping phenomena are ignored.

A collection optic is used to collect a fraction of the scattered light. For a circular lens with diameter d situated a distance L from the MOT, the solid angle of scattering captured is given by

$$d\Omega = 2\pi \left(1 - \cos \left(\arctan \left(\frac{d}{2L} \right) \right) \right), \quad (4.2)$$

and the fraction of scattering captured is $d\Omega/4\pi$. Using this lens to image the atom cloud onto a photodetector produces a constant voltage given by

$$V_{\text{PD}} = N_{\text{atoms}} G_{\text{PD}} E_{\gamma} \frac{d\Omega}{4\pi} R_{\text{sc}} \quad (4.3)$$

where N_{atoms} is the total number of atoms in the MOT, G_{PD} is the gain of the detector in V/W, and E_{γ} is the photon energy of the cooling transition in Joules. As such, using knowledge of the lens and detector assembly as well as the cooling laser power and detuning, one can calculate the number of atoms in a non-destructive fashion.

4.1.2 Implementation

We implement an out-of-vacuum imaging system for fluorescence capture to minimise the complexity of the apparatus. A *Thorlabs* flange-grabber is clamped to the viewport located at the end of the ion pump four-way cross (this flange is on the far left of [Figure 3.8](#), although this model does not include the fluorescence assembly), which is not used for any other optical access. The collection solid angle available from this viewport is small, however as this system is primarily used as a rough diagnostic tool, this is not overly detrimental.

The imaging system is mounted on the flange-grabber using an assortment of cage-mount components, shown in [Figure 4.1](#). This diagram shows the solid angle limiting aperture for the system, which is the inside edge of the 4-way cross where it meets the viewport. This aperture has $\varnothing 34$ mm at a distance 360 mm from the MOT, giving a full-angle of 5.4° , or a fractional solid angle of 0.056 %.

The imaging optic is a $\varnothing 2$ " plano-convex lens with $f = 75$ mm, which is located ~ 390 mm from the centre of the chamber. The image produced by this lens is at a distance of 93 mm from the lens, which is collected on a large-area photodetector, which is not shown in diagram. A narrow band-pass filter centred on the cooling transition (*Thorlabs* FBH780-10) is mounted to completely cover the detector and prevent any offsets due to room lights. The transmission through the filter is 94 % at 780 nm.

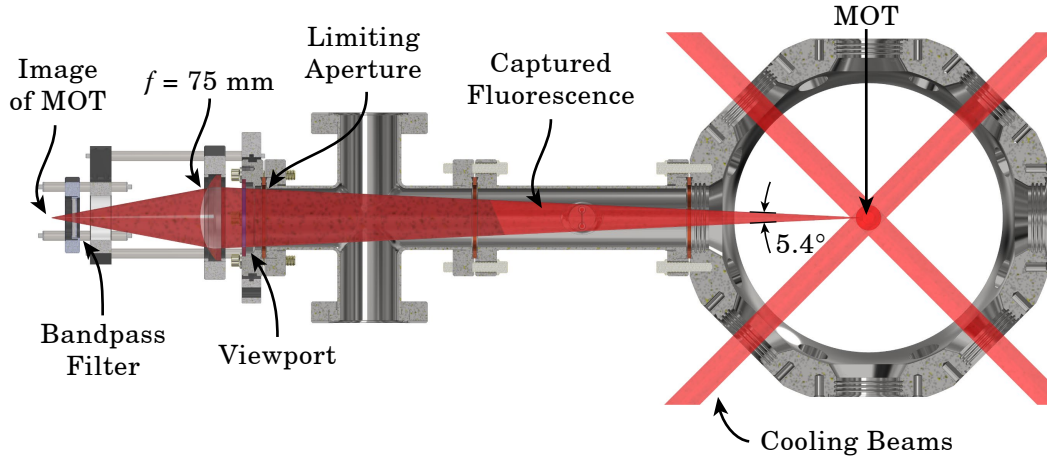


Figure 4.1: Model of the setup used to capture fluorescence from the MOT.

The photodetector used is a *New Focus* model 2032. This device has a responsivity of 0.4 A/W at 780 nm , and is operated either at ‘medium’ gain, which is 10^5 V/A , or ‘high’ gain for $2 \times 10^6 \text{ V/A}$. This typically produces voltages of tens (or hundreds on high) of millivolts. There is typically a small offset voltage generated by the photodetector in addition to the constant voltage produced by stray scattering of the cooling light off chamber. These effects are compensated for by measuring the photodetector output with the cooling lasers on, but the anti-Helmholtz coils turned off to prevent the MOT from forming. This value is then subtracted from the on-state measurements.

On medium gain, the combined response of the optical and detector is $G_{\text{PD}} = 3.8 \times 10^4 \text{ V/W}$. For typical values of the single-arm cooling power of 23 mW and cooling detuning of $2\pi \times -18 \text{ MHz}$, the scattering rate is $R_{\text{sc}} = 9.9 \times 10^6/\text{s}$. Using these values, the photon energy of $E_\gamma = 2.5 \times 10^{-19} \text{ J}$, and the fractional collection efficiency of 0.056% , the total conversion factor is $1.9 \times 10^{10} \text{ atoms/V}$.

4.2 MOT Loading Time

An extension of using fluorescence to measure the number of atoms in the trap is to measure the loading of the MOT as a function of time. The loading dynamics of the atom cloud can be simply modelled using a rate equation, where the loading rate of new atoms R is constant, and a combined loss rate $1/\tau$ is used [97]. The rate equation for this system can be written as

$$\frac{dN(t)}{dt} = R - \frac{N(t)}{\tau}. \quad (4.4)$$

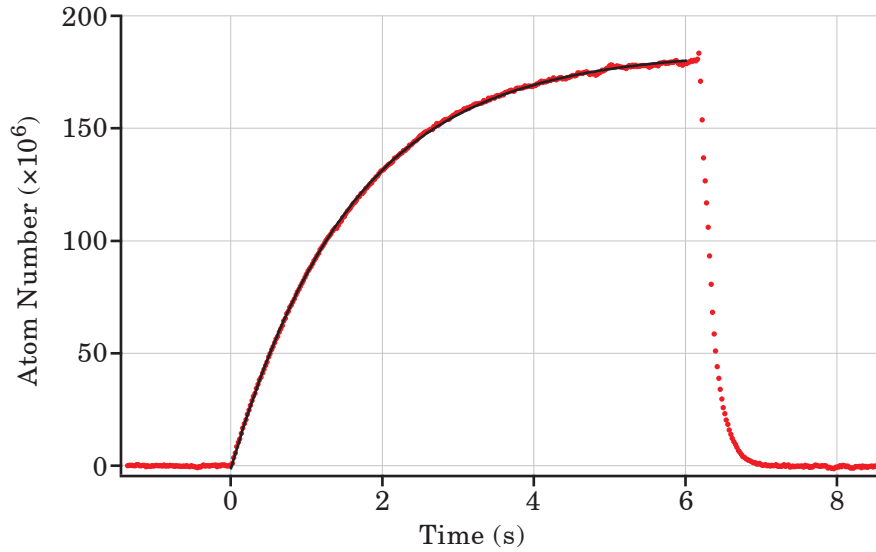


Figure 4.2: Measurement of the atom loading rate of the MOT at a dispenser current of 4.5 A with experimental data (red circles) and fit (black curve).

Solving this differential equation with the initial condition of $N(0) = 0$ gives the time dependent atom number as

$$N(t) = R\tau(1 - \exp(-t/\tau)) \quad (4.5)$$

which has a characteristic saturation effect for large t , in which the number of atoms in the MOT reaches $R\tau$.

Making this measurement is typically done by leaving the cooling and repump lasers in an active state, then switching on the atomic source. This is difficult to achieve when using a dispenser, as it has to heat up and reach temperature before providing a constant flux of atoms. Instead we use the fast (millisecond) switching time of the anti-Helmholtz coils to activate the trapping process, while recording a photodetector voltage on an oscilloscope. The resulting curve shown in Figure 4.2 has a high initial constant loading rate, which exponentially decays over time as the rate of newly captured atoms balances the loss of atoms due to collisions, as expected. This measurement was made with a dispenser current of 4.5 A. Fitting to the data with Equation 4.5 provides values of $R = 1.143(3) \times 10^8$ atoms/s, and $\tau = 1.616(3)$ s, with a total atom number of $1.842(5) \times 10^8$.

4.3 Shadow Imaging

Shadow imaging is a technique used to acquire information on the spatial distribution of atoms. While capturing fluorescence is a useful way of inferring the number of atom in the MOT, using the scattered photons to produce an image is less effective. Partially this is due to sensitivity issues: the captured solid angle is likely to be small, and imaging in this way is sensitive to scattered light from vacuum windows or clipping of optical elements, reducing the contrast. A more significant issue is that capturing fluorescence requires there to be fluorescence in the first place, which is typically done using the cooling lasers. This makes it difficult to capture an image of the cloud once it has left the central cooling region.

In contrast, shadow imaging uses a weak beam of light resonant with the cycling transition to illuminate the atomic ensemble while the cooling beams are switched off. Atoms within the extend of the shadow beam will strongly scatter photons over the full 4π sr of solid angle, casting a shadow onto the light. After leaving the chamber, the shadow beam is collected onto a CCD camera. By taking an image with the atoms present, and a second image a short time later with no atoms, a transmission map is calculated, compensating for the initial intensity profile of the beam and efficiency of the camera. Using an understanding of the interrogated transition, pixel size, and imaging system, the transmission measurement can be processed into a map of the atom number per pixel, or a column density.

This technique has strong advantages in that the contrast is good, the field of view can be much larger than the extent of the cooling beams, and the necessary optical power is very low (tens to hundreds of microwatts). A key downside is that this measurement is destructive, as significant impulse is given to the atoms in the direction of the beam, and requires unimpeded optical access in a line across the chamber. Despite this, the spatially resolved information that this method provides is of incredible value for both diagnostics and data collection.

Below is a description of the setup used in the experiment, the data processing and calibration used to interpret the images, and the method used to calculate the temperature of the atomic ensemble using these images.

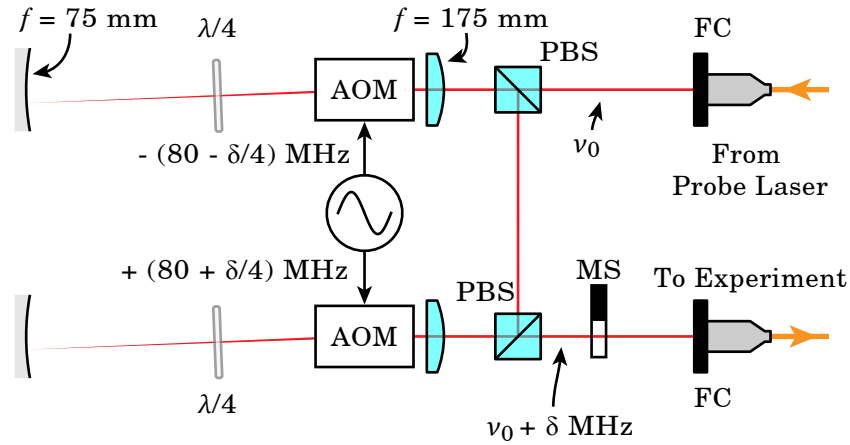


Figure 4.3: Diagram of the twice-double-passed AOM setup used to frequency shift and switch the shadow imaging light. This setup also used to perform wide-band DC spectroscopy by quickly changing the detuning δ in a pre-programmed way.

4.3.1 Implementation

The shadow imaging light is a small tap off of the probe laser described in subsection 3.5.1, which is locked to the $|F = 3\rangle \rightarrow |F' = 4\rangle$ cycling transition on the D_2 line. It is important to interrogate the cycling transition for this technique as it allows each atom to scatter many imaging photons without being lost to a dark state, maintaining a high contrast in the images.

The tapped off on-resonance light is frequency shifted using a pair of double-passed AA *Opto Electronic* 80 MHz AOMs operated in opposite refraction order, as shown in Figure 4.3. The technique results in a total frequency shift from the original source of δ , which is tuned by anti-symmetrically offsetting the two RF drive signals. These signals are both generated by a *Keysight* model 33612A dual-channel waveform generator.

The curved optics in each AOM path servo to efficiently retro-reflect the deflected optical beam over a wide range of frequency shifts, where the quarter-wave plate serves to distinguish the twice frequency-shifted light from the input beam by means of a full 90° of polarisation rotation. To optimise the efficiency of this setup, it is necessary to get the distances between the curved mirror, AOM, and convex lens as close to correct as possible. Ideally the focal point of the lens should lie on the surface of the curved mirror, while the active area in the AOM should lie at the radius of curvature of the mirror. This is done experimentally by introducing a slow frequency modulation onto the RF drive signal, and observing the resulting beam steering at the output with a camera. Small

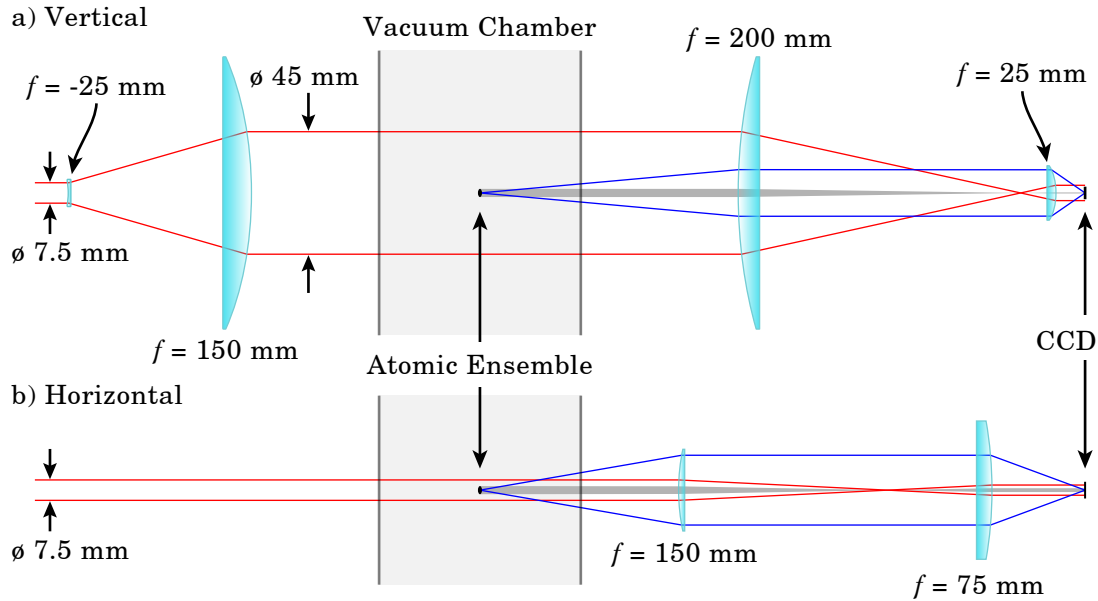


Figure 4.4: Diagram of the optics used to perform shadow imaging, where a) is the vertical axis and b) is the horizontal. All lenses are cylindrical, and shown only in the axis they act on. The diagrams are to scale, with a 2:1 aspect ratio (compressed width-ways across the page). The red lines represent the $1/e^2$ diameter of the shadow beam and the dark grey region represents the shadow of the MOT as it is imaged onto the camera. The blue lines are the maximum bounds of the MOT fluorescence that is captured when the cooling beams are on.

adjustments are made to each optic iteratively to best null the observed beam steering.

The resulting double-passed setup has a 3 dB tuning bandwidth of roughly ± 80 MHz, including the effect of beam steering on the fibre coupling after the system. In addition, the time response of the AOMs is 100 ns, allowing for relatively fast switching of the optical signal.

The imaging apparatus uses a series of cylindrical lenses to achieve different fields-of-view for the horizontal and vertical axes. This is important due to the combination of narrow transverse confinement of the dipole trap near the fibre tip ($33 \mu\text{m}$) and large vertical separation of the MOT and fibre end (25 mm). To achieve the maximum spatial resolution possible, the useful field of view must be imaged onto the full active area of the camera sensor, again achieved with a combination of cylindrical lenses.

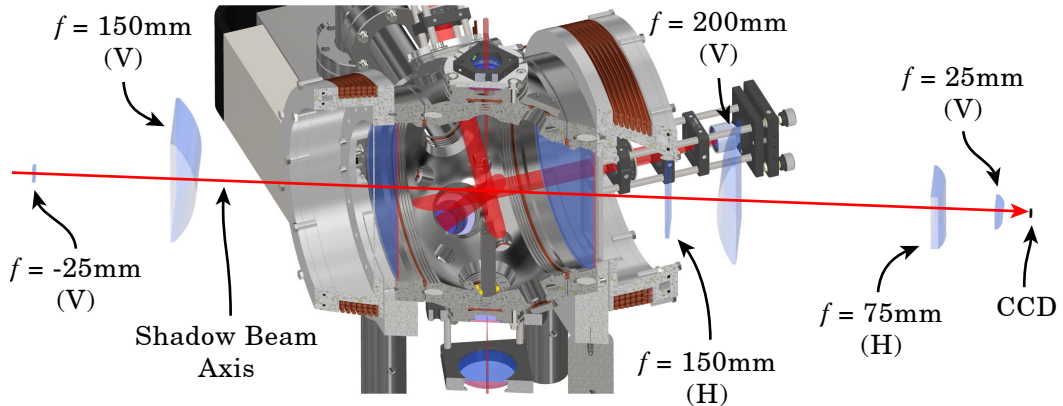


Figure 4.5: Model of the setup described, as it exists within the experiment. Lenses are labelled with (H) or (V) depending on the axis in which they act on the beam.

In addition to this, the imaging system is designed so that not only is the shadow beam collimated onto the sensing area, but fluorescence emitted from the atoms is also imaged onto the sensor. This is a useful diagnostic tool as it provides a bright image of the atomic cloud during the cooling stage, but implementing both techniques at once imposes strict limitations on the positions of the imaging optics. Specifically, the first lens in each axis must be located at a distance from the MOT equal to its focal length.

The setup use is shown diagrammatically in Figure 4.4, where each axis is shown independently. A Thorlabs F810APC-780 fibre collimator produces a free-space beam with $1/e^2$ diameter of 7.5 mm, which is then expanded in the vertical axis by a factor of $6\times$. The beam is passed through the chamber, then compressed down onto a Point Grey Flea3 camera. The magnification of the imaging setup is $0.125\times$ in vertical direction and $0.5\times$ in the horizontal. This magnification, combined with the $4.8\mu\text{m}$ pixel pitch of the camera, provides a spatial resolution in the object plane of $9.6\mu\text{m} \times 38.4\mu\text{m}$ in the horizontal and vertical directions respectively. The camera resolution of 1280×960 gives a total field of view of roughly $12\text{mm} \times 37\text{mm}$. A model of how this system fits around the vacuum chamber is shown in Figure 4.5.

4.3.2 Image Processing

Two images are taken each run to produce a useful image of the atomic ensemble: the signal image and the reference image. For each imaging run the MOT is made and dropped, and at the desired image time, the camera is triggered and a pulse of light on or near resonance is sent through the imaging system, producing the signal image.

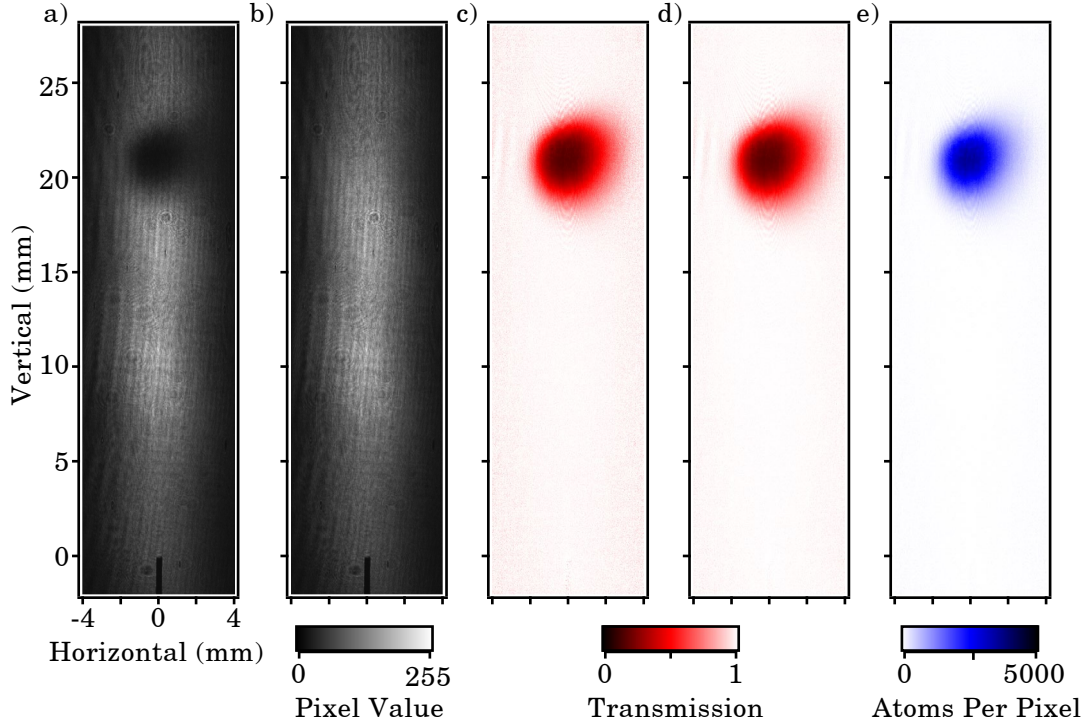


Figure 4.6: Stages of image processing include: a) the signal image, taken at the desired time after release, b) the reference image, taken 500 ms later once the atoms have dispersed, c) the single frame transmission image calculated from a) and b), d) the average of multiple transmission frames, and e) the per-pixel atom number map calculated using knowledge of the experimental and theoretical parameters. Axes are shown to scale.

Before the camera is triggered a short burst of repump is applied to the system, strongly pumping atoms into the $|F = 3\rangle$ ground state. The experiment is given half a second to relax, after which the reference is taken.

These images, shown as a) and b) in [Figure 4.6](#), contain the shadow of the atoms cast by the interrogating light, and the atom-free intensity profile of the beam. Performing a point-by-point division of signal by reference produces the transmission image, shown in c). Typically the experimental sequence is repeated a number of times to allow for averaging, improving the signal to noise. In this example, three images are taken, producing the small improvement seen in d). Finally, the transmission image is converted into an atomic number map using the following formula:

$$\mathcal{N}_{\text{atoms}}(x, y) = -\ln|T(x, y)| \frac{dx dy}{\sigma} \times \left(1 + 4 \left(\frac{\Delta}{\Gamma} \right)^2 + \frac{I(x, y)}{I_{\text{sat}}} \right) \quad (4.6)$$

where $|T(x, y)|$ is the absolute value of the transmission, $dx dy$ is the pixel size in the

object plane, σ is the atomic scattering cross section, Δ is the angular frequency detuning of the interrogating beam, Γ is the transition decay rate, $I(x, y)$ is the local intensity of the interrogation beam, and I_{sat} is the transmission saturation intensity. While the local beam intensity can be found by scaling the reference image, for low optical power and no frequency offset this can be ignored and the result simplifies to

$$\mathcal{N}_{\text{atoms}}(x, y) = -\ln|T(x, y)| \frac{dx dy}{\sigma}. \quad (4.7)$$

For a freely expanding cloud, the total number of atoms is calculated by fitting to the atom number map with a two-dimensional Gaussian of the form

$$f(x, y) = c + A \exp\left(\frac{-1}{2(1-e^2)} \left[\left(\frac{x-x_0}{\sigma_x}\right)^2 + \left(\frac{y-y_0}{\sigma_y}\right)^2 - \left(\frac{2e(x-x_0)(y-y_0)}{\sigma_x\sigma_y}\right) \right]\right) \quad (4.8)$$

where c is an offset, A is the peak value, x_0 and y_0 are the horizontal and vertical offsets, σ_x and σ_y are the Gaussian width parameters, and e is an ellipticity parameter. The total can then be calculated directly by

$$\mathcal{N}_{\text{atoms, total}} = 2\pi \frac{A}{dx dy} \sqrt{1-e^2} \sigma_x \sigma_y \quad (4.9)$$

where the division by $dx dy$ converts from atom number to atom number column-density. This is preferred over simple numerical summation as it well accounts for the background and other systematic imaging artefacts.

4.4 Temperature Calculation

The temperature of an atomic ensemble can be calculated by measuring its ballistic expansion under free-fall. This is easily done by taking a series of shadow images at a range of times after release from all cooling and trapping fields. The size and location of the atom cloud can be extracted at each time step by fitting with the method described in [subsection 4.3.2](#). Using a model for the free expansion of a Gaussian shaped atomic distribution it is possible to extract the width of the velocity distribution, and hence the temperature, in each of the projected axes.

The atomic distribution in a direction x is initially taken to be a Gaussian given by

$$f_{X_0}(x_0) = \frac{1}{\sqrt{2\pi\sigma_x^2}} \exp\left(\frac{-x_0^2}{2\sigma_x^2}\right) \quad (4.10)$$

where σ_x is the standard deviation. Taking the atomic cloud to be an ideal gas, the distribution of velocities in \hat{x} at any given location is given by the 1-D Maxwell-Boltzmann

velocity distribution

$$f_{V_x}(v_x) = \sqrt{\frac{m}{2\pi k_B T}} \exp\left(\frac{-mv_x^2}{2k_B T}\right) \quad (4.11)$$

where m is the atomic mass, k_B is the Boltzmann constant, and T is the temperature.

At a time t after release, in the centre-of-mass reference frame the atoms will have propagated in straight lines determined by their initial position and velocity. To find the number of atoms at a specific location and time $x(t)$, the initial position distribution is multiplied by the probability of an atom being at the requisite velocity $v = \frac{x(t)-x_0}{t}$, and the product is integrated over all possible initial locations:

$$f_{X(t)}(x(t)) = \int_{-\infty}^{\infty} f_{X_0}(x_0) f_{V_x}\left(\frac{x(t)-x_0}{t}\right) \left| \frac{dv}{dx_0} \right| dx_0 \quad (4.12)$$

$$= \frac{1}{\sqrt{2\pi\left(\frac{k_B T}{m}t^2 + \sigma_x^2\right)}} \exp\left(\frac{-x(t)^2}{2\left(\frac{k_B T}{m}t^2 + \sigma_x^2\right)}\right). \quad (4.13)$$

This integration is a convolution of two Gaussian functions, the result of which is another Gaussian with standard deviation given by $\sigma_x(t)^2 = \frac{k_B T}{m}t^2 + \sigma_x^2$.

Using this, the temperature of ensemble is extracted by taking images at a series of times after release from the trap. A Gaussian distribution is fit to each dimension and the width parameter is squared, and plotted against the square of the time after release. The resulting data is nominally a straight line with gradient $k_B T/m$ and y-intercept σ^2 . An example of this result is shown in [Figure 4.7](#), where measurements are made over 55 ms in 5 ms steps. The temperature in the vertical (y) axis is found to be 142(5) μK , and the initial cloud size $\sigma_y(t_0 = 0)$ is 1.7(2) mm.

4.5 Absorption spectroscopy

An alternative to spatial imaging is absorption spectroscopy, in which the profile of the atomic transition is mapped out in the frequency domain. In this case a single beam is passed through the sample of interest and collected on a photodetector, retaining no spatial information. In its simplest form the interrogating light is located near or on resonance with the atomic transition and is pulsed at a given time to produce a single absorption measurement. By changing the detuning δ and repeating this measurement it is possible to produce a full atomic absorption spectrum, however the process is slow and inefficient.

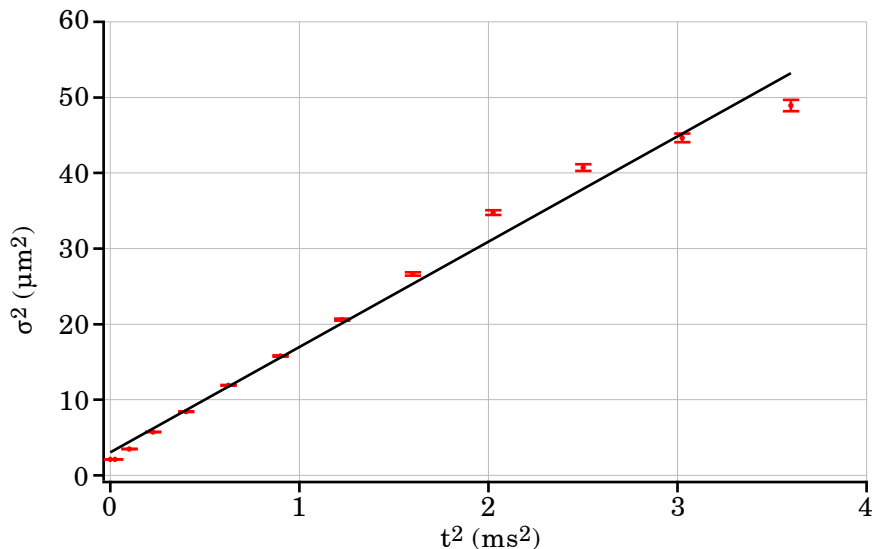


Figure 4.7: Plot of the square of the Gaussian width parameter in the vertical axis (σ_y^2) against time squared (red circles) with error bars from the uncertainties of 2-D Gaussian fit function applied to the images. A straight line is fit to the data (black curve), where the gradient provides a measurement of the thermodynamic temperature.

A much more useful method is to encode a large range of detunings into a single pulse sequence, as shown in Figure 4.8. In this case, a string of Gaussian shaped pulses are interleaved with momentary absences of dipole-trap light to avoid the effect of AC-Stark shifts. The pulse train is triggered at a time t , which is specified as a variable to the function that performs an experimental run. This allows for a snapshot in time to be taken, removing the influence of run-to-run variance in experiment and dramatically reducing the time taken to obtain a full spectrum. The difficulty in this technique is designing a detection and analysis protocol that is able to faithfully decode the individual frequency components and extract the desired spectrum. This is especially tricky for samples with extremely large absorption that may frustrate curve fitting techniques, or measurements with very low [signal-to-noise ratio \(SNR\)](#).

One way of achieving this is to use a dispersive optical element to spatially separate the different frequency components of the pulse train, and use a camera or linear photodetector array to acquire the decoded information. Unfortunately the frequency range of interest for the rubidium D_2 line is typically 1 MHz to 100 MHz, roughly an order of magnitude either side of the natural linewidth of 6.07 MHz. Spatially resolving this with a perfect diffraction grating would require a path length of tens of kilometres, and even

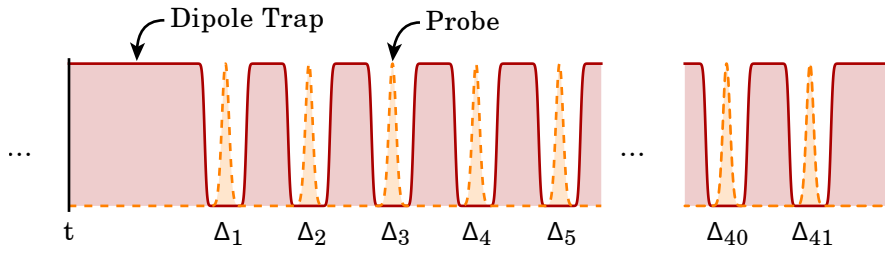


Figure 4.8: Diagram of a set of Gaussian pulses used to interrogate an atomic sample. Here the measurement is made at a time t , after which the shaped interrogation pulses (yellow dashed curve) are interleaved with momentary absences in dipole-trap light (brown solid curve). The optical frequency detuning Δ_i is changed between each pulse, in this case over 41 pulses.

more advanced étalon based devices are limited to picometre resolutions (500 MHz at 780 nm) [49].

The technique used here is to collect the interrogation light onto a high-speed photodetector and record the resulting electronic signals with an oscilloscope. By temporally resolving the individual pulses it is possible to extract the encoded information with careful data analysis algorithms. The following are the protocols developed during the project that achieve this goal.

4.5.1 Pulse Train Generation

Producing the nice pulse sequence shown diagrammatically in Figure 4.8 requires a significant level of calibration and waveform design. The first step is to produce a waveform that contains a series of signals with the appropriate frequencies and durations to produce the optical detunings desired, as shown in Figure 4.9 a). This stepped chirp signal can then be enveloped in amplitude to produce discrete pulses, each with a specific frequency, as in b). While this pulse sequence can now be uploaded to the arbitrary waveform generator and used in the experiment, it will produce a systematic non-uniformity in the optical power delivered over the pulses.

Even with the relatively wide-band tuning scheme shown in Figure 4.3, there will be still be a significant change in fibre-coupled power across the full tuning range of the system. This effect is primarily due to the frequency-dependent efficiency of the AOMs used to produce the shift in optical frequency. The solution to this problem is to account for the AOM drive efficiency when calculating the drive waveform by attenuating the more efficient drive frequencies as shown in c), at the cost of lower total optical power.

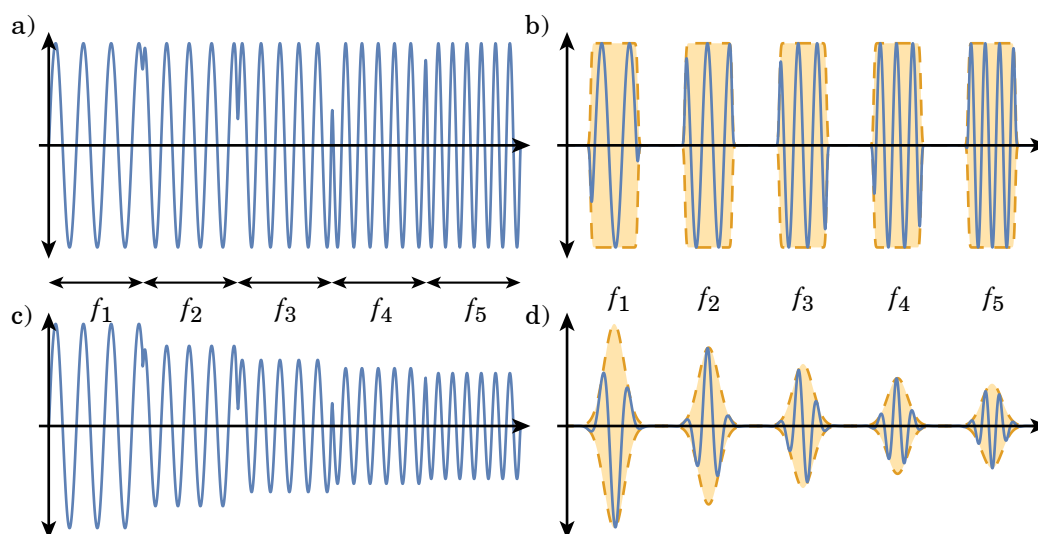


Figure 4.9: Diagram of the stages to generating useful pulse sequences. a) A fixed amplitude waveform is produced with discrete changes in frequency at periodic intervals. b) A rectangular envelope is applied to the stepped chirp, producing an uncalibrated pulse train. c) A measured calibration map is applied to the stepped chirp, accounting for the relative efficiency of each frequency component. d) A complex envelope function is applied to the chirp, producing a perfectly shaped pulse train.

In the context of this project this is not a problem as the in-fibre spectroscopy typically only uses nanowatts of optical power. An extension of this technique is to program more sophisticated envelope shapes for the optical pulses, typically Gaussian profiles as shown in **d**). The downside to this is that these pulse sequences cannot be altered on the fly, and changes to the **AOM** setup may require re-calibration of all the pulse sequences that have been written.

The calibration map necessary to achieve these results is experimentally measured by first generating a uniform RF drive voltage signal as in **b**), which is uploaded to the waveform generator. The control system then triggers the waveform, and acquires the trace from an oscilloscope recording the post-experiment photodetector. This produces a measurement of the response of the **AOM** system over the full range of frequencies desired at a specific drive voltage, shown in **Figure 4.10 a**). This measurement is repeated over the full voltage range of the device in small steps, producing a two-dimensional map of the response of the **AOM** system, shown in **b**).

Having made this calibration, it is now possible to produce a tailored optical pulse

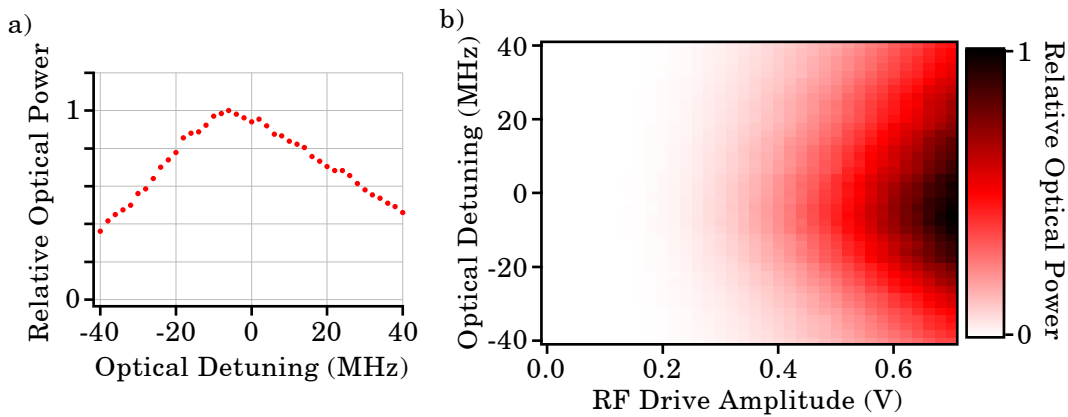


Figure 4.10: The [AOM](#) calibration data used to generate uniform-power optical pulses. a) The optical response for a single RF drive amplitude (0.7 V). b) The full two-dimensional map of the frequency and drive amplitude response of the system.

sequence. First a template of the pulse sequence envelope is calculated that possesses the desired pulse shape, number, width, and spacing. Next a one-dimensional array is made with the number of points available for use in the arbitrary waveform generator, which is then filled with the desired RF frequency at each point. A second array is generated that uses the device sampling rate and the instantaneous frequency array generated above to calculate the necessary phase at each time sample. Next, a sine function is applied to every phase element, producing the time-varying amplitude waveform. Finally, the 2-D calibration map is used as look-up table to calculate the RF voltage required at each time sample to reproduce the desired pulse-shape template, based on the instantaneous frequency.

The result of this process is an array of voltages that is uploaded to the waveform generator. The envelope of this array is shown in [Figure 4.11 a](#)), where the characteristic central droop identifies the peak [AOM](#) operating frequency. The voltage array is shown for a single pulse in [b](#)), where the RF drive is truncated for optical powers below 1% of the peak value. This process is tested by implementing the pulse sequence and processing the data using techniques described in [subsection 4.5.3](#). The resulting optical power is shown for a single pulse in [c](#)), where the [FWHM](#) extracted by a Gaussian fit is 0.999(3) μ s, in excellent agreement with the specified pulse width of 1 μ s. Fourier analysis of the measured pulse shows a frequency bandwidth of 470 kHz.

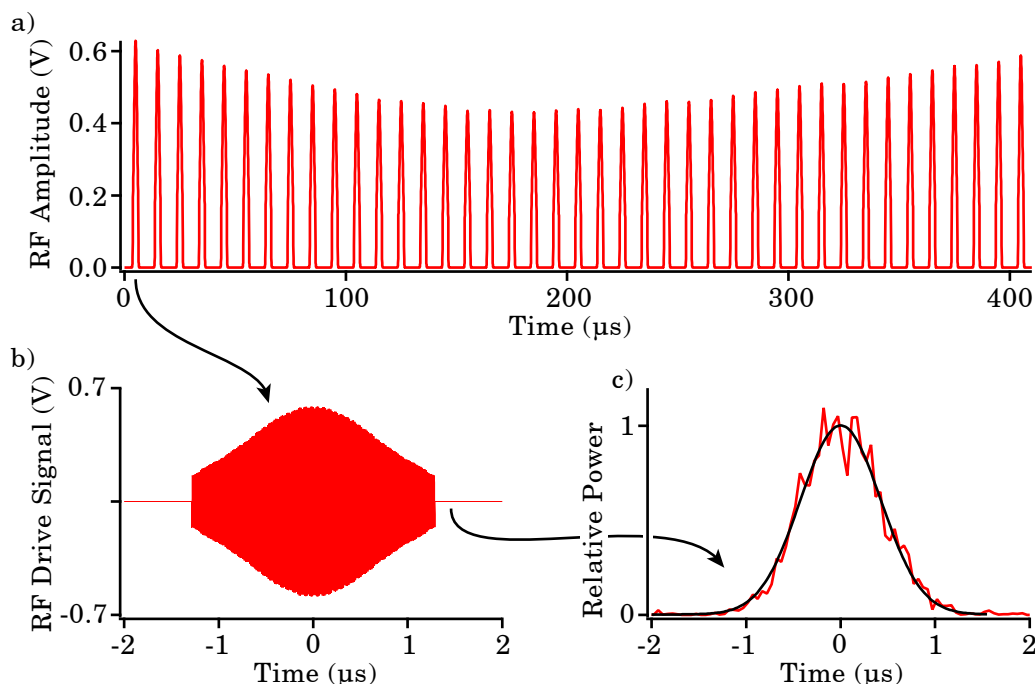


Figure 4.11: Production of a Gaussian pulse sequence. a) The amplitude envelope of the generated pulse sequence showing the pulse-to-pulse correction for **AOM** drive efficiency. b) A single pulse, showing the underlying sine wave and pulse envelope. c) A test measurement of the generated pulse sequence through the experiment, showing a good pulse shape with Gaussian fit (black curve).

4.5.2 Broadband DC Absorption Spectroscopy

The most conceptually simple broadband spectroscopy scheme is to use a series of a flat-topped pulses of different optical frequencies as an interrogating signal, and to extract the embedded information by directly measuring the optical power in each pulse using a photodetector. While this is still a pulsed interrogation scheme it is referred to here as ‘DC spectroscopy’ as the detection is sensitive to the DC component of the electronic signal. The recorded traces are converted to an atomic transmission by extracting the optical power in each pulse and comparing this a measurement with an atomic ensemble – the signal dataset – to one without cold atoms present taken a short time later – the reference dataset. Performing this calculation for each detuning value results in a full atomic transmission spectrum, from which various properties of the atomic system can be extracted via an appropriate fitting algorithm.

The benefits of this technique are that the DC nature of the detection system places

no limitations on the spectral range or resolution of the measurement. The bandwidth of the photodetector only limits the time resolution of the measurement. As such it is possible to use an extremely low-noise, high-sensitivity photodetector such as [avalanche photodiodes \(APDs\)](#), and a relatively low-speed oscilloscope.

The key limiting factors to this detection scheme is that the DC nature of the detection makes measurements extremely susceptible to offsets, drift, and other low-frequency electronic noise. There is also no ability to resolve between incident light of different origins on the detector, and leakage of the high-power guide beam is a serious issue. Some of these effects can be mitigated in post-processing, however this can result in relatively convoluted data analysis code that is difficult to maintain or susceptible to failure.

These aspects of the analysis are discussed in detail below.

4.5.2.1 Implementation

This spectroscopy technique is typically implemented on the $|F = 3\rangle \rightarrow |F' = 4\rangle$ transition of the D_2 line, interrogated with linear optical polarisation. This is a very strong transition with no direct decay path out of the $|F = 3\rangle$ ground state, removing the need to include population pumping mechanics in the analysis.

The light source and switching scheme used here is the same as setup that is used for shadow imaging described in [subsection 4.3.1](#), where a pair of double-passed [AOMs](#) are used to frequency shift a beam of light locked to the atomic transition. The [AOMs](#) are fed a pair of arbitrary waveforms, resulting in a stepped-detuning pulse sequence as described in [subsection 4.5.1](#). These waveforms are triggered at the interrogation time, producing an optical pulse sequence that is combined with the guide beam and passes through the atom-filled hollow-core fibre, as shown in [Figure 4.12](#). The guide beam is typically switched off in time with interrogation pulses to prevent perturbation of the atomic state during measurement.

The light exiting the vacuum chamber is collimated and is collected on an [APD](#) (*Thorlabs* APD410A). The sensitive detector is protected from the high power pulses of guide light using both polarisation ([PBS](#)) and spectral filtering (*Thorlabs* FBH780-10), giving roughly 80 dB of suppression. The output of the detector is recorded on an oscilloscope and the resulting traces for the signal and reference data sets are individually captured by the lab computer over a [USB](#) connection and saved for later analysis.

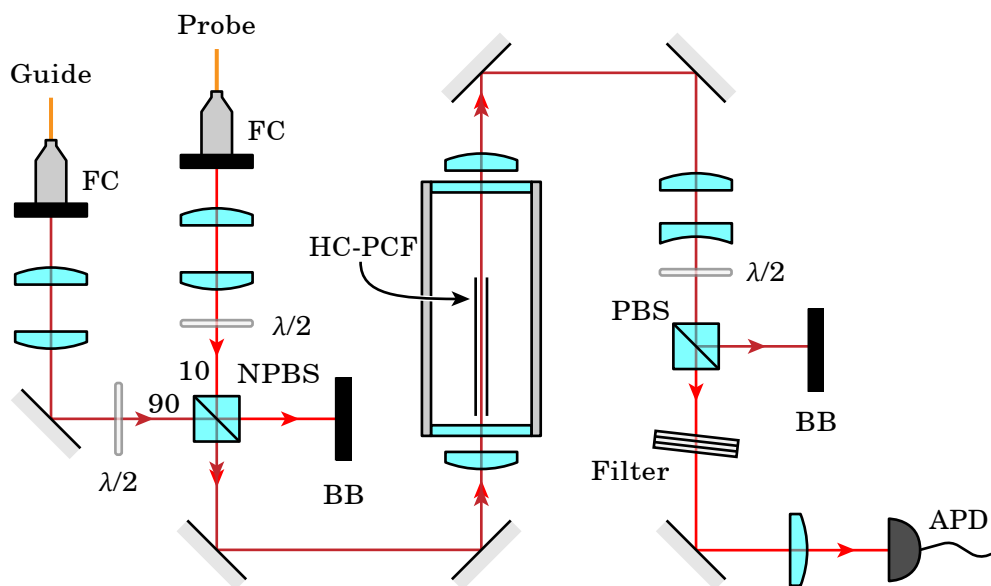


Figure 4.12: Diagram of the experimental setup used to interrogate an in-fibre atomic sample. Here the guide and probe light are combined in opposite linear polarisations on an NPBS, with 90 % of the guide and 10 % of the probe being send through the vacuum chamber. The weak probe is separated from the guide using both polarisation (PBS) and spectral filtering, and is collected on an APD.

In this system the linearity of the photodetector is relied upon to provide accurate transmission measurements, where the voltage out of the device is used to infer the optical power incident upon it. The voltage response of the photodetector is proportional to the time-dependent optical power when operated below the saturation level and within the bandwidth of the device. The gain (in V/W) is calculated using the manufacturer specification for the device and is confirmed experimentally using a CW light source. The optical power is measured with a calibrated power sensor (*Thorlabs S120C*), and the voltage out of the photodetector is recorded using the measurement device in its final operational state. The gain is then scaled by the measured transmission efficiency of the optical elements between the hollow-core fibre and the photodetector. This calibration is used to refer the measured power to the optical power present inside the hollow-core fibre, which is the experimentally relevant parameter.

4.5.2.2 Data Processing

The processing of a pair of signal and reference data sets is as follows. First both sets of data are imported into *Igor Pro*, where the recorded voltages are converted into optical powers referenced back to the levels in the hollow-core fibre, shown in [Figure 4.13 a](#)). A small DC offset is present, even with no optical power on the photodetector. This is

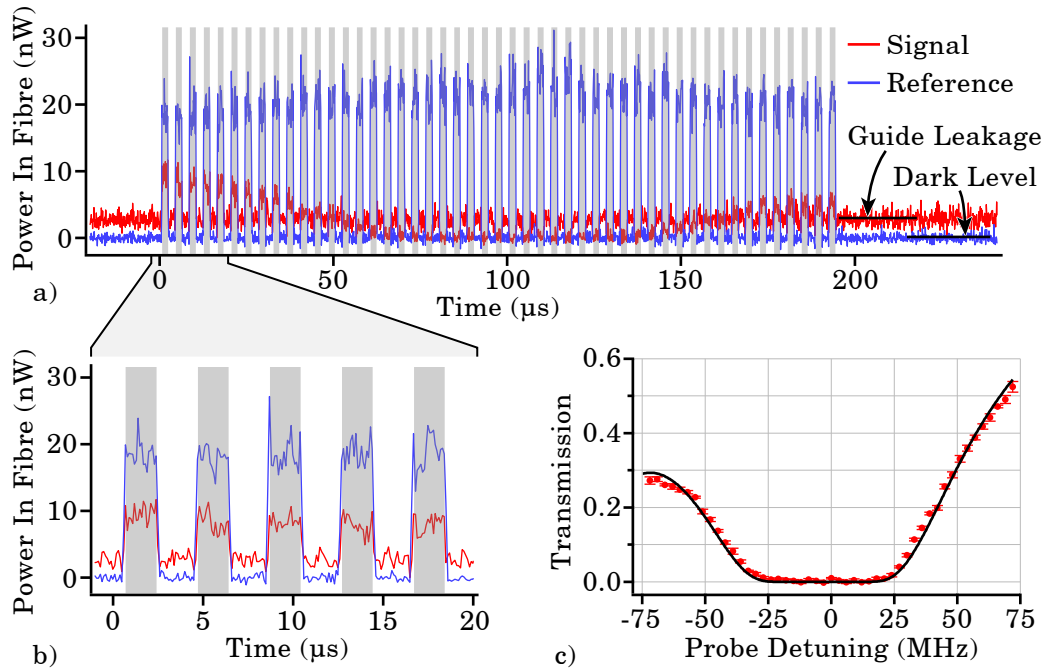


Figure 4.13: Processing broadband DC spectroscopy data. a) Two pulse sequences are sent through the experiment, the signal (red curve) and reference (blue curve) sequences. A mask of the active pulse times is generated and shown here as a sequence of transparent grey regions. b) A zoom around the first five pulses shows the mask matching to the on-states of the pulses. c) The calculated transmission spectrum (red circles) with measurement uncertainty and a spectral fit (black curve).

an inevitability when using DC-coupled devices, and is likely due to the dark current in the photodetector. The level of this offset is measured by taking the reference trace and averaging a time segment in which there are no pulses – typically several tens of microseconds before or after the pulse set. The resulting value is then subtracted from both data sets, correcting the zero level of the power calibration.

This dark level is not measured from the signal trace, as there is a small leakage of light from the guide laser onto the detector during the first pulse sequence, clearly visible in the figure. The level of guide leakage does not have to be subtracted from the signal for transmission measurements as the dipole trap is switched off during each probe pulse. This is seen where the strongly absorbed pulses in the central region of part a) drop below the guide-leakage level to lie on the dark level.

Next, a mask is generated that matches the pulse envelopes, allowing for the am-

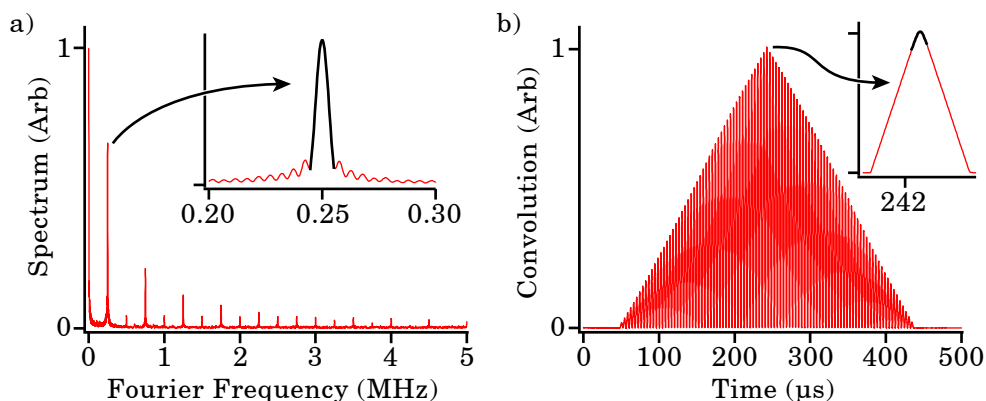


Figure 4.14: Calculating the period and offset of the pulse train. a) A Fourier transform of the reference trace is used to find the pulse period, with fit to the peak shown in the inset. b) A convolution with a test mask is used to find the pulse offset, with a fit to the peak shown in the inset.

plitude of each pulse to be calculated. This mask has four parameters: the number of pulses, the pulse width, the pulse period, and the initial time offset of the first pulse. These parameters can be user specified in the analysis software, or can be extracted from a reference trace with sufficiently high signal to noise. A trivial way to generate this mask would be to simply set all points in the reference trace to be either 0 or 1 based a chosen threshold value. In reality a complicated method is used that is able to cope with extremely low signal to noise, although for much of the time it is overkill.

In this method the number of pulses in the sequence and pulse width are still user specified, although the pulse width is slightly reduced to allow for the finite rise time of the AOMs. The periodicity is found by performing a [fast Fourier transform \(FFT\)](#) of the reference trace and extracting the fundamental frequency component present. This is demonstrated in [Figure 4.14 a](#)), where the period is found to be $4.00030(2) \mu\text{s}$. The time offset is found by generating a test mask with amplitudes of 0 and 1, using the other parameters found. This test mask is then linearly convolved with the reference trace, and the peak value of the resulting trace is used to calculate the best value of the offset over all the pulses. This is demonstrated in [Figure 4.14 b](#)), where the offset is found to be $1.5272(2) \mu\text{s}$ after comparison to a reference convolution.

Once these parameters are known, the signal and reference traces can be broken into segments containing only the on-time of each pulse. The data in each of these segments is averaged and the values are stored as single points in an aggregate data set, while the

standard error in the mean is stored in additional aggregate data set. The transmission for each detuning value is calculated by dividing the signal power by reference power, where the measurement uncertainty in the transmission is calculated from the standard errors in the means of both the signal and reference segments used.

For a single-run measurement the process is now complete and the resulting spectrum is shown in [Figure 4.13 c](#)) along with a fitted transmission profile, from which the optical depth of 350(3) is extracted. For multi-run data sets, all the signal and reference traces are processed and aggregated as for the single run case. The two-dimensional array of transmission values are then averaged along each detuning value to produce a single spectrum, where the uncertainties on each point are taken from the statistical uncertainty in the mean.

Even higher-dimensional data sets can be processed this way, where the aggregation tables are extended into the appropriately high dimension. A typical example of this is when data is collected for a range of times after release from the [MOT](#), with multiple runs of each data set taken for averaging purposes. In this case, the aggregate table has three dimensions (detuning, time, and run number), the spectral data has two dimensions (detuning and time), and the extracted [OD](#) is a one-dimensional trace where the x-axis is time.

For measurements such as this on the rubidium-85 D_2 line the fit function applied to the spectrum is a simple atomic absorption profile, complicated by the presence of multiple nearby hyperfine transitions. The full expected transmission profile is given by

$$T(\Delta) = \exp\left(-OD_{D_2} \times \sum_{F'} \frac{S_{3,F'}}{1 + 4\left(\frac{\Delta - \Delta_{3,F'} - \Delta_0}{\Gamma/2\pi}\right)^2}\right) \quad (4.14)$$

where Δ is the frequency detuning of the probe beam in the lab frame, OD_{D_2} is the combined optical depth on the D_2 line, $S_{3,F'}$ are the hyperfine strength coefficients, $\Delta_{3,F'}$ are the frequency separations of the excited-state hyperfine manifold, Δ_0 is an overall detuning offset between the lab and atomic reference frames, and Γ is the excited state decay rate. This profile is a product of the individual Lorentzian absorption profiles of each hyperfine transition, accounting for their strengths and frequency shifts. Typically it is possible to ignore all but a single transition, however for high-[OD](#) samples this is not the case, and there is significant overlap between adjacent transitions. In the processing of data all three hyperfine transitions are included ($|F = 3\rangle \rightarrow |F' = 2, 3, 4\rangle$),

and all transition properties are taken from [114]. The resulting fit has only two free parameters: the optical depth (OD_{D_2}) and the reference frame offset (Δ_0).

Once the fit has converged, these parameters and their uncertainties are stored in arrays of the appropriate dimension. At this point, the optical depth is scaled by $S_{3,4}$ to refer it to the cycling transition. This process is relatively fast, and takes less than a second per individual experimental run to import, process, fit, and analyse. This allows real-time analysis of data as the experiment itself takes just over a second between runs to allow for thermal effects to dissipate. The feedback from this process is exceptionally helpful during testing and optimisation procedures.

This technique works well and is very useful for diagnostic testing, however the susceptibility to small amounts of stray light and the involved data processing necessary are significant downsides. These limitations led to the development of a more sophisticated detection system known as heterodyne detection, which has allowed for a significant improvement in the quality of the absorption measurements.

4.5.3 Heterodyne Detection Absorption Spectroscopy

An alternative to DC technique described above, is heterodyne detection. The concept of optical heterodyne detection is to combine the desired signal field with a reference field of a different frequency. When this combination of fields is measured on a photodetector the power-to-voltage conversion produces an electronic tone at the difference between the two optical frequencies. The amplitude of this tone is proportional to the product of the amplitudes of the electromagnetic fields. In this scheme the reference optical field is typically referred to the [local oscillator \(LO\)](#) in reference to the RF technique of mixing.

There are three specific advantages to using this scheme for transmission measurements over simple detection of optical power, especially in the weak-signal regime. The first is that the useful information in the signal is frequency shifted far from DC by the relative optical frequency of the [LO](#). This significantly reduces the electronic noise contribution from flicker or $1/f$ noise, which typically dominates in semiconductors at low frequencies, as well as any other low-frequency noise such as DC drift or offset voltages inherent to the device.

The second advantage is the ability to amplify the signal before detection by raising the power in the [LO](#). While this does not reduce the effect of photon shot noise in the

signal field, it can be used to raise the signal level above the electronic noise of the detector. This allows low-level detection to be performed without the use of expensive and slow response detectors such as [APDs](#).

The third advantage to this technique is the specificity of the measurement. As the electronic field amplitude of the signal is encoded in the amplitude of a sine wave at a specific, well-known frequency, it is easily distinguished from stray light at other optical frequencies. This is particularly important for this experiment due to the large number of optical fields that propagate colinearly with the probe beam, including the guide and [EIT](#) control beams. These additional light sources are otherwise problematic to extinguish due to the sheer difference in optical powers (90 dB of guide power to probe power) or the close proximity in frequency (3 GHz between the [EIT](#) control and probe beams).

The setup and data processing used in the project to perform these measurements are described below.

4.5.3.1 Implementation

The implementation of this protocol is presented here in the case of an [EIT](#) experiment, in which the weak probe field is combined with a strong control field used to manipulate coupling between the atomic transitions. This experiment is done on the rubidium D_1 line at 795 nm, where the control field is tuned to the $|F = 3\rangle \rightarrow |F' = 3\rangle$ transition and the probe field is detuned around the $|F = 2\rangle \rightarrow |F' = 3\rangle$ transition by a frequency Δ_{probe} , as showed in [Figure 4.15 a](#)).

In this implementation, the light for the probe and [LO](#) fields is sourced from the re-pump laser which is locked to the $|F = 2\rangle \rightarrow |F' = 2 \times 3\rangle$ crossover transition, as described in [subsection 3.5.3](#). This light is split and frequency shifted to allow for tunability of the probe around the transition, while the [LO](#) is shifted a fixed frequency Δ_{LO} above the transition as shown in [Figure 4.15 b](#)). Given the excited-state hyperfine separation of 361.58(17) MHz [114], the frequency shifts used are $(180.8 + \Delta_{\text{probe}})$ MHz and $(180.8 + \Delta_{\text{LO}})$ MHz for the probe and [LO](#) respectively. While the probe detuning can be varied between each optical pulse in a long sequence of pulses as described in [subsection 4.5.1](#) the [LO](#) detuning is typically fixed at +80 MHz.

The experimental apparatus used to achieve these frequency shifts is shown in [Figure 4.16](#), where a double-passed [AOM](#) is used for each of the probe and [LO](#) beams.

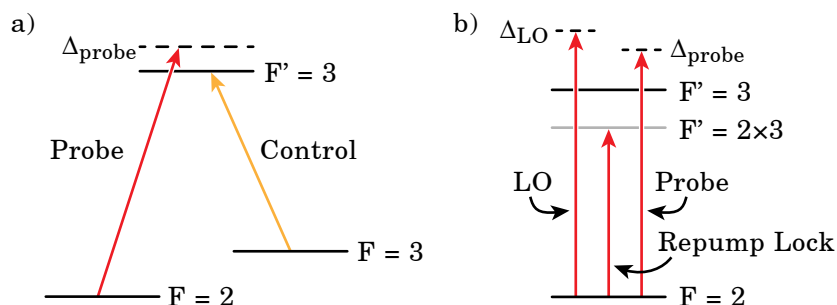


Figure 4.15: Diagram of the spectroscopy protocol used for EIT measurements. a) The energy levels of the D_1 transition used, where Δ_p is the probe detuning. b) The configuration of the probe and LO light fields, where Δ_{LO} is the detuning of the LO with respect to the $|F=2\rangle \rightarrow |F'=3\rangle$ transition.

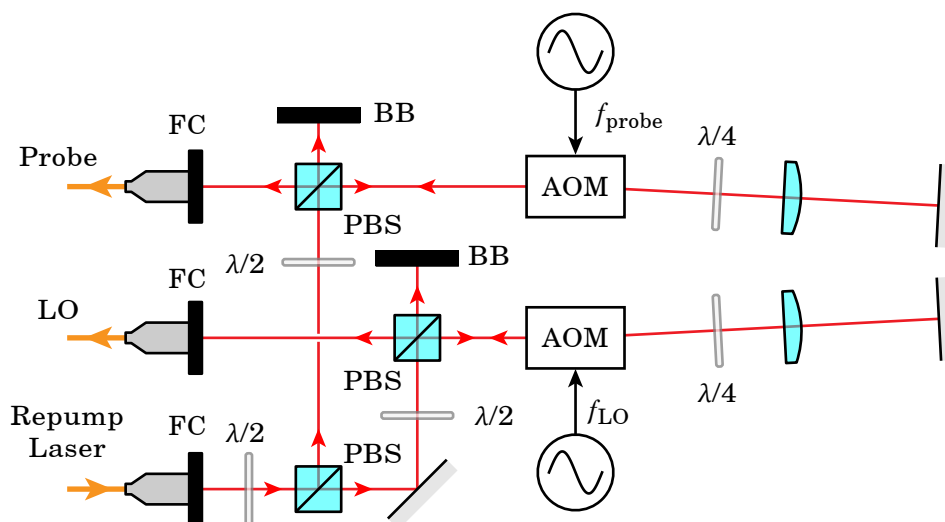


Figure 4.16: Diagram of the experimental setup used to produce the probe and LO fields for heterodyne spectroscopy. A fibre-coupled tap off of repump light is split into two arms, each of which contains a double-passed AOM to provide the frequency shifts and modulation necessary and a fibre collimator.

The RF drive frequencies used are half of the total shift required for each beam, and the use of three half-wave plate (HWP) and PBS combinations allows for independent control of the power in each output arm with minimal optical leakage between the two paths. The AOM for the LO is driven with a fixed frequency sine wave from a *Novatech 409B* signal generator, while the probe AOM is fed a pre-programmed arbitrary waveform from an *Keysight Technologies Trueform* waveform generator.

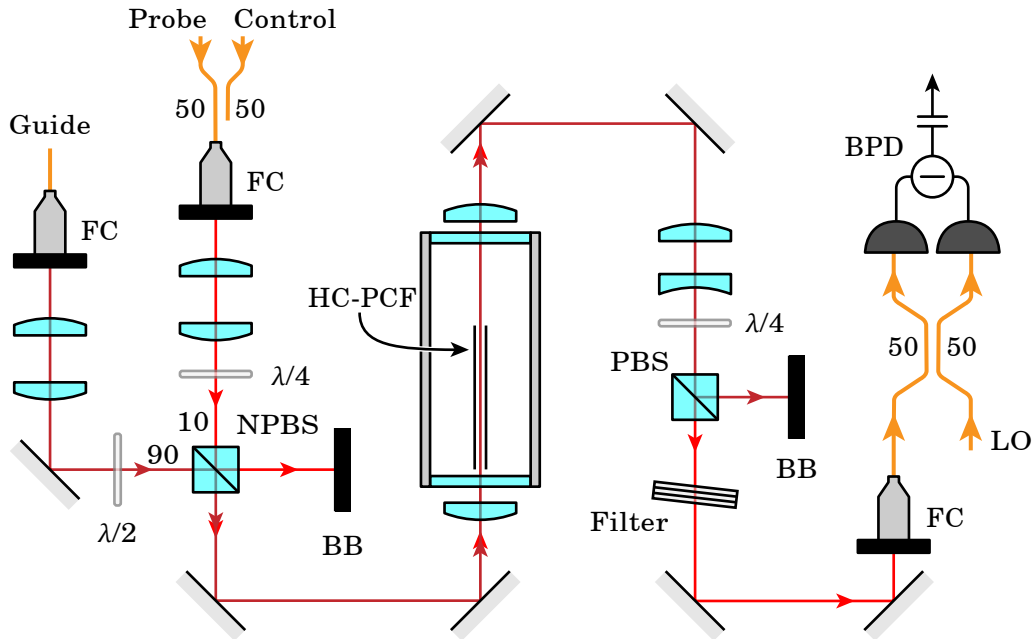


Figure 4.17: Diagram of the experimental setup used to interrogate an in-fibre atomic sample. Here the guide and probe light are combined in opposite linear polarisations on an NPBS, with 90 % of the guide and 10 % of the probe being send through the vacuum chamber. The weak probe is separated from the guide using both polarisation (PBS) and spectral filtering, and is coupled into PM fibre. The probe light is combined with the LO in fibre, and both optical beats are simultaneously measured on an AC-coupled balanced photodiode (BPD).

The interrogation of the atom-filled hollow-core fibre is much the same as in [subsection 4.5.2](#), where now the probe and control fields are combined in fibre before being coupled into the vacuum chamber along with the guide beam, as shown in [Figure 4.17](#). In this case the probe and control fields are circularly polarised, and QWPs are used before and after the vacuum chamber to match the polarisation of the light to the PM used. After separation from the guide beam after the vacuum chamber using a narrowband optical filter (*Thorlabs* FBH800-10), the probe light is coupled back into fibre and combined with the LO in a 50 : 50 fibre coupler. Both outputs of the splitter are attached to a balanced photodiode (BPD) (*Thorlabs* PDB435A-AC) which performs direct subtraction of the incident photocurrents, resulting in high sensitivity to the low-level RF beat note containing the signal information.

The resulting signal and reference time traces are recorded on an oscilloscope and saved to disc as before.

4.5.3.2 Data Processing

While the methods used for transmission calculation, data aggregation, error calculation, and averaging are the same for the heterodyne spectroscopy setup, the methods used to calculate the optical power per pulse are very different. Here the beat between signal and reference electric fields maps the different optical detunings of each probe pulse into a unique RF frequency. Instead of the careful analysis of the time-domain waveforms that were necessary to remove stray light and electronic backgrounds we can instead extract amplitude information directly in the frequency domain. This analysis is described below.

The data collected from a single pulse sequence in the absence of an atomic absorption is shown in [Figure 4.18 a](#)). Here the technique described in [subsection 4.5.1](#) has been used to generate a 41 pulse sequence, each 0.6 μs long and at 2 μs intervals. The first pulse in the sequence is shown in [Figure 4.18 b](#)), where the RF oscillations are clearly visible. In this measurement the optical frequency is stepped from + 40 MHz to – 40 MHz around resonance in 2 MHz steps, resulting in a 80 MHz range of beat frequencies centred at the LO detuning of + 80 MHz, as shown in [Figure 4.18 c](#)). Although all the information is present in the single full-span Fourier transform, it is more effective to roughly isolate each pulse before moving to the frequency domain, as shown in [Figure 4.18 d](#)). This improves the signal to noise by removing the unnecessary white noise contribution from time regions at which there is no useful signal.

At this point it is necessary to correctly convert voltage levels into optical power in the probe beam. This is somewhat more difficult due to the nature of heterodyne detection. We begin by considering the electric fields of the probe and LO in a single aligned polarisation axis expressed in terms of the time-averaged optical power P :

$$E_p(t) \propto \sqrt{2P_p} \sin(\omega_p t), \text{ and} \quad (4.15)$$

$$E_{LO}(t) \propto \sqrt{2P_{LO}} \sin(\omega_{LO} t) \quad (4.16)$$

where ω is the angular frequency of each field. When combined on a 50 : 50 beam splitter (fibre or free-space) each output contains a superposition of the two input fields, where the field that was reflected for each output possesses a $\pi/2$ phase lag induced by reflection from the interface. When incident on a photodiode, the induced photocurrents of each arm of the interferometer are given by

$$I_1(t) = \eta \left(\frac{1}{2} P_{LO} + \frac{1}{2} P_p - \sqrt{P_{LO} P_p} \sin((\omega_{LO} - \omega_p) t) \right), \text{ and} \quad (4.17)$$

$$I_2(t) = \eta \left(\frac{1}{2} P_{LO} + \frac{1}{2} P_p + \sqrt{P_{LO} P_p} \sin((\omega_{LO} - \omega_p) t) \right) \quad (4.18)$$

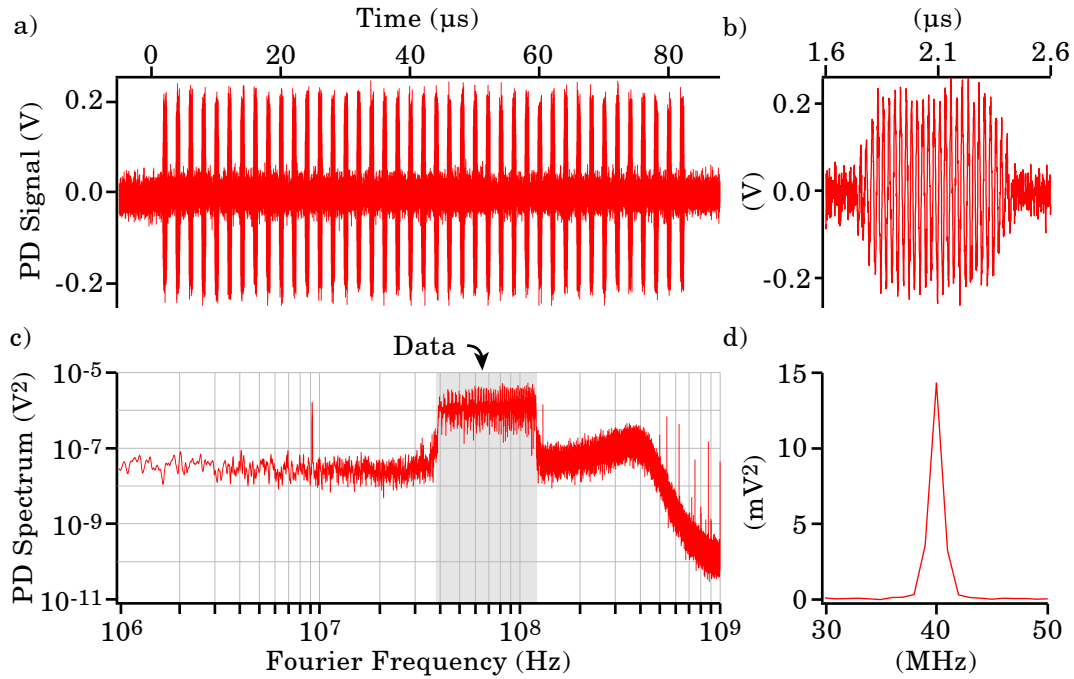


Figure 4.18: Demonstration of typical heterodyne spectroscopy data. a) The raw signal recorded from the photodetector. b) A zoom around the first pulse in the sequence, where the RF oscillation is visible. c) A Fourier transform of entire data trace shown in a), where the RF band containing the stepped-detuning pulse sequence is shaded. d) A Fourier transform of the single pulse shown in b).

where only the DC and low frequency terms have been kept. Here η is the quantum efficiency of the photodiodes, and the phase lag in each output of the beam splitter has resulted in a π phase difference between the RF tones produced by each photodiode. Subtraction of the two photocurrents and transimpedance amplification of the result by a factor G_{PD} produces an RF signal given by

$$V_{PD}(t) = 2G_{amp}G_{PD}\eta\sqrt{P_{LO}P_p}\sin((\omega_{LO} - \omega_p)t) \quad (4.19)$$

where a voltage gain of G_{amp} has been introduced to include a pre-amplification stage between the detector and the oscilloscope.

When the FFT is taken of a time segment containing this data, such as in [Figure 4.18 b](#)), the resulting spectrum must be normalised appropriately. In *Igor Pro* this is done by scaling the amplitude spectrum (in V) by a factor of $2/N$ where N is the number of data points in the time series. Finally, the optical power in a probe pulse is calculated by integrating the square of the Fourier spectrum over a small bandwidth BW around

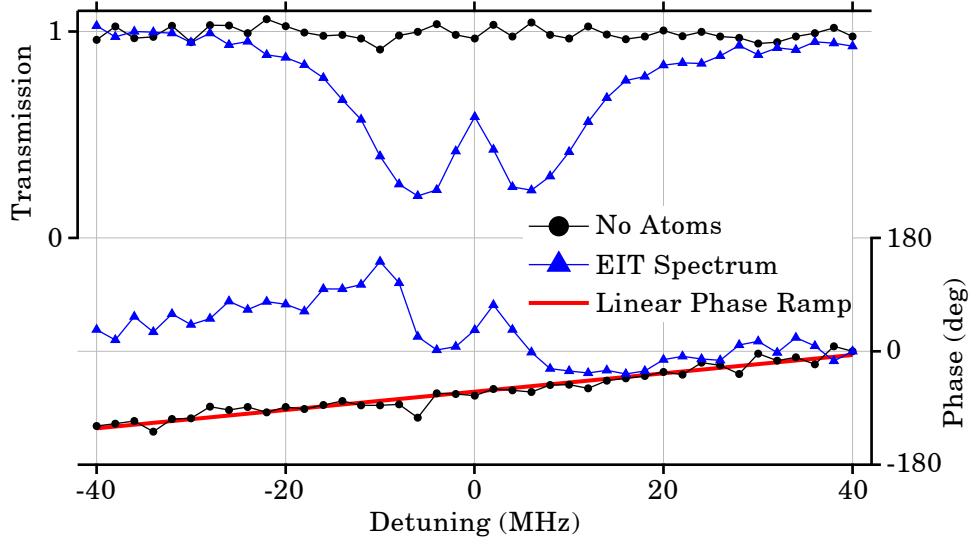


Figure 4.19: Processed heterodyne spectroscopy data for two single-shot measurements: one with no atoms present (black circles) and one with a weak EIT feature (blue triangles). A linear fit to the no-sample phase measurement is shown (red, bold) for illustration.

the known beat frequency f_B and scaling the result using Equation 4.19:

$$P_p = \frac{1}{G_{\text{amp}}^2 G_{\text{PD}}^2 \eta^2 N^2 P_{\text{LO}}} \times \frac{1}{\text{BW}} \int_{f_B - \text{BW}/2}^{f_B + \text{BW}/2} \mathcal{F}(V_{\text{PD}}(t))(f)^2 df. \quad (4.20)$$

By applying this process to each pulse in the both the signal and reference data sets we can calculate the optical power arriving at the photodetector for each optical detuning used, with and without an atomic ensemble. This is enough to calculate transmission of the atoms, however a final factor of $1/C_{\text{opt}}$ must be used to scale the measured power to the level present in hollow-core fibre, where C_{opt} is the efficiency of the optical coupling between the two locations, taking into account the transmission of various optics and fibre collimators. The resulting data is shown in Figure 4.19 for a test case with no atomic sample, and a real measurement of a weak EIT feature.

In addition to transmission, the FFT can be used to extract changes in phase across the pulse sequence, and hence a measure of perturbations to the optical phase in the beams. As the beam paths of the probe and LO are different, long, and uncontrolled, this information can only be used to provide qualitative information, and is difficult to average in any sensible fashion. As an example, Figure 4.19 also shows the phase shifts experienced between the two pulse sequences, relative to the first pulse. In the test

case with no atomic sample a linear phase ramp is seen, where the slope of the ramp is equivalent to an change in optical path length of one beam at a rate ~ 3 mm/s. When a sample is present, a similar phase ramp is overlaid with the dispersion of the atomic sample, which for the [EIT](#) experiment produces a weak S-shaped dispersive effect.

4.6 Summary

In this chapter I have detailed the wide variety of interrogation techniques that are routinely used in the cold atom experiment. These techniques include diagnostic methods such as fluorescence counting and [MOT](#) ballistic expansion imaging, as well as careful spectroscopic techniques used to capture detailed information from the cold-atom loaded hollow-core fibre.

The experimental setup used to perform each of these protocols has been presented, along with the data analysis methods used to extract the desired information. Further detail on the data processing code used can be found in [section A.1](#).

MONTE-CARLO MODELLING

Monte-Carlo modelling is a technique by which an image of the behaviour of a deterministic system is built through repeated random sampling of the input conditions and statistical analysis of the resulting outcomes. In a sense this is exactly the way an ensemble-based cold atom experiment works: each atom can be thought of as a random variate of an underlying initial distribution function. If the interaction between atoms is sufficiently weak, or can be well approximated by a some function of the atom's state, then the experimental system can be treated as a deterministic process that maps input states to output states. If enough of the physics involved can be captured mathematically then a Monte-Carlo simulation can be a powerful tool for predicting the behaviour of the experimental system.

In this chapter I present the theory behind the Monte-Carlo model we developed and a detailed description of how it is implemented.

5.1 Overview

A Monte-Carlo model can be divided into several discrete components. These are a mathematical description of the physics of interest, the generation of randomised inputs, the solving of the equations of motion for each input state, and the collection and processing of the output states of the model.

The system we model is the fall under gravity of cold atoms from a MOT, and the guidance of some of these atoms into the hollow-core fibre by the dipole trap coupled through the fibre. This model is built in *Mathematica* and uses the computationally efficient `NDSolve` function to numerically solve the equations of motion of the system and produce a trajectory through space for each atom. This trajectory can be differentiated to produce the full set of parameters of state for the atom: the position and velocity in three-dimensional space.

Key aspects we are able to investigate are the efficiency of the loading process for various experimental parameters, the effects of fast modulation of the guide beam for interrogation, and the statistics of the ensemble once inside the fibre. For more in-depth analysis the parameters of state can be used to calculate for each atom and moment in time the total kinetic energy, the depth in the potential, the instantaneous scattering rate, or even the expected absorption spectrum including spatially dependent AC-Stark shifts. In addition to these questions we have used the model to generate visually useful images of the process, both for outreach and education purposes as well as to provide a more tangible way of understanding the behaviour of the system.

While simulations are a useful tool, they have their limitations – it is impossible to produce a perfect model of a physical system. There are always higher order effects that will contribute at some small level, and there are always more and more complex interactions between elements to compute. As such, it is more important to identify the limitations to the model and understand how they affect the outcomes you measure.

In our case we only include the strongest forces on the atomic trajectories, and do not include any form of atom-atom interaction. In addition, we do not include the effects of optical pumping or stimulated emission. These effects should be minimal in the case of a low number density ensemble with a far-detuned guide beam.

5.2 Included Physics

To model the atom loading process we develop an equation of motion that governs the trajectory of the atom. This differential equation must contain all sources of acceleration, and can then be solved for a particular set of initial conditions to produce both the position and velocity of the atom at all points in the path.

We identify the primary contributions to an atomic trajectory as being the acceleration due to gravity, the dipole force from the guide field, and the scattering of photons from guide. The contributions from gravity and the guide field are continuous effects, and are directly included in the equations of motion which we write as

$$\frac{d^2 \mathbf{r}}{dt^2} = -\frac{\nabla U_{\text{dipole}}(\mathbf{r})}{m_{\text{Rb}}} + \mathbf{g} \quad (5.1)$$

where \mathbf{r} is the atomic position in three-dimensional Cartesian coordinates, U_{dipole} is the dipole potential produced by the guide, m_{Rb} is the atomic mass, and $\mathbf{g} = -9.81\hat{z} \text{ m/s}^2$ is the acceleration due to gravity.

The dipole potential we use is an approximation in the case of a light source far detuned from an atomic transition and includes the contributions of both the D_1 and D_2 transitions. This potential is given by

$$U_{\text{dipole}}(\mathbf{r}) = \frac{\pi c^2}{2} \left(\frac{\Gamma_{D_1}}{\omega_{D_1}^3 \Delta_{D_1}} + \frac{2\Gamma_{D_2}}{\omega_{D_2}^3 \Delta_{D_2}} \right) \cdot I(\mathbf{r}) \quad (5.2)$$

where Γ is the natural decay rate, ω is the angular frequency of the transition, and Δ is the angular frequency detuning of the guide from the transition, for each of the fine-structure split transitions.

The function $I(\mathbf{r})$ is the local intensity of the guide beam, which encodes both its transverse profile (fundamental Gaussian mode, hollow mode, etc.), its propagation in the z direction, and total optical power P . In the case of an attractive, red-detuned dipole trap the spatial intensity of the guide beam is calculated as

$$I(\mathbf{r}) = \frac{2P}{\pi w(z)^2} \exp\left(\frac{-2(x^2 + y^2)}{w(z)^2}\right) \quad (5.3)$$

where $w(z)$ is the Gaussian waist parameter. This is the parameter used to define the size of the beam inside the fibre, the length of the fibre, and the propagation of light into free space above and below the fibre.

While the use of a piecewise function to distinguish between the different zones of the guide is an easy solution, it can cause more problems later down the road. Specifically, we found that the *Mathematica* numerical differential equation solving tool `NDSolve` struggled with solving the trajectory across the interface between the zone of free Gaussian beam expansion, and the zone of fibre-confined light. As such we implemented a single

equation for $w(z)$ that uses the error function (erf) to produce a smooth transition in all derivatives of the dipole potential across each of these zones. This function is given by

$$w(z) = w_0 \left[\left(\frac{1}{2} + \frac{1}{2} \operatorname{erf}\left(\frac{-z}{\lambda}\right) \right) + \left(\frac{1}{2} + \frac{1}{2} \operatorname{erf}\left(\frac{z}{\lambda}\right) \right) \cdot \sqrt{1 + \left(\frac{z}{\pi w_0^2/\lambda}\right)^2} \right] \quad (5.4)$$

where w_0 is the waist inside the fibre and λ is the guide wavelength.

While this covers the gravitational and dipole contributions to the equation of motion, there is still the effect of scattering of guide photons to include. Unlike the other two effects, spontaneous absorption occurs in discrete events that produce quantised kicks of momentum $|p| = h/\lambda$ where h is the Planck constant. In addition, while we can assume that spontaneous absorption only occurs in the direction of the guide propagation, the spontaneous emission of a photon that follows produces a momentum kick in an a random direction. The rate at which this process occurs is given by

$$\Gamma_{\text{sc}}(\mathbf{r}) = \frac{\pi c^2}{2\hbar} \left(\frac{\Gamma_{D_1}^2}{\omega_{D_1}^3 \Delta_{D_1}^2} + \frac{2\Gamma_{D_2}^2}{\omega_{D_2}^3 \Delta_{D_2}^2} \right) \cdot I(\mathbf{r}) \quad (5.5)$$

While we could have chosen to approximate these effects by a continuous force in the direction of propagation of the guide with magnitude given by $\Gamma_{\text{sc}}(\mathbf{r}) \cdot h/\lambda$, we believed that discrete scattering events could be a important aspect of the model. As such we instead include a second equation of that is calculated at the same time as the first:

$$\frac{dN_{\text{sc}}}{dt} = \Gamma_{\text{sc}}(\mathbf{r}) \quad (5.6)$$

where N_{sc} is the total number of photon scattering events. Using this counter of the estimated number of expected photon scattering events we can choose to perturb the trajectory of the atom each time N_{sc} increments by a full integer. The perturbation to atomic velocity is given by

$$\delta v_{\text{atom}} = h/\lambda \hat{z} + h/\lambda \hat{\xi} \quad (5.7)$$

where $\hat{\xi}$ is a unit vector randomly generated in spherical coordinates.

With these equations of motion, the geometry of the fibre, and the choice of guide parameters, it is possible to calculate the trajectory of an atom from a set of starting conditions.

5.3 Starting Conditions

Each atom possesses an initial position and velocity in three dimensions, each component of which is a random variate from an different distribution. The choice these generating functions allow us to simulate the size, distribution, and temperature of the atomic cloud at $t = 0$.

The initial spatial distribution of atoms is approximated by a normal distribution in each Cartesian axis, calculated by

$$f(x_i) = \frac{1}{\sigma_i \sqrt{\pi}} \exp\left(-\frac{(x_i - \mu_i)^2}{\sigma_i^2}\right) \quad (5.8)$$

where x is the initial location, μ is the offset of the cloud from zero, σ is the $1/e$ radius of the cloud, and each parameter is specified in each of the Cartesian coordinates with associated index i . Similarly, the atomic velocities in each dimension are generated by sampling a one-dimensional Maxwell-Boltzmann velocity distribution. This distribution is given by

$$f(v_i) = \sqrt{\frac{m_{\text{Rb}}}{2\pi k_{\text{B}} T_i}} \exp\left(\frac{-m_{\text{Rb}} v_i^2}{2k_{\text{B}} T_i}\right) \quad (5.9)$$

where k_{B} is the Boltzmann constant, v is the velocity, T is the temperature, and each is specified for a coordinate with index i as before. Although it is strange to specify different thermodynamic temperatures for each direction, this allows us to match the model to the experiment in which we do see different temperatures in the horizontal and vertical axes.

With each of the six distributions given above it is possible to generate a set of initial conditions for a single atom by sampling a random variate from each distribution. In reality it is significantly more computationally efficient to generate n random variates from each distribution and store the values in an array. During the calculation for each atom a set of initial conditions is allocated from the array of (x, y, z, v_x, v_y, v_z) values.

In simulations where very few atoms are expected to be useful, for example when testing a weak trapping field or high temperature MOT, this array of initial conditions can be pre-tested against some selection criteria. By removing the atoms that can be ruled out of entering the fibre, we reduce the computational overheads associated with starting a new thread, constructing the NDSolve environment, and recording the trajectory.

5.4 Solving the Equations of Motion

Having both the initial conditions and the equations of motion, it is now a matter of implementing an algorithm capable of solving the differential system efficiently and recording the desired information. Our choice of modelling guide photon scattering as discrete events complicates this, as we need to be able to identify when N_{sc} increments by an integer value, and be able to pause the differential evaluation to affect the momentum kick. Helpfully, *Mathematica*'s `NDSolve` algorithm provides the capability to perform this task, while still abstracting all the complexity of the differential system solver away from the user.

The element that makes this work is the `WhenEvent[event, action]` function which takes a boolean condition *event* and continuously monitors its value during the evaluation of the differential equation solver. Upon triggering the condition, the solver pauses its evaluation to enact the *action* function or code block. The event condition we use is

$$\text{mod}(N_{sc} - 0.5, 1) > 0.5 \tag{5.10}$$

which guarantees that the event is triggered at integer values of N_{sc} and that this event is a clearly identifiable condition and not at a discontinuity. The *action* component of this function enacts the momentum kick given in [Equation 5.7](#).

Having the components clearly identified, the actual matter of running the differential-equation solver is trivial. The `NDSolve` function is supplied with three arguments; the first is a set of differential equations including the equations of motion, the `WhenEvent`, and the initial positions and velocities for atom. The second is the functions to solve for, in our case these the trajectory in Cartesian coordinates which we specify as the components $x(t)$, $y(t)$, and $z(t)$. The final argument is the independent variable with the range over which to evaluate the system. We use the time t , which is typically evaluated over the range 0 to 80 ms – from the drop of the cloud to a short time after the ensemble should enter the fibre. This is written in *Mathematica* as:

```
soln=NDSolve[Evaluate[DEqns[t]],{x[t],y[t],z[t]},{t,Tinit,Tdur}]
```

The equations of motion for this system are not inherently difficult, and the solver completes the evaluation of a single atom typically within half a second, including the time spent saving trajectory data to disc. To process enough atoms to build useful statistics we employ parallel-processing techniques to maximise the throughput possible.

Implementing this is not difficult, as without atom-atom interaction the evaluation of each atom trajectory is inherently independent. As such, moving from single- to multi-threaded operation is as easy as wrapping the calculation in a `ParallelDo`.

Another computation optimisation technique implemented is the use of pre-compiled numeric functions for the dipole force and the scattering rate. This is done using the `Compile` tool, and as long as the functions are carefully designed to be entirely numeric, can provide a steep improvement in evaluation speed. Although we have the option of using the *Phoenix* High Performance Computing infrastructure at the University of Adelaide, we have not yet found that the processing time on a local multi-core machine is the limiting factor. The typical calculation time for 10^4 atoms is less than 20 min, depending on how many atoms are successfully guided into the fibre – atoms that do not enter the fibre core when passing through the z_0 plane are terminated.

5.5 Processing Results

Once the solver has completed its evaluation it returns a solution that contains the time values at which the system was evaluated and the associated x , y , and z values at each time. The increments in the independent variable are not necessary uniform across the solution as the solver dynamically alters the resolution of the mesh to keep the accuracy and precision of the solution within tolerance while minimising the computation time. Although there are many settings and parameters that can be user specified to tailor the way this dynamic process works, we have found the default settings adequate for our needs. To simplify data aggregation at a later point we resample the provided solution on a known and evenly spaced time axis, and save the resulting array of position values to a binary file for storage and later processing.

In addition to the position data we often also calculate the instantaneous velocity at each time value by performing a time derivative of the full solution and again resampling it on our chosen time spacing. There are other calculations that we have at one time or another implemented at this stage of the process, such as the calculation of the AC-Stark broadened absorption profile of each atom as would be measured by a probe beam coupled through the fibre.

Another common use for the model is calculation of the expected loading efficiency. In this case the full trajectories are not required, and we discard all position and velocity data after calculation and simply record whether or not the atom was successfully coupled

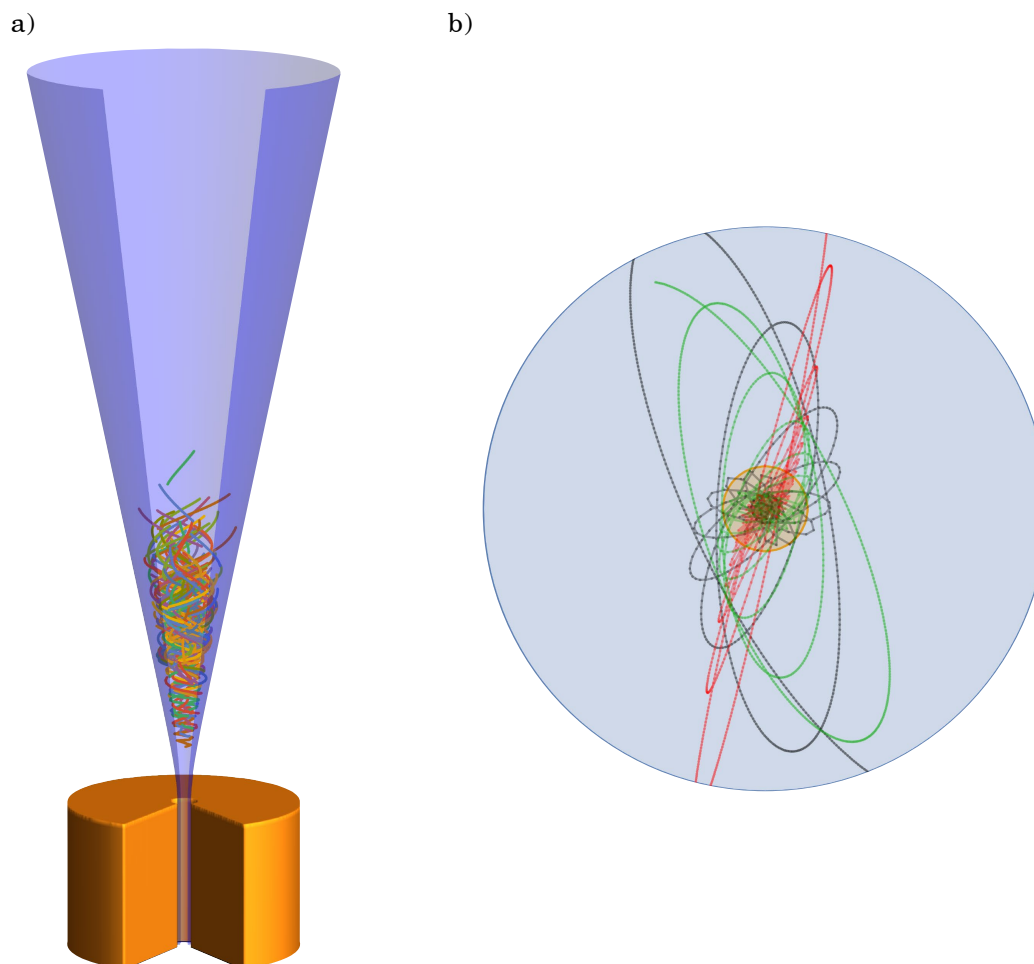


Figure 5.1: A typical set of atomic trajectories calculated using the Monte-Carlo model. Here only atoms are shown that successfully enter the fibre. a) The trails of 100 atoms over 5 ms as they approach the fibre tip, where the blue geometry shows the location of ‘wall’ of the hollow dipole trap being simulated. b) The trajectories of three atoms as they approach the tip of the fibre, as seen from above. Here the blue region is the face of the fibre, and the inner yellow region is the core.

into the fibre. The evaluation and writing to disc of the trajectory corresponds to a significant fraction of the computation time of each atom, and as such removing this element speeds up the calculation significantly.

While most of the data processing and analysis is very specific the question being asked, a generally useful aspect of this model is the ability to visualise the atom-loading process. This is done by using standard data visualisation techniques to present the trajectories of a few or many atoms, either in a three-dimensional format or projected along a desired axis. A demonstration of each of these techniques is shown in [Figure 5.1](#) for the repulsive, hollow guide beam described in [subsection 3.2.2](#). An example of the way these visualisations help us understand the physical process can be seen in the orbital-like motion visible in the top-down view of [Figure 5.1 b](#)). Here we see that the radial and azimuthal components of the initial velocity of atom translate into eccentricity and precession of the atomic trajectory.

In addition to this direct feedback into our own understanding, these visualisations are of great use for helping others understand the project. This has been very useful for outreach and educational purposes, providing a visually aesthetic-way for someone with very little classical education in physics to connect to a very complicated and technical experiment. An example of this can be seen in the movies we have uploaded to *Figshare* containing these simulations (available at [doi : 10.25909/5bd115c35eb1b](https://doi.org/10.25909/5bd115c35eb1b)) which have received an extraordinary number of the views and surprising publicity.

5.6 Summary

The Monte-Carlo simulation developed during this project is a powerful resource for supporting the experimental and lab-based work. Despite only including a few physical processes the resulting model is capable of predicting complex behaviour and is capable of being run on a local machine on the timescale of tens of minutes, providing fast feedback to the experiment. The ability to easily input real, experimentally measured system parameters into the model provides an excellent way to predict the effect of changes to these physical parameters.

The validity of the model has been well tested by direct comparison between both the qualitative predictions of the atomic motion, and the quantitative predictions of atom loading efficiency, and the experiment itself. Details on this can be found in [chapter 6](#), however I show here (as [Figure 5.2](#)) a modified excerpt from the publication *High-efficiency*

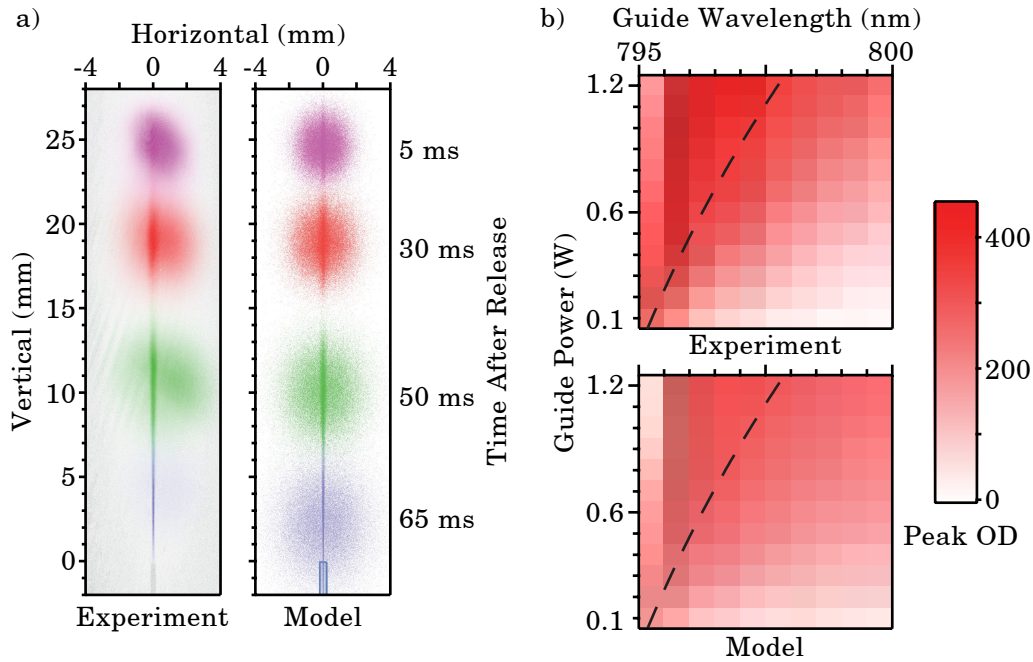


Figure 5.2: A comparison between experimentally measured atom dynamics and the corresponding Monte-Carlo model. These graphs are reproduced from APS journal Physical Review Applied article [High-efficiency cold-atom transport into a waveguide trap](#). a) Shadow images of the atom cloud as it falls and is guided into the fibre, and a computer-generated images of the same process mimicking the experimental technique. b) Two-dimensional maps of the in-fibre *OD* made over the guide power and wavelength, where the dashed black line represents a constant trap depth contour.

cold-atom transport into a waveguide trap [43] in which this juxtaposition is made clear.

Part III

Publications

HIGH-EFFICIENCY COLD-ATOM TRANSPORT INTO A WAVEGUIDE TRAP

Statement of authorship

Title of publication

High-efficiency cold-atom transport into a waveguide trap

Authors

Ashby P. Hilton,¹ Christopher Perrella,¹ Fetah Benabid,² Ben M. Sparkes,¹ Andre N. Luiten,¹ and Philip S. Light¹.

¹*Institute for Photonics and Advanced Sensing and School of Physical Sciences, The University of Adelaide, Adelaide, South Australia 5005, Australia.*

²*GPPMM Group, Xlim Research Institute, UMR CNRS 7252, Université de Limoges, 87032 Limoges, France.*

Publication details

This work is a research article published in the American Physical Society peer-reviewed journal *Physical Review Applied*, volume 10, issue 4, October 2018 with page number 044034 and DOI: [10.1103/PhysRevApplied.10.044034](https://doi.org/10.1103/PhysRevApplied.10.044034).

Context

The first aim of the overall research project was to achieve repeatable, efficient loading of cold rubidium atoms into a 10 cm length of kagome-lattice fibre. This publication was the first central research outcome from this project, and covered the successful demonstration of this goal.

The article focuses on the high atom-loading efficiency we achieved, and the high optical depth generated in a relatively large core [HC-PCF](#). The experimental apparatus used to perform these experiments are described in [chapter 3](#), and the interrogation techniques are described in [chapter 4](#).

This result was aided by a powerful mathematical simulation of the experiment, allowing us to optimise various physical parameters and predict the dynamical behaviour of the system. This model is described in detail in [chapter 5](#). The optical depths we achieved remain the second highest obtained in the field, while the loaded atom number is an order of magnitude larger than the next highest achieved.

While the strong light-atom interaction generated could form the basis for a powerful quantum optics platform, further development of our experimental design and interrogation techniques would be necessary to effectively investigate these phenomena. The mathematical model described here provides useful insight into the cold-atom system, which will aid in this.

Continuation of this work will be to move from a two-level absorption measurement of atom number using the D_2 transition to a three-level Λ scheme on the D_1 line. This will permit the measurement of the coherence time of the confined atomic ensemble, and allow exploration of pulse storage and few-photon-switching phenomena.

Contribution to the paper

The underlying concept and experimental design were developed by Dr. Light in the years leading up to my candidature. I took ownership of the direction of the experiment over the duration of this work, under the supervision of Dr. Light, Dr. Perrella and Prof. Luiten.

The vacuum chamber, laser systems and supporting infrastructure were built by Dr.

Light, while the hollow-core fibre was developed by Dr. Light and Prof. Benabid. A significant fraction of the work that went into this publication was the long-term upgrade of the experimental setup to achieve the reliability and functionality necessary. This included designing and building electronic devices, optical setups, high-bandwidth laser stabilisation systems, and experimental oversight systems. This work was chiefly driven by myself, with support from Dr. Light. Dr. Sparkes assisted with the redesign of the dipole trap infrastructure and its implementation.

A key aspect of this publication is a detailed mathematical model that was used to optimise experimental parameters of the system. This model was built from the ground up by myself under the guidance of Dr. Light and Dr. Perrella. I developed the theoretical background necessary and wrote the code for the Monte-Carlo simulation and analysis.

Obtaining useful information from a cold-atom system requires careful interrogation protocols. I designed the experimental protocols, built the necessary apparatus, and wrote the mathematical analysis used to extract and interpret transmission spectra to obtain useful information.

The article itself was primarily written by myself, with comments and corrections provided all co-authors.

Overall percentage contribution

60%

Certification

This paper reports on original research I conducted during the period of my Higher Degree by Research candidature and is not subject to any obligations or contractual agreements with a third party that would constrain its inclusion in this thesis. I am the primary author of this paper.

Signed:

_____, Date: 29 / 10 / 19

Co-Author Acknowledgement

By signing the Statement of Authorship, each author certifies that:

- i. the candidate's stated contribution to the publication is accurate; and
- ii. permission is granted for the candidate to include the publication in the thesis;

Signed: _____, Date: 25 / 11 / 19
Dr. Christopher Perrella


Signed: _____, Date: 30 / 10 / 19
Prof. Fetah Benabid



Signed: _____, Date: 29 / 10 / 19
Dr. Ben Sparkes

Signed:  _____, Date: 29 / 10 / 19
Prof. Andre Luiten

Signed: _____, Date: 30 / 10 / 19
Dr. Philip Light

High-efficiency cold-atom transport into a waveguide trapA.P. Hilton,^{1,*} C. Perrella,¹ F. Benabid,² B.M. Sparkes,¹ A.N. Luiten,¹ and P.S. Light¹¹*Institute for Photonics and Advanced Sensing and School of Physical Sciences, The University of Adelaide, Adelaide, South Australia 5005, Australia*²*GPPMM Group, Xlim Research Institute, UMR CNRS 7252, Université de Limoges, 87032 Limoges, France* (Received 13 February 2018; revised manuscript received 14 August 2018; published 12 October 2018)

We develop and characterize an atom-guiding technique that loads 3×10^6 cold rubidium atoms into a hollow-core optical fiber, an order-of-magnitude greater than previously reported results. This result is possible because it is guided by a physically realistic simulation that can provide the specifications for a loading efficiency of 3.0% and a peak optical depth of 600. The simulation further shows that the loading efficiency is limited solely by the geometric overlap of the atom cloud and the optical guide beam, and is thus open to further improvement with experimental modification. The experimental arrangement allows observation of the real-time effects of light-assisted cold-atom collisions and background-gas collisions by tracking the dynamics of the cold-atom cloud as it falls into the fiber. The combination of these observations, and physical understanding from the simulation, allows estimation of the limits to loading cold atoms into hollow-core fibers.

DOI: [10.1103/PhysRevApplied.10.044034](https://doi.org/10.1103/PhysRevApplied.10.044034)**I. INTRODUCTION**

Cold atoms have been a transformational tool for sensing [1–3], measurement [4–8], emulation [9], and simulation [10,11]. The specific properties of cold matter that make it useful for these applications is its high atomic density, low velocity, and excellent isolation from the environment. Furthermore, alkali metals are commonly used in cold-matter experiments as they confer strong atom-light interaction, allowing both efficient measurement and manipulation. The figures of merit that quantify these properties for an atomic ensemble are its coherence time, τ , and optical depth, defined as $\mathcal{D}^{\text{opt}} = -\ln T$, where T is the transmission. Examples where overall performance depends crucially on these figures of merit include quantum-state storage [1,12], strong photon-photon interaction for quantum-information processing [13], and interferometric magnetic gradiometry [14].

A promising approach to attain a high \mathcal{D}^{opt} is the loading of cold atoms into a hollow-core photonic crystal fiber (HC PCF) [15–17]. The tight confinement of atoms to the core of the fiber delivers a close match between the optical cross section of the cold atom and the transverse-mode diameter of the light field. The close matching leads to an optimal \mathcal{D}^{opt} for a given number of atoms. Further, the guidance of the fiber means the match can be extended over lengths that are not limited by diffraction—up to tens of centimeters.

Previous experiments aimed at loading cold atoms into a HC PCF achieved \mathcal{D}^{opt} up to 1000 [18] and were used

to demonstrate slow and stopped light [19] as well as highly efficient few-photon all-optical switching [20] and excitation of Rydberg atoms [21]. Similar systems have shown coherence times not limited by atom-wall or atom-guide interactions using Lamb-Dicke spectroscopy in a one-dimensional lattice [22], or atom interferometry using optically confined free-falling cold atoms [23].

These preliminary explorations show promising results; however, the limitations and dynamics of the atomic loading and trapping process are still not well understood. This work provides a detailed simulation of the cold-atom loading of an optical fiber, which is augmented with an innovative experimental design that can follow the atoms during the loading and trapping process. The simulation is seen to be in excellent agreement with the experiment, and the imbued confidence allows rapid pinpointing of the optimal conditions in which more than 3×10^6 cold atoms can be loaded into the fiber. Using the validated simulation, we are able to predict the limits to optical depth and coherence lifetimes and suggest techniques to expand the capacity of this platform for implementation of coherent-state storage and manipulation.

II. METHODS

The experiment uses cold rubidium-85 atoms produced in a standard three-dimensional magneto-optical trap (MOT). The atoms are cooled on the $F = 3 \rightarrow F' = 4$ cycling transition of the D_2 line, and are repumped on the $F = 2 \rightarrow F' = 3$ transition of the D_1 line, shown in Fig. 1(a). We trap 1×10^8 atoms in a cloud 2 mm in

*ashby.hilton@adelaide.edu.au

diameter with a steady-state temperature of $150\ \mu\text{K}$. The ensemble temperature is reduced below $5\ \mu\text{K}$ with use of $\sigma_+\sigma_-$ polarization gradient cooling (PGC) [24]. A 10-cm length of $45\text{-}\mu\text{m}$ -core-diameter kagome-lattice fiber [see Fig. 1(b)] is situated 25 mm under the MOT as shown in Fig. 1(c). This fiber has low loss between 600 and 1600 nm, and we are able to achieve a combined efficiency of guidance and coupling into the fundamental mode of more than 70% at 780 nm. After the PGC phase, an intense guide laser [25] is switched on, producing trapping forces that cause the falling atoms within the laser field to be guided toward the core of the fiber. The guide beam is coupled into the fiber from below, which produces an attractive dipole trap within the hollow-core fiber that diverges from the output to produce a conical, self-aligning optical funnel that steers atoms into the fiber. With more than 1 W of guide light detuned by 1 THz to the red of the D_1 transition, we produce a radial trapping field with a peak trap depth U_{dip} of $20\ \mu\text{K}$ at the MOT location without the need for intricate magnetic field guides [26]. The eventual fraction of atoms guided into the fiber depends on the velocity and density distributions of the initial ensemble as well as its position with respect to the guide beam. These are complicated functions of the MOT and PGC parameters as well as the settings of the background-magnetic-field

cancellation coils. We maximize the loading dependence on the initial state of the MOT by placing ten of the most sensitive of these variables under the control of a neural-net learning tool, M-Loop [27,28], which is capable of efficiently optimizing the in-fiber optical depth over this multidimensional space.

The number of atoms contained within the guide beam is estimated with use of the transmission of a weak (5-nW) copropagating light field that is tuned around the D_2 transition. The transmitted probe is separated from the guide with use of high-extinction polarization optics, an optical grating, and a narrow band-pass filter, which suppresses the guide light by 90 dB. Prior work [18,22,23,29] implemented a spatial-mode filter of the probe light on exit from the fiber: we do not do that here as strong lensing effects within the large fiber core [30,31] would lead to an overestimate of the optical depth.

The intense guide light introduces inhomogeneous broadening of the probe transition through its transverse intensity variation [32]. This effect is circumvented by our probing in the dark: the guide beam is rapidly intensity modulated, and probing is performed only in the absence of the guide light. We use two double-pass acousto-optic modulators in the probe path to perform the fast (30-ns) switching required. This fast switching speed provides an additional advantage in that we can step the optical frequency between each probing phase, thereby observing the full spectral width of the absorption feature over 144 MHz in a cycle lasting just $100\ \mu\text{s}$. A small amount of repump light is present with the probe, ensuring that the population is not lost to the $F=2$ ground state during measurement. We confirm that our technique is nondestructive by applying two consecutive probe sequences and measuring less than 10% variation between measurements. During each cycle of the experiment, we probe the cold cloud with one laser pulse sequence at a predetermined time following its release from the MOT; a second identical pulse sequence is then applied 500 ms following the first. This second pulse sequence is used to normalize the cold-atom absorption as it is sufficiently delayed that it sees only a small residual absorption associated with the background of hot rubidium atoms—less than 1%.

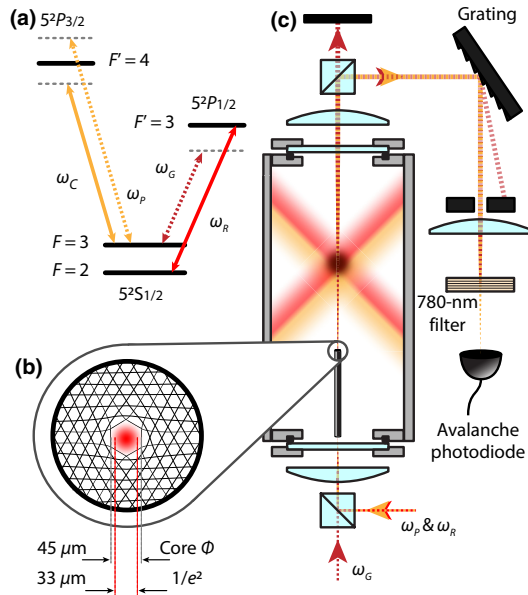


FIG. 1. Experimental setup with (a) the relevant energy levels in the D_1 and D_2 transitions, along with the relative frequency of the MOT cooling laser ω_C , the repump laser ω_R , the guide laser ω_G , and the probe laser ω_P , (b) a cross section of the kagome HC PCF, and (c) the fiber coupling system.

III. ATOM-LOADING RESULTS

We compare the probe absorption when the atoms are just released from the MOT (time: 5 ms) with that observed as they just enter the fiber (time 70 ms) in Fig. 2(a). We see a peak optical depth, \mathcal{D}^{opt} of 600(10), comparable to the greatest depths measured in other fiber-loading experiments [18–20], and approaching the greatest depths possible with other techniques [12,33–35].

By calculating the number of atoms from \mathcal{D}^{opt} (see Appendix A), we estimate we have guided $3.3(1) \times 10^6$ atoms into the fiber, which is approximately 3% of the

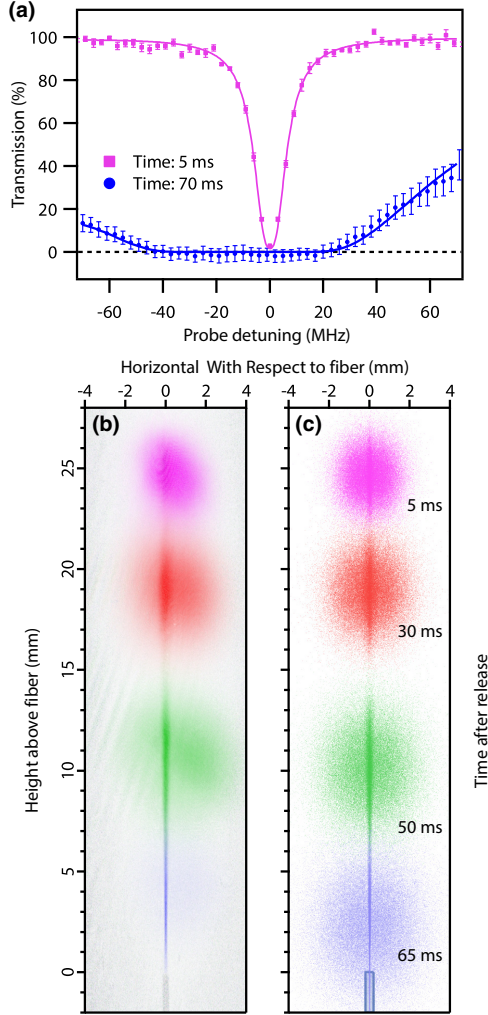


FIG. 2. Atom loading with 1 W of guide power detuned by 1 THz below the D_1 transition, with (a) transmission measurements through the fiber at 5 ms (magenta squares) and 70 ms (blue circles) with fits to data, (b) optical depth map calculated from absorption imaging from the side at 5 ms (magenta), 30 ms (red), 50 ms (green), and 65 ms (blue) after release, and (c) simulated optical depth map that matches the experimental conditions at the same instants.

MOT cloud. Using near-resonance absorption imaging from the side [see Fig. 2(b)], we can directly see the intensifying atomic density in the guide field as the atoms drop.

Because of the relatively small diffraction angle of the guide from the fiber, only 3.2% of the atoms in the initial

ensemble experience a trap depth greater than the average temperature of the ensemble. The Gaussian form of the trap depth in the radial direction from the guide axis and linear scaling of trap depth with guide power impose harsh diminishing returns on atom-coupling performance for fixed cloud and trap geometries (see Appendix B). This strongly suggests that the transfer efficiency could be significantly increased by use of density-enhancing techniques in the MOT region (e.g., spatial dark spot [34,36], magnetic compression [37,38], or a vertically aligned cigar-shaped trap [39]) or by increase of the divergence of the guide by use of a smaller-core fiber.

IV. MONTE CARLO SIMULATION

The underlying physics of the atom-light interaction can be modeled with a detailed Monte Carlo simulation of the loading process. The simulation picks atoms from within a three-dimensional position and velocity distribution that is matched to the experimentally measured atom-cloud size and temperature. The evolution of the atomic position, \mathbf{r} , and velocity is then modeled with use of the differential equation

$$\frac{d^2 \mathbf{r}}{dt^2} = -\frac{\nabla U_{\text{dip}}(\mathbf{r})}{m_{\text{Rb}}} + \mathbf{g}, \quad (1)$$

where m_{Rb} is the atomic mass of rubidium-85 and

$$U_{\text{dip}}(\mathbf{r}) = \frac{\pi c^2}{2} \left(\frac{\Gamma_{D_1}}{\omega_{D_1}^3} \frac{1}{\Delta_{D_1}} + \frac{\Gamma_{D_2}}{\omega_{D_2}^3} \frac{2}{\Delta_{D_2}} \right) I(\mathbf{r}), \quad (2)$$

describes the potential experienced by a neutral atom in a linearly polarized dipole trap where detunings from the D_1 and D_2 transitions, Δ_{D_1} and Δ_{D_2} , are much larger than the ground-state hyperfine splitting [25] and in which the atom is subject to gravitational acceleration, $\mathbf{g} = -9.81 \text{ m s}^{-2} \hat{z}$. Here Γ and ω are the decay rates and optical angular frequencies for specified transitions, and $I(\mathbf{r})$ is the local intensity of the guide beam. The simulation includes the spontaneous absorption and emission of guide photons as well as atom loss due to background-gas collisions (see Appendix C).

We are able to qualitatively test our simulation by comparing the time dynamics of the ensemble with that of the experiment. A large number (10^5) of atoms are simulated, and by calculating the position and optical depth for each atom at several time steps, we are able to replicate the data obtained experimentally using both absorption-imaging and in-fiber spectroscopy techniques. As seen in Fig. 2(c), there is excellent agreement between the experiment and the simulation. It is clear from these images that a large fraction of the initial atom cloud is not guided by the dipole trap, which highlights the importance of improving the mode overlap of the guide and the MOT.

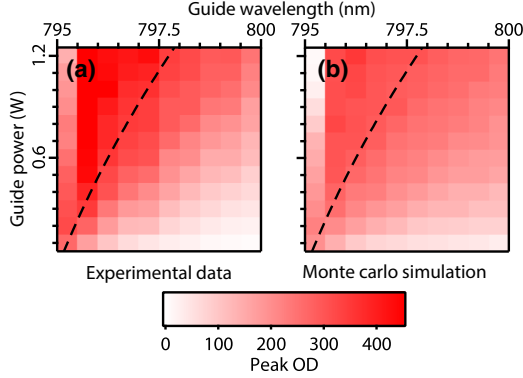


FIG. 3. Peak optical depth (OD) as a fraction of the number of atoms in the initial MOT (a) measured experimentally and (b) calculated by Monte Carlo simulation, both with the line of $U_{\text{dip}} = -3 \mu\text{K}$ at the cloud (dashed black line).

We experimentally investigate the dependence of the atom-loading process on dipole-trap parameters by measuring the peak optical depth as a function of guide powers and wavelengths. These measurements, shown in Fig. 3(a), provide a quantitative means to compare the experimental results against the simulation results shown on Fig. 3(b). To ensure that the experimental atom-density distribution is a match for the assumed initial distribution in the simulation, we reduce the total atom number density by about a factor of 2 from the values shown before (since it is known that high-density MOTs have complex atomic distributions [40,41]). We see excellent agreement between experiment and simulation, both in the absolute values and in the overall shape. For conditions in which the guide is nearly resonant [the leftmost column in Fig. 3(a)], we see a reduction in the number of loaded atoms as we increase the guide depth. The simulation provides the physical understanding that this comes because of the high photon scattering rates that drive the atoms away from the fiber. We also see a plateau in the number of atoms loaded as the guide power is increased (marked by a dashed line in Fig. 3), corresponding to a trap deep enough to catch all the atoms in the volume defined by the overlap of the guide and initial atom ensemble. We note that there are no free parameters in the simulation, which emphasizes the strength of the model.

V. TIME DYNAMICS

We investigate the time dynamics of the loading process by taking absorption measurements at 4-ms intervals following the release of the MOT [similar to that shown in Fig. 2(a)]. Fitting to each spectrum with the expected line shape provides D^{opt} , and we convert this to the equivalent number of atoms in the fiber. To estimate the uncertainty

of each measurement and also improve the statistics, we use five averages for each time step.

This procedure is performed in guide detuning steps of approximately 200 GHz out to 2.5 THz below the D_1 transition. We show in Fig. 4 the temporal evolution of the number of atoms for three of these different wavelengths. We note that these curves display considerably different loading behaviors. For a near-detuned guide we see a very clear peak in the number of atoms in the fiber, followed by a rapid decay, and a weak resurgence at 250 ms. For a 1.1-THz guide detuning we see a similar dramatic increase in the number of atoms at approximately 70 ms but with a much slower exponential decay of the number of atoms. For a 2.1-THz guide detuning, where one might have expected weaker interaction with the guide and thus similar behavior to the 1.1 THz result, we observe an initially higher decay rate. At longer times we see a return to an exponential decay with a similar coefficient as for the 1.1-THz detuning situation. Between these specific examples, the loading dynamics follow a smooth transition between each regime.

Our simulation allows us to explain these behaviors: for near detuning the rate of photon scattering from the guide is high and atoms are quickly expelled from the fiber, leading to the strong decay. As seen in Fig. 4, some of the atoms that have been pushed upward eventually reenter the fiber at a later time, leading to the observation of the resurgence of absorption associated with “bouncing” atoms. The theoretical treatment allows us to observe these “bouncing” atoms in the simulated absorption images [42]. For the case with 1.1-THz detuning, the scattering rate is small enough that we do not see this repulsive effect of the guide. In this case, the residual exponential loss is associated with background-gas collisions; the observed decay rate allows calculation of the residual-background-gas density within

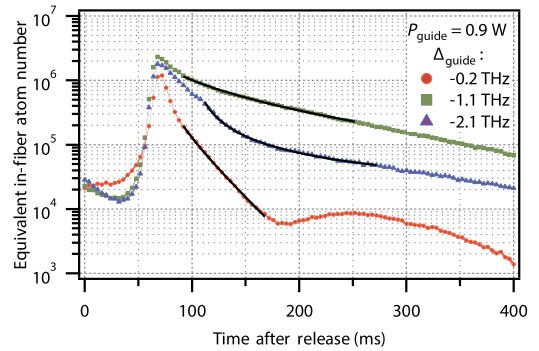


FIG. 4. Number of atoms in the fiber calculated from the optical depth at three different guide detunings. The trap depths at the cloud are 150, 22, and 13 μK for detunings of 0.2, 1.1, and 2.1 THz respectively.

the fiber (see below). For the 2.1-THz guide detuning, we believe that we are driving a photoassociation transition resulting in the formation of excited Rb_2 molecules that are lost from the trap [43]. The photoassociation rate is proportional to the density of Rb atoms and hence becomes negligible once the density has fallen sufficiently.

We fit the evolution of the number of atoms for the family of guide detunings to an equation of the form

$$\frac{dN(t)}{dt} = -\gamma N(t) - \beta'(\lambda)N(t)^2, \quad (3)$$

where γ is the loss rate due to atomic collisions, and $\beta'(\lambda)$ is the wavelength-dependent photoassociation loss coefficient, to extract a collisional loss rate γ of $7.6(2) \text{ s}^{-1}$. The derived density-independent loss rate has a similar value to measurements made by Osaka *et al.* [22] (2.9 s^{-1}) in a shorter section of fiber (32 mm). The background rubidium densities in the chamber and the fiber are below 1×10^{-10} Torr, which results in a Rb-Rb collision rate that is 100-fold too low to explain the observed collision-related loss [44]. We thus attribute these losses to collisions with background-gas atoms; if, as expected, this background is dominated by N_2 due to outgassing, we can calculate the background pressure from the in-fiber collision rate as $1.4(2) \times 10^{-7}$ Torr [44,45]. We can separately calculate the N_2 pressure in the chamber from the measured MOT loading time constant, giving a value of $2.0(2) \times 10^{-8}$ Torr. The N_2 pressure inside the fiber appears reasonable in light of the unfavorable vacuum geometry of the core of the fiber.

The value for $\beta'(\lambda)$ is more difficult to obtain precisely as it describes a density-squared dependent process that is dominant during the peak loading time, while there are other, strongly competing processes. We choose a fit window that contains the corner between the fast- and slow-loss processes (shown as solid black lines in Fig. 4). The fit quality is sensitive to the chosen start and end of this fitting window due to the simplicity of the two-parameter model and the complexity of the experimental system. As such, the results of this fitting, shown in Fig. 5, are intended only as a qualitative description. The form of $\beta'(\lambda)$ shows a decrease from the rapid decay experienced near resonance to a minimum at a detuning of approximately -1 THz, before smoothly increasing as the guide is detuned further. Is it possible to convert the number loss rate β' to the density loss rate β by estimation of the total volume of the atomic sample, which we calculate from the Monte Carlo simulation to be $6 \times 10^{-6} \text{ cm}^3$. Using this value for the volume, we calculate $\beta(\lambda)$ to be as low as $5 \times 10^{-11} \text{ cm}^3 \text{ s}^{-1}$ and as high as $2 \times 10^{-9} \text{ cm}^3 \text{ s}^{-1}$, values that are comparable to values in the literature for similarly sized dipole traps [46,47].

As the density-dependent loss term restricts the usable optical depth of the system, the ability to select a

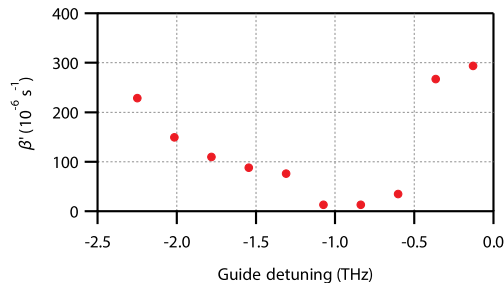


FIG. 5. Estimation of $\beta'(\lambda)$ from fits to atom-decay curves as in Fig. 4.

wavelength for which the coefficient is minimized is of key importance.

VI. PERFORMANCE AND LIMITATIONS

We demonstrate a highly efficient mechanism for transferring cold atoms into a waveguide. Most applications to which this extreme medium could be targeted will depend on the achievable optical depth and coherence time of the medium.

The highest optical depth attained in our system is 600(10) under typical operating conditions. The current limit to this performance is due to the geometric mismatch between the guide beam and the MOT, with approximately 3% of the initial cloud coupled into the fiber. This fraction could be dramatically increased by use of densifying techniques such as a spatial dark spot MOT, or by change to a high-aspect-ratio cigar-shaped MOT.

We also investigate the dependence and dynamics of the loading process on wavelength and power of the guide; in this process we identify a density-dependent atom-loss term that is likely associated with photoassociation. This process can result in an unwanted reduction in the number of loaded atoms, but can be alleviated by the tuning of the guide wavelength to avoid a photoassociation transition.

The atomic coherence time will be limited by the faster of two effects: decoherence induced by interaction between trapped atoms and the optical guide field, or the loss of atoms. Photon scattering in the current experiment limits the atomic coherence time to around $200 \mu\text{s}$, although this rate could be much reduced by replacement of the attractive guide with a hollow repulsive guide mode [48]. This trap geometry would confine atoms predominantly within the low-intensity region, vastly reducing the scattering rate. We simulate this situation, using a hollow trap of the same peak intensity as our Gaussian trap, to predict the time between photon-scattering events of 10 ms—a 100-fold improvement over the current lifetime. An alternative approach to the same end would be the use of a weak far-off-resonance red-detuned trap; this approach has

been shown to work by use of an initial ensemble with a lower temperature or by only trapping the coldest fraction of the atomic cloud [22,23]. In these weaker red- or blue-detuned traps, the background-gas collisions will set a coherent light-atom interaction limit of 130 ms; however, even this limit can likely be extended by careful baking of the fiber to reduce outgassing.

VII. CONCLUSION

We demonstrated a HC PCF cold-atom-loading technique that is capable of loading 3×10^6 atoms into the fiber—a state-of-the-art result. Aided by a robust Monte Carlo simulation, we explore the dependence of the loading efficiency on the parameters of the optical guide beam, enabling us to generate confined-atom samples with optical depths as great as 600(10). Our rapid probing technique allows us to follow the evolution of atoms in real time, and we can use this to observe the fundamental decoherence processes that apply to the approach. Our simulation allows us to show that one could maintain these great optical depths while extending the coherence time to beyond 10 ms.

ACKNOWLEDGMENTS

We thank the South Australian Government for supporting this research through the PRIF program. This research was funded by the Australian Government through the Australian Research Council (Grant No. DE12012028). B.M.S. acknowledges support from an ARC Discovery Early Career Researcher Award (Grant No. DE170100752). We thank Marcin Witkowski for his contribution to the design and construction of the scalar-magnetic-field cancellation coils.

APPENDIX A: OPTICAL DEPTH CALCULATIONS

The optical depth for a single atom in a Gaussian probe field is given by

$$\mathcal{D}_{\text{atom}}^{\text{opt}}(\Delta') = \frac{2\sigma_{D_2}}{\pi w(z)^2} e^{-\frac{2(x^2+y^2)}{w(z)^2}} \sum_{F'} \frac{S_{3,F'}}{1 + 4\left(\frac{\Delta' - \Delta_{3,F'}}{\Gamma}\right)^2}, \quad (\text{A1})$$

where Δ' is the optical detuning in the atomic reference frame, σ_{D_2} is the photon scattering cross section for the interrogated transition, $w(z)$ is the local waist of the probe, $S_{3,F'}$ are the hyperfine strength factors, and $\Delta_{3,F'}$ are the optical detunings of hyperfine levels. The velocity of the atom is accounted for by our moving to the laboratory reference frame using $\Delta' = \Delta + v_z(\omega_0/c)$.

The optical depth for an ensemble of atoms can be estimated by our summing the optical depth over each atom,

or equivalently, one can integrate the product of the optical depth and the atom number density $n(\rho, z)$ over the volume:

$$\mathcal{D}^{\text{opt}} = \int_0^L \int_0^{r_{\text{core}}} n(\rho, z) \mathcal{D}_{\text{atom}}^{\text{opt}} 2\pi\rho d\rho dL, \quad (\text{A2})$$

where L and r are the length and radius of the ensemble, respectively.

One can simplify this calculation by making the assumption that an ensemble of N_{atom} atoms is uniformly populated over L , and that the radial dependence of the atom density follows a Gaussian distribution with standard deviation x_0 :

$$n(\rho, z) = \begin{cases} 0, & |z| > L/2, \\ N_{\text{atom}} \frac{1}{L} \sqrt{\frac{2}{\pi x_0^2}} e^{-\rho^2/2x_0^2}, & |z| < L/2. \end{cases} \quad (\text{A3})$$

The integration now reduces to

$$\mathcal{D}^{\text{opt}} = \eta N_{\text{atom}} \frac{2\sigma_{D_2} S_{3,4}}{\pi w_0^2}, \quad (\text{A4})$$

for the peak optical depth on the $F = 3 \rightarrow F = 4$ hyperfine transition, where η is a coefficient that describes the level of spatial overlap between a cloud of atoms with Gaussian radial density and uniform longitudinal density, and a Gaussian intensity profile:

$$\eta = \frac{(w/2)^2}{x_0^2 + (w/2)^2}. \quad (\text{A5})$$

APPENDIX B: ATOM-COUPPLING DEPENDENCE

The atom-capture efficiency strongly depends on the initial MOT and guide geometries. A brief algebraic analysis is done to determine the scaling of efficiency with the power and size of the guide beam.

We first approximate the guide beam to be collimated through the length of the atom cloud, and we assume that the waist, w_G , is sufficiently small at the initial atom cloud location, z_0 , that the cloud can be approximated as having a uniform column number density given by \mathcal{N} . At z_0 the trap depth in the radial direction can be described by

$$U_{\text{dip}}(\rho) = U_0(P, \lambda) e^{-2\rho^2/w_G^2}, \quad (\text{B1})$$

where ρ is the radial coordinate, P and λ are the optical power and wavelength of the guide, and

$$U_0(P, \lambda) = U_{\text{dip}}(0), \quad (\text{B2})$$

$$= \alpha(\lambda) \frac{2P}{\pi w_G^2}, \quad (\text{B3})$$

is the peak trap depth, with wavelength dependence $\alpha(\lambda)$.

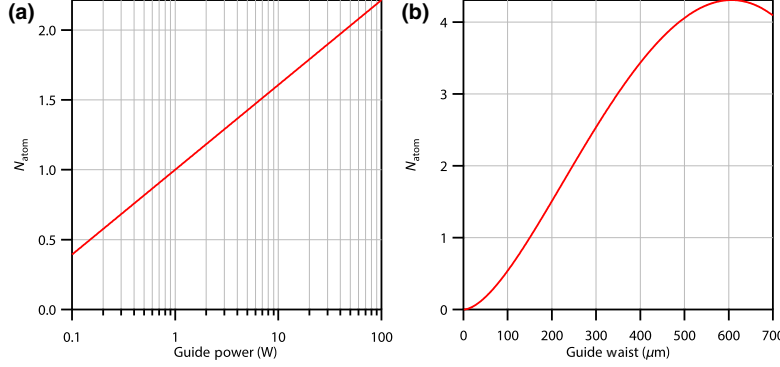


FIG. 6. Number of atoms trapped calculated with Eq. (B8), given relative to the number of atoms for $U_0(797.25 \text{ nm}, 1 \text{ W})$ and $w_G = 150 \mu\text{m}$, with (a) λ fixed at 797.25 nm with P varied and (b) P fixed at 1 W with w_G varied.

We consider atoms to be trapped if the trap depth at their location is greater in magnitude than the kinetic energy of the atom, and negative in sign; that is,

$$U_{\text{dip}}(\rho) + KE_{\text{atom}} < 0. \quad (\text{B4})$$

The radius at which this is true for a fixed ensemble temperature is

$$\rho_{\text{trap}} = w_G \sqrt{\frac{1}{2} \ln \left[-\frac{U_0(P, \lambda)}{KE_{\text{atom}}} \right]}, \quad (\text{B5})$$

and the number of trapped atoms is thus given by

$$N_{\text{atom}} = \pi \rho_{\text{trap}}^2 \mathcal{N}, \quad (\text{B6})$$

$$= \frac{1}{2} \pi w_G^2 \mathcal{N} \ln \left[-\frac{U_0(P, \lambda)}{KE_{\text{atom}}} \right], \quad (\text{B7})$$

$$= \frac{1}{2} \pi w_G^2 \mathcal{N} \ln \left[-\frac{2P\alpha(\lambda)}{\pi w_G^2 KE_{\text{atom}}} \right]. \quad (\text{B8})$$

From this we can find the dependence of trapped atoms on guide power and guide waist:

$$\frac{dN_{\text{atom}}}{dP} = \mathcal{N} \frac{\pi w_G^2}{2P}, \quad (\text{B9})$$

$$\frac{dN_{\text{atom}}}{dw_G} = \mathcal{N} \pi w_G \left\{ \ln \left[-\frac{2P\alpha(\lambda)}{\pi w_G^2 KE_{\text{atom}}} \right] - 1 \right\}. \quad (\text{B10})$$

We conclude that the scaling of the number of atoms with power offers strongly diminishing returns, while increasing the divergence of the guide or the distance from the fiber to the cloud could increase the number of trapped atoms, as shown in Fig. 6.

APPENDIX C: MONTE CARLO SIMULATION

The local photon-scattering rate for an alkali-metal atom in a light field detuned from an optical transition by a distance greater than the hyperfine splitting and less than the fine splitting is given by

$$\Gamma_{\text{sc}}(\mathbf{r}) = \frac{\pi c^2 \Gamma}{2 \hbar \omega_0^3} \left(\frac{1}{\Delta_{D_1}^2} + \frac{2}{\Delta_{D_2}^2} \right) I(\mathbf{r}), \quad (\text{C1})$$

where c is the speed of light, \hbar is the reduced Planck constant, ω_0 is the resonance angular frequency, Δ_{D_1} and Δ_{D_2} are the detunings from the centers of the D_1 and D_2 lines, respectively, and $I(\mathbf{r})$ is the guide intensity.

We integrate $\Gamma_{\text{sc}}(\mathbf{r})$ while numerically solving the equations of motion for each atom to find the total number of scattering events up to a time t :

$$N_{\text{sc}}(t) = \int_0^t \Gamma_{\text{sc}}(\mathbf{r}(\tau)) d\tau. \quad (\text{C2})$$

Each time $N_{\text{sc}} t$ crosses an integer, we perturb the atom velocity with a kick, δv_{atom} , of

$$\delta v_{\text{atom}} = \frac{\hbar \omega_G}{m_{\text{Rb}} c} \hat{z} + \frac{\hbar \omega_{D_1}}{m_{\text{Rb}} c} \hat{\zeta}, \quad (\text{C3})$$

where ω_G is the optical angular frequency of the guide and $\hat{\zeta}$ is a unit vector randomly generated in spherical coordinates. The first term represents a velocity kick in the direction of the guide due to spontaneous absorption, and the second term represents a velocity kick in a random direction due to spontaneous emission.

The simulation also allows for background-gas collisions by probabilistically eliminating atoms from the simulation. The probability that an atom does not experience a collision in the time frame δt is given by

$$P_c = e^{-\gamma_i \delta t}, \quad (\text{C4})$$

where γ_i is the atom-loss rate either outside or inside of the fiber, γ_{chamber} or γ_{fiber} . By sampling of this probability

at sufficiently fine time intervals during the calculation, the population decays by the appropriate rate.

-
- [1] M. Kasevich and S. Chu, Atomic Interferometry using Stimulated Raman Transitions, *Phys. Rev. Lett.* **67**, 181 (1991).
- [2] I. Dutta, D. Savoie, B. Fang, B. Venon, C. L. Garrido Alzar, R. Geiger, and A. Landragin, Continuous Cold-Atom Inertial Sensor with 1 Rotation Stability, *Phys. Rev. Lett.* **116**, 183003 (2016).
- [3] B. Canuel, F. Leduc, D. Holleville, A. Gauguier, J. Fils, A. Virdis, A. Clairon, N. Dimarcq, Ch J. Bordé, A. Landragin, and P. Bouyer, Six-Axis Inertial Sensor using Cold-Atom Interferometry, *Phys. Rev. Lett.* **97**, 010402 (2006).
- [4] A. Peters, K. Y. Chung, and S. Chu, High-precision gravity measurements using atom interferometry, *Metrologia* **38**, 25 (2001).
- [5] J. K. Stockton, K. Takase, and M. A. Kasevich, Absolute Geodetic Rotation Measurement Using Atom Interferometry, *Phys. Rev. Lett.* **107**, 133001 (2011).
- [6] N. Hinkley, J. A. Sherman, N. B. Phillips, M. Schioppa, N. D. Lemke, K. Beloy, M. Pizzocaro, C. W. Oates, and A. D. Ludlow, An atomic clock with 10–18 instability, *Science* **341**, 1215 (2013).
- [7] A. D. Cronin, J. Schmiedmayer, and D. E. Pritchard, Optics and interferometry with atoms and molecules, *Rev. Mod. Phys.* **81**, 1051 (2009).
- [8] P. A. Altin, M. T. Johnsson, V. Negnevitsky, G. R. Dennis, R. P. Anderson, J. E. Debs, S. S. Szigeti, K. S. Hardman, S. Bennetts, G. D. McDonald, L. D. Turner, J. D. Close, and N. P. Robins, Precision atomic gravimeter based on Bragg diffraction, *New J. Phys.* **15**, 1 (2013).
- [9] A. W. Glaetzle, R. M. W. vanBijnen, P. Zoller, and W. Lechner, A coherent quantum annealer with Rydberg atoms, *Nat. Commun.* **8**, 15813 (2017).
- [10] C. Gross and I. Bloch, Quantum simulations with ultracold atoms in optical lattices, *Science* **357**, 995 (2017).
- [11] J.-C. Garreau, Quantum simulation of disordered systems with cold atoms, *C. R. Phys.* **18**, 31 (2017).
- [12] B. M. Sparkes, J. Bernu, M. Hosseini, J. Geng, Q. Glorieux, P. A. Altin, P. K. Lam, N. P. Robins, and B. C. Buchler, Gradient echo memory in an ultra-high optical depth cold atomic ensemble, *New J. Phys.* **15**, 085027 (2013).
- [13] Z.-Y. Liu, Y.-H. Chen, Y.-C. Chen, H.-Y. Lo, P.-J. Tsai, I. A. Yu, Y.-C. Chen, and Y.-F. Chen, Large Cross-Phase Modulations at the Few-Photon Level, *Phys. Rev. Lett.* **117**, 203601 (2016).
- [14] K. S. Hardman, P. J. Everitt, G. D. McDonald, P. Manju, P. B. Wigley, M. A. Sooriyabandara, C. C. N. Kuhn, J. E. Debs, J. D. Close, and N. P. Robins, Simultaneous Precision Gravimetry and Magnetic Gradiometry with a Bose-Einstein Condensate: A High Precision, Quantum Sensor, *Phys. Rev. Lett.* **117**, 138501 (2016).
- [15] R. F. Cregan, B. J. Mangan, J. C. Knight, T. A. Birks, P. St J. Russell, P. J. Roberts, and D. C. Allan, Single-mode photonic band gap guidance of light in air, *Science* **285**, 1537 (1999).
- [16] F. Couny, F. Benabid, and P. S. Light, Large-pitch kagome-structured hollow-core photonic crystal fiber, *Opt. Lett.* **31**, 3574 (2006).
- [17] C. Markos, J. C. Travers, A. Abdolvand, B. J. Eggleton, and O. Bang, Hybrid photonic-crystal fiber, *Rev. Mod. Phys.* **89**, 045003 (2017).
- [18] F. Blatt, T. Halfmann, and T. Peters, One-dimensional ultracold medium of extreme optical depth, *Opt. Lett.* **39**, 446 (2014).
- [19] F. Blatt, L. S. Simeonov, T. Halfmann, and T. Peters, Stationary light pulses and narrowband light storage in a laser-cooled ensemble loaded into a hollow-core fiber, *Phys. Rev. A* **94**, 043833 (2016).
- [20] T. Peyronel, M. Bajcsy, S. Hofferberth, V. Balic, M. Hafezi, Q. Liang, A. Zibrov, V. Vuletic, and M. D. Lukin, Switching and counting with atomic vapors in photonic-crystal fibers, *IEEE J. Sel. Top. Quantum Electron.* **18**, 1747 (2012).
- [21] M. Langbecker, M. Noaman, N. Kjrgaard, F. Benabid, and P. Windpassinger, Rydberg excitation of cold atoms inside a hollow-core fiber, *Phys. Rev. A* **96**, 041402 (2017).
- [22] S. Okaba, T. Takano, F. Benabid, T. Bradley, L. Vincetti, Z. Maizelis, V. Yampol'skii, F. Nori, and H. Katori, Lamb-Dicke spectroscopy of atoms in a hollow-core photonic crystal fibre, *Nat. Commun.* **5**, 4096 (2014).
- [23] M. Xin, W. S. Leong, Z. Chen, and S.-Y. Lan, An atom interferometer inside a hollow-core photonic crystal fiber, *Sci. Adv.* **4**, e1701723 (2018).
- [24] J. Dalibard and C. Cohen-Tannoudji, Laser cooling below the Doppler limit by polarization gradients: Simple theoretical models, *J. Opt. Soc. Am. B* **6**, 2023 (1989).
- [25] R. Grimm, M. Weidemüller, and Y. Ovchinnikov, Optical dipole trap for neutral atoms, *Adv. At. Mol. Opt. Phys.* **42**, 95 (2000).
- [26] M. Bajcsy, S. Hofferberth, T. Peyronel, V. Balic, Q. Liang, A. S. Zibrov, V. Vuletic, and M. D. Lukin, Laser-cooled atoms inside a hollow-core photonic-crystal fiber, *Phys. Rev. A* **83**, 063830 (2011).
- [27] P. B. Wigley, P. J. Everitt, A. van den Hengel, J. W. Bastian, M. A. Sooriyabandara, G. D. McDonald, K. S. Hardman, C. D. Quinlivan, P. Manju, C. C. N. Kuhn, I. R. Petersen, A. N. Luiten, J. J. Hope, N. P. Robins, and M. R. Hush, Fast machine-learning online optimization of ultra-cold-atom experiments, *Sci. Rep.* **6**, 25890 (2016).
- [28] M. R. Hush, M-loop: Machine-learning online optimization package, <https://github.com/michaelhush/M-LOOP> (2017).
- [29] M. Bajcsy, S. Hofferberth, V. Balic, T. Peyronel, M. Hafezi, A. S. Zibrov, V. Vuletic, and M. D. Lukin, Efficient All-Optical Switching Using Slow Light within a Hollow Fiber, *Phys. Rev. Lett.* **102**, 203902 (2009).
- [30] M. Noaman, M. Langbecker, and P. Windpassinger, Micro-lensing-induced line shapes in a single-mode cold-atom-hollow-core-fiber interface, *Opt. Lett.* **43**, 3925 (2018).
- [31] S. Roof, K. Kemp, M. Havey, I. M. Sokolov, and D. V. Kupriyanov, Microscopic lensing by a dense, cold atomic sample, *Opt. Lett.* **40**, 1137 (2015).
- [32] N. Davidson, H. J. Lee, C. S. Adams, M. Kasevich, and S. Chu, Long Atomic Coherence Times in an Optical Dipole Trap, *Phys. Rev. Lett.* **74**, 1311 (1995).

- [33] Y.-F. Hsiao, P.-J. Tsai, H.-S. Chen, S.-X. Lin, C.-C. Hung, C.-H. Lee, Y.-H. Chen, Y.-F. Chen, I. A. Yu, and Y.-C. Chen, Highly Efficient Coherent Optical Memory based on Electromagnetically Induced Transparency, *Phys. Rev. Lett.* **120**, 183602 (2018).
- [34] K. T. Kaczmarek, D. J. Saunders, M. R. Sprague, W. S. Kolthammer, A. Feizpour, P. M. Ledingham, B. Brecht, E. Poem, I. A. Walmsley, and J. Nunn, Ultrahigh and persistent optical depths of cesium in Kagomé-type hollow-core photonic crystal fibers, *Opt. Lett.* **40**, 5582 (2015).
- [35] Y.-F. Hsiao, H.-S. Chen, P.-J. Tsai, and Y.-C. Chen, Cold atomic media with ultrahigh optical depths, *Phys. Rev. A* **90**, 055401 (2014).
- [36] W. Ketterle, K. B. Davis, M. A. Joffe, A. Martin, and D. E. Pritchard, High Densities of Cold Atoms in a Dark Spontaneous-Force Optical Trap, *Phys. Rev. Lett.* **70**, 2253 (1993).
- [37] M. T. Depue, S. LukmanWinoto, D. J. Han, and D. S. Weiss, Transient compression of a MOT and high intensity fluorescent imaging of optically thick clouds of atoms, *Opt. Commun.* **180**, 73 (2000).
- [38] W. Petrich, M. H. Anderson, J. R. Ensher, and E. A. Cornell, Behavior of atoms in a compressed magneto-optical trap, *J. Opt. Soc. Am. B* **11**, 1332 (1994).
- [39] Y.-W. Lin, H.-C. Chou, P. P. Dwivedi, Y.-C. Chen, and I. A. Yu, Using a pair of rectangular coils in the MOT for the production of cold atom clouds with large optical density, *Opt. Express* **16**, 3753 (2008).
- [40] T. Walker, D. Sesko, and C. Wieman, Collective Behavior of Optically Trapped Neutral Atoms, *Phys. Rev. Lett.* **64**, 408 (1990).
- [41] G. L. Gattobigio, T. Pohl, G. Labeyrie, and R. Kaiser, Scaling laws for large magneto-optical traps, *Phys. Scr.* **81**, 025301 (2010).
- [42] See Supplemental Material at <http://link.aps.org/supplemental/10.1103/PhysRevApplied.10.044034> for simulation atom-bounce absorption images.
- [43] J. D. Miller, R. A. Cline, and D. J. Heinzen, Photo Association Spectrum of Ultracold Rb Atoms, *Phys. Rev. Lett.* **71**, 2204 (1993).
- [44] U. D. Rapol, A. Wasan, and V. Natarajan, Loading of a Rb magneto-optic trap from a getter source, *Phys. Rev. A* **64**, 023402 (2001).
- [45] T. Arpornthip, C. A. Sackett, and K. J. Hughes, Vacuum-pressure measurement using a magneto-optical trap, *Phys. Rev. A* **85**, 033420 (2012).
- [46] S. J. M. Kuppens, K. L. Corwin, K. W. Miller, T. E. Chupp, and C. E. Wieman, Loading an optical dipole trap, *Phys. Rev. A* **62**, 013406 (2000).
- [47] A. Fuhrmanek, R. Bourgain, Y. R. P. Sortais, and A. Browaeys, Light-assisted collisions between a few cold atoms in a microscopic dipole trap, *Phys. Rev. A* **85**, 062708 (2012).
- [48] J. Poulin, P. S. Light, R. Kashyap, and A. N. Luiten, Optimized coupling of cold atoms into a fiber using a blue-detuned hollow-beam funnel, *Phys. Rev. A* **84**, 053812 (2011).

DUAL-COLOR MAGIC-WAVELENGTH TRAP FOR SUPPRESSION OF LIGHT SHIFTS IN ATOMS

Statement of authorship

Title of publication

Dual-Color Magic-Wavelength Trap for Suppression of Light Shifts in Atoms

Authors

Ashby P. Hilton,¹ Christopher Perrella,¹ Andre N. Luiten,¹ and Philip S. Light¹.

¹*Institute for Photonics and Advanced Sensing and School of Physical Sciences, The University of Adelaide, Adelaide, South Australia 5005, Australia.*

Publication details

This work is a research article published in the American Physical Society peer-reviewed journal *Physical Review: Applied*, volume 11, issue 2, February 2019 with page number 024065 and DOI: [10.1103/PhysRevApplied.11.024065](https://doi.org/10.1103/PhysRevApplied.11.024065).

Context

This publication was the second research outcome from the project and was the first experimental demonstration of a technique for interrogating ensembles of optical dipole

trapped cold atoms.

When we first attempted to perform direct spectroscopy through the atom-loaded hollow-core fibre it became apparent that the spatially varying ac-Stark shift produced by the dipole trap dominated the measured lineshape. This is a well known difficulty in fields that involve trapped atomic ensembles, and the typical solution is to switch the trapping laser off during measurement periods. This stroboscopic technique is perfectly acceptable in many cases, however it does limit the maximum interaction time to much less than $2\pi/\omega_{\text{trap}}$, where ω_{trap} is the trapping frequency.

An alternative solution that is chiefly employed in the ultra-stable atomic clock field is the ‘magic-wavelength’ technique, in which the wavelength of the trap laser is tuned such that its interaction with the probe, ground, and excited states are identical. In this configuration not only is the spatially varying ac-Stark shift cancelled, but there is also no sensitivity of the atomic state to time-varying power fluctuations in the trap beam.

While this is an excellent solution, it is not necessary easy to achieve. Not only does it require a rigorous mathematical analysis of the coupling strengths between all combinations of allowed optical transitions for the particular atom, but the resulting magic-wavelengths must also be experimentally practical. There is no point implementing such a trap if it couples so weakly with the states involved that hundreds of kilowatts are required, or if the resulting wavelength is effectively unattainable.

Driven by this concept, we implemented a similar scheme, called the ‘dual-colour magic-wavelength’, in which the limitations of a conventional magic-wavelength trap are avoided by the introduction of a second optical beam that is spatially mode-matched to the primary trapping beam. This second field is used to compensate for the ac-Stark shift of the ground state by directly perturbing the excited state by the same amount. This allows interrogation of the probe transition to be unaffected by the spatially varying light shifts of the trapping field, at the cost of increased sensitivity to the frequencies and powers of both the trap and compensation fields.

This publication presents the first experimental demonstration of the dual-colour magic-wavelength technique in the literature. We present the theory behind the scheme, experimental results demonstrating its performance, and a comparison with the expected behaviour extracted from a numerical model of the system.

Contribution to the paper

The underlying concept was conceived by Prof. Luiten, while direct supervision was provided by Dr. Light. I developed the theory behind the technique to determine its applicability, and the experimental configuration required to test and validate the idea.

The modifications to the apparatus necessary to perform experiment were made by myself under the supervision of Dr. Light. These additions included a new spectroscopic interrogation platform, an additional laser with computer oversight, and new core for data analysis and interpretation.

I collected and collated the large quantities of data necessary to compare the experimental data to the theoretical model, and developed the measure of quality of the protocol.

The numerical modelling in Section IV as a comparison to the experimental results was performed by Dr. Perrella, as was the associated section of the article.

The article itself was primarily written by myself, excluding section IV, with comments and corrections provided by all co-authors.

Overall percentage contribution

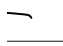
60%

Certification

This paper reports on original research I conducted during the period of my Higher Degree by Research candidature and is not subject to any obligations or contractual agreements with a third party that would constrain its inclusion in this thesis. I am the primary author of this paper.

Signed:

Ashby Hilton

 , Date: 29 / 10 / 19

Co-Author Acknowledgement


By signing the Statement of Authorship, each author certifies that:

- i. the candidate's stated contribution to the publication is accurate; and
- ii. permission is granted for the candidate to include the publication in the thesis;

Signed: _____, Date: 25 / 11 / 19
Dr. Christopher Perrella

Signed: _____, Date: 28 / 10 / 19
Prof. Andre Luiten

Signed: _____, Date: 28 / 10 / 19
Dr. Philip Light

Dual-Color Magic-Wavelength Trap for Suppression of Light Shifts in AtomsA.P. Hilton,^{*} C. Perrella, A.N. Luiten, and P.S. Light*Institute for Photonics and Advanced Sensing (IPAS) & School of Physical Sciences, The University of Adelaide, Adelaide, South Australia 5005, Australia* (Received 9 November 2018; revised manuscript received 15 January 2019; published 26 February 2019)

We present an optical approach to compensating for spatially varying ac-Stark shifts that appear on atomic ensembles subject to strong optical control or trapping fields. The introduction of an additional weak light field produces an intentional perturbation between atomic states that is tuned to suppress the influence of the strong field. The compensation field suppresses sensitivity in one of the transition frequencies of the trapped atoms to both the atomic distribution and motion. We demonstrate this technique in a cold rubidium ensemble and show a reduction in inhomogeneous broadening in the trap. This two-color approach emulates the magic-trapping approach that is used in modern atomic-lattice clocks but provides greater flexibility in choice of atomic species, probe transition, and trap wavelength.

DOI: [10.1103/PhysRevApplied.11.024065](https://doi.org/10.1103/PhysRevApplied.11.024065)**I. INTRODUCTION**

Cold atomic ensembles are broadly applied in the highest-precision sensing and measurement applications. These samples have nearly ideal properties, including strong interaction with light for measurement and preparation, finely tuned internal interactions, as well as high environmental isolation and long internal-state lifetimes. As such, atom ensembles are being applied to quantum-logic operations [1–3], quantum memories [4–8], optical atomic clocks [9–11], atomic interferometers [12], and tests of fundamental physics [13–15]. To make the most of the advantageous properties of cold atomic ensembles, it is frequently necessary to trap and position the ensemble [16]. This optical manipulation necessarily alters the energies of the internal atomic states to produce the attractive potential, which in turn results in a distribution of light-induced shifts of the transition frequencies as atoms sample the intensity distribution of the trapping field. Frequently, one is forced into making a trade-off between the benefits of a tight and deep trap and the undesirable shifting and broadening of the atomic states that are used in the experiment.

The solution to this problem, developed in state-of-the-art atomic-lattice clocks, has been termed the magic-wavelength trap [17–19]. In this case, a careful choice of trap wavelength can eliminate unwanted shifts in a particular transition. This effect is tailored to be independent of trap intensity by creating equal light shifts in the two states connected by the transition. This technique has become universally adopted and a number of magic wavelengths

have been calculated and/or demonstrated for a variety of atomic species [20–24].

Despite its revolutionary impact in creating the ultimate high-performance atomic clocks, the magic technique is not universally applicable. Many commonly used species do not possess a suitable energy-level structure, while for others the necessary wavelengths and powers for the trapping field may not be viable.

In such cases, more complex solutions have been developed in which auxiliary magnetic fields or particular polarization states are used [25,26]. In other circumstances, it has been suggested that bichromatic traps might offer a solution [27–29]. Indeed, some calculated possibilities for Rb and Cs have been published [28–30]. Nonetheless, as yet no one has demonstrated suppression of trap-induced inhomogeneous broadening of an optical transition using a bichromatic magic trap.

We present a simple theoretical prescription of the bichromatic magic-wavelength technique and demonstrate it in a four-level system in a cold rubidium ensemble. We provide a numerical model using the density-matrix formalism and show excellent agreement between the experimental results and the simulation. This opens up the benefits of the magic-wavelength technique for canceling spatially dependent light shifts to a much broader array of atomic species and transitions.

II. METHODS

We implement this technique on dipole-trapped Rb atoms. The Rb is trapped using the $5S_{1/2} \rightarrow 5P_{1/2}$ $D1$ line, labeled $|g\rangle \rightarrow |d\rangle$ [see Fig. 1(a)]. For a light field detuned far from an optical transition such as this, the energy levels are simply shifted symmetrically in lower (δE^-) and

^{*} ashby.hilton@adelaide.edu.au

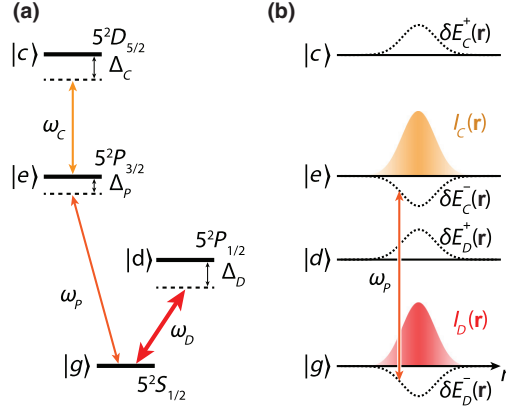


FIG. 1. Diagrams of (a) the relevant energy levels and applied optical fields with frequency detunings shown explicitly and (b) the spatially varying light shifts induced by the dipole and compensation fields on the targeted states in the desired magic regime.

upper (δE^+) states. The magnitude of this shift in energy is given by the product of the reduced Planck's constant and the generalized Rabi frequency, $\hbar\Omega$, and, for a far-detuned dipole field, the shift in $|g\rangle$ and $|d\rangle$ is found by a series expansion around $\Omega/\Delta \rightarrow 0$:

$$\delta E^\pm = \mp \hbar\Omega \approx \mp \frac{1}{2\epsilon_0 c \hbar} |\langle g|\mu|g\rangle|^2 \frac{I_D(\mathbf{r})}{\Delta_D}, \quad (1)$$

where $I_D(\mathbf{r})$ is the intensity of the optical field, $\langle g|\mu|d\rangle$ and Δ_D are the transition dipole moment and optical detuning from states $|g\rangle$ and $|d\rangle$, and ϵ_0 and c are the vacuum permittivity and speed of light, respectively.

A probe laser interrogates the atomic ensemble on the $5S_{1/2} \rightarrow 5P_{3/2}$ D_2 line, labeled $|g\rangle \rightarrow |e\rangle$. For an ensemble of atoms in a spatially varying field, such as a focused dipole trap or lattice trap, the spatial dependence of the intensity leads to an apparent broadening of the transition as the probe transition (ω_p) is perturbed by the light shift of the ground state $|g\rangle$. To correct for this, we apply a compensation field (ω_c) tuned to the $5P_{3/2} \rightarrow 5D_{5/2}$ transition, labeled $|e\rangle \rightarrow |c\rangle$, that intentionally induces a compensatory light shift in the excited state $|e\rangle$. The total frequency shift of the probe transition frequency is given to first order by the sum of the perturbations due to the dipole and compensation fields:

$$\delta\omega_p(\mathbf{r}) = \frac{1}{2\epsilon_0 c \hbar^2} \left(|\langle d|\mu|g\rangle|^2 \frac{I_D(\mathbf{r})}{\Delta_D} - |\langle e|\mu|e\rangle|^2 \frac{I_C(\mathbf{r})}{\Delta_C} \right). \quad (2)$$

It is evident that, for a given trap field and energy-level structure, it is possible to choose an intensity and detuning

for the compensation field that eliminates the light shift on probe transition. Mode matching of the compensation and probe fields automatically compensates for light shifts over the whole beam profile, as shown in Fig. 1(b). This decouples the motion of the atomic ensemble from line-shape modification of the probe transition, achieving the desired magic regime. In order to maintain the compensation, it is necessary to stabilize the ratios of I_D/Δ_D and I_C/Δ_C . In practice, this means implementing frequency and power control on both the dipole and compensation lasers.

One difficulty arises when the desired probe transition involves multiple degenerate Zeeman sublevels. While there may not be a magnetic field to couple to the different angular-momentum-projection states, the differences in the Clebsch-Gordan coefficients lead to a vector polarizability shift that cannot be simultaneously compensated over all transitions between the substates. This residual broadening is avoided by ensuring that the probe addresses only one specific $|F, m_F\rangle \rightarrow |F', m'_F\rangle$ transition. This could be done by applying a strong bias magnetic field to lift the Zeeman-state degeneracy or by pumping atomic population into a single ground state and using an accurately polarized probe beam such that only one excited state is addressed. In this experiment, we do the latter.

III. EXPERIMENTAL DEMONSTRATION

We demonstrate this technique in a dipole-trapped cold atom ensemble (Fig. 2) that is loaded from a standard three-axis magneto-optical trap (MOT). The dipole field is generated using a titanium-sapphire continuous-wave (cw) laser that is detuned between the gigahertz and terahertz ranges below the D_1 line. The light field generates strong trapping forces in the order of several millikelvins.

The probe and compensation lasers are provided by external-cavity diode lasers at 780 and 776 nm, respectively. The probe laser is stabilized to the ^{85}Rb D_2 , $|F=3\rangle \rightarrow |F'=4\rangle$ transition and can be tuned up to

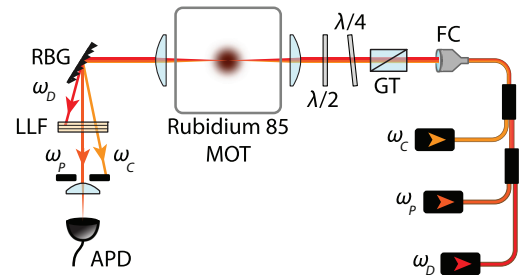


FIG. 2. The experimental setup for demonstrating the compensation technique: RBG, ruled Bragg grating; LLF, laser line filter centered at 780 nm; APD, avalanche photodiode; GT, Glan-Taylor polarizer; FC, fiber collimator.

72 MHz either side of the transition. The compensation laser is coarsely stabilized within 2 MHz to a wave meter, allowing us to tune over the gigahertz range via computer control.

We measure the ensemble absorption with a series of 49 light pulses that are 1 μ s long with a 50% duty cycle, each pulse stepped in frequency 3 MHz from the preceding pulse, allowing us to scan over 144 MHz in 98 μ s. We use an optical power of about 10 nW, with a Rabi frequency of $0.2 \Gamma_e$, where Γ_e is the excited-state decay rate. We can choose to interrogate the ensemble when the dipole laser is on or off. In the first case, the trapping field is left on during probing, while for the latter, we switch the trapping field off momentarily.

To achieve good cancellation of the inhomogeneous broadening in the dipole trap, there needs to be excellent overlap of all the optical beams. This is achieved by combining all the beams within single-mode fiber. To avoid additional broadening by the partially resolved Zeeman manifolds (as explained earlier), we strongly pump the $|F = 3, m_F = +3\rangle \rightarrow |F' = 4, m'_F = +4\rangle$ cycling transition on the D_2 line and use a very pure right-hand-circular polarization for the probe. The polarization quality of the dipole and compensation beams is not important as long as there is a nonzero transition dipole moment between the pumped Zeeman substates for each field. The polarization-tailored combination of fields is then focused through a window into the MOT, producing a waist with a radius of 27 μ m. The beam is recollimated after exiting the chamber and the probe is separated from the other optical fields using a ruled diffraction grating and an etalon filter and is then collected onto an avalanche photodiode.

In order to demonstrate the effect of the compensation technique, we intentionally apply an extremely strong dipole field using 300 mW of light detuned 250 GHz below the D_1 transition, with an on-resonance Rabi frequency of approximately $1000 \Gamma_e$, resulting in a frequency shift of $\delta\omega_p \approx 2\pi \times 14$ MHz. This shift and the associated inhomogeneous broadening are clearly visible if one compares the untrapped and unperturbed atoms (black circles, bottom panel) and the trapped atoms (green triangles, top panel) in Fig. 3. To produce a light shift so that $\delta E_C^- = \delta E_D^-$, we use 1 mW of light in the compensation beam, with a Rabi frequency of $30 \Gamma_e$, and calculate a required detuning of $\Delta_C = -250$ MHz. The compensated spectrum (red squares, bottom panel) in Fig. 3 shows that this has successfully returned the line shape to closely match the unperturbed spectrum. Turning off the trapping field while leaving the compensation on (blue diamonds, top panel) demonstrates that the spectrum has been distorted in the mirror image of that of the trapping field alone, as expected. We attribute the small residual broadening present in the compensated spectrum to imperfect population pumping and polarization selection, resulting in a

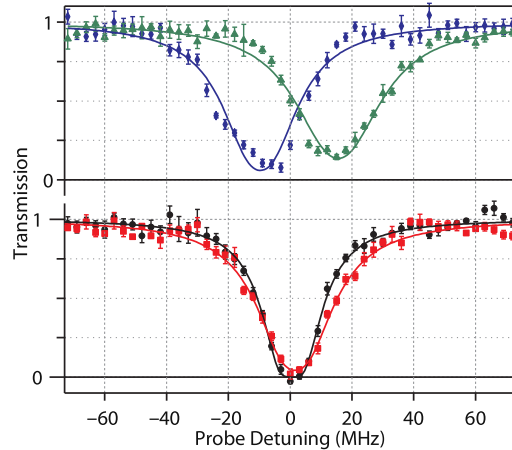


FIG. 3. Transmission spectra of the probe with only the dipole field (green triangles) and only the compensation field (blue diamonds) shown on the top and with neither field (black circles) and both fields (red squares) on the bottom. The compensation field is shown for the optimal detuning calculated. Solid lines are used to show fits to the data, using the form given in Eq. (4).

small fraction of atoms that do not experience the full effect of the compensation.

IV. MODELING

The interaction between the Rb atoms and the three light fields can be approximated to the four-level system shown in Fig. 1(a). This approximation can be made since the guide is sufficiently detuned from state $|d\rangle$ that the hyperfine splitting is negligible; thus the hyperfine levels can be “averaged” into a single level. The same argument holds for the compensation laser and state $|e\rangle$, while the probe beam only interacts with the $|F = 3, m_F = +3\rangle \rightarrow |F' = 4, m'_F = +4\rangle$ level. The second ground state of Rb is not modeled, as none of the dipole, probe, or compensation lasers are tuned to this level. Furthermore, the probe laser is tuned to the cycling transition of the D_2 line; thus negligible decay to the uncoupled ground state is experienced. The trapping laser repopulates atoms into both ground states via scattering through D_1 transition; however, this effect is slow and any population that does decay to dark ground state during the loading process is pumped with a repump laser back to $|g\rangle$ prior to interrogation. The repump remains switched off during spectroscopy. The steady-state absorption of this four-level atomic system is modeled using the density matrix, ρ , which is governed by the Liouville equations [31,32] of the general form

$$\frac{d\rho}{dt} = -\frac{i}{\hbar} [\mathcal{H}_{\text{atom}} + \mathcal{H}_{\text{int}}, \rho] + \Lambda(\rho), \quad (3)$$

where $\mathcal{H}_{\text{atom}}$ and \mathcal{H}_{int} are the atomic and atom-light interaction Hamiltonians under the rotating-wave approximation. Relaxation is included via the $\Lambda(\rho)$ term, which accounts for spontaneous emission from the excited states.

As the Stark-shift broadening is associated with the motion and position of the atomic sample, it is necessary to include a realistic description of these in the model. We use a Gaussian beam intensity and fix the waist, w , at $27\ \mu\text{m}$ to match the expected spot size at the MOT. Within the dipole trap, atoms orbit around the longitudinal axis due to the dipole potential. We approximate the spatial variation of the atomic density as a Gaussian peak that is offset from the beam center by $w/\sqrt{2}$ and has a $1/e$ half width of approximately $w/3.5$. This choice of parameters is based on the modeling of atomic ensembles in traps with depths similar to the kinetic energy of the sample [33].

The four-level density-matrix model is numerically evaluated to produce absorption values for the probe transition for a variety of probe detunings and atomic distances from the center of the dipole beam. The Rabi frequency of the probe, trap, and compensation lasers, along with the detuning of the trap and compensation lasers, is held to experimentally measured values and at each radial evaluation point the absorption is scaled with the local atomic density. By including the measured physical parameters for our system, we are able to test the model against our experimental results.

V. ANALYSIS

We compare the performance of both the experimental and simulated systems by investigating their dependence on the compensation field as the detuning is varied from far below to far above the direct transition. This allows us to cover the full range of behaviors: (a) undercompensated, (b) optimal detuning for the choice of optical intensities, (c) overcompensation, and (d) anticompensation when tuned above $|e\rangle \rightarrow |c\rangle$.

We quantify the effects of the trapping and compensation fields on the atomic transition by fitting to the measured optical depth (\mathcal{D}) with the form:

$$\mathcal{D}(\Delta) = \frac{\mathcal{D}_0}{1 + 4[(\Delta - \Delta_{\text{offset}}) / \Gamma]^2}, \quad (4)$$

where \mathcal{D}_0 is the on-resonance optical depth, Δ and Δ_{offset} are the frequency detuning and frequency offset from the theoretically expected line center, and Γ is the full width at half maximum (FWHM) of the optical depth. We extract the offset and width of the absorption feature over the wide range of Δ_C for both the experimental (markers) and the modeled system (solid lines), with the results shown in Fig. 4. We present two data sets for each of the fit parameters: with (blue and red) and without (purple and yellow) the dipole field turned on during the measurement

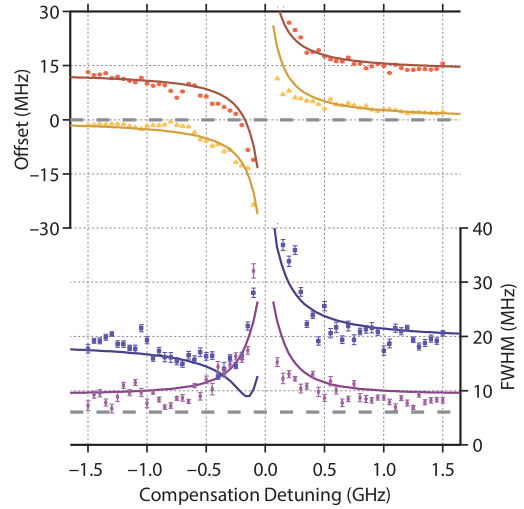


FIG. 4. The offset (top) and full width at half maximum (FWHM) (bottom) of the probe transition against the compensation laser detuning for experimental data (markers) and density-matrix modeling (solid lines). The two data sets are for the compensation field only (red circles and purple diamonds), and both compensation and dipole fields (yellow triangles and blue squares), where the gray dashed lines represent the expected offset and FWHM with no additional fields.

pulses. This allows us to isolate the detrimental effects of the compensation laser from the dipole compensation.

For the frequency offset in the unperturbed case (yellow triangles), we see an avoided crossing feature that is associated with light shift on $|e\rangle$ by the compensation field: just as one expects from a strong optical field. When the dipole field is present (red circles), there is a large constant shift that corresponds to the average potential depth experienced by the atoms. As the compensation field is tuned below resonance, the frequency offset crosses through zero, demonstrating that the line center has been returned to the unperturbed value.

For both of these cases, the corresponding theory curve shows excellent agreement, both qualitatively and quantitatively. This provides confidence in the veracity of the experimental parameters used in the model.

The width parameter shows more complex behavior. With just the compensation field (purple diamonds), we see broadening as we approach the two-color resonant excitation due to saturation of the excited states, which approaches the natural line width at large detunings. The presence of the dipole field (blue squares) shows a dramatic increase in the spectral width that is highly asymmetric. For positive detunings, the sign of the ac-Stark shift induced by the compensation field is the same as that for the dipole field resulting in increased broadening, while

for negative detunings the two optical fields have two opposing ac-Stark effects on the probe transition, resulting in narrowing. This narrowing improves as the compensation field approaches the detuning necessary to completely compensate for the dipole field until it hits a floor set by the width in the compensation-field-only case. We suggest that this is due to a small fraction of the population that remains distributed over a variety of ground m_F states and is not correctly compensated due to the differential light shift over Zeeman substates.

The theory curves agree well with the experimental data for this parameter, although due to the simplified four-level system used, the limit set by residual population is not present. Instead, the system is able to truly approach the natural line width at the optimal choice of compensation detuning.

VI. DISCUSSION

While the demonstrated technique is able to compensate for trap-induced broadening of the atomic transition, the dual-color approach does not provide the first-order immunity to intensity fluctuations in the trapping laser of the traditional magic-wavelength trap. Instead, the system is made sensitive to instability in the power and frequency of both the dipole trap and compensation lasers, making it unlikely that it will be applicable to the ultrastable-clock community. Instead, we see application in precision-spectroscopy experiments where to avoid ac-Stark shifts and broadening, it is otherwise necessary to release the sample from the trap during spectroscopy.

Interrogating the atoms during free fall alleviates light-shift effects at the cost of introducing a lower limit on the achievable resolution due to time-of-flight (TOF) broadening given by $\gamma_{\text{TOF}} \approx 1/\tau_{\text{TOF}}$, where τ_{TOF} is the interrogation time. Stroboscopic techniques, as used in this work, can be employed to make multiple measurements while retaining the atomic sample. In this case, the interrogation time must be short enough that the atoms are not lost from the trap in each cycle. This upper bound is set by the trapping frequency: $1/\tau_{\text{TOF}} > \omega_{\text{trap}}/2\pi$, where $\omega_{\text{trap}} = \sqrt{4U_0/mw^2}$, in which U_0 is the peak trap depth and m is the atomic mass.

For the dual-color technique to be preferential over a stroboscopic measurement, it is necessary for the induced frequency instability in the probe transition due to the trapping and compensation fields to be less than the Fourier limit set by modulating the trap depth. Assuming uncorrelated white power and frequency noise of σ_P and σ_ω , one can calculate from Eq. (2) that the resulting fluctuation in frequency of the probe transition, σ_{ω_p} , is given by

$$\sigma_{\omega_p} = \delta\omega_P \sqrt{\left(\frac{\sigma_{P_D}}{P_D}\right)^2 + \left(\frac{\sigma_{\omega_D}}{\Delta_D}\right)^2 + \left(\frac{\sigma_{P_C}}{P_C}\right)^2 + \left(\frac{\sigma_{\omega_C}}{\Delta_C}\right)^2}. \quad (5)$$

The far-detuned nature of the trapping and compensation fields, combined with easily achievable subkilohertz laser line widths, renders the contribution from laser-frequency instability negligible. As such, the dominant terms in Eq. (5) are the fractional power stability of both lasers. For the trap described in this work, the trapping frequency is $\omega_{\text{trap}} = 2\pi \times 34$ kHz. As such, we calculate that a fractional power stability of better than 0.2% in both lasers is necessary to match the performance achieved by strobing the trap. This level is easily achievable with conventional dc power-control techniques.

We now estimate the performance of this technique, as applied to the far-off-resonance traps (FORTs) used in state-of-the-art experiments. These traps typically utilize very high intensities to achieve background scattering rates as low as 1 s^{-1} . Considering a millikelvin-deep FORT with a large light shift of 50 MHz, such as in Ref. [34], and with a power control of 1 ppm as shown in Ref. [35], one could achieve a light-shift instability limit of 70 Hz. This would be nearly a thousandfold increase in resolution over the Fourier limit set by the trapping frequency of 41.4 kHz and would represent the ability to interrogate extremely narrow atomic features. This would permit the use of continuous nondestructive spectroscopy of an atomic sample held in a tightly confined geometry.

VII. CONCLUSION

We present an experimental implementation of the bichromatic magic-wavelength technique in a cold rubidium ensemble. This is a demonstration of a concept that has been long theoretically described in the literature.

We show narrowing of a strongly distorted optical transition and compare our results over a large range of compensation laser detunings to a numerically evaluated density-matrix model, showing excellent agreement. We estimate the limit to precision spectroscopy set by this technique for our experiment, and for state-of-the-art systems, and predict significant increases in possible interrogation times over stroboscopic methods. This provides confidence in the implementation of two-color optical-dipole traps for long-lifetime spectroscopy of any choice of atomic sample.

The technique uses a single additional weak optical field, which allows significant relaxation of the requirements on the energy-level structure of the atomic sample. This technique opens up a much wider range of possibilities to make use of the revolutionary magic-trap techniques, for systems where either there is no practical magic wavelength available for the desired probe transition or there are limitations on the optical wavelengths that are usable.

ACKNOWLEDGMENTS

We would like to thank the South Australian Government for supporting this research through the PRIF program. This work was performed in part at the OptoFab node of the Australian National Fabrication Facility, utilizing Commonwealth and South Australian Government funding. This research was funded by the Australian Government through the Australian Research Council (Project DE12012028).

- [1] Hsiang-Yu Lo, Yen-Chun Chen, Po-Ching Su, Hao-Chung Chen, Jun-Xian Chen, Ying-Cheng Chen, Ite A. Yu, and Yong-Fan Chen, Electromagnetically-induced-transparency-based cross-phase-modulation at attojoule levels, *Phys. Rev. A* **83**, 041804 (2011).
- [2] Amir Feizpour, Matin Hallaji, Greg Dmochowski, and Aephraim M. Steinberg, Observation of the nonlinear phase shift due to single post-selected photons, *Nat. Phys.* **11**, 905 (2015).
- [3] Zi-Yu Liu, Yi-Hsin Chen, Yen-Chun Chen, Hsiang-Yu Lo, Pin-Ju Tsai, Ite A. Yu, Ying-Cheng Chen, and Yong-Fan Chen, Large Cross-Phase Modulations at the Few-Photon Level, *Phys. Rev. Lett.* **117**, 203601 (2016).
- [4] B. M. Sparkes, J. Bernu, M. Hosseini, J. Geng, Q. Glorieux, P. A. Altin, P. K. Lam, N. P. Robins, and B. C. Buchler, Gradient echo memory in an ultra-high optical depth cold atomic ensemble, *New J. Phys.* **15**, 085027 (2013).
- [5] Y.-W. Cho, G. T. Campbell, J. L. Everett, J. Bernu, D. B. Higinbottom, M. T. Cao, J. Geng, N. P. Robins, P. K. Lam, and B. C. Buchler, Highly efficient optical quantum memory with long coherence time in cold atoms, *Optica* **3**, 100 (2016).
- [6] Frank Blatt, Lachezar S. Simeonov, Thomas Halfmann, and Thorsten Peters, Stationary light pulses and narrow-band light storage in a laser-cooled ensemble loaded into a hollow-core fiber, *Phys. Rev. A* **94**, 043833 (2016).
- [7] Lijun Ma, Oliver Slattery, and Xiao Tang, Optical quantum memory based on electromagnetically induced transparency, *J. Opt.* **19**, 043001 (2017).
- [8] Ya-Fen Hsiao, Pin-Ju Tsai, Hung-Shiue Chen, Sheng-Xiang Lin, Chih-Chiao Hung, Chih-Hsi Lee, Yi-Hsin Chen, Yong-Fan Chen, Ite A. Yu, and Ying-Cheng Chen, Highly Efficient Coherent Optical Memory Based on Electromagnetically Induced Transparency, *Phys. Rev. Lett.* **120**, 183602 (2018).
- [9] Masao Takamoto, Feng-Lei Hong, Ryoichi Higashi, and Hidetoshi Katori, An optical lattice clock, *Nature* **435**, 321 (2005).
- [10] R. Le Targat, L. Lorini, Y. Le Coq, M. Zawada, J. Guéna, M. Abgrall, M. Gurov, P. Rosenbusch, D. G. Rovera, B. Nagómy, R. Gartman, P. G. Westergaard, M. E. Tobar, M. Lours, G. Santarelli, A. Clairon, S. Bize, P. Laurent, P. Lemonde, and J. Lodewyck, Experimental realization of an optical second with strontium lattice clocks, *Nat. Commun.* **4**, 2109 (2013).
- [11] B. J. Bloom, T. L. Nicholson, J. R. Williams, S. L. Campbell, M. Bishop, X. Zhang, W. Zhang, S. L. Bromley, and J. Ye, An optical lattice clock with accuracy and stability at the 10–18 level, *Nature* **506**, 71 (2014).
- [12] K. S. Hardman, P. J. Everitt, G. D. McDonald, P. Manju, P. B. Wigley, M. A. Sooriyabandara, C. C. N. Kuhn, J. E. Debs, J. D. Close, and N. P. Robins, Simultaneous Precision Gravimetry and Magnetic Gradiometry with a Bose-Einstein Condensate: A High Precision, Quantum Sensor, *Phys. Rev. Lett.* **117**, 138501 (2016).
- [13] J. B. Fixler, G. T. Foster, J. M. McGuirk, and M. A. Kasevich, Atom interferometer measurement of the Newtonian constant of gravity, *Science* **315**, 74 (2007).
- [14] T. Rosenband, D. B. Hume, P. O. Schmidt, C. W. Chou, A. Brusch, L. Lorini, W. H. Oskay, R. E. Drullinger, T. M. Fortier, J. E. Stalnaker, S. A. Diddams, W. C. Swann, N. R. Newbury, W. M. Itano, D. J. Wineland, and J. C. Bergquist, Frequency ratio of Al⁺ and Hg⁺ single-ion optical clocks; metrology at the 17th decimal place, *Science* **319**, 1808 (2008).
- [15] Rym Bouchendira, Pierre Cladé, Saïda Guellati-Khélifa, Francois Nez, and Francois Biraben, New Determination of the Fine Structure Constant and Test of the Quantum Electrodynamics, *Phys. Rev. Lett.* **106**, 080801 (2011).
- [16] Rudolf Grimm, Matthias Weidemüller, and Yurii B. Ovchinnikov, Optical dipole traps for neutral atoms, *Adv. At., Mol., Opt. Phys.* **42**, 95 (2000).
- [17] J. McKeever, J. R. Buck, A. D. Boozer, A. Kuzmich, H.-C. Nägerl, D. M. Stamper-Kurn, and H. J. Kimble, State-Insensitive Cooling and Trapping of Single Atoms in an Optical Cavity, *Phys. Rev. Lett.* **90**, 133602 (2003).
- [18] J. Ye, H. J. Kimble, and H. Katori, Quantum state engineering and precision metrology using state-insensitive light traps, *Science* **320**, 1734 (2008).
- [19] Hidetoshi Katori, Koji Hashiguchi, E. Yu. Il'inova, and V. D. Ovsiannikov, Magic Wavelength to Make Optical Lattice Clocks Insensitive to Atomic Motion, *Phys. Rev. Lett.* **103**, 153004 (2009).
- [20] Hidetoshi Katori, Masao Takamoto, V. G. Pal'chikov, and V. D. Ovsiannikov, Ultrastable Optical Clock with Neutral Atoms in an Engineered Light Shift Trap, *Phys. Rev. Lett.* **91**, 173005 (2003).
- [21] Bindhya Arora, M. S. Safronova, and Charles W. Clark, Magic wavelengths for the *np*-*ns* transitions in alkali-metal atoms, *Phys. Rev. A* **76**, 052509 (2007).
- [22] Z. W. Barber, J. E. Stalnaker, N. D. Lemke, N. Poli, C. W. Oates, T. M. Fortier, S. A. Diddams, L. Hollberg, C. W. Hoyt, A. V. Taichenachev, and V. I. Yudin, Optical Lattice Induced Light Shifts in an Yb Atomic Clock, *Phys. Rev. Lett.* **100**, 103002 (2008).
- [23] N. Hinkley, J. A. Sherman, N. B. Phillips, M. Schioppa, N. D. Lemke, K. Beloy, M. Pizzocaro, C. W. Oates, and A. D. Ludlow, An atomic clock with 10–18 instability, *Science* **341**, 1215 (2013).
- [24] Qiang Wang, Yi-Ge Lin, Fei Meng, Ye Li, Bai-Ke Lin, Er-Jun Zang, Tian-Chu Li, and Zhan-Jun Fang, Magic wavelength measurement of the 87Sr optical lattice clock at NIM, *Chin. Phys. Lett.* **33**, 103201 (2016).
- [25] V. V. Flambaum, V. A. Dzuba, and A. Derevianko, Magic Frequencies for Cesium Primary-Frequency Standard, *Phys. Rev. Lett.* **101**, 220801 (2008).

- [26] Sukhjit Singh, B. K. Sahoo, and Bindhya Arora, Magnetic-sublevel-independent magic wavelengths: Application to Rb and Cs atoms, *Phys. Rev. A* **93**, 063422 (2016).
- [27] P. F. Griffin, K. J. Weatherill, S. G. MacLeod, R. M. Potvliege, and C. S. Adams, Spatially selective loading of an optical lattice by light-shift engineering using an auxiliary laser field, *New J. Phys.* **8**, 11 (2006).
- [28] Bindhya Arora, M. S. Safronova, and Charles W. Clark, State-insensitive bichromatic optical trapping, *Phys. Rev. A* **82**, 022509 (2010).
- [29] M. M. Metbulut and F. Renzoni, Bichromatic state-insensitive trapping of caesium atoms, *J. Mod. Opt.* **62**, S46 (2015).
- [30] Junmin Wang, Shanlong Guo, Yulong Ge, Yongjie Cheng, Baodong Yang, and Jun He, State-insensitive dichromatic optical-dipole trap for rubidium atoms: Calculation and the dichromatic laser's realization, *J. Phys. B: At., Mol. Opt. Phys.* **47**, 095001 (2014).
- [31] S. C. Rand, *Lectures on Light* (Oxford University Press, Oxford, 2016).
- [32] M. Auzinsh, D. Budker, and S. Rochester, *Optically Polarized Atoms: Understanding Light-Atom Interactions* (Oxford University Press, Oxford, 2010).
- [33] Ashby P. Hilton, Christopher Perrella, Andre N. Luiten, and Philip S. Light, "Dynamics and Distribution of Atoms in a Radial Trapping Field" (to be published).
- [34] Jun He, Bao-dong Yang, Yong-jie Cheng, Tian-cai Zhang, and Jun-min Wang, Extending the trapping lifetime of single atom in a microscopic far-off-resonance optical dipole trap, *Front. Phys.* **6**, 262 (2011).
- [35] F. Tricot, D. H. Phung, M. Lours, S. Guérandel, and E. de Clercq, Power stabilization of a diode laser with an acousto-optic modulator, *Rev. Sci. Instrum.* **89**, 113112 (2018).

LIGHT-SHIFT SPECTROSCOPY OF OPTICALLY TRAPPED ATOMIC ENSEMBLES

Statement of authorship

Title of publication

Light-shift spectroscopy of optically trapped atomic ensembles

Authors

Ashby P. Hilton,¹ Andre N. Luiten,¹ and Philip S. Light¹.

¹*Institute for Photonics and Advanced Sensing and School of Physical Sciences, The University of Adelaide, Adelaide, South Australia 5005, Australia.*

Publication details

This work has been submitted for consideration to the Institute of Physics peer-reviewed journal *New Journal of Physics* as a research article. The manuscript has positive reviews from its referees, and is undergoing revision for final decision by the journal. It is currently available as a pre-print at the arXiv with ID [1911.02708](https://arxiv.org/abs/1911.02708).

Context

This publication was the third research outcome from the project and was the first demonstration of a method for inferring the physical properties of an ensemble of optical dipole trapped cold atoms.

While developing the theory behind the article *Dual-Color Magic-Wavelength Trap for Suppression of Light Shifts in Atoms* it became apparent that the shifted and skewed transmission spectrum produced by a spatially varying light-shift must inherently contain information of the underlying atomic distribution. During the data acquisition stage of the publication we attempted to mathematically invert the measured atomic spectrum to back-calculate the shape of the atomic density. This attempt was a failure, primarily due to the high sensitivity the resulting density profile had on supposedly well-known experimental parameters. These calculations produced an exponentially increasing atomic density for increasing radius – a nonphysical result.

Later attempts along these lines began instead with a model of the atomic distribution, which was then used to generate the expected absorption profile. Careful development of the mathematics produced an analytic expression for the detuning-dependent transmission spectrum with four free parameters, each an interesting property of the atomic ensemble. This method was significantly more successful, with the model showing excellent agreement with our experimental results.

As a test of the sensitivity of this technique with regards to the input atomic distribution function we repeated the analysis using a ring-like distribution profile, as suggested by Peyronel *et al.* [88]. The resulting fit from this secondary model showed coarse agreement with both our data and data from the referenced article but, unlike the original Gaussian model, failed to capture the full shape of the spectrum.

The outcome of this work is a new technique for extracting the relevant physical parameters for an atomic ensemble in an optical dipole trap. This measurement can be made without modulating the trap or introducing additional interrogation apparatus. Using a standard detuning sweep of the probe laser we show it is possible to calculate the ensemble temperature and trap depth, as well as the linewidth of the transition and the total number of atoms, in a single-run measurement. This is a powerful tool for real-time interrogation of atomic ensembles, especially in confined geometries where additional optical access is not available.

Contribution to the paper

The fundamental concept of this technique was an original development of my own work. Direct supervision was provided by Dr. Light, with Prof. Luiten providing high-level support and guidance.

The theoretical background for this work loosely originated during the preparation of *Dual-Color Magic-Wavelength Trap for Suppression of Light Shifts in Atoms*. Further detailed development of the theory was driven by myself.

I designed the mathematical models of the atomic distribution required for the paper, and produced the full experimentally-testable model of the light-shift-perturbed transmission spectrum. The work on extracting useful physical parameters from the model was done by myself, with guidance from Dr. Light.

The experimental data used a test case was taken and analysed by myself. I acquired and analysed the comparison data set by Peyronel *et al.*, which was provided with explicit permission by the authors.

The article and figures were primarily written by myself, with strong support by Dr. Light and Prof. Luiten, and corrections by all co-authors.

Overall percentage contribution

75 %

Certification


This paper reports on original research I conducted during the period of my Higher Degree by Research candidature and is not subject to any obligations or contractual agreements with a third party that would constrain its inclusion in this thesis. I am the primary author of this paper.

Signed: _____, Date: 29 / 10 / 19
A

Co-Author Acknowledgement

By signing the Statement of Authorship, each author certifies that:

- i. the candidate's stated contribution to the publication is accurate; and
- ii. permission is granted for the candidate to include the publication in the thesis;

Signed:  , Date: 13 / 1 / 20
Prof. Andre Luiten

Signed:  , Date: 20 / 1 / 20
Dr. Philip Light

Light-shift spectroscopy of optically trapped atomic ensembles

Ashby P Hilton¹, Andre N Luiten¹, Philip S Light¹

¹ Institute for Photonics and Advanced Sensing (IPAS) & School of Physical Sciences, The University of Adelaide, Adelaide, South Australia 5005, Australia

E-mail: Ashby.Hilton@Adelaide.edu.au

October 2019

Abstract.

We develop a method for extracting the physical parameters of interest for a dipole trapped cold atomic ensemble. This technique uses the spatially dependent ac-Stark shift of the trap itself to project the atomic distribution onto a light-shift broadened transmission spectrum. We develop a model that connects the atomic distribution with the expected transmission spectrum. We then demonstrate the utility of the technique by deriving the temperature, trap depth, lifetime, and trapped atom number from data was taken in a non-destructive single shot experimental measurement.

Submitted to: *New J. Phys.*

1. Introduction

Cold atomic ensembles are a staple in the world of precision measurement and fundamental physics due to the high atomic densities and low kinetic energies attainable. These properties, combined with a wide range of internal degrees of freedom, make for a versatile tool capable of high sensitivity measurement [1, 2, 3, 4, 5, 6, 7, 8], quantum storage and manipulation [1, 9, 10, 11, 12, 13], and highly accurate metrology [14, 15, 16, 17, 18, 19].

In many cases optical dipole traps are used to localise the atomic ensemble in a controllable way. This can be used to hold the atomic sample for a long duration [15, 20, 21] or to transport the atoms into a confined geometry such as a hollow-core fibre [22, 23, 24, 25, 26, 27, 28, 29] or near to a structured device such as an atomic chip [30, 31, 32, 33]. The act of trapping can itself alter the temperature and size of the ensemble from that which might be derived from a post-facto measurement.

A standard technique for calculating temperature of a trapped ensemble is direct absorption imaging, by which the ensemble is released from the trap and illuminated with resonant light, casting a silhouette or shadow onto a waiting camera [34]. While this

is effective, it is necessary to take many images at various times after release to obtain reliable temperature information. As the imaging pulse imparts significant momentum on the atoms, each time slice must be taken on a separate run of the experiment, making this a slow process that can be susceptible to experimental fluctuations over multiple imaging cycles. Additionally, this method requires direct optical access to both sides of the atomic cloud, which is not always possible.

A similar approach is the release and recapture technique, which also uses the ballistic expansion of the cloud to estimate its thermodynamic properties. !!! This technique is commonly used to measure the temperature of cold-atom ensembles confined to hollow-core fibre, as the atoms can be interrogated using a weak probe field overlapping the trapping beam [35, 36, 25, 26, 28, 37, 29]. However, multiple interrogation sequences with increasing free expansion periods are still necessitated to extract the temperature of the ensemble.

Our approach is an in-situ method that exploits the effect of the trapping field's ac-Stark shift on the absorption of the trapped atoms. This can be used to map the location of an atom in the trap into a shift of the atomic transition through the spatially varying trap intensity. We calculate the expected atomic distribution within a stable Gaussian trapping field, and identify how temperature and other properties of the ensemble affect the functional form of the light shifted absorption spectrum. We show that each of the interesting parameters are sufficiently different in their effect on the absorption spectrum that they can be individually extracted from a single measurement of the broadened spectrum. This negates the need for destructive release and recapture techniques.

We also consider the sensitivity of this technique to the shape of the atomic distribution. It has been suggested within the community that the spatial distribution of atoms within a trap might be ring-like, with its peak density away from the central axis. We develop a self-consistent model for the atomic distribution that produces such an atomic profile and apply our light-shift spectroscopy approach to calculate the absorption spectrum that would be obtained under this assumption. We test both the conventional Gaussian model and the ring-like model against experimental data gathered from our experiment and that of Peyronel et al. [35], and show that our ring-like model does not well match the experimental results. Using the Gaussian model, we find a good agreement with the measured spectra, and are able to extract a range of experimentally useful parameters. This demonstrates the power of this technique for performing fast, single-shot interrogation of dipole-trapped atomic ensembles. This approach also has great merit under some circumstances, such as when direct imaging is not feasible. In addition, as it is not necessary to modulate or switch off the trapping field during measurement, this process is relatively non-destructive allowing multiple measurements to be made during a single experimental run.

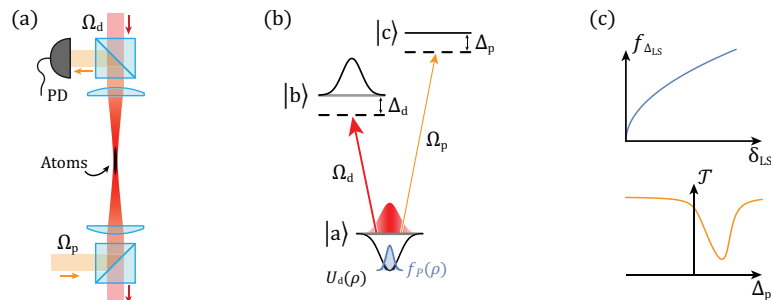


Figure 1. a) The basic experiment system typically used, in which the probe field (Ω_p) is combined with and separated from the trap field (Ω_d), and incident on a photo-detector (PD). b) The energy level structure modelled with the ground-state $|a\rangle$, upper trap-state $|b\rangle$, and upper probe-state $|c\rangle$, including the perturbative effect of the dipole trap, $U_d(\rho)$, and the resulting radial probability distribution function $f_P(\rho)$. c) The calculated atomic distribution as a function of the light-shift (top), and the resulting in-trap transmission spectrum as measured by the probe (bottom).

2. Light-shift spectroscopy

The basis of optical dipole trapping is well known: a strong light field far red-detuned from a two-level atomic system produces a reduction in energy of the ground state. This perturbation is proportional to the local intensity of the dipole beam, and as such a typical Gaussian beam can produce a potential capable of confining atoms. The spatially dependent energy shift serves not only to trap the atoms, but also produces a shift in the line-centre of any transition from the ground state, typically referred to as a light-shift. This effect is typically undesirable, producing an additional source of ensemble decoherence and broadening of the transition [38, 39, 40]. However this lifting of the spatial degeneracy of the atomic ensemble can be performed in a predictable way, giving rise to the possibility of extracting information regarding the distribution of atoms in the trapping light field and the absolute depth of the trap. To understand the effect of both the trap profile and atomic distribution on the measurable absorption spectrum, we build a model using a typical single beam optical trap and a thermal atomic ensemble.

We consider the potential generated by a collimated dipole beam far detuned from an atomic transition, which can be written in cylindrical coordinates as

$$U_d(\mathbf{r}) = U_d(\rho, \theta, z) = U_0 u(\rho) \quad (1)$$

where U_0 is the peak trap amplitude, and $u(\rho)$ is the relative optical intensity in the radial direction $\hat{\rho}$. For a Gaussian dipole beam with power P_d and waist w , the relative intensity is simply $u(\rho) = \exp(-2\rho^2/w^2)$, and the depth of the trap on axis is

$$U_0 = \frac{3\pi c^2 \Gamma_d}{2\omega_0^3 \Delta_d} \frac{2P_d}{\pi w^2} \quad (2)$$

where c is the speed of light, ω_0 and Γ_d are the angular frequency and natural linewidth of the atomic transition, and Δ_d is the angular frequency detuning of the dipole trap laser from ω_0 .

In the thermal regime the atomic density $n(\mathbf{r})$ is determined by the shape of the trapping potential. We expect the atomic ensemble to be strongly defined in the transverse plane, and to simplify our model we assume a uniform dependence on z over a finite length L . As such we write the atomic density as

$$n(\rho, \theta, z) = \begin{cases} \frac{N}{2\pi\rho L} f_P(\rho) & \text{for } 0 \leq z \leq L \\ 0 & \text{otherwise} \end{cases} \quad (3)$$

where $f_P(\rho)$ is the radial probability density function (PDF), or equivalently the radial population density, that satisfies the condition $\int_0^\infty f_P(\rho) d\rho = 1$ such that the integrated density returns the total number of atoms, N . The likelihood of finding an atom at a radius ρ is determined using the Boltzmann factor by calculating the probability that a state with energy $E = U_d(\rho)$ is occupied [41]. This process, described in detail in Appendix A, results in

$$f_P(\rho) = \frac{4\alpha\rho}{w^2} \exp\left(\frac{-2\alpha\rho^2}{w^2}\right), \quad (4)$$

where we have introduced the parameter $\alpha = -U_0/(k_B T)$ as the magnitude of the trap depth relative to the thermal energy of the ensemble. This PDF represents a Gaussian density distribution centred on axis with $1/e$ radius of $w/\sqrt{2\alpha}$.

We introduce a weak probe beam that is spatially matched to the dipole beam and interrogates an auxiliary upper state $|c\rangle$. We consider this state sufficiently detuned from the dipole trap that it remains unperturbed. In the absence of the dipole trap, the effect of the atomic ensemble on a resonant probe field is given by

$$dP_p(\mathbf{r}) = -\sigma n(\mathbf{r}) I_p(\mathbf{r}) dV, \quad (5)$$

where P_p is the power of the probe, I_p is the optical intensity of the probe, and σ is the transition-specific scattering cross section of the atom. Rearranging and integrating in cylindrical coordinates gives us total transmission on-resonance of $\mathcal{T} = \exp(-\mathcal{D}_{\text{opt}})$, where optical depth is:

$$\mathcal{D}_{\text{opt}} = \int_0^L \int_0^{2\pi} \int_0^\infty \frac{\sigma N}{2\pi L \rho} f_P(\rho) \frac{2}{\pi w^2} u(\rho) \rho d\rho d\theta dz \quad (6)$$

$$= N \frac{2\sigma}{\pi w^2} \int_0^\infty f_P(\rho) u(\rho) d\rho \quad (7)$$

$$= N \frac{2\sigma}{\pi w^2} \eta \quad (8)$$

where η is the geometrical overlap between the atomic density and optical field strength. For our choice of $f_P(\rho)$ and $u(\rho)$, we find that the geometric overlap can be given analytically as

$$\eta = \frac{\alpha}{1 + \alpha} \quad (9)$$

which approaches unity for a deep trap (large α).

To include the effect of the dipole trap on the system we calculate the spatially dependent light shift in $|a\rangle$ that will be experienced by the probe beam. This relation is simply given by

$$\delta_{\text{LS}}(\rho) = -U_{\text{d}}(\rho)/\hbar, \quad (10)$$

which we can rearrange using knowledge of the shape of the potential to find the radial location as a function of the light shift:

$$\rho(\delta_{\text{LS}}) = \frac{w}{\sqrt{2}} \sqrt{\ln\left(\frac{-U_0}{\delta_{\text{LS}}\hbar}\right)}. \quad (11)$$

We now calculate the atomic distribution in terms of the light shift, which can be found using the following change of variables:

$$f_{\Delta}(\delta_{\text{LS}}) = \left| \frac{d\rho(\delta_{\text{LS}})}{d\delta_{\text{LS}}} \right| \cdot f_P(\rho(\delta_{\text{LS}})) \quad (12)$$

$$= \frac{\alpha}{\delta_{\text{LS}}} \left(\frac{-U_0}{\delta_{\text{LS}}\hbar} \right)^{-\alpha}, \quad (13)$$

which integrates to unity over the bounds $0 < \delta_{\text{LS}} \leq -U_0/\hbar$. This dipole trap intensity profile in this basis is given by $u(\delta_{\text{LS}}) = -\delta_{\text{LS}}\hbar/U_0$.

The final piece required to calculate the light-shift perturbed spectrum is the absorption profile of the probe transition. Assuming the probe transition is Lorentzian in lineshape with linewidth Γ_{p} , the absorption profile is given by

$$\mathcal{L}(\Delta_{\text{p}}) = \frac{1}{1 + 4(\Delta_{\text{p}}/\Gamma_{\text{p}})^2}. \quad (14)$$

We are now able to calculate the probe-detuning dependent transmission spectrum $\mathcal{T}(\Delta_{\text{p}})$ by performing the integral in Equation 6 but where we also include the Lorentzian profile from Equation 14 and change the integration variable to δ_{LS} .

$$\begin{aligned} \mathcal{T}(\Delta_{\text{p}}) &= \exp\left(-\int_0^{-U_0/\hbar} N \frac{2\sigma}{\pi w^2} f_{\Delta}(\delta_{\text{LS}}) u(\delta_{\text{LS}}) \mathcal{L}(\Delta_{\text{p}} - \delta_{\text{LS}}) d\delta_{\text{LS}}\right) \\ &= \exp\left(-\frac{\mathcal{D}_{\text{opt}}}{1 + 4(\Delta_{\text{p}}/\Gamma_{\text{p}})^2} \frac{2}{\Gamma_{\text{p}}} \right. \\ &\quad \left. \times \text{Im}\left[(\Delta_{\text{p}} + i\Gamma_{\text{p}}/2) {}_2F_1\left(1, \alpha + 1; \alpha + 2; \frac{-U_0/\hbar}{\Delta_{\text{p}} - i\Gamma_{\text{p}}/2}\right)\right]\right) \end{aligned} \quad (15)$$

Here ${}_2F_1(a, b; c; z)$ is the hypergeometric function, which for physical choices of α , is quick to evaluate, and can easily be fit to experimental data over all four physical parameters in real time.

3. Parameter determination

Having calculated the transmission spectrum of a light-shift broadened atomic ensemble, we now seek to understand its shape as well as its dependence on the underlying physical

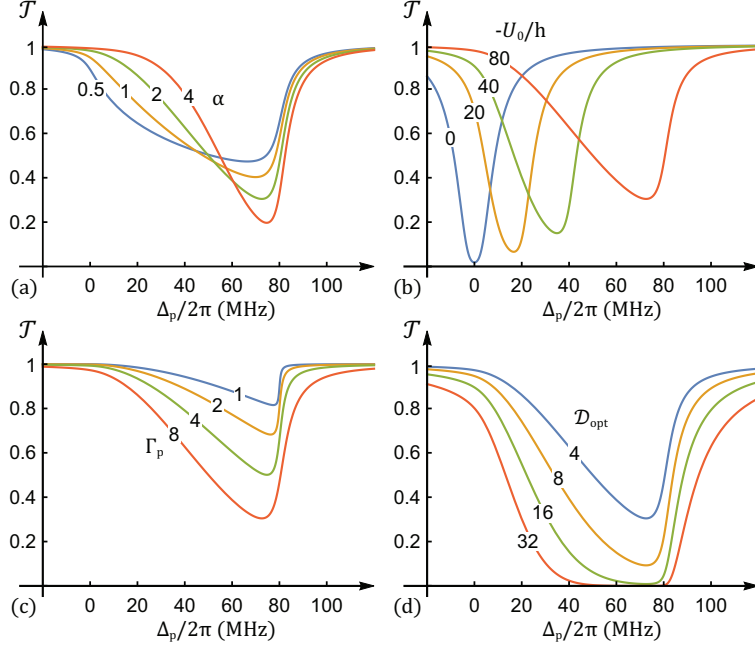


Figure 2. Demonstration of the effect on the modelled transmission spectrum for variation in each physical parameter. In each subfigure a single parameter is varied: a) α , b) U_0 , c) Γ_p , and d) \mathcal{D}_{opt} , while the other parameters are held constant. In all subfigures the unvaried parameters are $\alpha = 2$, $-U_0/h = 80$ MHz, $\Gamma_p = 2\pi \times 8$ MHz, and $\mathcal{D}_{\text{opt}} = 4$.

parameters. To do this we calculate the spectral lineshape, and analyse physical meaning behind the mathematical parameters remaining in our model, and their effect on the resulting spectrum.

There are four physical parameters present in Equation 15: α , the ratio of trap-depth to ensemble kinetic energy; U_0 , the on-axis trap depth - or equivalently expressed as $-U_0/h$, the peak light-shift due to the trap; Γ_p , the probe transition linewidth for atoms in the trap; and \mathcal{D}_{opt} , the optical depth on the probe transition. All four of these parameters provide insight into the trapped ensemble that are not always derivable from conventional measurements. For example, the extracted value of U_0 from this model is an in-situ measurement of the strength of the interaction between the dipole-trap laser and the atomic ensemble that does not rely on knowledge of the optical power, the size of the beam, or the quantum state of the ensemble. As such this can be a powerful tool for verification of the true conditions experienced by the atoms.

Similarly the measurement of α , and thus the temperature T , does not rely on imaging the free expansion of the ensemble over a long relaxation time and many runs of the experiment. This eliminates the effect of shot-to-shot variation in the measured

temperature, allowing one to instead track these processes on a nearly continuous basis.

To understand the influence of these parameters on the absorption spectrum, we calculate it for a realistic choice of experimental parameters and systematically vary one parameter at a time over a range of values. We choose the common parameter set to be: $\alpha = 2$, $-U_0/h = 80$ MHz, $\Gamma_p = 2\pi \times 8$ MHz, and $\mathcal{D}_{\text{opt}} = 4$. The calculated transmission curve for this set of values is shown in Figure 2, where each parameter is varied in subfigures (a) through (d) respectively. A brief description of the influence of each parameter is given below.

The parameter α determines the breadth of the spectrum, predominantly modifying the shape of the low frequency side of the absorption peak. This is due to the effect α has on the spatial extent of the atomic distribution: tightly confined ensembles are held on axis and experience a single light shift, while weakly trapped ensembles sample a large range of the trap intensity, resulting in a wide range of light-shifts. The trap-depth itself determines the depth of the potential, and as such the largest light-shift experienced. The dependence of α on U_0 makes these parameters interdependent, and for a fixed temperature ensemble, inversely proportional. The transition linewidth strongly affects the sharpness of the high Δ_p edge of the spectrum, which is physically determined by the high density of atoms that are closest to the optical axis. The optical depth remains as a simple scaling factor on the overall absorption of the ensemble. Broadening of the absorption feature is seen for high \mathcal{D}_{opt} , as is typical for high dense, strongly interacting samples.

4. Atomic distribution models

Until now we have used a Gaussian distribution for the atomic density, based on the expected distribution from a well founded statistical mechanics approach. While we have no reason not to expect the thermodynamic derivation to well describe a system such as a laser-cooled and trapped atomic ensemble, there may be circumstance in which a non-central distribution may appear. There has been speculation in the literature that this might be the case for a very tightly confined ensemble within a $7\ \mu\text{m}$ core hollow optical fibre [35].

We have used the idea as a means for testing the sensitivity of our technique to variations in atomic distribution within the trap. To do this, we construct a model from first principles that predicts a non-central distribution of atoms where we assume that all atoms in the trap are enforced to undergo pure circular motion in the transverse plane. Using the kinetic energy of the atom to determine the inwards acceleration required to maintain a constant radius, we are able to map the thermal distribution of energy onto the radial distribution of atoms within the trap, and as such find an expression for $f_{P, \text{Ring}}(\rho)$. The derivation for this term is given in full in Appendix B, where the result is

$$f_{P, \text{Ring}}(\rho) = \tag{16}$$

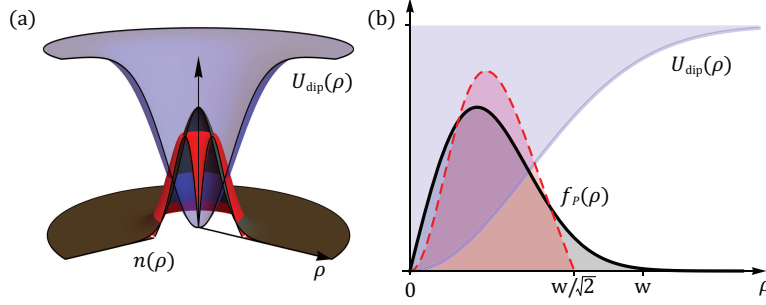


Figure 3. Depiction of the Gaussian and ring-like atomic distributions used for a value of $\alpha = 3$. a) The spatial atomic density $n(\rho)$, where the Gaussian model (Black) has a maximum density on axis, and the ring-like model (Red) is zero on axis. b) The radial population density $f_P(\rho)$ which is proportional to $\rho \times n(\rho)$, where both models have a zero on axis, but the ring-like model (Red, dashed) is also zero for $\rho > w/\sqrt{2}$. The dipole potential (pale blue) is shown for both cases as a visual aid.

$$\begin{cases} 8\sqrt{\frac{2\alpha^3}{\pi}} \frac{\rho^2}{w^3} \left| 1 - 2\frac{\rho^2}{w^2} \right| \exp\left(-\frac{\rho^2}{w^2} \left[3 + 2\alpha \exp\left(-\frac{2\rho^2}{w^2}\right) \right]\right) & \text{for } 0 \leq \rho \leq w/\sqrt{2} \\ 0 & \text{for } \rho > w/\sqrt{2} \end{cases}$$

which integrates to unity over $0 \leq \rho \leq w/\sqrt{2}$ for $\alpha \gg 1$.

We show both the Gaussian and ring-like atomic distributions in Figure 3. In (a) the spatial density $n(\rho)$ is displayed, where the Gaussian model is clearly maximum on-axis, while the ring-like model is zero on axis and peaks off-axis. When the radial PDF is calculated in (b), both models have peak population off-axis. At first sight this is surprising, however it is a consequence of the scaling of the area in an infinitesimal radial band with radius, given by $\rho d\rho$. As a result, while the two models for atomic distribution are essentially orthogonal in density, in radial population density they are remarkably similar. The primary difference between the two models is that, as a result of the circular motion condition enforced in the derivation, the ring-like distribution is has an upper bound at $\rho = w/\sqrt{2}$. On the other hand the Gaussian model is able to extend indefinitely in radius, giving it a distinctly different behaviour for medium to small values of α .

5. Experimental comparison

To test our models for the light-shift perturbed atomic spectra we use a cold-atom loaded hollow-core fibre platform. The experimental setup is described in detail in [27], however a brief overview is provided below.

A magneto optical trap (MOT) prepares a sample of 10^9 ^{85}Rb atoms a short distance above the tip of a 10 cm long segment of $45 \mu\text{m}$ core kagome-lattice hollow-core photonic-crystal fibre (HC-PCF). A 1 W dipole trap beam detuned roughly 1 THz below the D_1 transition is coupled through the fibre from below, intersecting the cold-atom cloud.

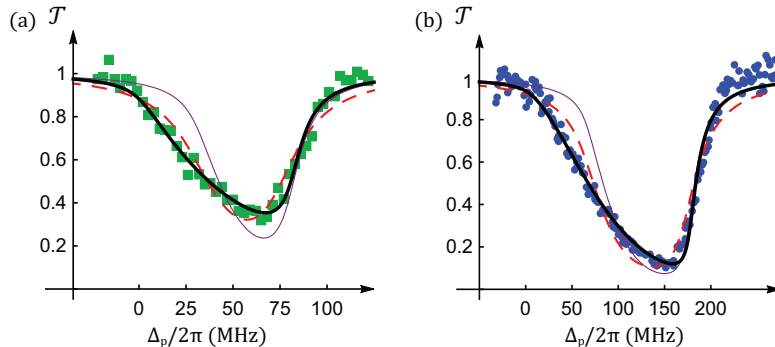


Figure 4. Transmission measurements of an atomic ensemble in a dipole trap, with (a) our data (green squares) and (b) data from [35] (blue circles). Both sets of data are shown with fitted light-shift spectra based on the Gaussian model (thick black curve), the ring-like model (dashed red curve), and the ring-like model using the fit parameters from the Gaussian (thin purple curve).

Upon release of the MOT fields, the atoms that begin deep enough within the dipole trap are confined during their fall under gravity, and smoothly guided into the fibre core. Once inside the fibre the atoms are interrogated by a counter-propagating probe field tuned around the $F = 3 \rightarrow F' = 4$ cycling transition on the D_2 line, which is separated from the dipole trap after exiting the fibre and incident upon an avalanche photodiode.

The interrogation protocol consists of a series of short pulses of weak probe light, each pulse stepped in detuning using a pair of pre-programmed waveforms fed to two double-passed acousto-optic modulators. Using this technique we are able to measure a 144 MHz span in a single 98 μ s window, allowing a true 'snapshot' of the atomic absorption to be taken. While usually the dipole trap is switched off during probe pulses to avoid AC-Stark shifts, for this experiment we left the trap on in order to measure its effect on the spectrum. This data is shown as the green squares in Figure 4 (a), where the spectrum has been spread over a 100 MHz range above the unperturbed linecentre.

To compare our models to this data we run a least-squares fitting algorithm for all four physical parameters using both Gaussian and ring-like transmission curves, which we show as thick black, and red dashed lines respectively. We also show the ring-like model for which we have used the physical parameters obtained from the Gaussian model fit as a thin purple curve. It is clear that the best match to our results is given by the fitted Gaussian model, which captures the full asymmetry seen in the experimental data. In comparison, the ring-like fit is able to match the depth, location, and width of the absorption feature, but fails to capture the asymmetric shape. The ring-like model with Gaussian fit parameters is an easily worse match to the data, and shows that the two models have not converged on similar solutions for the fit parameters.

In addition to our experimental results, we perform the same analysis to the data

Table 1. Results of fitting to AC-Stark shifted data with mathematical models based on ring-like and Gaussian atomic distributions.

| Source | Model | α | T (mK) | $-U_0/h$ (MHz) | \mathcal{D}_{opt} | $\Gamma_p/2\pi$ (MHz) |
|------------------------|-----------|----------|-------------|-------------------|----------------------------|--------------------------|
| Our Data | Gaussian | 1.0(1) | 4.0(4) | 81(1) | 2.8(3) | 16(2) |
| | Ring-like | 0.0(40) | | 74(8) | 1.5(2) | 32(6) |
| <i>Peyronel et al.</i> | Gaussian | 1.59(7) | 5.4(2) | 177(1) | 8.0(6) | 17(1) |
| | Ring-like | 0.0(20) | | 172(5) | 4.4(4) | 33(2) |

used by *Peyronel et al.* to suggest a ring-like distribution, in figure 6(A.1) in [35]. This analysis is shown in (b), where the experimental data is shown as blue circles, and the mathematical fits are the same colour as in (a). As for our work, the best fit is found by the Gaussian model, which fully captures the shape of the data, while the ring-like models are both unable to capture the asymmetry in the light-shift broadened spectrum.

The best fit parameters with associated uncertainties are given in Table 1, where one notes that the fit uncertainties are fractionally lower for Gaussian model, and where the ring-like model is found to be very insensitive to α . The ensemble temperature is calculated for the Gaussian model fits using $T = -U_0/\alpha k_B$.

It is worth mentioning that the linewidth $\Gamma_p/2\pi$ is consistently much larger than the expected natural linewidth of ~ 6 MHz. Assuming that the atoms are otherwise unperturbed, this additional broadening can be caused by two effects: power broadening by spontaneous absorption of the trap beam, and the differential light shifts associated with different m_F ground states. Power broadening should be small due to the weak scattering rate of trap photons which, even for a near-detuned trap, will be under 10 kHz. Differential light-shifts arise from variance in the Clebsch-Gordan coefficients, and hence coupling strength, between the $m_F \rightarrow m'_F$ manifold in the trapping transition. As a result, atoms in the $2n + 1$ different Zeeman sub-states experience different trap depths, the overlap of which produces a broader spectrum. A more appropriate fit function would be the product of $2n + 1$ separate transmission spectra with U_0 , α , and \mathcal{D}_{opt} for each spectrum appropriately weighted by the relative transition strengths. For the data presented here the differential light shifts are small relative to the total trap depth, and the result is broadening of the Lorentzian component. In a sense this is a useful measure of the real dephasing due to the presence of the dipole trap.

6. Discussion

When comparing the fitted theoretical curves to experimental data, it is clear that the Gaussian distribution model is a much better description of the underlying atomic profile for the two cases analysed. This agrees with the statistical mechanics analysis of population in a harmonic potential. One of the key reasons this approximation works so well is that the light-atom interaction scales with the local probe intensity, and as

such the measurable behaviour is dominated by close-to-axis atoms, where the Gaussian dipole trap is well approximated by a parabola.

While the ring-like distribution is capable of broadly matching the depth, location, and width of the absorption feature, it is incapable of producing the observed asymmetric shape. This is also seen in the best-fit parameters and their uncertainties: the fitting process has forced the linewidth to be large and α to be very small in an attempt to match the observed spectrum. The reason our ring-like model does not well match reality is likely in our constraint of circular motion. While this assumption is intuitively reasonable and permits a closed form expression to be found for $f_{P, \text{Ring}(\rho)}$ to be found, it confines the energy of the system entirely to one degree of freedom in cylindrical coordinates. This results in a highly non-thermalised system that does not well match a well mixed system, such as would be found in a cold atom ensemble. The use of both atom distribution models show that not only is the Gaussian model a good description of the atomic ensemble, but also that the spectroscopic technique is sensitive enough to the underlying distribution to discriminate between distributions.

The power of this technique lies in its ability to make single-shot measurements of the physical state of a trapped atomic system without having to modulate the trap, as is typically required. As such, this technique could be used to make continuous measurements of an atomic system over the course of an experimental run. Alternatively one could make a single calibration measurement each run before performing the desired experimental protocol. In addition to its versatility, our technique's use of the potential of the trap itself to map distribution into frequency removes the need to know any theoretical values for the light-atom interaction strength, or experimental quantities such as trap laser power.

7. Conclusion

We have developed a technique that uses the spatially varying light-shift inherent to a dipole trap as a means to perform spectroscopy on the trapped atomic ensemble. The trap itself provides the perfect reference, mapping the radial location of each atom into a unique frequency shift. Using an understanding of the shape of the dipole trap and the resulting spatial distribution of atoms, we produce a testable model of the light-shift broadened atomic absorption spectrum. This technique is able to rapidly infer the number of atoms, temperature of the ensemble, depth of trap, and transition linewidth, with a high level of independence between each of the experimental parameters.

We experimentally test this technique using a hollow-core fibre loaded cold-atom ensemble and are able to take a single-shot snapshot of the light-shift broadened spectrum. Fitting to this data with two models for the distribution of atoms in a radial trapping field we find strong agreement with the Gaussian distribution model, and are able to extract the relevant physical parameters from the shape of the measured spectrum.

We hope this analysis provides insight into the dynamics of a trapped atomic

system, and expect our interrogation scheme to be instrumental in acquiring rapid feedback on the parameters of state of cold atom systems that would otherwise require slow and repetitive interrogation sequences over many experimental cycles.

Acknowledgments

We would like to thank the South Australian government for supporting this research through the PRIF program.

This research was funded by the Australian government through the Australian Research Council (Project: DE12012028).

Appendix A. Calculation of radial probability density function

To find the likelihood of finding an atom at a radius ρ , we use the Boltzmann factor to calculate the probability of a state with energy $E = U_d(\mathbf{r})$ being occupied. Using the radial dependent trap depth to define the energy of the state, the atomic density is found to be

$$\begin{aligned} n(\rho) &\propto \exp(-U_d(\rho)/k_B T) \\ &\propto \exp\left(\frac{U_0}{k_B T} \exp(-2\rho^2/w^2)\right) \end{aligned} \quad (\text{A.1})$$

where k_B is the Boltzmann constant, and T is the ensemble temperature.

This is simplified to a useful form by assuming that the atoms remain close to the central axis, and as such the potential can be assumed to be harmonic. Taking a power series to second order in the radius, we find a Gaussian distribution centred on axis with the form

$$n(\rho) \propto \exp\left(\alpha - \frac{2\alpha\rho^2}{w^2}\right), \quad (\text{A.2})$$

where we have introduced the parameter $\alpha = -U_0/(k_B T)$ as the magnitude of the trap depth relative to the thermal energy of the ensemble.

Integrating $n(\mathbf{r})$ and using Equation 3 we calculate the normalised PDF

$$f_P(\rho) = \frac{4\alpha\rho}{w^2} \exp\left(\frac{-2\alpha\rho^2}{w^2}\right) \quad (\text{A.3})$$

which integrates to unity over $0 \leq \rho < \infty$.

Appendix B. Ring-like atomic distribution

To generate a ring-like atomic distribution we begin by simplifying the atomic motion by considering only trajectories that have constant radius. This is helpful in two ways: it allows us to include the full Gaussian form of the potential and removes the need to perform spatial integration over the atomic trajectory for all choices of ellipticity.

The equation of motion for a circular orbit is trivial, and is given by

$$-\mathbf{a} \cdot \boldsymbol{\rho} = v_{\perp}^2 \quad (\text{B.1})$$

where v_{\perp} is the speed perpendicular to $\boldsymbol{\rho}$, which is simply the magnitude of the total velocity in the transverse plane due to our choice of trajectory. Similarly, $\mathbf{a} = a_{\rho} \hat{\boldsymbol{\rho}}$ is the radial acceleration due to the trap potential, which for a particle with mass m can be calculated as a function of radius as

$$\begin{aligned} a_{\rho}(\rho) &= \frac{1}{m} \cdot \frac{-dU_d(\rho)}{d\rho} \\ &= \frac{4\rho U_0}{mw^2} \exp\left(\frac{-2\rho^2}{w^2}\right). \end{aligned} \quad (\text{B.2})$$

We calculate the kinetic energy of the trajectory, ϵ , using

$$\epsilon(\rho) = \frac{1}{2}mv^2 = \frac{-2\rho^2 U_0}{w^2} \exp\left(\frac{-2\rho^2}{w^2}\right) \quad (\text{B.3})$$

in which we have assume the axial component is negligible. Assuming the atomic ensemble is in thermal equilibrium, we can describe the energy distribution in the system using a Maxwell-Boltzmann distribution:

$$f_E(\epsilon) = 2\sqrt{\frac{\epsilon}{\pi}} \left(\frac{1}{k_B T}\right)^{3/2} \exp\left(\frac{-\epsilon}{k_B T}\right). \quad (\text{B.4})$$

By implementing a change of variables as in Equation 12, we can generate the radial distribution of atoms for the ring-like model using Equation B.3

$$\begin{aligned} f_{P, \text{Ring}}(\rho) &= \left| \frac{d\epsilon(\rho)}{d\rho} \right| \cdot f_E(\epsilon(\rho)) \\ &= 8\sqrt{\frac{2\alpha^3}{\pi}} \frac{\rho^2}{w^3} \left| 1 - 2\frac{\rho^2}{w^2} \right| \exp\left(-\frac{\rho^2}{w^2} \left[3 + 2\alpha \exp\left(-\frac{2\rho^2}{w^2}\right) \right]\right) \end{aligned} \quad (\text{B.5})$$

where again we have introduced the substitution $\alpha = -U_0/k_B T$.

It should be noted that for a Gaussian beam the trap depth $U_d(\rho)$ is deepest at $\rho = 0$ and monotonic in ρ , while the orbital energy $\epsilon(\rho)$ is zero at $\rho = 0$, and has a maximum at $\rho = w/\sqrt{2}$. From this we can infer that we expect to find two distinct circular orbits for each possible value of the kinetic energy: one for $0 \leq \rho < w/\sqrt{2}$, and one for $\rho > w/\sqrt{2}$. The set of solutions with large ρ represent trajectories with orbital energy is greater than the trap depth. While these are still valid solutions to the equations of motion, the orbits are unstable and an infinitesimal increase in velocity will free the atoms from the trap. To produce a physically realistic model we truncate the radial distribution at $\rho = w/\sqrt{2}$, choosing only to count stable orbits.

While the ring-like model radial distribution $f_{P, \text{Ring}}(\rho)$ integrates to unity over the bounds $0 \leq \rho \leq w/\sqrt{2}$ for large α , for small α this is not the case. In our model there is a maximum orbital energy that can maintain a circular orbit. For small α there is a non-zero fraction of the Maxwell-Boltzmann distribution that that has energy greater than this upper bound. Our use of the change of variables intrinsically includes this

overlap issue, and the resulting integral $\int_0^{w/\sqrt{2}} f_{P, \text{Ring}}(\rho) d\rho$ produces the fraction of the energy distribution that is capable of being trapped.

While this useful information, for our purposes we scale the radial distribution by its numerically calculated integral in order to produce an atomic distribution function that is relative to the fraction of a thermal cloud with temperature T that is successfully trapped. This is considered in the fit model used in section 5.

References

- [1] Mark Kasevich and Steven Chu. Atomic interferometry using stimulated Raman transitions. *Physical Review Letters*, 67(2):181–184, jul 1991.
- [2] A Peters, K Y Chung, and S Chu. High-precision gravity measurements using atom interferometry. *Metrologia*, 38(1):25–61, feb 2001.
- [3] B. Canuel, F. Leduc, D. Holleville, A. Gauguet, J. Fils, A. Viridis, A. Clairon, N. Dimarcq, Ch J. Bordé, A. Landragin, and P. Bouyer. Six-axis inertial sensor using cold-atom interferometry. *Physical Review Letters*, 97(1):1–4, 2006.
- [4] Alexander D. Cronin, Jörg Schmiedmayer, and David E. Pritchard. Optics and interferometry with atoms and molecules. *Reviews of Modern Physics*, 81(3):1051–1129, jul 2009.
- [5] J. K. Stockton, K. Takase, and M. A. Kasevich. Absolute Geodetic Rotation Measurement Using Atom Interferometry. *Physical Review Letters*, 107(13):133001, sep 2011.
- [6] N. Hinkley, J. A. Sherman, N. B. Phillips, M. Schioppo, N. D. Lemke, K. Beloy, M. Pizzocaro, C. W. Oates, and A. D. Ludlow. An Atomic Clock with 10-18 Instability. *Science*, 341(6151):1215–1218, sep 2013.
- [7] P. A. Altin, M. T. Johnsson, V. Negnevitsky, G. R. Dennis, R. P. Anderson, J. E. Debs, S. S. Szigeti, K. S. Hardman, S. Bennetts, G. D. McDonald, L. D. Turner, J. D. Close, and N. P. Robins. Precision atomic gravimeter based on Bragg diffraction. *New Journal of Physics*, 15(2):023009, feb 2013.
- [8] I. Dutta, D. Savoie, B. Fang, B. Venon, C. L. Garrido Alzar, R. Geiger, and A. Landragin. Continuous Cold-Atom Inertial Sensor with 1 nrad / sec Rotation Stability. *Physical Review Letters*, 116(18):183003, may 2016.
- [9] B. M. Sparkes, J. Bernu, M. Hosseini, J. Geng, Q. Glorieux, P. A. Altin, P. K. Lam, N. P. Robins, and B. C. Buchler. Gradient echo memory in an ultra-high optical depth cold atomic ensemble. *New Journal of Physics*, 15(8):085027, aug 2013.
- [10] Zi-Yu Liu, Yi-Hsin Chen, Yen-Chun Chen, Hsiang-Yu Lo, Pin-Ju Tsai, Ite A. Yu, Ying-Cheng Chen, and Yong-Fan Chen. Large Cross-Phase Modulations at the Few-Photon Level. *Physical Review Letters*, 117(20):203601, nov 2016.
- [11] A. J. F. de Almeida, M.-A. Maynard, C Banerjee, D Felinto, F Goldfarb, and J W R Tabosa. Nonvolatile optical memory via recoil-induced resonance in a pure two-level system. *Physical Review A*, 94(6):063834, dec 2016.
- [12] Kwang-Kyoon Park, Young-Wook Cho, Young-Tak Chough, and Yoon-Ho Kim. Experimental Demonstration of Quantum Stationary Light Pulses in an Atomic Ensemble. *Physical Review X*, 8(2):021016, 2018.
- [13] Ya-Fen Hsiao, Pin-Ju Tsai, Hung-Shiue Chen, Sheng-Xiang Lin, Chih-Chiao Hung, Chih-Hsi Lee, Yi-Hsin Chen, Yong-Fan Chen, Ite A Yu, and Ying-Cheng Chen. Highly Efficient Coherent Optical Memory Based on Electromagnetically Induced Transparency. *Physical Review Letters*, 120(18):183602, may 2018.
- [14] Hidetoshi Katori, Masao Takamoto, V. G. Pal’chikov, and V. D. Ovsianikov. Ultrastable Optical Clock with Neutral Atoms in an Engineered Light Shift Trap. *Physical Review Letters*, 91(17):173005, oct 2003.
- [15] Masao Takamoto, Feng-Lei Hong, Ryoichi Higashi, and Hidetoshi Katori. An optical lattice clock. *Nature*, 435(7040):321–324, may 2005.
- [16] J Ye, H J Kimble, and H Katori. Quantum State Engineering and Precision Metrology Using State-Insensitive Light Traps. *Science*, 320(5884):1734–1738, jun 2008.
- [17] B. J. Bloom, T. L. Nicholson, J. R. Williams, S. L. Campbell, M. Bishof, X. Zhang, W. Zhang, S. L. Bromley, and J. Ye. An optical lattice clock with accuracy and stability at the 10¹⁸ level. *Nature*, 506(7486):71–75, feb 2014.
- [18] J. Huang, S. Wu, H. Zhong, and C. Lee. *QUANTUM METROLOGY WITH COLD ATOMS*, chapter 7, pages 365–415. World Scientific, 2014.

- [19] Xibo Zhang and Jun Ye. Precision measurement and frequency metrology with ultracold atoms. *National Science Review*, 3(2):189–200, 2016.
- [20] R. Le Targat, L. Lorini, Y. Le Coq, M. Zawada, J. Guéna, M. Abgrall, M. Gurov, P. Rosenbusch, D. G. Rovera, B. Nagórny, R. Gartman, P. G. Westergaard, M. E. Tobar, M. Lours, G. Santarelli, A. Clairon, S. Bize, P. Laurent, P. Lemonde, and J. Lodewyck. Experimental realization of an optical second with strontium lattice clocks. *Nature Communications*, 4(1):2109, dec 2013.
- [21] Christian Gross and Immanuel Bloch. Quantum simulations with ultracold atoms in optical lattices. *Science*, 357(6355):995–1001, sep 2017.
- [22] S. Vorrath, S. A. Möller, P. Windpassinger, K. Bongs, and K. Sengstock. Efficient guiding of cold atoms through a photonic band gap fiber. *New Journal of Physics*, 12:123015, 2010.
- [23] M. Bajcsy, S. Hofferberth, T. Peyronel, V. Balic, Q. Liang, a. S. Zibrov, V. Vuletic, and M. D. Lukin. Laser-cooled atoms inside a hollow-core photonic-crystal fiber. *Physical Review A - Atomic, Molecular, and Optical Physics*, 83(6):1–9, 2011.
- [24] Shoichi Okaba, Tetsushi Takano, Fetah Benabid, Tom Bradley, Luca Vincetti, Zakhar Maizelis, Valery Yampol'skii, Franco Nori, and Hidetoshi Katori. Lamb-Dicke spectroscopy of atoms in a hollow-core photonic crystal fibre. *Nature Communications*, 5:4096, jun 2014.
- [25] Frank Blatt, Lachezar S. Simeonov, Thomas Halfmann, and Thorsten Peters. Stationary light pulses and narrowband light storage in a laser-cooled ensemble loaded into a hollow-core fiber. *Physical Review A*, 94(4):043833, oct 2016.
- [26] Mingjie Xin, Wui Seng Leong, Zilong Chen, and Shau-Yu Lan. An atom interferometer inside a hollow-core photonic crystal fiber. *Science Advances*, 4(1):e1701723, jan 2018.
- [27] A.P. Hilton, C. Perrella, F. Benabid, B.M. Sparkes, A.N. Luiten, and P.S. Light. High-efficiency cold-atom transport into a waveguide trap. *Physical Review Applied*, 10(4):044034, 2018.
- [28] Maria Langbecker, Ronja Wirtz, Fabian Knoch, Mohammad Noaman, Thomas Speck, and Patrick Windpassinger. Highly controlled optical transport of cold atoms into a hollow-core fiber. *New Journal of Physics*, 20(8):083038, aug 2018.
- [29] Taehyun Yoon and Michal Bajcsy. Laser-cooled cesium atoms confined with a magic-wavelength dipole trap inside a hollow-core photonic-bandgap fiber. *Physical Review A*, 99(2):023415, feb 2019.
- [30] A P Chikkatur. A Continuous Source of Bose-Einstein Condensed Atoms. *Science*, 296(5576):2193–2195, jun 2002.
- [31] A. E. Leanhardt, A. P. Chikkatur, D. Kielpinski, Y. Shin, T. L. Gustavson, W. Ketterle, and D. E. Pritchard. Propagation of Bose-Einstein Condensates in a Magnetic Waveguide. *Physical Review Letters*, 89(4):040401, jul 2002.
- [32] A. E. Leanhardt, A. Görlitz, A. P. Chikkatur, D. Kielpinski, Y. Shin, D. E. Pritchard, and W. Ketterle. Imprinting Vortices in a Bose-Einstein Condensate using Topological Phases. *Physical Review Letters*, 89(19):190403, oct 2002.
- [33] A E Leanhardt. Cooling Bose-Einstein Condensates Below 500 Picokelvin. *Science*, 301(5639):1513–1515, sep 2003.
- [34] W. Ketterle, D. S. Durfee, and D. M. Stamper-Kurn. Making, probing and understanding Bose-Einstein condensates. In *Proceedings of the International School of Physics "Enrico Fermi"*, volume 140, pages 67–176, 1999.
- [35] Thibault Peyronel, Michal Bajcsy, Sebastian Hofferberth, Vlatko Balic, Mohammad Hafezi, Qiyu Liang, Alexander Zibrov, Vladan Vuletic, and Mikhail D. Lukin. Switching and counting with atomic vapors in photonic-crystal fibers. *IEEE Journal on Selected Topics in Quantum Electronics*, 18(6):1747–1753, 2012.
- [36] F. Blatt, T. Halfmann, and T. Peters. One-dimensional ultracold medium of extreme optical depth. *Optics Letters*, 39(3):446, 2014.
- [37] Roman Sulzbach, Thorsten Peters, and Reinhold Walser. Optimal pulse propagation in an inhomogeneously gas-filled hollow-core fiber. *Physical Review A*, 100(1):013847, 2019.
- [38] H. Häffner, S. Gulde, M. Riebe, G. Lancaster, C. Becher, J. Eschner, F. Schmidt-Kaler, and

- R. Blatt. Precision Measurement and Compensation of Optical Stark Shifts for an Ion-Trap Quantum Processor. *Physical Review Letters*, 90(14):143602, apr 2003.
- [39] Tao Hong, Claire Cramer, Warren Nagourney, and E. N. Fortson. Optical Clocks Based on Ultranarrow Three-Photon Resonances in Alkaline Earth Atoms. *Physical Review Letters*, 94(5):050801, feb 2005.
- [40] Robin Santra, Ennio Arimondo, Tetsuya Ido, Chris H. Greene, and Jun Ye. High-Accuracy Optical Clock via Three-Level Coherence in Neutral Bosonic ^{88}Sr . *Physical Review Letters*, 94(17):173002, may 2005.
- [41] Rudolf Grimm, Matthias Weidemüller, and Yurii B. Ovchinnikov. Optical Dipole Traps for Neutral Atoms. *Adv. At. Mol. Opt. Phys.*, 42:95–170, 2000.

OPTIMAL DESIGN FOR SPECTRAL NARROWING AND FAST
FREQUENCY SWEEP OF AN INTERFEROMETER-STABILIZED
LASER

Statement of authorship

Title of publication

Optimal design for spectral narrowing and fast frequency sweep of an interferometer-stabilized laser

Authors

Ashby P. Hilton,¹ Philip S. Light,¹ Lauris Talbot,² and Andre N. Luiten¹.

¹*Institute for Photonics and Advanced Sensing and School of Physical Sciences, The University of Adelaide, Adelaide, South Australia 5005, Australia*

²*Centre d'Optique, Photonique et Laser, Université Laval, Québec, QC, G1V 0A6, Canada.*

Publication details

This work is a research article published in the Optical Society peer-reviewed journal *Optics Letters*, volume 45, issue 1, January 2020 with page number 45 and DOI: [10.1364/OL.45.000045](https://doi.org/10.1364/OL.45.000045).

Context

This publication is the result of work done on an adjacent project, the goal of which is to measure the Boltzmann constant with extreme precision using direct optical spectroscopy of a Doppler-broadened atomic vapour [118]. This project is in the process of being revived, with the goal of overcoming the previous limitations to achieve part-per-million or better absolute measurements of temperature.

The major limitations to the previous results attained by *Truong et al.* were the spectral width of the interrogation laser, and the limited range of the frequency axis over which spectra could be measured. To address these issues, Prof. Luiten and Dr. Light decided to implement a new laser-locking scheme based on an unbalanced fibre-delay-line Michelson interferometer as a frequency discriminator. This technique has been demonstrated in the past (by Jiang *et al.* for example [50]) and allows for both extreme tunability and high levels of suppression of laser frequency-noise.

I was involved early on in the project to assist with building the locking electronics and optimisation of the performance of the stabilisation system. As the project developed, we realised that the fibre-interferometer lock allowed for extremely high slew rates of the laser – much greater than other published results for similar systems. While investigating the performance limitations to the stabilisation system we found a relationship between the length of the fibre delay-line and ultimate performance of the scheme.

Further development of this idea, as well as optimisation of the experimental system, lead to the writing of this manuscript in which we demonstrate that an effective choice of fibre delay-line length can be used to significantly improve the performance of both the frequency noise suppression and frequency sweep rate.

In addition to this work, a second paper further developing this technique to achieve rapid and agile tuning of lasers while retaining the frequency-noise suppression granted by the fibre interferometer is in the process of being submitted.

Contribution to the paper

This project was conceptualised and designed by Prof. Luiten and Dr. Light.

The experimental apparatus was developed by Dr. Light and myself. My contribution

included design and implementation of electronic systems for high-speed, low-noise stabilisation of the laser, troubleshooting the device, and identifying limiting noise floors.

The optical frequency comb comparisons were implemented by myself and Dr. Light, and I had significant involvement in the stabilisation of the high-finesse Fabry-Pérot optical cavity that is used as an optical reference for the comb.

Collection and analysis of the experimental results was done jointly by myself and Dr. Light.

The theoretical model of the stabilised laser performance was developed by myself, with the inclusion of the fibre delay-line length as a parameter to optimise over.

The optimisation of the laser frequency sweep and its measurement and analysis was done by myself with supervision by Dr. Light.

Mr. Talbot was involved in the construction of the apparatus, testing, and collection of data as the research component of an undergraduate exchange program.

The manuscript was written primarily by myself, with comments and correction provided by all co-authors.

Overall percentage contribution

50%

Certification

This paper reports on original research I conducted during the period of my Higher Degree by Research candidature and is not subject to any obligations or contractual agreements with a third party that would constrain its inclusion in this thesis. I am the primary author of this paper.

Signed

Ashby Hilton

_____, Date: 29 / 10 / 19

Co-Author Acknowledgement

By signing the Statement of Authorship, each author certifies that:

- i. the candidate's stated contribution to the publication is accurate; and
- ii. permission is granted for the candidate to include the publication in the thesis;

Signed _____, Date: 2 / 1 / 20
Dr. Philip Light

Signed: _____, Date: 11 / 11 / 19
Mr. Lauris Talbot

Signed: _____, Date: 2 / 1 / 20

LIBRARY NOTE:

**The following article (pages
196-199) has been removed due to copyright.**

**Ashby P. Hilton, Philip S. Light, Lauris Talbot, and Andre N.
Luiten, "Optimal design for spectral narrowing and fast
frequency sweep of an interferometer-stabilized laser,"
Opt. Lett. 45, 45-48 (2020)**

It is also available online to authorised users at:
<https://doi.org/10.1364/OL.45.000045>

Part IV

Conclusion and Outlook

CONCLUSION AND FUTURE WORK

This project was focused around the development of a platform for the laser cooling, trapping, and loading of rubidium atoms into a specialised hollow-core photonic crystal fibre. Considerable work was done in the construction of robust laser-frequency stabilisation systems, implementation of sophisticated atomic interrogation protocols, and creation of a detailed Monte-Carlo model of the atom loading process. Along the way opportunities arose to investigate novel methods of manipulating the energy levels of trapped atoms through their interaction with far-detuned optical fields – a technique known as light-shift engineering.

This project however is not over, and in many ways the system and techniques that were built over the course of this work are only the beginning. Here I provide a short summary of the content of this thesis and outline the first steps that have been taken towards using this platform to perform cutting-edge physics experiments.

10.1 Summary

Over course of this work the experimental apparatus has been dismantled and rebuilt many times over as our understanding and needs have developed. In its current iteration the system is capable of performing experiments on an ensemble of 10^6 cold rubidium atoms confined inside the kagome-lattice fibre.

Continued development of the computer oversight for the experiment has resulted in a sophisticated and interconnected system capable of controlling (nearly) every aspect of the apparatus. Not only does this allow the user to remotely change parameters and perform experimental runs, but also allows for dynamic control during operation as well as machine-learning optimisation. This has been used to perform tasks such as drift detection and relocking of the guide laser during long data collection runs. In addition, these systems have enabled the development of complex interrogation pulse sequences and on-the fly data processing and that have been used to perform optimisation over any and all experimental parameters.

We have implemented laser frequency stabilisation systems that utilise a range of laser-locking techniques based on their individual needs. These systems are capable of staying locked for days on end, and the transition to rack-mounted storage of the [ECDLs](#) lasers and fibre-coupling optics has allowed for unhindered manual work on the table. This has been a dramatic improvement to the quality of life in the lab. In addition, the low-noise analog lock boxes developed for the project have found use in many other precision metrology experiments in the group.

We have developed broadband spectroscopy techniques capable of acquiring an entire transmission spectrum on each run of the experiment. This has allowed us to extract the optical depth and group velocity of the atomic ensemble in a single measurement, opening up the ability to take large data sets over multiple experimental parameters in realistic time frames. In addition, the development of sophisticated and fast data processing software has enabled us to operate in real time, extracting a value for the [OD](#) from each run before the next run begins.

A detailed Monte-Carlo model of the atom loading system was developed to improve our understand of the atom-loading process. This model includes the shape of the trapping potential and uses the wavelength and power of the guide to include photon-scattering and dipole-trapping effects. The validity of the model has been rigorously tested against the experiment over a wide range of guide wavelengths and detunings, providing confidence in its predictive power. This is a powerful tool for investigating atomic dynamics that are otherwise difficult to predict.

Using the experimental system we have been able to successfully load a large number of cold atoms into the kagome-lattice fibre. With the combination of computer-controlled

optimisation software and the Monte-Carlo model we have achieved extremely high optical depths despite the relatively large core diameter of the fibre. Analysis of the atomic lifetime inside the fibre shows that we retain a large number of atoms for tens of milliseconds. These results have been published as *High-efficiency cold-atom transport into a waveguide trap* in the peer reviewed journal *Physical Review Applied*.

We have investigated the strong and asymmetric broadening of the atom transition by the AC-Stark shift of the guide beam. In typical operation we use fast, interleaved modulation of the probe and guide fields to avoid this broadening, however we have also showed that the effect of the guide can be mitigated by the introduction of an additional laser field. We have shown that by carefully tuning the wavelength of this additional laser field we can compensate for the spectral broadening of the guide, operating in a two-colour equivalent of the magic-wavelength traps used in atomic lattice clocks. This is the first demonstration of the technique, and these results have been published as *Dual-Color Magic-Wavelength Trap for Suppression of Light Shifts in Atoms* in the peer-reviewed journal *Physical Review Applied*.

Following this work on light-shift engineering we investigated the relationship between the atomic distribution inside a one-dimensional optical trap and the AC-Stark shift the atoms experience. We found that the spatially-varying light shift induced by the dipole trap can be used to map the atomic distribution into a frequency-shifted absorption spectrum. We developed a model that predicts the measurable absorption spectrum for a given atomic distribution, and by testing these models against our data we showed an excellent agreement with one of the two models. Using this technique we were able to extract a range of useful experimental values for the dipole trap and the atomic ensemble from a single, minimally destructive measurement. These results have received positive feedback and are currently awaiting final peer review for publication as *Light-shift spectroscopy of optically trapped atomic ensembles* in the peer-reviewed journal *New Journal of Physics*.

Included in this thesis is a publication from a tangential project on laser stabilisation and dynamic frequency sweeping using a self-heterodyne fibre interferometer. This work was born from the need to narrow the linewidth of an [ECDL](#) while retaining the ability to arbitrarily tune its frequency. The eventual use of this platform is to perform highly accurate measurements of temperature using Doppler-broadened thermometry of caesium vapour. These results have been published as *Optimal design for spectral narrowing and fast frequency sweep of an interferometer-stabilized laser* in the peer-reviewed journal

Optics Letters.

In the following section I describe the path forward for the experiment, including preliminary results that have been acquired in these directions.

10.2 Future Work

Some of the potential applications of cold-atom filled hollow-core fibre platforms have been described in detail in [chapter 2](#). A long-term goal for this project has been to replace the red-detuned attractive guide with a blue-detuned repulsive hollow guide. This could be used to extend the ground-state coherence time of the atomic ensemble by minimising the spatial overlap of the trapping field and the atoms. When combined with the extremely strong light-atom interaction demonstrated previously the resulting platform would be a powerful tool for implementing long-lived coherent storage of optical pulses for quantum information processing. Here I give a brief overview of the preliminary work in this direction.

10.2.1 Hollow-Mode Optical Guide

One of the key decisions behind the use of a relatively large core 45 μm kagome-lattice fibre was its ability to support higher-order optical modes, in particular the hollow LG_{01} -like mode. Although all the work on atom loading presented here has used an attractive guide coupled to the fundamental Gaussian mode, preliminary work has been done on using the hollow mode to trap and guide atoms into the fibre. This is of particular interest to the field as the motion of atoms across the fibre core during interrogation has been shown to be the limiting factor to the lifetime of coherently-stored optical pulses using this technology [16].

To move from an attractive to a repulsive trap the SolsTiS laser is tuned from 1 THz red of the D_1 transition to 200 GHz blue of the D_2 . The hollow mode is generated using a vortex half-wave retarder (*Thorlabs* WPV10L-780). This specific optic is required to produce not only the ring-shaped intensity, but also the cylindrical vector polarisation mode that is supported by the fibre, shown in [Figure 10.1 a](#)). The introduction of this optic into the beam path produces only a minimal change in divergence and very little beam steering. This combined with the ease of tuning the guide laser wavelength makes switching back and forth between the two methods both fast and repeatable.

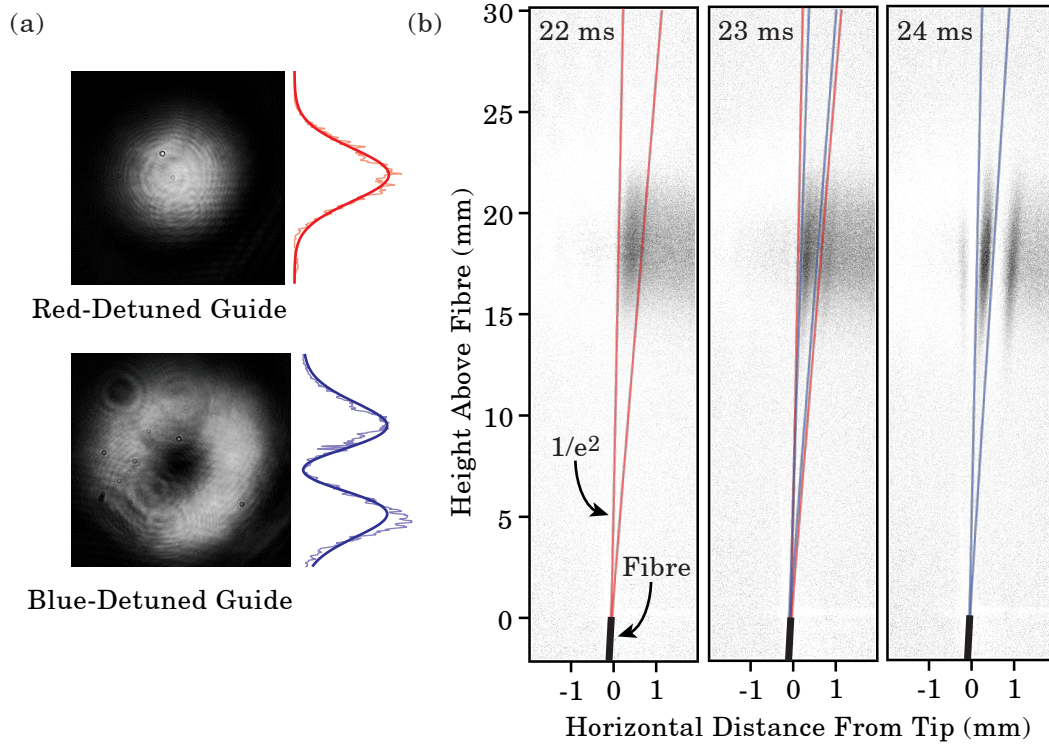


Figure 10.1: Demonstration of hollow-mode guidance of atoms with a) the intensity profiles of the red Gaussian and blue hollow modes and b) shadow imaging showing the transfer of atoms from the attractive guide (red overlay) into the repulsive guide (blue overlay).

Initial attempts to directly load atoms from the MOT into the fibre with the hollow guide failed, with atoms visibly bouncing off the tip of the fibre. Subsequent simulations using the Monte-Carlo model confirmed this behaviour as actually being a predictable effect due to the higher than expected ensemble temperature of the atoms (for these experiments) and the sharp gradient of the potential in the vertical direction. This acts as barrier for any atoms not directly on axis, and if the height of the barrier is greater than the initial gravitational potential energy of the atoms then they experience an elastic reflection from potential, returning to the original height of the MOT. Reducing the potential of the barrier results in a proportional reduction in transverse trap depth, and due to the temperature of the atom cloud it has not been possible to capture atoms transversely while also guiding them vertically into the fibre. Experimental work is ongoing to attempt to solve these issues.

To test the effectiveness of the blue-detuned guide to confine atoms once they are inside the fibre we implement a second dipole trap using the conventional red-detuned

attractive potential. This trap is generated by an amplified [ECDL](#) coarsely tuned several hundred gigahertz red of the D_2 transition. The attractive dipole trap beam is combined with probe beam in free space with a 50 : 50 [NPBS](#) and coupled into the kagome-lattice fibre from below. By implementing an additional fast optical switch we are able to use this attractive guide to collect and couple atoms into the fibre as usual before switching to the repulsive hollow guide with a short 10 μ s handover period.

When this technique is performed in free space above the fibre we see an efficient transfer from one potential to the other, as shown in [Figure 10.1 b](#)). Atoms outside the walls of the ring-like potential are forced strongly away from the beam, while those inside the walls are further compressed. This is an extremely hopeful result, showing that the hollow-mode guide is capable of capturing atoms after having passed through the kagome-lattice fibre.

When this handover process is performed after the falling atomic ensemble has entered the fibre we expect a similarly efficient transfer of atoms from one potential to the other. However, [EIT](#) spectroscopy taken at various time steps through the process reveal a different outcome. The results, shown in [Figure 10.2](#), show that the majority of the atoms in the fibre are lost during the handover. Although the cause of this has not yet been identified, we see that the atoms that survive the handover process remain trapped inside the ring-like potential 2 ms later. This confirms that the shape of the potential within the fibre forms a fully closed ring as the time between these two measurements is large relative to the orbital period.

The path forward to achieving direct hollow-mode guidance of atoms into the kagome-lattice fibre lies in either a reduction in the temperature of the atom cloud, or translation of the [MOT](#) location closer to the fibre tip. Both of these options result in an increase in depth of the dipole trap relative to the temperature of the ensemble, which would in turn allow the dipole trap to be reduced in strength as required to couple into the fibre. As the temperature of the [MOT](#) is already as low as 5 μ K, I suspect that translation of the trap location will provide an easier way forwards in this regard. We have confirmed using the Monte-Carlo simulation that both approaches will yield a significant increase in the number of atoms trapped using this technique. This work is still under active investigation by the next generation of PhD students.

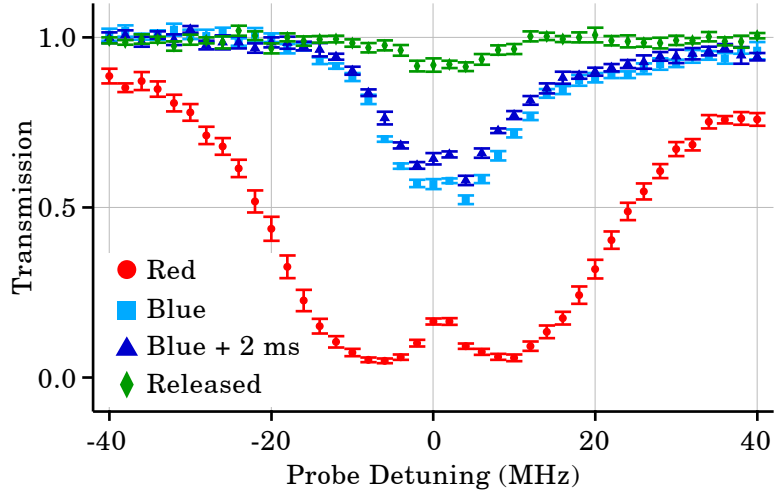


Figure 10.2: Transmission spectra of the atomic ensemble as it is transferred from one potential to the other while inside the fibre. Many atoms are lost during the handover, however a small fraction survives. The loss of atoms in the blue guide over the next 2 ms is minimal, showing a fully closed potential. When the guide is switched off there is only a very weak residual absorption from atoms that bounced off the fibre tip and still exist above the fibre.

10.2.2 Raman EIT Coherent Phenomena

Although probing a two-level atomic transition is an effective method for measurement of the interaction strength of the medium, a Raman three-level system provides access to more interesting physical phenomena. Towards this end we have implemented the probe and control fields necessary to perform EIT experiments on the D_1 line. In particular this system allows for the direct measurement of the dephasing rates of the ground states, which in turn provides information regarding the decoherence effects of the fibre confinement on the atomic sample. Ideally this could be used to demonstrate the advantage of the hollow guide in extending the coherence time of the atomic medium.

Our first measurements in this direction involve probing the $|F = 2, mF\rangle \rightarrow |F' = 3, mF' = mF + 1\rangle$ manifold using σ_+ polarised light, with the control field on the $|F = 3, mF\rangle \rightarrow |F' = 3, mF' = mF + 1\rangle$ manifold. This forms a set of five single-photon absorptions and EIT windows that are degenerate under zero external fields. Any DC magnetic field will however lift the degeneracy, separating the atomic transitions and broadening the expected narrow transmission feature.

Stepping the probe field across the atomic transition as in Figure 10.3 shows both

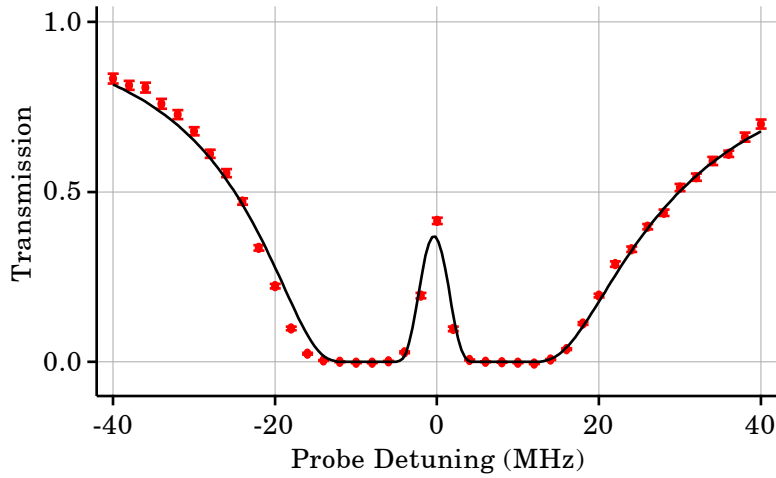


Figure 10.3: An EIT measurement of the $|F = 2, mF = +2\rangle \rightarrow |F' = 3, mF' = 3\rangle$ made with low optical power and 100 averages (red circles) along with a theoretical fit with the functional form given in [57] (black, bold).

the broad single-photon absorption as well as a narrow increase in transmission centred around the detuning of the control field, which in this case is zero. Reducing the optical depth of the ensemble such that the transmission window is clearly distinguishable allows for fitting to the spectrum with an appropriate model of the system. Here we use a reduced two-field model adapted from [33]

$$T = \exp(-(OD + \alpha\Delta_p) \text{Im}[\chi]) \quad (10.1)$$

where χ is the complex susceptibility given by

$$\chi = i\Gamma_e \left(\Gamma_e - 2i\Delta_p + \frac{|\Omega_c|^2}{\Gamma_g - 2i(\Delta_c - \Delta_p)} \right)^{-1} \quad (10.2)$$

where Γ_g and Γ_e are the decay rate of the excited state and the dephasing rate between ground states, Δ_p and Δ_c are the single-photon angular-frequency detunings of the probe and control fields, and Ω_c is the Rabi frequency of the control field. The term $\alpha\Delta_p$ is included to accommodate for a small decrease in atom number from pulse to pulse over the interrogation sequence, and Γ_e is fixed at $2\pi \cdot 5.75$ MHz.

The data shown consists of 100 experimental runs with error bars given by the standard error in the mean for detuning value. Here the optical power used in the probe is only 300 pW. The fit parameters with their uncertainties are given in Table 10.1. The value found for the ground-state dephasing of $2\pi \cdot 0.8(1)$ MHz is significantly smaller

| OD | α (Γ_e^{-1}) | $2\pi \cdot \Gamma_g$ (MHz) | $2\pi \cdot \Gamma_e$ (MHz) | $2\pi \cdot \Delta_c$ (MHz) | $2\pi \cdot \Omega_c$ (MHz) |
|-------|------------------------------|-----------------------------|-----------------------------|-----------------------------|-----------------------------|
| 53(1) | 0.045(4) | 0.8(1) | 5.75 | 0.4(2) | 15.4(6) |

Table 10.1: Fit parameters to the EIT spectrum shown in Figure 10.3.

than the excited state decay rate, which is a promising start. Further exploration of the sensitivity of the dephasing rate to other experimental parameters will be necessary. In particular it is expected that both DC offsets in the magnetic field and magnetic field gradients along the fibre axis will strongly determine the dephasing rate. As such, plans for the immediate future include the implementation of two-stage μ -metal shielding around the fibre to minimise the effects of low-frequency external magnetic fields.

In addition to measuring the Raman-EIT spectrum we have made a first attempt to store and recall optical pulses in the ground-state coherence, repeating the method used by [16] and described in section 2.7. Here a short pulse of light resonant to the $|F = 2\rangle \rightarrow |F' = 3\rangle$ transition is sent through the atomic medium. In addition, a control field is applied on the $|F = 3\rangle \rightarrow |F' = 3\rangle$ transition, producing a transmission window for the probe pulse. The probe pulse is collected and analysed in the time domain using digital demodulation techniques.

The results of this test are shown in Figure 10.4. When no atoms are present the probe pulse propagates through the system with no additional delay and zero absorption. When a cold atom ensemble is present and the control field is active the probe pulse is delayed by 50 ns due to the dispersion of the medium. By switching off the control field while the probe pulse is within the medium, a fraction of probe is written into the atomic ground states. Reapplying the control field at a later time retrieves the stored pulse which is then able to leave the medium.

In our initial tests we have been able to store pulses for as long as 1 μ s, with an exponential decay in retrieval efficiency with time constant of 319(7) ns. It is clear from the plot that a large fraction of the input pulse is escaping the atomic medium before the control field is turned off. Further optimising of the pulse timing, bandwidth limitations, and efficiency will be required to fully understand the performance of the system. While still early days, this result is the second demonstration of optical pulse storage in a fibre-confined cold-atom system. In addition, the measured coherence lifetime of 319(7) ns is already longer than both the typically measured transit time in hot-atom-in-fibre experiments of 100 ns [113] and the 238 ns lifetime of the rubidium $5D_{3/2}$ state used in

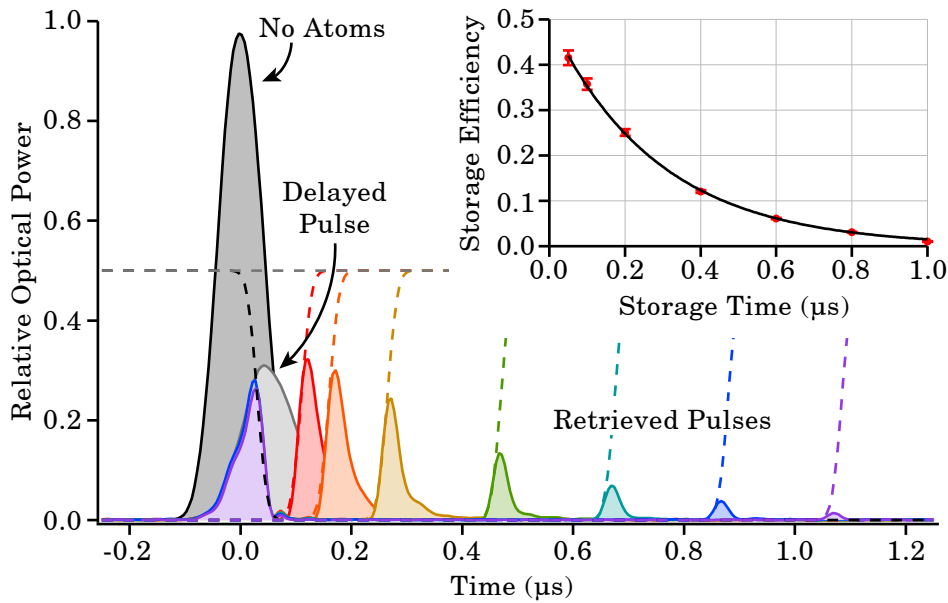


Figure 10.4: Demonstration of optical pulse storage using the cold-atom-in-fibre platform. The optical power is scaled to the input pulse when no atoms are present (black), and the transmitted pulse (grey) is slightly delayed by dispersion of the **EIT** window. When the control field is turned off (black, dashed) the pulse is stored in the ground state coherence. When the control pulse is turned back on at a later time (various colours, dashed) the pulse is released from the atomic medium (various colours). The inset shows the integrated pulse power normalised to the delayed pulse against the storage time, with an exponential fit.

two-photon ladder schemes [83].

10.3 Concluding Remarks

This bulk of this thesis is related to the construction and development of the systems and techniques required to trap atoms within the hollow-core fibre and perform in-fibre interrogation. While this has not always been the most exciting work, it is satisfying to bring an new experiment to life. Now the exciting work begins, there are experiments to be done that have never been done before – *new physics* awaits. The future of this project lies in the investigation of long-lived quantum memories and other exciting coherent phenomena, and I wish those who continue this story all the best.

Regards,

Ashby Hilton

Part V

Appendices



CODE SNIPPETS

The following are code snippets for various data processing or modelling tasks. Each is commented and reference is given to the section of the thesis proper in which the code is used. All code is given as either the final version in current use, or the version that best illustrates its purpose and structure.

Every code segment given here was written for task by the author.

A.1 Data Processing

The following are procedures written for processing data of various origins.

A.1.1 Heterodyne Absorption Spectroscopy

The following is an *Igor Pro* procedure used to process a single signal and reference trace pair taken using the system described in [subsection 4.5.3](#).

```
1 function singleshotFFT()
2
3 // Detuning parameters
4 variable/G d0
5 variable/G nd
6 variable/G dstep
7
8 // Experimental AOM shifts
```

```
9   variable fLO = 2*130.4e6
10  variable dshift = 2*90.4e6
11
12  // Data pulse parameters
13  variable/G pulsewidth
14  variable/G pulseperiod
15  variable/G pulseoffset
16
17  // Data type
18  variable DataType=1 // 0 for csv, 1 for bin
19  variable nchannels = 1
20  variable ndatapoints = 500e3
21
22  // Detector gain calibration
23  variable pLo=3.4e-3 // mW
24  variable gain = 14*0.5*0.5*1e4 // V/W including detector sensitivity, gain, and amplifier
25  variable coupling=1.8/5 // Efficiency from kagome to detector
26
27  // User input for folder name & data type
28  string fldrName;
29  Prompt fldrName, "folder_name"
30  Prompt datatype, "0: csv, 1: bin"
31  DoPrompt "Enter Params ", fldrName,datatype
32
33  // Abort if user cancels
34  if(V_flag==1)
35    Abort
36  endif
37
38  // Looping parameters
39  variable i,j
40
41  // Save root folder reference
42  DFREF saveDFR = GetDataFolderDFR()
43
44  // Check for existing folder, if valid then make and move into
45  if(datafolderExists(fldrname)==1)
46    Abort "Folder_exists"
47  endif
48  newdatafolder $fldrname
49  setdatafolder $fldrname
50
51  // Import data
52  variable numitems
53  if(datatype == 0)
54
```

```

55     // CSV data
56     numitems = LoadFewCSVs()
57     else
58
59     // Binary Data
60     numitems = LoadFewBins(ndatapoints,nchannels)
61     endif
62
63     // Make local refs
64     wave sigw = $("ywav"+num2str(numitems-2))
65     wave refw = $("ywav"+num2str(numitems-1))
66
67     // Make storage and output waves
68     make/O/N=(nd) $("PulsePowerwav_"+fldrname),$("Transmissionwav_"+fldrname),SigPhaseWav,
        RefPhaseWav,$("PhaseShiftwav_"+fldrname)
69     wave PulsePowerwav=$("PulsePowerwav_"+fldrname)
70     wave Transmissionwav=$("Transmissionwav_"+fldrname)
71     wave phaseshiftwav=$("PhaseShiftwav_"+fldrname)
72
73     // Setup wave scaling
74     setscale/P x,d0,dstep,"MHz", PulsePowerwav,transmissionwav,SigPhaseWav,RefPhaseWav,
        PhaseShiftWav
75     setscale d,0,0,"W",PulsePowerwav
76     setscale d,0,0,"deg",SigPhaseWav,RefPhaseWav,PhaseShiftWav
77
78     // For each detuning pulse
79     for(j=0;j<nd;j+=1)
80
81     // Downmixed frequency for this detuning
82     variable f=abs(fLO-(dshift+d0+j*dstep))
83
84     // Collect snippets
85     duplicate/O/R=(pulseoffset+j*pulseperiod-0.5*pulsewidth,pulseoffset+j*pulseperiod+0.5*
        pulsewidth) sigw $("Sigw_snippet_"+num2str(j))
86     duplicate/O/R=(pulseoffset+j*pulseperiod-0.5*pulsewidth,pulseoffset+j*pulseperiod+0.5*
        pulsewidth) refw $("Refw_snippet_"+num2str(j))
87
88     // Local references to snippets
89     wave Sigw_snippet=$("Sigw_snippet_"+num2str(j))
90     wave Refw_snippet=$("Refw_snippet_"+num2str(j))
91
92     // Make odd number of points for FFT
93     if(mod(numpts(Sigw_snippet),2)==1)
94         deletepoints 0,1,Sigw_snippet
95         deletepoints 0,1,Refw_snippet
96     endif

```

APPENDIX A. CODE SNIPPETS

```

97
98 // Do signal FFT
99 FFT/OUT=4/DEST=$( "Sigw_snippet_" + num2str(j) + "_FFT" ) Sigw_snippet
100 FFT/OUT=5/DEST=$( "Sigw_snippet_" + num2str(j) + "_PHS" ) Sigw_snippet
101 wave sigw_snippet_FFT=$( "Sigw_snippet_" + num2str(j) + "_FFT" )
102 wave sigw_snippet_PHS=$( "Sigw_snippet_" + num2str(j) + "_PHS" )
103
104 // Do reference FFT
105 FFT/OUT=4/DEST=$( "refw_snippet_" + num2str(j) + "_FFT" ) refw_snippet
106 FFT/OUT=5/DEST=$( "refw_snippet_" + num2str(j) + "_PHS" ) refw_snippet
107 wave refw_snippet_FFT=$( "refw_snippet_" + num2str(j) + "_FFT" )
108 wave refw_snippet_PHS=$( "refw_snippet_" + num2str(j) + "_PHS" )
109
110 // Calculate energy in FFT spikes
111 variable BW=0.8e6
112 variable sigw_Power = (1/4)*(1/pLO)*(1/gain)^2*(1/coupling)^2*sum(sigw_snippet_FFT,(f-0.5*BW)
    ,(f+0.5*BW))*(2/(pulsewidth/dimdelta(sigw_snippet,0)))^2
113 variable sigw_Power_BG = (1/4)*(1/pLO)*(1/gain)^2*(1/coupling)^2*(BW/dimdelta(
    sigw_snippet_FFT,0))*mean(sigw_snippet_FFT,150e6,250e6)*(2/(pulsewidth/dimdelta(
    sigw_snippet,0)))^2
114 variable refw_Power = (1/4)*(1/pLO)*(1/gain)^2*(1/coupling)^2*sum(refw_snippet_FFT,(f-0.5*BW)
    ,(f+0.5*BW))*(2/(pulsewidth/dimdelta(refw_snippet,0)))^2
115 variable refw_Power_BG = (1/4)*(1/pLO)*(1/gain)^2*(1/coupling)^2*(BW/dimdelta(
    refw_snippet_FFT,0))*mean(refw_snippet_FFT,150e6,250e6)*(2/(pulsewidth/dimdelta(
    refw_snippet,0)))^2
116
117 // Store ref energy
118 PulsePowerwav[j] = refw_Power
119
120 // Calculate transmission
121 Transmissionwav[j] = (sigw_Power - sigw_Power_BG)/(refw_Power - refw_Power_BG)
122
123 // Calculate phases
124 sigphasewav[j] = (180/pi)*(pi/2 - sigw_snippet_PHS(f))
125 unwrap 360,sigphasewav
126
127 refphasewav[j] = (180/pi)*(pi/2 - refw_snippet_PHS(f))
128 unwrap 360,refphasewav
129
130 // Cleanup
131 killwaves/Z sigw_snippet,refw_snippet,sigw_snippet_FFT,sigw_snippet_PHS,refw_snippet_FFT,
    refw_snippet_PHS
132
133 endfor
134
135 // Calculate difference in phases

```

```
136 PhaseShiftwav=sigphasewav-refphasewav
137
138 // Check if plot window exists
139 DoWindow /F singleshot
140
141 // If it doesn't then make it
142 if(V_Flag == 0)
143     Display/N=singleshot Transmissionwav
144     AppendToGraph/R PhaseShiftWav
145     ModifyGraph rgb($nameofwave(PhaseShiftWav))=(0,0,65535)
146     ModifyGraph grid(left)=1,grid(bottom)=1
147     ModifyGraph mirror(bottom)=1
148     ModifyGraph gridRGB(left)=(30583,30583,30583),gridRGB(bottom)=(30583,30583,30583)
149     ModifyGraph gridStyle(left)=1,gridStyle(bottom)=1
150     Label left "TransmissionU\s(TransmissionWav)"
151     Label bottom "ProbeUDetuningU(\U)"
152     Label right "Phase(\U)U\s(PhaseShiftWav)"
153     SetAxis left -0.1,1.1
154 else
155     appendtograph transmissionwav
156     appendtograph/R phaseshiftwav
157 endif
158
159 // Return to root
160 setdatafolder savedfr
161
162 end
```

A.1.2 DC Absorption Spectroscopy

The following is a set of *Igor Pro* procedures used to process a single signal and reference trace pair taken using the system described in [subsection 4.5.2](#).

```
1  function processSingleSweep()
2
3  string fldrName = "data" //Folder to put all data in
4  variable gain = 3e6 //Gain in V/W of the detection system
5  variable npulses = 49 //Number of data pulses per run
6  variable nAVG = 1 //Number of runs (averages)
7  variable d0 = 72 //Start detuning (MHz)
8  variable detStep = -3 //detuning steps (MHz)
9  variable pulsewidth = 0.5e-6 //width of each pulse (s)
10 variable pulseperiod = 2e-6 //Period of pulse train (s)
11 variable fitperiod
12 variable fitoffset
13
14 //Global variables
15 variable i,j,k //Loop parameters
16 variable sig0=1.55e-13 //scattering cross section in m^2, using the linear D2 value from Steck
17 variable G=6.07 //natural line width in MHz
18 variable Psat=20e-9 //Saturation power in fibre in W (measured)
19
20 //Find and put data files in list
21 NewPath /O folderPath "D:\\Frames\\"
22 String list = IndexedFile(folderPath, -1, ".csv")
23 list = SortList(list, ";", 16)
24 variable numItems = ItemsInList(list)
25
26 //Import data files
27 LoadWave /Q/N='temp' /G /P=folderPath "Data0Sc"+num2str(numitems-1)+".csv"
28 wave temp0,temp1
29 duplicate/O temp0 timew
30 duplicate/O temp1 sigw
31 killwaves/Z temp0,temp1,temp2,temp3
32
33 LoadWave /Q/N='temp' /G /P=folderPath "Data0Sc"+num2str(numitems)+".csv"
34 wave temp0,temp1
35 duplicate/O temp1 refw
36 killwaves/Z temp0,temp1,temp2,temp3
37
38 //Set time and voltage scale for the data wave
39 SetScale/P x (timew[0]),(timew[1]-timew[0]),"s", sigw,refw
40 SetScale d 0,0,"W", sigw,refw
41 sigw/=gain
42 refw/=gain
```

```

43
44 // Make 1D output waves
45 make /O/N=(npulses) transWav,transErrWav,transFitWav
46 setscale/P x d0,detStep,"MHz", transWav,transErrWav, transFitWav
47
48 // Find period and offset:
49
50 fitperiod = findperiod(refw,pulseperiod)
51 fitoffset = findoffset(refw,pulsewidth,fitperiod,npulses)
52
53 // Extract data
54 newExtractData(npulses,pulsewidth,fitperiod,fitoffset,SigW,RefW)
55 wave transmission
56 wave transmissionerr
57 transwav[]=transmission[p]
58 transerrwav[]=transmissionerr[p]
59
60 // Fit with absorption profile
61 make/O/N=3 W_Coef={100,1,6.07}
62 variable V_FitError=0
63 FuncFit/Q/H="011"/L=10000 D2Spectrum W_Coef transwav /W=transerrwav /I=1/D=transFitWav
64 wave w_sigma
65
66 // Extract OD
67 variable/G OD=w_coef[0]*(9/14)
68 variable/G ODerr=3*w_sigma[0]*(9/14)
69 print(num2str(round(OD)))
70
71 // Plotting for fun & aesthetics
72 if(strlen(WinList("img",";",""))==0)
73     display /N=img transwav;
74     appendtograph transfitwav;
75     ErrorBars transwav Y,wave=(transerrwav,transerrwav)
76     modifygraph muloffset={0,100},lblPosMode=3,lblPos=40,margin(left)=42,margin(bottom)=42,
77         margin(right)=14,margin(top)=14,width=297.638,height=170.079,gfSize=12,gmSize=2,expand
78         =1.5
79     ModifyGraph zero(Res_Left)=2,mirror=2,nticks(Res_Left)=3,lblPosMode(left)=3,lblPosMode(
80         Res_Left)=3,lblPos(left)=40,lblPos(Res_Left)=40,standoff=0;
81     Label left "Transmission (%) ";
82     Label bottom "Detuning (\U)"
83     SetAxis left -10,130;
84     SetAxis bottom -72,72;
85     SetAxis Res_Left -15,15
86     ModifyGraph gfSize=12,expand=1.5
87     ModifyGraph lstyle(transFitWav)=3,lsize(transFitWav)=2,rgb(transFitWav)=(0,0,0)
88 endif

```

APPENDIX A. CODE SNIPPETS

```
86   TextBox/C/N=text0/A=LB/X=1/Y=1/F=0 "0D : □"+num2str(Round(OD))  
87  
88   end
```

The following function is used to extract transmission and optical power data from a pair of imported and processed traces.

```

1  function newExtractData(npulses,pulsewidth,pulseperiod,pulseoffset,SigW,RefW)
2
3  // Access parameters
4  variable npulses
5  variable pulsewidth
6  variable pulseperiod
7  variable pulseoffset
8  wave SigW,RefW
9
10 // Make output waves
11 make/O/N=(npulses) Transmission,transmissionErr,optpower,optpowererr
12 setscale d,0,0,"W", optpower,optpowererr
13
14 // Find where references pulses start, take data before this for background
15 findlevel/Q/Edge=1/P refw, 0.5*(wavemax(refw)+wavemin(refw))
16 wavestats/Q/R=(pnt2x(RefW,0),0) refW
17 variable DetOffset=V_avg
18 variable DetNoise=V_sem
19 variable DetWhiteLevel = V_sdev
20 sigw--=DetOffset
21 refw--=Detoffset
22
23 // Process pulses
24 variable i
25 variable startp,endp,sigmean,refmean,sigdev,refdev
26 duplicate/O refw testmask
27 testmask=0
28 for(i=0;i<npulses;i+=1)
29 // Find start and end of each pulse
30 startp=x2pnt(refw,i*pulseperiod+pulseoffset-0.5*pulsewidth)+2;
31 endp=x2pnt(refw,i*pulseperiod+pulseoffset+0.5*pulsewidth)-2;
32
33 // Calculate mean and error of each pulse
34 sigmean = mean(sigw,pnt2x(sigw,startp),pnt2x(sigw,endp))
35 refmean = mean(refw,pnt2x(refw,startp),pnt2x(refw,endp))
36 sigdev = sqrt(variance(sigw,pnt2x(sigw,startp),pnt2x(sigw,endp))/(endp-startp))
37 refdev = sqrt(variance(refw,pnt2x(refw,startp),pnt2x(refw,endp))/(endp-startp))
38
39 // Generate the test mask for each pulse
40 testmask[startp,endp]=1
41
42 // Calculate and store the transmission and error, as well as pulse power
43 transmission[i]= sigmean/refmean
44 transmissionerr[i]=transmission[i] * sqrt((sigdev/sigmean)^2 + (refdev/refmean)^2)

```

```
45     optpower[i]=refmean
46     optpowererr[i]=refdev
47     endfor
48
49     // Try to identify and discard the data set if it was corrupt
50     if(wavemax(transmission)>2 || wavemin(transmission)<-1)
51         transmission=nan
52         transmissionerr=nan
53     endif
54
55 end
```

The following function is used to generate a pulse train mask for comparison.

```
1 function maketrain(refw,pulseoffset,pulsewidth,pulseperiod,npulses)
2
3 // Collect parameters
4 wave refw
5 variable pulseoffset,pulsewidth,pulseperiod,npulses
6
7 // Generate an empty mask
8 duplicate/O refw maskw
9 maskw=0
10
11 // Set pulse locations to 1
12 variable j,startp,endp
13 for(j=0;j<npulses;j+=1)
14     startp=x2pnt(refw,j*pulseperiod+pulseoffset-0.5*pulsewidth)+2;
15     endp=x2pnt(refw,j*pulseperiod+pulseoffset+0.5*pulsewidth)-2;
16     maskw[startp,endp]=1
17 endfor
18 end
```

The following function is used to calculate the period of the pulse train.

```
1 function findperiod(refw,guessperiod)
2
3 // Collect parameters
4 wave refw
5 variable guessperiod
6
7 // Optional plot parameter
8 variable plotq=0
9
10 // Calculate the fourier spectrum
11 FFT/OUT=3/PAD={2^ceil(2+log(numpts(refw))/log(2))}/DEST=W_FFT refw
12
13 // Fit to the expected peak location with a Gaussian
14 duplicate/O W_FFT W_FFT_FIT
15 W_FFT_FIT=nan
16 smooth 5, w_fft
17 CurveFit/Q gauss W_FFT[x2pnt(W_FFT,1/(guessperiod))-10,x2pnt(W_FFT,1/(guessperiod))+10] /D
   =W_FFT_FIT
18 wave w_coef
19
20 // Calculate the period
21 variable calcperiod = 1/w_coef[2]
22
23 // If desired, plot the fit for 2 seconds
24 if(plotq==1)
25   display/N=temp
26   appendtograph/W=temp W_FFT,W_FFT_FIT
27   SetAxis bottom 0.9*1/(guessperiod),1.1*1/(guessperiod)
28   modifygraph/W=temp log(left)=1,rgb(W_FFT_FIT)=(0,0,0)
29   TextBox/W=temp/C/N=text0/X=1.00/Y=-31.55/F=0/S=3/A=MC "Periodis" + num2str(1e6*
   calcperiod) + "us";
30   DoUpdate/W=temp
31   sleep/B/S 2
32   killwindow temp
33   print calcperiod*1e6
34 endif
35
36 // Cleanup
37 killwaves/Z W_FFT,W_FFT_FIT
38
39 return calcperiod
40 end
```

The following function is used to calculate the offset of the pulse train with respect to the oscilloscope trigger.

```

1  function findoffset(refw,pulsewidth,pulseperiod,npulses)
2
3  // Collect parameters
4  wave refw
5  variable pulsewidth,pulseperiod,npulses
6
7  // Optical plot parameter
8  variable plotq=0;
9
10 // Generate a test train
11 maketrain(refw,0,pulsewidth,pulseperiod,npulses)
12 wave maskw
13
14 // Perform a test convolution of mask with itself to calculate the reference x value
15 Duplicate/O maskw,W_Convolution;
16 Convolve maskw, W_Convolution
17 Wavestats/Q W_Convolution
18 CurveFit/Q lor W_Convolution[V_maxRowLoc-10,V_maxRowLoc+10]
19 wave w_Coef
20 wave W_sigma
21 variable xref=w_Coef[2]
22
23 // Perform the real convolution to calculate the signal x value
24 Duplicate/O maskw,W_Convolution;
25 Convolve refw, W_Convolution
26 duplicate/O W_Convolution W_convolution_FIT
27 W_convolution_FIT = nan
28 Wavestats/Q W_Convolution
29 CurveFit/Q lor W_Convolution[V_maxRowLoc-10,V_maxRowLoc+10] /D=W_convolution_FIT
30 variable xsig=w_coef[2]
31
32 // Calculate pulse train offset and generate corrected pulse train
33 variable calcoffset = xsig-xref
34 maketrain(refw,calcoffset,pulsewidth,pulseperiod,npulses)
35
36 // Plot fit if desired
37 if(plotq==1)
38   display/N=temp
39   appendtograph/W=temp W_Convolution,W_convolution_FIT
40   SetAxis bottom pnt2x(w_convolution,V_maxRowLoc-100),pnt2x(w_convolution,V_maxRowLoc
41     +100)
41   modifygraph/W=temp log(left)=0,rgb( W_convolution_FIT)=(0,0,0)
42   TextBox/W=temp/C/N=text0/X=1.00/Y=-31.55/F=0/S=3/A=MC "offset_{}_is_{}"+num2str(1e6*
43     calcoffset)+"us";

```



```
43 DoUpdate/W=temp
44 sleep/B/S 2
45
46 killwindow temp
47
48 display/N=temp
49 appendtograph/W=temp refw
50 appendtograph/W=temp/R maskw
51 SetAxis bottom calcoffset-1*pulseperiod,calcoffset+4*pulseperiod
52 modifygraph/W=temp rgb(maskw)=(0,0,0)
53 DoUpdate/W=temp
54 sleep/B/S 5
55 SetAxis bottom npulses*pulseperiod+calcoffset-4*pulseperiod,npulses*pulseperiod+calcoffset+1*
    pulseperiod
56 DoUpdate/W=temp
57 sleep/B/S 5
58 killwindow temp
59
60 print 1e6*calcoffset
61 endif
62
63 // Cleanup
64 killwaves W_Convolution,W_convolution_FIT,W_coef,W_sigma
65
66 return calcoffset
67 end
```

A.2 Monte-Carlo Simulation

The following is a full *Mathematica* document that perform a minimum-case Monte Carlo simulation, as described in [chapter 5](#).

Monte Carlo Model

Ashby Hilton - 22/01/2020

Set Up Physics

```
SetDirectory[NotebookDirectory[]]  
C:\Users\hilton\Desktop\TEST
```

Constants

Physical

```
c = 2.99792458*^8;  
h = 1.054571800*^-34;  
kB = 1.3806504*^-23;  
amu = 1.660538782*^-27;  
GravitationalAcceleration = {0, 0, -9.81};  
cm = 72 / 2.54; (* 72 pp per inch*)
```

Fibre

```
w0 = 16.5*^-6; (* Guided mode field radius *)  
FibreRegion =  
  z > -100*^-3 && z < 0 && Norm[{x, y}] > 22.5*^-6 && Norm[{x, y}] < 225*^-6;  
ImplicitFibreRegion = ImplicitRegion[FibreRegion, {x, y, z}];  
FibreEnd = -0.1;
```

Rubidium

$$\nu D2 = 384.230406373 * 10^{12};$$

$$\omega D2 = 2 \pi * \nu D2;$$

$$\lambda D2 = 780.241368271 * 10^{-9};$$

$$\Gamma D2 = 2 \pi * 6.0666 * 10^6;$$

$$f D2 = 0.69577;$$

$$\nu D1 = 377.107385690 * 10^{12};$$

$$\omega D1 = 2 \pi * \nu D1;$$

$$\lambda D1 = 794.979014933 * 10^{-9};$$

$$\Gamma D1 = 2 \pi * 5.75 * 10^6;$$

$$f D1 = 0.34231;$$

$$m Rb85 = 84.911 \text{ amu};$$

$$\sigma D2 = 1.55 * 10^{-13};$$

$$I_{\text{sat}\Delta D1} = 4.4876 * 10^{-3} * \frac{1}{(0.01)^2}; (* \text{ mW/cm}^2 \text{ to W/m}^2 *)$$

$$I_{\text{sat}\Delta D1} = 3.4 * 10^{-3} * \frac{1}{(0.01)^2}; (* \text{ mW/cm}^2 \text{ to W/m}^2 *)$$

$$SD2_{Fg, Fe} :=$$

$$\text{Normal}[\text{SparseArray}[\{\{2, 1\} \rightarrow 3/10, \{2, 2\} \rightarrow 7/18, \{2, 3\} \rightarrow 14/45, \{3, 2\} \rightarrow 5/63, \\ \{3, 3\} \rightarrow 5/18, \{3, 4\} \rightarrow 9/14\}]] [[Fg, Fe]]$$

$$\delta D2_{Fg, Fe} := \text{Normal}[\text{SparseArray}[\{\{2, 1\} \rightarrow 3.035732439060 * 10^9 -$$

$$(120.64068 * 10^6 + 63.40161 * 10^6 + 29.37290 * 10^6),$$

$$\{2, 2\} \rightarrow 3.035732439060 * 10^9 - (120.64068 * 10^6 + 63.40161 * 10^6), \{2, 3\} \rightarrow$$

$$3.035732439060 * 10^9 - 120.64068 * 10^6, \{3, 2\} \rightarrow -(120.64068 * 10^6 + 63.40161 * 10^6),$$

$$\{3, 3\} \rightarrow -120.64068 * 10^6, \{3, 4\} \rightarrow 0\}]] [[Fg, Fe]]$$

Equations

Gaussian wave propagation

$$w[\lambda_-, z_-] = w0 \sqrt{1 + \left(\frac{z}{\frac{\pi w0^2}{\lambda}}\right)^2} * \left(0.5 + 0.5 \text{Erf}\left[\frac{z}{\lambda}\right]\right) + \\ w0 * \left(0.5 + 0.5 \text{Erf}\left[\frac{-z}{\lambda}\right]\right) - w0 \left(0.5 + 0.5 \text{Erf}\left[\frac{-(z + 0.1)}{\lambda}\right]\right) + \\ w0 \sqrt{1 + \left(\frac{-(z + 0.1)}{\frac{\pi w0^2}{\lambda}}\right)^2} * \left(0.5 + 0.5 \text{Erf}\left[\frac{-(z + 0.1)}{\lambda}\right]\right);$$

(* Gaussian propagation - Using erfs to generate a smooth transition from guided to propagating mode*)

Intensity profile

$$\text{GaussianI}[\lambda_{-}, P_{-}, \{x_{-}, y_{-}, z_{-}\}] = I\theta \left(\frac{w\theta}{w[\lambda, z]} \right)^2 e^{-\frac{2(x^2+y^2)}{w[\lambda, z]^2}} / . \left\{ I\theta \rightarrow \frac{2P}{\pi w\theta^2} \right\};$$

(*Gaussian in the fibre, expanding outside fibre, fibre tip at z=0*)

$$\text{HollowI}[\lambda_{-}, P_{-}, \{x_{-}, y_{-}, z_{-}\}] = I\theta \left(\frac{w\theta}{w[\lambda, z]} \right)^2 \left(\frac{2(x^2+y^2)}{w[\lambda, z]^2} \right) e^{-\frac{2(x^2+y^2)}{w[\lambda, z]^2}} / . \left\{ I\theta \rightarrow \frac{2P}{\pi w\theta^2} \right\};$$

$$I[\lambda_{-}, P_{-}, \{x_{-}, y_{-}, z_{-}\}] = \text{GaussianI}[\lambda, P, \{x, y, z\}];$$

Photon scattering

$$\begin{aligned} \text{ScatteringRate}[\lambda_{-}, P_{-}, \{x_{-}, y_{-}, z_{-}\}] = \\ \left(\left(\frac{\pi c^2 \Gamma D1^2}{2 \hbar \omega D1^3} \frac{1}{\Delta D1^2} + \frac{\pi c^2 \Gamma D2^2}{2 \hbar \omega D2^3} \frac{2}{\Delta D2^2} \right) I[\lambda, P, \{x, y, z\}] / . \right. \\ \left. \left\{ \Delta D2 \rightarrow 2\pi \left(-\nu D2 + \frac{c}{\lambda} \right), \Delta D1 \rightarrow 2\pi \left(-\nu D1 + \frac{c}{\lambda} \right) \right\} \right); \end{aligned}$$

(*Scattering rate is an I/Isat <<1 approximation, for non-degenerate fine structure*)

Dipole trap depth, force, and acceleration

$$\begin{aligned} \text{TrapDepth}[\lambda_{-}, P_{-}, \{x_{-}, y_{-}, z_{-}\}] = \left(\frac{\pi c^2 \Gamma D1}{2 \omega D1^3} \frac{1}{\Delta D1} + \frac{\pi c^2 \Gamma D2}{2 \omega D2^3} \frac{2}{\Delta D2} \right) I[\lambda, P, \{x, y, z\}] / . \\ \left\{ \Delta D2 \rightarrow 2\pi \left(-\nu D2 + \frac{c}{\lambda} \right), \Delta D1 \rightarrow 2\pi \left(-\nu D1 + \frac{c}{\lambda} \right) \right\}; \end{aligned}$$

(*Scattering rate is an I/Isat <<1 approximation, for non-degenerate fine structure*)

$$\text{DipoleForce}[\lambda_{-}, P_{-}, \{x_{-}, y_{-}, z_{-}\}] = -\text{Grad}[\text{TrapDepth}[\lambda, P, \{x, y, z\}], \{x, y, z\}];$$

(*Grad. of the trap depth*)

$$\text{DipoleAcceleration}[\lambda_{-}, P_{-}, \{x_{-}, y_{-}, z_{-}\}] = \left(\frac{\text{DipoleForce}[\lambda, P, \{x, y, z\}]}{m\text{Rb85}} \right);$$

(*3 vector acceleration from dipole force, used in NDSolve*)

Total acceleration

$$\begin{aligned} \text{TotalAcceleration}[\lambda_{-}, P_{-}, \{x_{-}, y_{-}, z_{-}\}] := \\ \text{DipoleAcceleration}[\lambda, P, \{x, y, z\}] + \text{GravitationalAcceleration} \end{aligned}$$

(*Total acceleration is the sum of gravity and the dipole acceleration. The scattering acceleration is accounted for using discrete momentum kicks*)

Calculate OD vs Δ

$$\text{ODAtom}[\delta_]=\sigma\text{D2}\ast\left(\frac{\text{SD2}_{3,2}}{1+4\left(\frac{2\pi(\delta-\delta\text{D2}_{3,2})}{\text{rD2}}\right)^2}+\frac{\text{SD2}_{3,3}}{1+4\left(\frac{2\pi(\delta-\delta\text{D2}_{3,3})}{\text{rD2}}\right)^2}+\frac{\text{SD2}_{3,4}}{1+4\left(\frac{2\pi(\delta-\delta\text{D2}_{3,4})}{\text{rD2}}\right)^2}\right);$$

$$\text{OD}[\delta_,\{x_,\text{y_},z_],\{vx_,\text{vy_},vz_}\]=\text{GaussianI}[\lambda\text{D2},1,\{x,\text{y},z\}]\text{ODAtom}\left[\delta+v\text{D2}\ast\frac{vz}{c}\right];$$

$\delta\text{list}=\text{Table}[i\ast 10^6,\{i,-80,80,1\}];$

Set up NDSolve

Basic

$\text{pos}[t_]=\{\text{px}[t],\text{py}[t],\text{pz}[t]\};$

Solve event setup

```

(*NotCapturedEvent:={
  WhenEvent[(Norm[{px[t],py[t]}]>22.5*^-6)&&pz[t]<0.,
    lifetime=t;
    status="HitWall";
    "StopIntegration"
  ],
  WhenEvent[pz[t]<0.,
    If[(Norm[{px[t],py[t]}]>22.5*^-6),
      lifetime=t;
      status="Lost";
      "StopIntegration"
    ]
  ],
  WhenEvent[pz[t]<-0.1,
    lifetime=t;
    status="Through";
    "StopIntegration"
  ],
  WhenEvent[t>0.15,
    status="Bounce";
  ](*,
  WhenEvent[Mod[t,1*^-3]>0.5*1*^-3,
    If[
      RandomReal[{0,1}]>Piecewise[{{Exp[-1*^-3*1],pz[t]>0}},Exp[-1*^-3*7.6]],
      lifetime=t;
      status="BGCollision";
      "StopIntegration"
    ]
  ]*)
};*)

```

```

NotCapturedEvent := {
  WhenEvent[(Norm[{px[t], py[t]}) > 22.5*^-6) && pz[t] < 0. && pz[t] > -0.1,
    Lifetime = t;
    status = "HitWall";
    "StopIntegration"
  ], WhenEvent[pz[t] < 0.,
    If[(Norm[{px[t], py[t]}) > 22.5*^-6),
      Lifetime = t;
      status = "Lost";
      "StopIntegration"
    ]
  ] (*,
  WhenEvent[Mod[t, 1*^-3] > 0.5*1*^-3,
    If[
      RandomReal[{0, 1}] > Piecewise[{{Exp[-1*^-3*1], pz[t] > 0}}, Exp[-1*^-3*7.6]],
      Lifetime = t;
      status = "Collision";
      "StopIntegration"
    ]
  ] *)
};

ScatteringEvent[λ_] =
{WhenEvent[(Mod[NScattEvents[t] - 0.5, 1]) < 0.5,
  {dummy = 1 (

$$\frac{2 \pi \hbar}{mRb85 \lambda D2} \{0, 0, 1\} + \frac{2 \pi \hbar}{mRb85 \lambda D2}$$

    With[{theta = 2 * Pi * RandomReal[], phi = ArcCos@RandomReal[{-1, 1}]},
      {Cos[theta] Sin[phi], Sin[theta] Sin[phi], Cos[phi]}]
  )},
  px'[t] → px'[t] + dummy[[1]], py'[t] → py'[t] + dummy[[2]],
  pz'[t] → pz'[t] + dummy[[3]], Sow[dummy]}]};

log3[{x1_, x2_, x3_}] = {x1 * 109, x2, Piecewise[{{Log10[x3], x3 > 0}}, -1]};

```

Run Blue Hollow Data

Run

```

Module[{λ =  $\frac{c}{\sqrt{D1 - 500*^9}}$ , P = 1, s0 = {0., 0., 25.4} * 10-3, σ0 = {1, 1, 1.0} * 10-3,
  T0 = {3., 3., 6.} * 10-6, n = 100, Tinit = 0., Tdur = 0.075, Tstep = 0.1*^-3},
  (*Reset Kernels*)
  StartTime = AbsoluteTime[];
  (*Generate location and velocity distributions from initial data*)
  SDist = Map[Apply[NormalDistribution], Transpose[{s0, σ0}]];

```



```

VDist = Map[Apply[NormalDistribution], Transpose[{{0, 0, 0},  $\sqrt{\frac{kB T0}{mRb85}}$  }]];

(*Generate the status list to fill with atoms that do not get in fibre*)
PosList = ConstantArray[0, {n, Round[(Tdur - Tinit) / Tstep], 3}];
VelList = ConstantArray[0, {n, Round[(Tdur - Tinit) / Tstep], 3}];
progress = Table[0, {i, 1, n}];
Clear[pos0, vel0, DEqns];
CloseKernels[];
LaunchKernels[];
DistributeDefinitions[λ, P, s0, σ0, T0, n, Tinit, Tdur,
  Tstep, SDist, VDist, pos, TotalAcceleration, ScatteringRate];
SetSharedVariable[PosList, VelList, progress];
(*Loop over atoms*)
Monitor[ParallelDo[
  Off[NDSolve::precw];
  (*Sample distributinos for initial data*)
  pos0 = Map[RandomVariate, SDist];
  vel0 = Map[RandomVariate, VDist];
  status = "Active";
  Lifetime = Tdur;
  (*Generate equations of motion*)
  DEqns[t_] =
  Flatten[
    (*a= (d2/dt2) s*)
    {Flatten[Thread[D[D[pos[t], t], t] == TotalAcceleration[λ, P, pos[t]]]},
    (*Initial position*)
    Flatten[Thread[pos[Tinit] == pos0]},
    (*Initial velocity*)
    Flatten[Thread[D[pos[t], t] == vel0]] /. t → Tinit,
    (*Checks for scattered photon*)
    ScatteringEvent[λ],
    (*Integrate the scattering rate for total scattered photons*)
    {D[NScattEvents[t], t] == (1) * ScatteringRate[λ, P, pos[t]] + 1*^-10,
    NScattEvents[t] == 0. /. t → Tinit}
  ]
];

(*Solve DEs for trajectory, scattering data, and hit fibre data*)
sol = NDSolve[Evaluate[DEqns[t]],
  {px[t], py[t], pz[t], NScattEvents[t]}, {t, Tinit, Tdur}, MaxSteps → 1*^7];
p = Join[Table[(pos[t] /. sol[[1]]) /. t → τ, {τ, Tinit, Lifetime, Tstep}],

  ConstantArray[{Null, Null, Null}, {Round[ $\frac{Tdur - Tinit - Lifetime}{Tstep}$ ]}]];

```

```

v = Join[Table[(D[pos[t] /. sol[[1]], t]) /. t -> τ,
  {τ, Tinit, Lifetime, Tstep}],
  ConstantArray[{Null, Null, Null}, {Round[ $\frac{Tdur - Tinit - Lifetime}{Tstep}$ ]}]];

PosList[[j]] = p;
VellList[[j]] = v;
progress[[j]] = 1;
(*Export[StringJoin["Atom", ToString[j], "Pos.m"], p];
Export[StringJoin["Atom", ToString[j], "Vel.m"], v];*)
, {j, 1, n, 1}], {Grid[Partition[progress, 50], Total[progress],
StringJoin["Progress: ", ToString[100. * Total[progress] / n], "%"],
StringJoin["Time taken: ", ToString[Round[AbsoluteTime[] - StartTime]]],
StringJoin["Time Left: ", ToString[
  Piecewise[{{Round[((AbsoluteTime[] - StartTime) / (Total[progress] / n)) -
(AbsoluteTime[] - StartTime)], Total[progress] > 0}}, "Start"]}]];

Print[
StringJoin["Time taken: ", ToString[Round[AbsoluteTime[] - StartTime]]];
TimeList = Table[t, {t, Tinit, Tdur, Tstep}];
];
BinaryWrite["PosList.bin", BinarySerialize[PosList]];
Close["PosList.bin"];
BinaryWrite["VellList.bin", BinarySerialize[VellList]];
Close["VellList.bin"];
BinaryWrite["TimeList.bin", BinarySerialize[TimeList]];
Close["TimeList.bin"];

Time taken: 23

PosList = BinaryDeserialize[ByteArray[BinaryReadList["PosList.bin"]]];
VellList = BinaryDeserialize[ByteArray[BinaryReadList["VellList.bin"]]];
TimeList = BinaryDeserialize[ByteArray[BinaryReadList["TimeList.bin"]]];

ListPointPlot3D[PosList, BoxRatios -> {1, 1, 5},
ImageSize -> Large, PlotRange -> 0.001 * {{-3, 3}, {-3, 3}, {-50, 50}}]

```

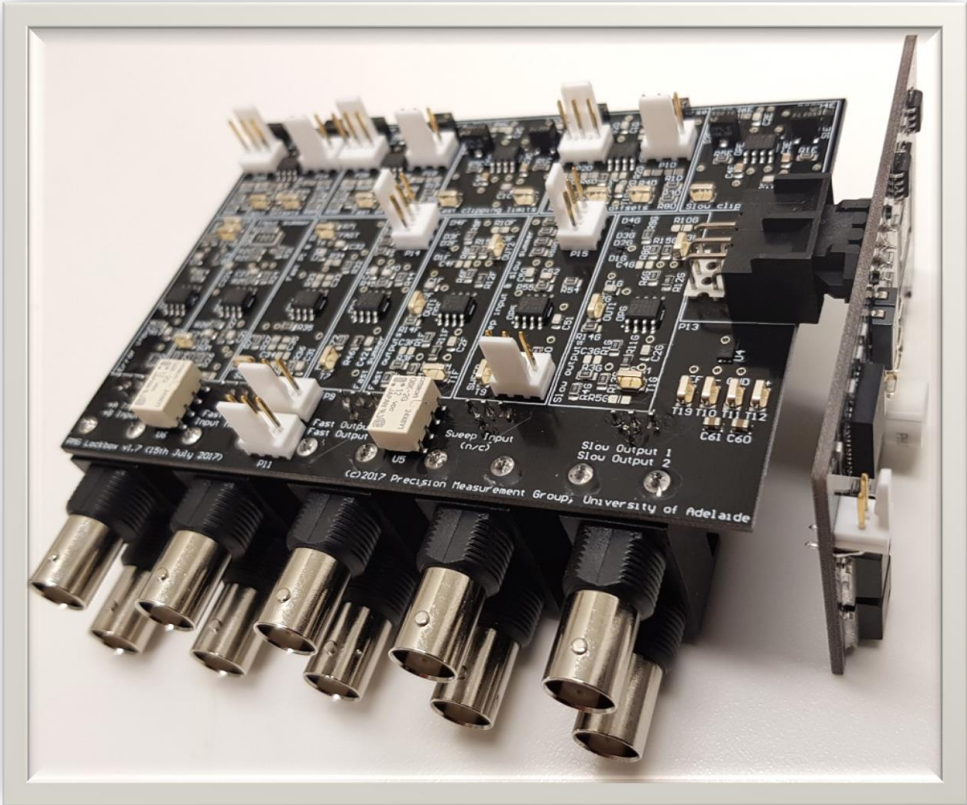

LOW-NOISE ANALOG LOCK BOX MANUAL

The following is a manual written for the high-speed, low-noise dual-stage analog lock box that was developed by myself and Dr. Light. The resulting device is in version 1.7, and possesses an input voltage noise floor at $20 \text{ nV}/\sqrt{\text{Hz}}$, with useful bandwidth of 1 MHz. The electronics are capable of operating over a full $\pm 10 \text{ V}$ range, with fine and coarse input and output offsets over this range.

This text is still in a draft format and is presented as it stands.

PMG Lockbox Manual

PCB Revision v1.7



V1.7 – 18th May 2018 – Ashby Hilton & Philip Light

Introduction

The PMG Lockbox is designed as a low noise, two stage PI servo controller.

Before powering up...

- Remove R17 on power board
- 10uF cap pin 7 -> pin 4, U104 (VRef buff)

Changes for next revision

- Remove R17 on power board
- 10uF cap pin 7 -> pin 4, U104 (VRef buff)
- Change output clipping diodes to Toshiba 1SS387CT. These have much lower $C_j=0.5\text{pF}$ than current diodes. With current caps $C_j=30\text{pF}$ which forms a LPF with output resistor and limits bandwidth.

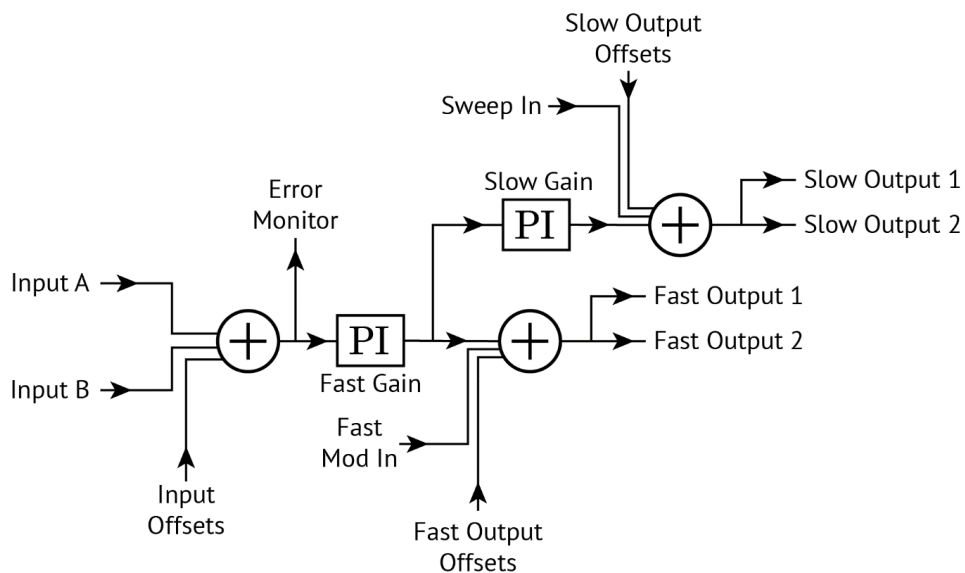


Figure 1 – Lockbox Block Diagram

Stages

Error inputs

The error input stage buffers the servo input signals. The pre-populated boards are set with 50Ω input impedance, which can be adjusted by changing resistors. Both inputs are seen as non-inverting at the error monitor.

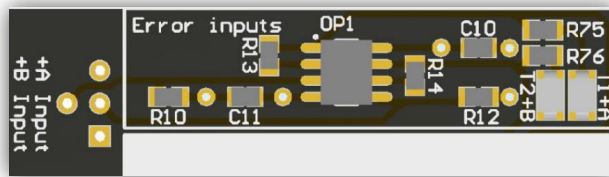


Figure 2 – PCB layout of error input stage

+A Input

The error is input via **B1** (dual BNC – closest to board). The input must be 50Ω terminated if unused and **R10** is not installed. The input impedance is set by **R10**, if populated.

Testpoint **T1** measures the buffered +A input.

+B Input

The error is input via **B1** (dual BNC – furthest from board). The input must be 50Ω terminated if unused and **R12** is not installed. The input impedance is set by **R12**, if populated.

Testpoint **T2** measures the buffered +B input.

Input noise

TODO: Document input noise with/without impedance setting resistor.

Input offsets

The lockbox has two input offsets available: coarse and fine. These input offsets are identically designed, and the level of adjustment of each is achieved independently by setting their gain through the input summer. These offsets are summed to the error inputs.

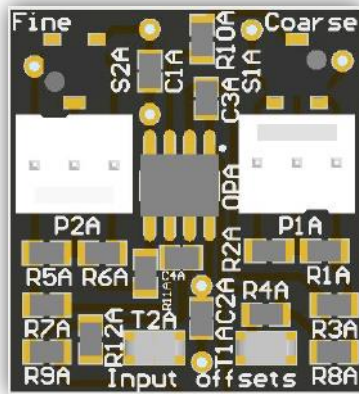


Figure 3 – PCB layout of input offset stage

Coarse input offset

The coarse input offset can be one of three options (only one of which should be populated):

- A fixed voltage by populating **R1A**, and **R2A**. In this case, the voltage at the centre of the divider will be:

$$V_{\text{tune}} = -V_{\text{ref}} + 2V_{\text{ref}} \left(\frac{R2A}{R1A + R2A} \right)$$
- A voltage adjustable via the PCB mounted potentiometer, **S1A**.
- A voltage adjustable via the externally mounted potentiometer via header **P1A**, where wiper should be connected to the centre pin.

The voltage set by one of these options is passed through a low pass filter, with corner:

$$f_c = \frac{1}{2\pi \times R3A \times C3A}$$

The gain of this offset voltage is set by **G=R25/R22** in the input summer.

The pre-populated boards are set with the PCB mounted pot, **S1A**, and have a pre-set coarse gain of 1 with no low pass filter.

Testpoint **T1A** measures the pre-gain coarse input offset.

Fine input offset

The coarse input offset can be one of three options (only one of which should be populated):

- a) A fixed voltage by populating **R5A**, and **R6A**. In this case, the voltage at the centre of the divider will be:

$$V_{\text{tune}} = -V_{\text{ref}} + 2V_{\text{ref}} \left(\frac{R6A}{R5A + R6A} \right)$$

- b) A voltage adjustable via the PCB mounted potentiometer, **S2A**.
- c) A voltage adjustable via the externally mounted potentiometer via header **P2A**, where wiper should be connected to the centre pin.

The voltage set by one of these options is passed through a low pass filter, with corner:

$$f_c = \frac{1}{2\pi \times R7A \times C4A}$$

The gain of this offset voltage is set by **G=R25/R23** in the input summer.

The pre-populated boards are set with the PCB mounted pot, **S2A**, and have a pre-set coarse gain of 1/20 with no low pass filter.

Testpoint **T2A** measures the pre-gain fine input offset.

Input summer and monitor

The input summer combines both buffered error input signals and coarse and fine input offsets. Optionally, a low-pass filter can be populated, allowing, for example, filtering of the 2nd harmonic after demodulation.

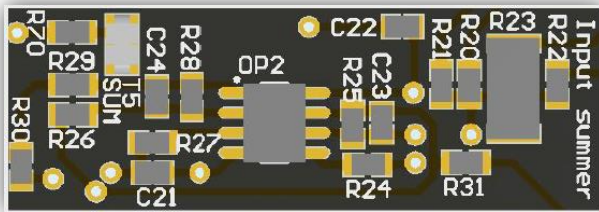


Figure 4 – PCB layout of input summer and monitor

The input summer is a summing inverting amplifier that presents an output signal equal to the sum of each input scaled by the ratio R_{25}/R_i where R_i is the resistor at the i th input.

Populating **C23** introduces a low pass filter to output of the summer, with a corner at:

$$f_c = \frac{1}{2\pi \times R_{25} \times C_{23}}$$

The prepopulated board has unity gain for inputs A and B, and a low pass filter corner at 10 MHz.

Testpoint **T5** measures the input summer output.

Input monitor

The input monitor allows the user to see the signal that will arrive at the first PI stage. This signal is the output of the summer, and contains both A, B, and the coarse and fine input offsets, all scaled appropriately by the summer. The sign of the monitor port shows the correct sign of A + B.

The gain of the input monitor is set by the ratio R_{28}/R_{26} .

Populating **C24** introduces a low pass filter with corner at $f_c = \frac{1}{2\pi \times R_{22} \times C_{24}}$.

The output impedance of the monitor is set by **R29**.

Populating **R20** introduces a passive attenuator after **OP2A**, and the amplitude gain is given by

$$\frac{R_{30}}{R_{30} + R_{29}}$$

The prepopulated board has unity gain, with a low pass filter corner at 10MHz, and 450Ω output impedance.

The voltage noise performance at this port is shown in Figure 5.

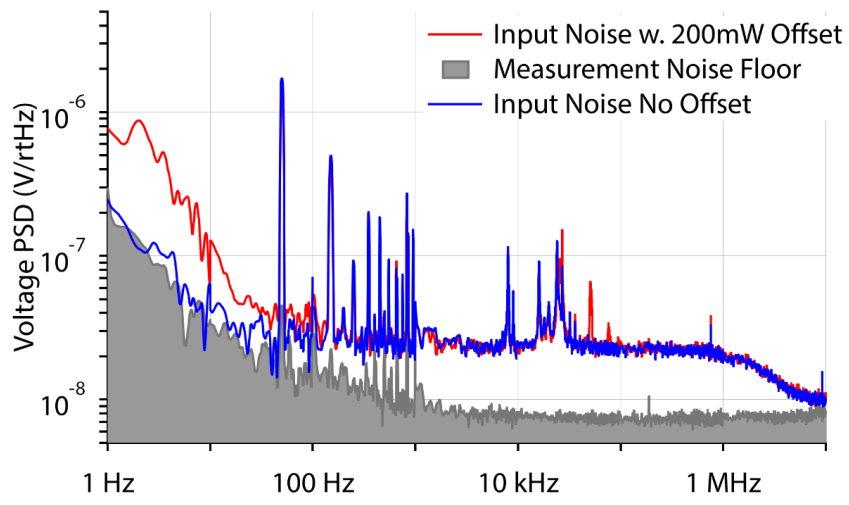


Figure 5 – Measured input noise at the error monitor

Fast PI & Slow PI

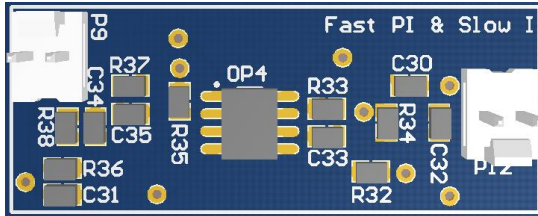


Figure 5 – PCB layout of fast PI and slow PI

The fast PI is the first feedback amplifier stage. It has multiple feedback paths to allow for a choice of transfer function shape, and is defeated by a DPDT switch.

The fast PI is an inverting amplifier with four feedback paths, each path offering a different gain over different frequency ranges.

Low Frequency Gain Limit

The feedback by $R34$ provides a maximum limit to the gain of the stage, denoted as the LFGL.

The limit in amplitude gain is $\frac{R34}{R31}$.

The phase shift in this region is $\sim 0^\circ$.

Proportional + Integrator

The feedback through $C33$ and $R33$ provides an integrator (-20 dB/decade) at low frequencies, with a proportional or flat minimum gain region at high frequencies.

The corner between the P and I regions is set by $f_c = \frac{1}{2\pi R33 \times C33}$.

The gain in the P region is set by $\frac{R33}{R31}$, although if the LFGL is in use, the gain is $\frac{R33 \times R34}{R31 \times (R33 + R34)}$.

The ideal phase shift will be -90° in the I region, moving through -45° at f_c to become $\sim 0^\circ$ in the P region.

High Frequency Roll-off

The feedback through $C32$ provides a low-pass filter at high frequencies if high frequency filtering is needed.

The corner between the flat gain (P) region and the HFR is at $f_c = \frac{1}{2\pi R33 \times C32}$.

The ideal phase shift will move from $\sim 0^\circ$ in the P region, through -45° at f_c to become -90° in the HDR region.

Defeat Switch

The header *P12* should connect to a DPDT switch on the box. When open, all other feedback paths will operate as described. When the switch closes the connection between pins 1 and 2, this path acts as a proportional gain stage with gain equal to $\frac{R_{sw}}{R_{31}}$, where R_{sw} is the residual resistance of the tracks and switch.

For R_{31} in the order of 1 k Ω , and R_{sw} in the order of 0.1 Ω , the gain is -80 dB and the output is essentially nothing.

Bode Plot

The above feedback paths are described visually in Figures 7&8 for an example setup of the PI.

In this example, the LFGL is 20 dB, the PI corner is 100 Hz, the proportional gain is 0 dB (but is shifted down to -0.83 dB by the LFGL resistor), and the HFR corner is 10 kHz.

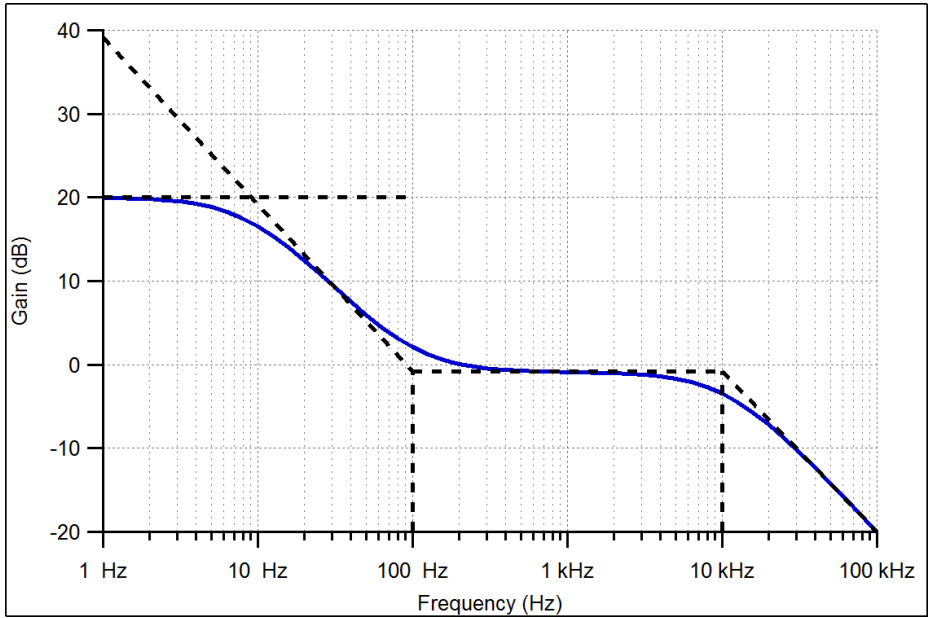


Figure 7 – Demonstration gain plot

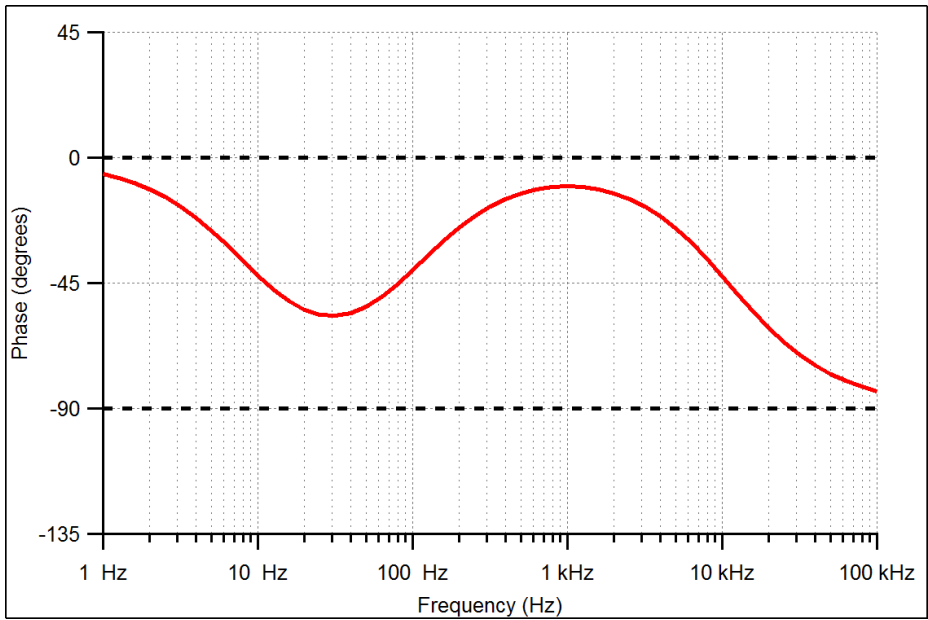


Figure 8 – Demonstration phase plot

Output Stages

The output stages (fast and slow) take the summer outputs, and feed them through two output buffers. These buffers can be toggled between non-inverting and inverting operation, and can also provide upper and lower voltage clipping limits, and optionally apply output attenuation.

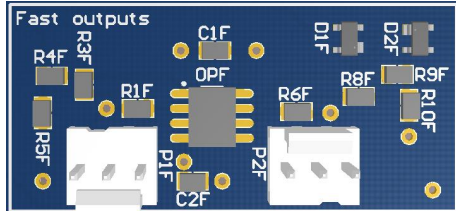


Figure 9 – PCB layout of fast output stage

Important! Read this before powering!

In order to provide protection to the op-amp in the event that ground falls outside of the power supply rails (as discussed earlier in the manual), it is important to put a ~500kΩ resistor between pins 1 & 2 of both **P1** & **P2** directly on the board. A surface mount resistor can be installed directly between the pins on the back of the board.

It is also necessary, to reduce oscillation in the non-inverting configuration, to put a 5kΩ resistor in path of pin 2 on headers **P1** & **P2**.

With pins 1 & 2 connected, such that V_{in} is applied to only non-inverting input, the output is given by:

$$V_{out} = -V_{in} \left(\frac{R_3}{R_1} \right) + 0 \left(\frac{R_{protect}}{R_{inline} + R_{protect}} \right) \left(\frac{R_1 + R_3}{R_1} \right) = -V_{in}$$

With pins 2 & 3 connected, V_{in} is applied to both inverting and non-inverting inputs, giving the output:

$$V_{out} = -V_{in} \left(\frac{R_3}{R_1} \right) + V_{in} \left(\frac{R_{protect}}{R_{inline} + R_{protect}} \right) \left(\frac{R_1 + R_3}{R_1} \right) \approx -V_{in} + 2V_{in} = V_{in}$$

Output attenuation and impedance

There is a resistor bridge to ground given by **R4** & **R5** for **OPA**, and **R9** & **R10** for **OPB**. This allows for attenuation out of the output signal.

The output for **OPA** is scaled by a factor of $R_5 / (R_4 + R_5)$, and **OPB** by $R_{10} / (R_9 + R_{10})$.

On the pre-populated boards, **R5** & **R10** are unpopulated, leaving no attenuation, but an output impedance of 50Ω set by **R4** and **R9**.

Output clipping

The output stages are clipped by diodes D1 & D2.

Diode D1 prevents the output from going above one diode voltage drop (0.57V) above the level set by the clipping stage VHigh reference.

Diode D2 prevents the output from going above one diode voltage drop (0.57V) below the level set by the clipping stage VLow reference.

If clipping is required, the output stage output impedances must be high enough such that the clipping op amps can sink/source the output stage current. The prepopulated resistor of 5K Ω is enough to satisfy this for the prepopulated boards.

Sweep input & slow summer

This stage allows input of a scalable sweep signal to the slow output, and sums the output of the slow PI stage with the sweep signal, and coarse and fine slow output offsets.

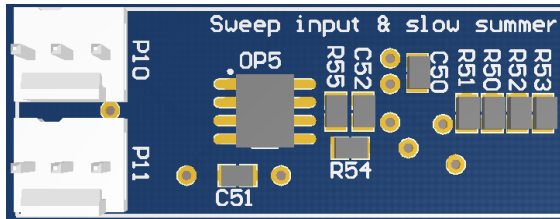


Figure 10 – PCB layout of sweep input and slow summer stage

Important! Read this before powering!

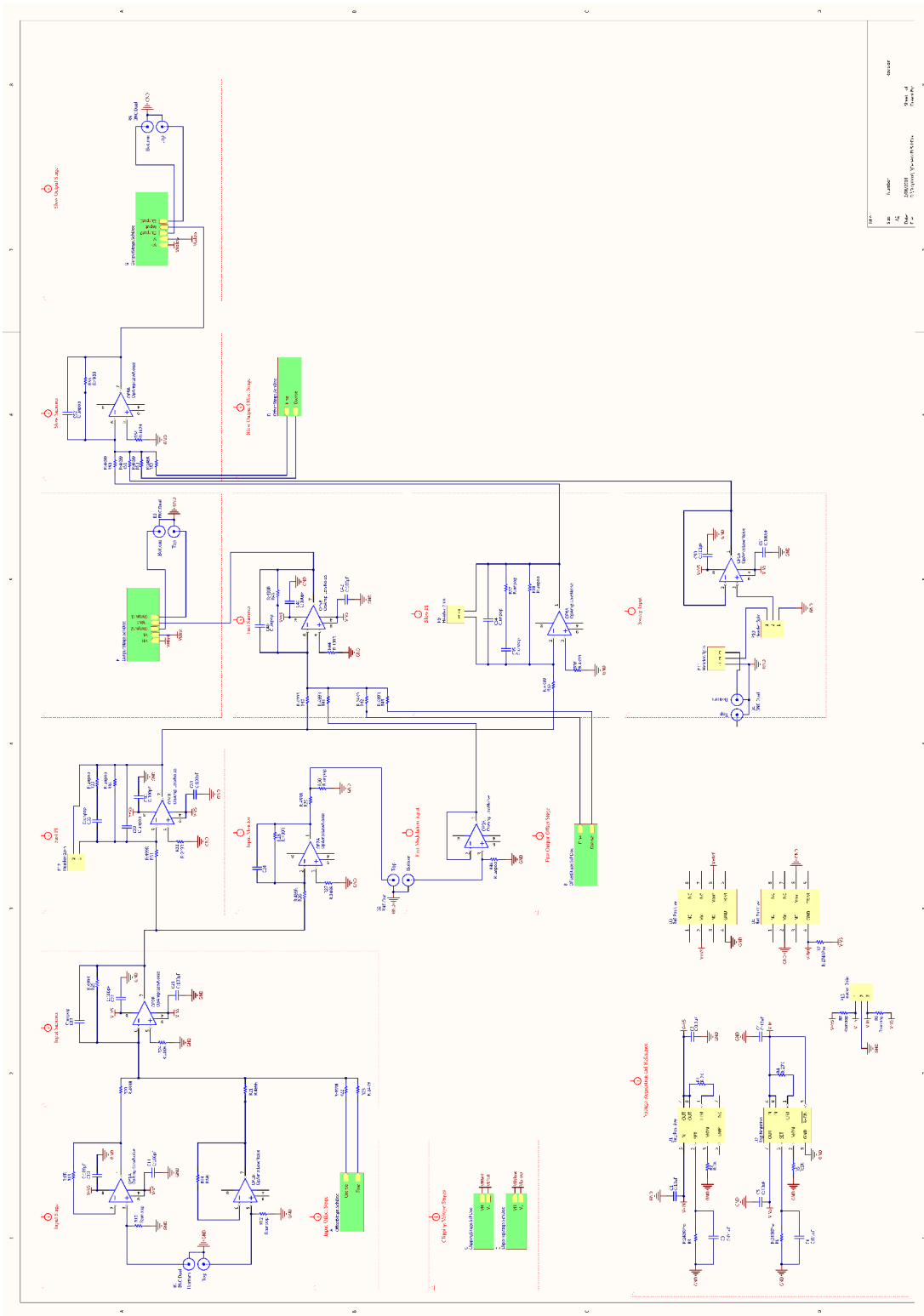
In order to provide protection to the op-amp in the event that ground falls outside of the power supply rails (as discussed earlier in the manual), it is important to put an inline 5kΩ resistor on pin 2 of **P10** (i.e. between pin 2 and the wiper of the sweep scaling potentiometer).

If sweep input is not required, a surface mount 5kΩ resistor can be placed between pins 1 & 2 on the back of the board.

Slow Summer

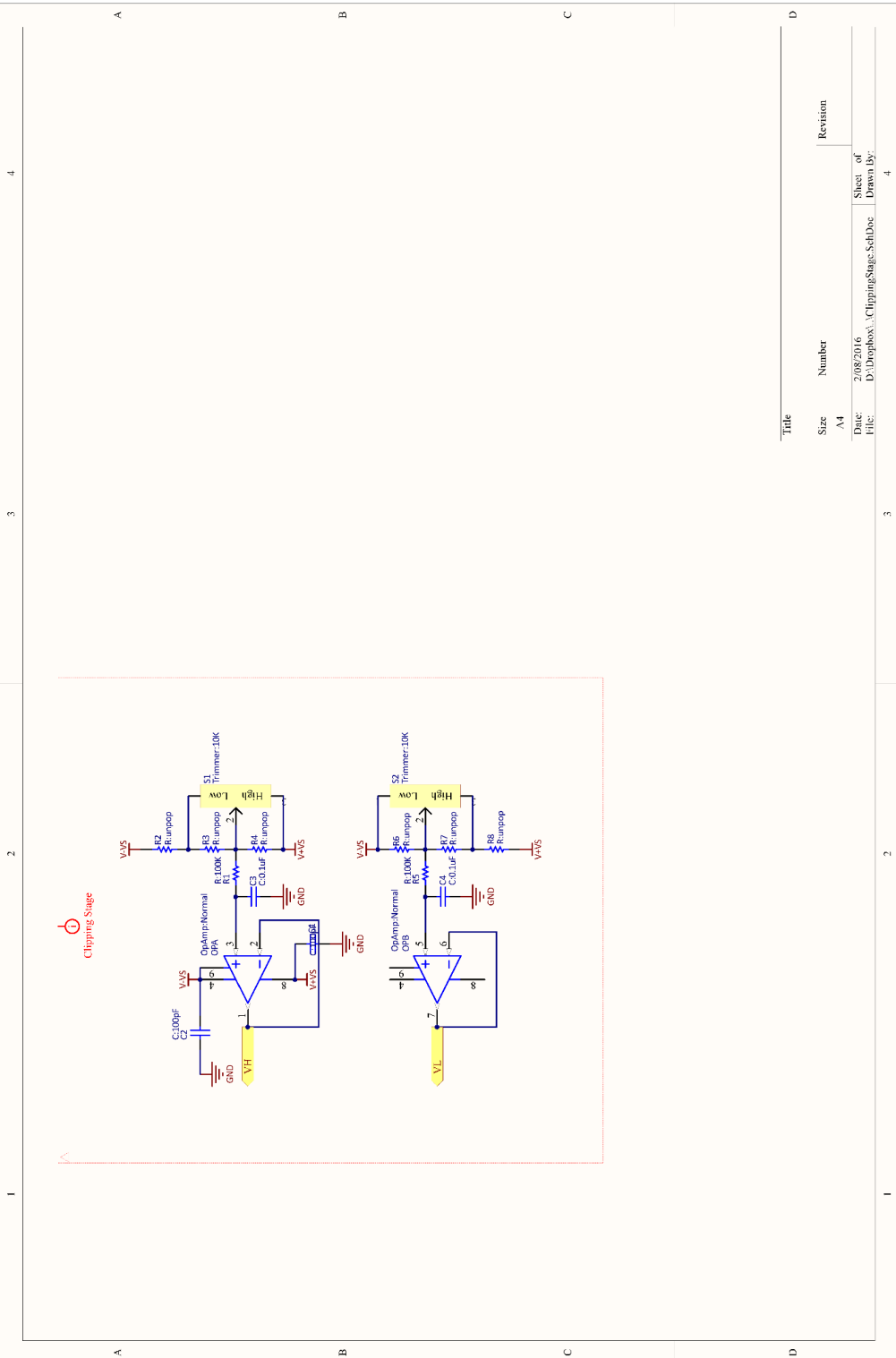
Populating **C52** introduces a low pass filter with corner at $f_c = \frac{1}{2\pi R22 \times C24}$.

Main Schematic



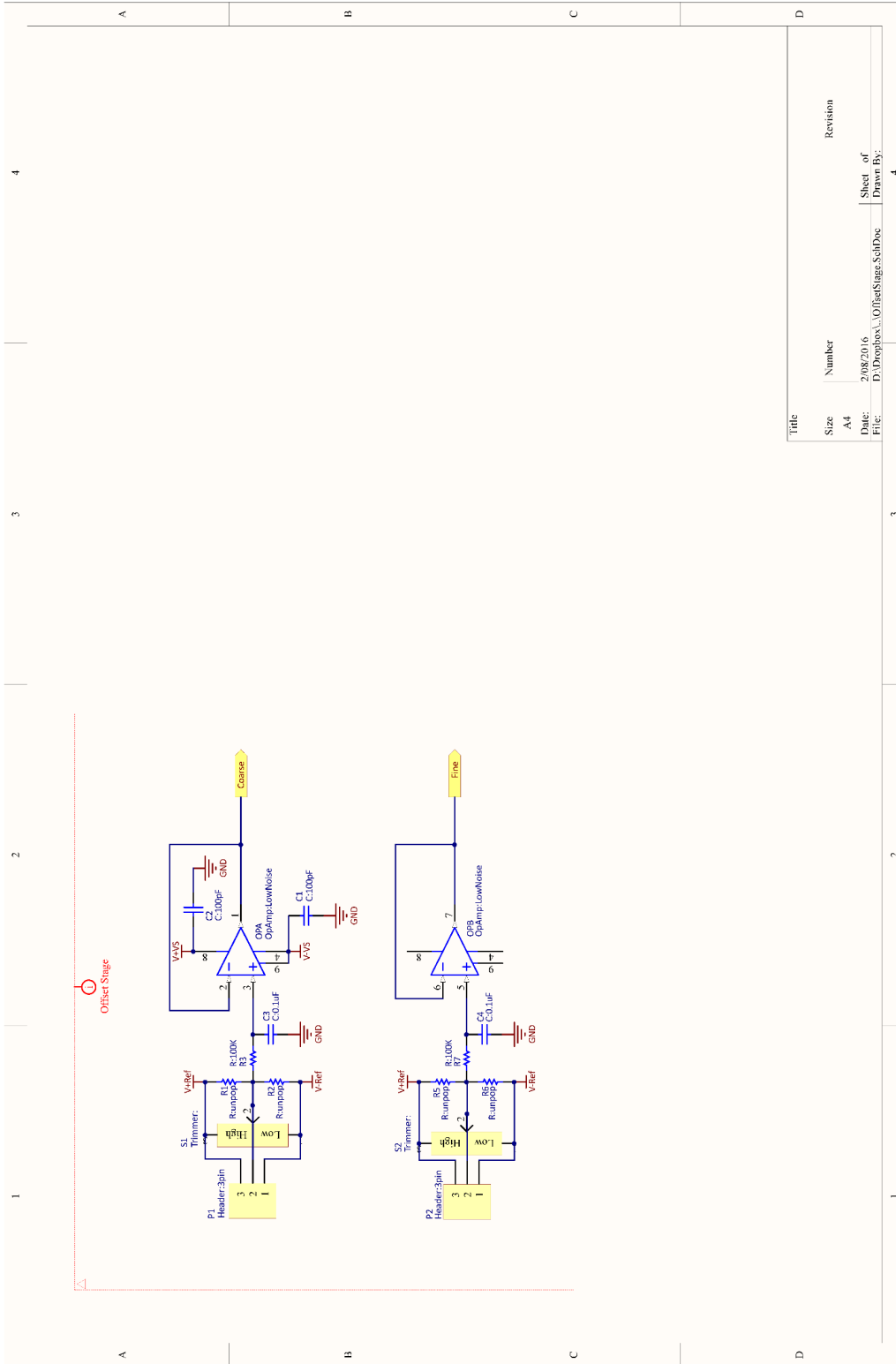
| Rev | Author | Checked | Date |
|-----|--------|---------|------|
| 1 | ... | ... | ... |

Clipping Stage Schematic



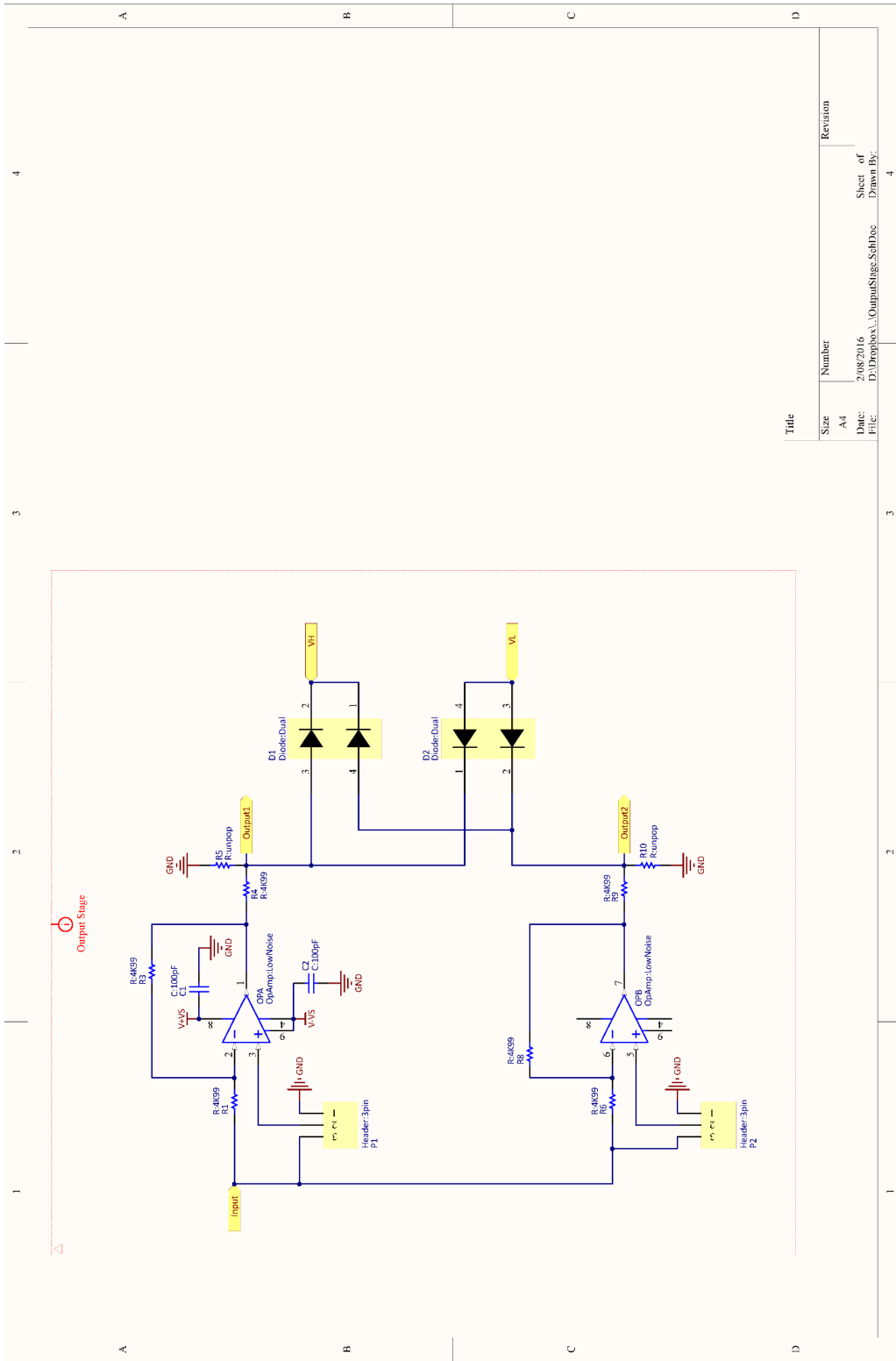
| Title | | Revision | |
|-------|----------------------------------|-----------|---|
| Size | Number | | |
| A4 | | | |
| Date | 2/08/2016 | Sheet of | 4 |
| File: | D:\Diplobox\ClippingStage.SchDoc | Drawn By: | |

Offset Stage Schematic



| Title | | Revision | |
|-------|-------------------------------|-----------|----------|
| Size | Number | Sheet of | Revision |
| A4 | | 4 | |
| Date: | 2/08/2016 | Sheet of | 4 |
| File: | D:\Dropbox\OffsetStage.SchDoc | Drawn By: | |

Output Stage Schematic



Title

| Size | Number | Revision |
|-------|-----------------------------------|------------|
| A4 | 2/08/2016 | Sheet of 4 |
| File: | D:\Dropbox\...\OutputStage.SchDoc | Drawn By: |

BIBLIOGRAPHY

- [1] M. ALHARBI, T. BRADLEY, B. DEBORD, C. FOURCADE-DUTIN, D. GHOSH, L. VINCETTI, F. GÉRÔME, AND F. BENABID, *Hypocycloid-shaped hollow-core photonic crystal fiber Part II: Cladding effect on confinement and bend loss*, *Optics Express* **21**, p. 28609, (2013), doi: [10.1364/OE.21.028609](https://doi.org/10.1364/OE.21.028609).
- [2] A. ARGYROS AND J. PLA, *Hollow-core polymer fibres with a kagome lattice: potential for transmission in the infrared.*, *Optics express* **15**, pp. 7713–7719, (2007), doi: [10.1364/OE.15.007713](https://doi.org/10.1364/OE.15.007713).
- [3] T. ARPORNTHIP, C. A. SACKETT, AND K. J. HUGHES, *Vacuum-pressure measurement using a magneto-optical trap*, *Physical Review A* **85**, p. 033420, (2012), doi: [10.1103/PhysRevA.85.033420](https://doi.org/10.1103/PhysRevA.85.033420).
- [4] A. ASHKIN, *Trapping of atoms by resonance radiation pressure*, *Physical Review Letters* **40**, pp. 729–732, (1978), doi: [10.1103/PhysRevLett.40.729](https://doi.org/10.1103/PhysRevLett.40.729).
- [5] M. BAJCSY, S. HOFFERBERTH, V. BALIC, T. PEYRONEL, M. HAFEZI, A. S. ZIBROV, V. VULETIC, AND M. D. LUKIN, *Efficient All-Optical Switching Using Slow Light within a Hollow Fiber*, *Physical Review Letters* **102**, p. 203902, (2009), doi: [10.1103/PhysRevLett.102.203902](https://doi.org/10.1103/PhysRevLett.102.203902).
- [6] M. BAJCSY, S. HOFFERBERTH, T. PEYRONEL, V. BALIC, Q. LIANG, A. S. ZIBROV, V. VULETIC, AND M. D. LUKIN, *Laser-cooled atoms inside a hollow-core photonic-crystal fiber*, *Physical Review A - Atomic, Molecular, and Optical Physics* **83**, pp. 1–9, (2011), doi: [10.1103/PhysRevA.83.063830](https://doi.org/10.1103/PhysRevA.83.063830).
- [7] V. I. BALYKIN, V. S. LETOKHOV, Y. B. OVCHINNIKOV, AND A. I. SIDOROV, *Quantum-state-selective mirror reflection of atoms by laser light*, *Physical Review Letters* **60**, pp. 2137–2140, (1988), doi: [10.1103/PhysRevLett.60.2137](https://doi.org/10.1103/PhysRevLett.60.2137).
- [8] M. BANU, S. NAWAZUDDIN, N. V. WHEELER, J. R. HAYES, S. R. SANDOGHCHI, T. D. BRADLEY, G. T. JASION, AND R. SLAV, *Lotus-Shaped Negative Curvature*

- Hollow Core Fiber With 10.5 dB/km at 1550 nm Wavelength*, *Journal of Light-wave Technology* **36**, pp. 1213–1219, (2018), doi: [10.1109/JLT.2017.2787197](https://doi.org/10.1109/JLT.2017.2787197).
- [9] F. BENABID, *Hollow-core photonic bandgap fibre: new light guidance for new science and technology*, *Philosophical Transactions of the Royal Society A: Mathematical, Physical and Engineering Sciences* **364**, pp. 3439–3462, (2006), doi: [10.1098/rsta.2006.1908](https://doi.org/10.1098/rsta.2006.1908).
- [10] F. BENABID, F. COUNY, J. C. KNIGHT, T. A. BIRKS, AND P. ST. J. RUSSELL, *Compact, stable and efficient all-fibre gas cells using hollow-core photonic crystal fibres*, *Nature* **434**, pp. 488–491, (2005), doi: [10.1038/nature03349](https://doi.org/10.1038/nature03349).
- [11] F. BENABID, J. C. KNIGHT, G. ANTONOPOULOS, AND P. ST. J. RUSSELL, *Stimulated Raman scattering in hydrogen-filled hollow-core photonic crystal fiber.*, *Science (New York, N.Y.)* **298**, pp. 399–402, (2002), doi: [10.1126/science.1076408](https://doi.org/10.1126/science.1076408).
- [12] F. BENABID, P. S. LIGHT, F. COUNY, AND P. ST. J. RUSSELL, *Electromagnetically-induced transparency grid in acetylene-filled hollow-core PCF*, *Optics Express* **13**, p. 5694, (2005), doi: [10.1364/OPEX.13.005694](https://doi.org/10.1364/OPEX.13.005694).
- [13] T. A. BIRKS, J. C. KNIGHT, AND P. ST. J. RUSSELL, *Endlessly single-mode photonic crystal fiber*, *Optics Letters* **22**, p. 961, (1997), doi: [10.1364/OL.22.000961](https://doi.org/10.1364/OL.22.000961).
- [14] J. E. BJORKHOLM, R. R. FREEMAN, A. ASHKIN, AND D. B. PEARSON, *Observation of focusing of neutral atoms by the dipole forces of resonance-radiation pressure*, *Physical Review Letters* **41**, pp. 1361–1364, (1978), doi: [10.1103/PhysRevLett.41.1361](https://doi.org/10.1103/PhysRevLett.41.1361).
- [15] F. BLATT, T. HALFMANN, AND T. PETERS, *One-dimensional ultracold medium of extreme optical depth*, *Optics Letters* **39**, p. 446, (2014), doi: [10.1364/OL.39.000446](https://doi.org/10.1364/OL.39.000446).
- [16] F. BLATT, L. S. SIMEONOV, T. HALFMANN, AND T. PETERS, *Stationary light pulses and narrowband light storage in a laser-cooled ensemble loaded into a hollow-core fiber*, *Physical Review A* **94**, p. 043833, (2016), doi: [10.1103/PhysRevA.94.043833](https://doi.org/10.1103/PhysRevA.94.043833).
- [17] D. J. BROD AND J. COMBES, *Passive CPHASE Gate via Cross-Kerr Nonlinearities*, *Physical Review Letters* **117**, p. 080502, (2016), doi: [10.1103/PhysRevLett.117.080502](https://doi.org/10.1103/PhysRevLett.117.080502).

-
- [18] L. CHEN AND D. M. BIRD, *Guidance in Kagome-like photonic crystal fibres II: perturbation theory for a realistic fibre structure*, Optics Express **19**, p. 6957, (2011), doi: [10.1364/oe.19.006957](https://doi.org/10.1364/oe.19.006957).
- [19] L. CHEN, G. J. PEARCE, T. A. BIRKS, AND D. M. BIRD, *Guidance in Kagome-like photonic crystal fibres I: analysis of an ideal fibre structure*, Optics Express **19**, p. 6945, (2011), doi: [10.1364/OE.19.006945](https://doi.org/10.1364/OE.19.006945).
- [20] Y.-W. CHO, G. T. CAMPBELL, J. L. EVERETT, J. BERNU, D. B. HIGGINBOTTOM, M. T. CAO, J. GENG, N. P. ROBINS, P. K. LAM, AND B. C. BUCHLER, *Highly efficient optical quantum memory with long coherence time in cold atoms*, Optica **3**, p. 100, (2016), doi: [10.1364/OPTICA.3.000100](https://doi.org/10.1364/OPTICA.3.000100).
- [21] C. A. CHRISTENSEN, S. WILL, M. SABA, G.-B. JO, Y.-I. SHIN, W. KETTERLE, AND D. PRITCHARD, *Trapping of ultracold atoms in a hollow-core photonic crystal fiber*, Physical Review A **78**, p. 033429, (2008), doi: [10.1103/PhysRevA.78.033429](https://doi.org/10.1103/PhysRevA.78.033429).
- [22] S. CHU, *Nobel Lecture: The manipulation of neutral particles*, Reviews of Modern Physics **70**, pp. 685–706, (1998), doi: [10.1103/RevModPhys.70.685](https://doi.org/10.1103/RevModPhys.70.685).
- [23] C. N. COHEN-TANNOUDJI, *Nobel Lecture: Manipulating atoms with photons*, Reviews of Modern Physics **70**, pp. 707–719, (1998), doi: [10.1103/RevModPhys.70.707](https://doi.org/10.1103/RevModPhys.70.707).
- [24] F. COUNY, F. BENABID, AND P. LIGHT, *Large-pitch kagome-structured hollow-core photonic crystal fiber*, Optics Letters **31**, pp. 3574–3576, (2006), doi: [10.1364/OL.31.003574](https://doi.org/10.1364/OL.31.003574).
- [25] F. COUNY, F. BENABID, P. J. ROBERTS, P. S. LIGHT, AND M. G. RAYMER, *Generation and Photonic Guidance of Multi-Octave Optical-Frequency Combs*, Science **318**, pp. 1118–1121, (2007), doi: [10.1126/science.1149091](https://doi.org/10.1126/science.1149091).
- [26] F. COUNY, P. S. LIGHT, F. BENABID, AND P. ST. J. RUSSELL, *Electromagnetically induced transparency and saturable absorption in all-fiber devices based on $^{12}\text{C}_2\text{H}_2$ -filled hollow-core photonic crystal fiber*, Optics Communications **263**, pp. 28–31, (2006), doi: [10.1016/j.optcom.2006.01.004](https://doi.org/10.1016/j.optcom.2006.01.004).
- [27] F. COUNY, P. J. ROBERTS, T. A. BIRKS, AND F. BENABID, *Square-lattice large-pitch hollow-core photonic crystal fiber*, Optics Express **16**, p. 20626, (2008), doi: [10.1364/OE.16.020626](https://doi.org/10.1364/OE.16.020626).

- [28] R. F. CREGAN, B. J. MANGAN, J. C. KNIGHT, T. A. BIRKS, P. ST. J. RUSSELL, P. J. ROBERTS, AND D. C. ALLAN, *Single-Mode Photonic Band Gap Guidance of Light in Air*, *Science* **285**, pp. 1537–1539, (1999), doi: [10.1126/science.285.5433.1537](https://doi.org/10.1126/science.285.5433.1537).
- [29] J. DALIBARD AND C. COHEN-TANNOUDJI, *Laser cooling below the Doppler limit by polarization gradients: simple theoretical models*, *Journal of the Optical Society of America B* **6**, p. 2023, (1989), doi: [10.1364/JOSAB.6.002023](https://doi.org/10.1364/JOSAB.6.002023).
- [30] R. G. DALL, M. D. HOOGERLAND, K. G. BALDWIN, AND S. J. BUCKMAN, *Guiding of metastable helium atoms through hollow optical fibres*, *Journal of Optics B: Quantum and Semiclassical Optics* **1**, pp. 396–401, (1999), doi: [10.1088/1464-4266/1/4/307](https://doi.org/10.1088/1464-4266/1/4/307).
- [31] B. DEBORD, M. ALHARBI, T. BRADLEY, C. FOURCADE-DUTIN, Y. WANG, L. VINCETTI, F. GÉRÔME, AND F. BENABID, *Hypocycloid-shaped hollow-core photonic crystal fiber Part I: Arc curvature effect on confinement loss*, *Optics Express* **21**, p. 28597, (2013), doi: [10.1364/OE.21.028597](https://doi.org/10.1364/OE.21.028597).
- [32] P. S. DONVALKAR, S. RAMELOW, S. CLEMMEN, AND A. L. GAETA, *Continuous generation of rubidium vapor in hollow-core photonic bandgap fibers*, *Optics Letters* **40**, p. 5379, (2015), doi: [10.1364/ol.40.005379](https://doi.org/10.1364/ol.40.005379).
- [33] M. FLEISCHHAUER, A. IMAMOGLU, AND J. MARANGOS, *Electromagnetically induced transparency: Optics in coherent media*, *Reviews of Modern Physics* **77**, pp. 633–673, (2005), doi: [10.1103/RevModPhys.77.633](https://doi.org/10.1103/RevModPhys.77.633).
- [34] G. L. GATTOBIGIO, T. POHL, G. LABEYRIE, AND R. KAISER, *Scaling laws for large magneto-optical traps*, *Physica Scripta* **81**, p. 025301, (2010), doi: [10.1088/0031-8949/81/02/025301](https://doi.org/10.1088/0031-8949/81/02/025301).
- [35] S. GHOSH, A. R. BHAGWAT, C. K. RENSHAW, S. GOH, A. L. GAETA, AND B. J. KIRBY, *Low-Light-Level Optical Interactions with Rubidium Vapor in a Photonic Band-Gap Fiber*, *Physical Review Letters* **97**, p. 023603, (2006), doi: [10.1103/PhysRevLett.97.023603](https://doi.org/10.1103/PhysRevLett.97.023603).
- [36] S. GHOSH, J. E. SHARPING, D. G. OUZOUNOV, AND A. L. GAETA, *Resonant optical interactions with molecules confined in photonic band-gap fibers*, *Physical Review Letters* **94**, pp. 1–4, (2005), doi: [10.1103/PhysRevLett.94.093902](https://doi.org/10.1103/PhysRevLett.94.093902).
- [37] A. GOZZINI, F. MANGO, J. H. XU, G. ALZETTA, F. MACCARRONE, AND R. A. BERNHEIM, *Light-induced ejection of alkali atoms in polysiloxane coated cells*, *Il Nuovo Cimento D* **15**, pp. 709–722, (1993), doi: [10.1007/BF02482437](https://doi.org/10.1007/BF02482437).

- [38] R. GRIMM, M. WEIDEMÜLLER, AND Y. B. OVCHINNIKOV, *Optical Dipole Traps for Neutral Atoms*, *Adv. At. Mol. Opt. Phys.* **42**, pp. 95–170, (2000), doi: [10.1016/S1049-250X\(08\)60186-X](https://doi.org/10.1016/S1049-250X(08)60186-X).
- [39] J. V. HAJNAL AND G. I. OPAT, *Diffraction of atoms by a standing evanescent light wave - A reflection grating for atoms*, *Optics Communications* **71**, pp. 119–124, (1989), doi: [10.1016/0030-4018\(89\)90411-2](https://doi.org/10.1016/0030-4018(89)90411-2).
- [40] J. HALD, J. C. PETERSEN, AND J. HENNINGSEN, *Saturated Optical Absorption by Slow Molecules in Hollow-Core Photonic Band-Gap Fibers*, *Physical Review Letters* **98**, p. 213902, (2007), doi: [10.1103/PhysRevLett.98.213902](https://doi.org/10.1103/PhysRevLett.98.213902).
- [41] T. HÄNSCH AND A. SCHAWLOW, *Cooling of gases by laser radiation*, *Optics Communications* **13**, pp. 68–69, (1975), doi: [10.1016/0030-4018\(75\)90159-5](https://doi.org/10.1016/0030-4018(75)90159-5).
- [42] J. HENNINGSEN, J. HALD, AND J. C. PETERSON, *Saturated absorption in acetylene and hydrogen cyanide in hollow-core photonic bandgap fibers*, *Optics Express* **13**, p. 10475, (2005), doi: [10.1364/OPEX.13.010475](https://doi.org/10.1364/OPEX.13.010475).
- [43] A. HILTON, C. PERRELLA, F. BENABID, B. SPARKES, A. LUITEN, AND P. LIGHT, *High-efficiency cold-atom transport into a waveguide trap*, *Physical Review Applied* **10**, p. 044034, (2018), doi: [10.1103/PhysRevApplied.10.044034](https://doi.org/10.1103/PhysRevApplied.10.044034).
- [44] N. HINKLEY, J. A. SHERMAN, N. B. PHILLIPS, M. SCHIOPPO, N. D. LEMKE, K. BELOY, M. PIZZOCARO, C. W. OATES, AND A. D. LUDLOW, *An Atomic Clock with 10-18 Instability*, *Science* **341**, pp. 1215–1218, (2013), doi: [10.1126/science.1240420](https://doi.org/10.1126/science.1240420).
- [45] S. HOSSEINI-ZAVAREH, R. LUDER, M. THIRUGNANASAMBANDAM, H. W. KUSHAN WEERASINGHE, B. R. WASHBURN, AND K. L. CORWIN, *Fabrication and characterization of short acetylene-filled photonic microcells*, *Applied Optics* **58**, p. 2809, (2019), doi: [10.1364/AO.58.002809](https://doi.org/10.1364/AO.58.002809).
- [46] H. ITO, T. NAKATA, K. SAKAKI, M. OHTSU, K. I. LEE, AND W. JHE, *Laser Spectroscopy of Atoms Guided by Evanescent Waves in Micron-Sized Hollow Optical Fibers*, *Physical Review Letters* **76**, pp. 4500–4503, (1996), doi: [10.1103/PhysRevLett.76.4500](https://doi.org/10.1103/PhysRevLett.76.4500).
- [47] H. ITO, K. SAKAKI, W. JHE, AND M. OHTSU, *Evanescent-light induced atom-guidance using a hollow optical fiber with light coupled sideways*, *Optics Communications* **141**, pp. 43–47, (1997), doi: [10.1016/S0030-4018\(97\)00217-4](https://doi.org/10.1016/S0030-4018(97)00217-4).

- [48] H. ITO, K. SAKAKI, T. NAKATA, W. JHE, AND M. OHTSU, *Optical potential for atom guidance in a cylindrical-core hollow fiber*, *Optics Communications* **115**, pp. 57–64, (1995), doi: [10.1016/0030-4018\(95\)00003-Q](https://doi.org/10.1016/0030-4018(95)00003-Q).
- [49] H. JEAL-RUEL, J. REID, AND G. DODD, *Resolving the magnetic hyperfine structure of hg isotopes using a vipa grating spectrometer*.
[White paper](#) by *LightMachinery*.
- [50] H. JIANG, F. KÉFÉLIAN, P. LEMONDE, A. CLAIRON, AND G. SANTARELLI, *An agile laser with ultra-low frequency noise and high sweep linearity*, *Optics Express* **18**, p. 3284, (2010), doi: [10.1364/OE.18.003284](https://doi.org/10.1364/OE.18.003284).
- [51] K. T. KACZMAREK, P. M. LEDINGHAM, B. BRECHT, S. E. THOMAS, G. S. THEKKADATH, O. LAZO-ARJONA, J. H. MUNNS, E. POEM, A. FEIZPOUR, D. J. SAUNDERS, J. NUNN, AND I. A. WALMSLEY, *High-speed noise-free optical quantum memory*, *Physical Review A* **97**, pp. 1–10, (2018), doi: [10.1103/PhysRevA.97.042316](https://doi.org/10.1103/PhysRevA.97.042316).
- [52] K. T. KACZMAREK, D. J. SAUNDERS, M. R. SPRAGUE, W. S. KOLTHAMMER, A. FEIZPOUR, P. M. LEDINGHAM, B. BRECHT, E. POEM, I. A. WALMSLEY, AND J. NUNN, *Ultrahigh and persistent optical depths of cesium in Kagomé-type hollow-core photonic crystal fibers*, *Optics Letters* **40**, p. 5582, (2015), doi: [10.1364/OL.40.005582](https://doi.org/10.1364/OL.40.005582).
- [53] H. KATORI, K. HASHIGUCHI, E. Y. IL'INOVA, AND V. D. OVSIANNIKOV, *Magic Wavelength to Make Optical Lattice Clocks Insensitive to Atomic Motion*, *Physical Review Letters* **103**, p. 153004, (2009), doi: [10.1103/PhysRevLett.103.153004](https://doi.org/10.1103/PhysRevLett.103.153004).
- [54] W. KETTERLE, K. B. DAVIS, M. A. JOFFE, A. MARTIN, AND D. E. PRITCHARD, *High densities of cold atoms in a dark spontaneous-force optical trap*, *Physical Review Letters* **70**, pp. 2253–2256, (1993), doi: [10.1103/PhysRevLett.70.2253](https://doi.org/10.1103/PhysRevLett.70.2253).
- [55] K. KNABE, S. WU, J. LIM, K. A. TILLMAN, P. S. LIGHT, F. COUNY, N. WHEELER, R. THAPA, A. M. JONES, J. W. NICHOLSON, B. R. WASHBURN, F. BENABID, AND K. L. CORWIN, *10 kHz accuracy of an optical frequency reference based on $^{12}\text{C}_2\text{H}_2$ -filled large-core kagome photonic crystal fibers*, *Optics Express* **17**, p. 16017, (2009), doi: [10.1364/OE.17.016017](https://doi.org/10.1364/OE.17.016017).
- [56] J. C. KNIGHT, T. A. BIRKS, P. S. J. RUSSELL, AND D. M. ATKIN, *All-silica single-mode optical fiber with photonic crystal cladding*, *Optics Letters* **21**, p. 1547, (1996), doi: [10.1364/OL.21.001547](https://doi.org/10.1364/OL.21.001547).

- [57] M. LANGBECKER, M. NOAMAN, N. KJÆRGAARD, F. BENABID, AND P. WINDPASSINGER, *Rydberg excitation of cold atoms inside a hollow-core fiber*, Physical Review A **96**, p. 041402, (2017), doi: [10.1103/PhysRevA.96.041402](https://doi.org/10.1103/PhysRevA.96.041402).
- [58] M. LANGBECKER, R. WIRTZ, F. KNOCH, M. NOAMAN, T. SPECK, AND P. WINDPASSINGER, *Highly controlled optical transport of cold atoms into a hollow-core fiber*, New Journal of Physics **20**, p. 083038, (2018), doi: [10.1088/1367-2630/aad9bb](https://doi.org/10.1088/1367-2630/aad9bb).
- [59] R. LE TARGAT, L. LORINI, Y. LE COQ, M. ZAWADA, J. GUÉNA, M. ABGRALL, M. GUROV, P. ROSENBUSCH, D. G. ROVERA, B. NAGÓRNY, R. GARTMAN, P. G. WESTERGAARD, M. E. TOBAR, M. LOURS, G. SANTARELLI, A. CLAIRON, S. BIZE, P. LAURENT, P. LEMONDE, AND J. LODEWYCK, *Experimental realization of an optical second with strontium lattice clocks*, Nature Communications **4**, p. 2109, (2013), doi: [10.1038/ncomms3109](https://doi.org/10.1038/ncomms3109).
- [60] H. J. LEE, C. S. ADAMS, M. KASEVICH, AND S. CHU, *Raman Cooling of Atoms in an Optical Dipole Trap*, Physical Review Letters **76**, pp. 2658–2661, (1996), doi: [10.1103/PhysRevLett.76.2658](https://doi.org/10.1103/PhysRevLett.76.2658).
- [61] V. S. LETOKHOV, *Generation of Light by a Scattering Medium with Negative Resonance Absorption*, Soviet Physics JETP **26**, p. 835, (1968).
- [62] P. S. LIGHT, J. D. ANSTIE, F. BENABID, AND A. N. LUITEN, *Hermetic optical-fiber iodine frequency standard*, Optics Letters **40**, p. 2703, (2015), doi: [10.1364/OL.40.002703](https://doi.org/10.1364/OL.40.002703).
- [63] P. S. LIGHT, F. BENABID, F. COUNY, M. MARIC, AND A. N. LUITEN, *Electromagnetically induced transparency in Rb-filled coated hollow-core photonic crystal fiber*, Optics Letters **32**, p. 1323, (2007), doi: [10.1364/OL.32.001323](https://doi.org/10.1364/OL.32.001323).
- [64] P. S. LIGHT, F. COUNY, Y. Y. WANG, N. V. WHEELER, P. J. ROBERTS, AND F. BENABID, *Double photonic bandgap hollow-core photonic crystal fiber*, Optics Express **17**, p. 16238, (2009), doi: [10.1364/OE.17.016238](https://doi.org/10.1364/OE.17.016238).
- [65] P. LONDERO, V. VENKATARAMAN, A. R. BHAGWAT, A. D. SLEPKOV, AND A. L. GAETA, *Ultralow-Power Four-Wave Mixing with Rb in a Hollow-Core Photonic Band-Gap Fiber*, Physical Review Letters **103**, p. 043602, (2009), doi: [10.1103/PhysRevLett.103.043602](https://doi.org/10.1103/PhysRevLett.103.043602).
- [66] R. LOUDON, *The Quantum Theory of Light*, Oxford University Press, 2nd ed., (1983).

- [67] L. P. MAGUIRE, S. SZILAGYI, AND R. E. SCHOLTEN, *High performance laser shutter using a hard disk drive voice-coll actuator*, Review of Scientific Instruments **75**, pp. 3077–3079, (2004), doi: [10.1063/1.1786331](https://doi.org/10.1063/1.1786331).
- [68] E. A. J. MARCATILI AND R. A. SCHMELTZER, *Hollow metallic and dielectric waveguides for long distance optical transmission and lasers*, The Bell System Technical Journal **43**, pp. 1783–1809, (1964), doi: [10.1002/j.1538-7305.1964.tb04108.x](https://doi.org/10.1002/j.1538-7305.1964.tb04108.x).
- [69] C. MARKOS, J. C. TRAVERS, A. ABDOLVAND, B. J. EGGLETON, AND O. BANG, *Hybrid photonic-crystal fiber*, Reviews of Modern Physics **89**, p. 045003, (2017), doi: [10.1103/RevModPhys.89.045003](https://doi.org/10.1103/RevModPhys.89.045003).
- [70] S. MARKSTEINER, C. M. SAVAGE, P. ZOLLER, AND S. L. ROLSTON, *Coherent atomic waveguides from hollow optical fibers: Quantized atomic motion*, Physical Review A **50**, pp. 2680–2690, (1994), doi: [10.1103/PhysRevA.50.2680](https://doi.org/10.1103/PhysRevA.50.2680).
- [71] M. MAUREL, M. CHAFER, A. AMSANPALLY, M. ADNAN, F. AMRANI, B. DEBORD, L. VINCETTI, F. GÉRÔME, AND F. BENABID, *Optimized inhibited-coupling Kagome fibers at Yb-Nd:Yag (85 dB/km) and Ti:Sa (30 dB/km) ranges*, Optics Letters **43**, p. 1598, (2018), doi: [10.1364/ol.43.001598](https://doi.org/10.1364/ol.43.001598).
- [72] D. J. MCCARRON, S. A. KING, AND S. L. CORNISH, *Modulation transfer spectroscopy in atomic rubidium*, Measurement Science and Technology **19**, (2008), doi: [10.1088/0957-0233/19/10/105601](https://doi.org/10.1088/0957-0233/19/10/105601).
- [73] J. MCKEEVER, J. R. BUCK, A. D. BOOZER, A. KUZMICH, H.-C. NÄGERL, D. M. STAMPER-KURN, AND H. J. KIMBLE, *State-Insensitive Cooling and Trapping of Single Atoms in an Optical Cavity*, Physical Review Letters **90**, p. 133602, (2003), doi: [10.1103/PhysRevLett.90.133602](https://doi.org/10.1103/PhysRevLett.90.133602).
- [74] H. J. METCALF AND P. VAN DER STRATEN, *Laser Cooling and Trapping*, Graduate Texts in Contemporary Physics, Springer New York, New York, NY, 1st ed., (1999).
- [75] D. MÜLLER, E. CORNELL, D. ANDERSON, AND E. ABRAHAM, *Guiding laser-cooled atoms in hollow-core fibers*, Physical Review A **61**, pp. 1–6, (2000), doi: [10.1103/PhysRevA.61.033411](https://doi.org/10.1103/PhysRevA.61.033411).
- [76] W. J. MUNRO, K. NEMOTO, AND T. P. SPILLER, *Weak nonlinearities: a new route to optical quantum computation*, New Journal of Physics **7**, pp. 137–137, (2005), doi: [10.1088/1367-2630/7/1/137](https://doi.org/10.1088/1367-2630/7/1/137).

- [77] M. NOAMAN, M. LANGBECKER, AND P. WINDPASSINGER, *Micro-lensing-induced line shapes in a single-mode cold-atom-hollow-core-fiber interface*, *Optics Letters* **43**, p. 3925, (2018), doi: [10.1364/OL.43.003925](https://doi.org/10.1364/OL.43.003925).
- [78] J. NUNN, N. K. LANGFORD, W. S. KOLTHAMMER, T. F. M. CHAMPION, M. R. SPRAGUE, P. S. MICHELBERGER, X.-M. JIN, D. G. ENGLAND, AND I. A. WALMSLEY, *Enhancing Multiphoton Rates with Quantum Memories*, *Physical Review Letters* **110**, p. 133601, (2013), doi: [10.1103/PhysRevLett.110.133601](https://doi.org/10.1103/PhysRevLett.110.133601).
- [79] S. OKABA, T. TAKANO, F. BENABID, T. BRADLEY, L. VINCETTI, Z. MAIZELIS, V. YAMPOL'SKII, F. NORI, AND H. KATORI, *Lamb-Dicke spectroscopy of atoms in a hollow-core photonic crystal fibre*, *Nature Communications* **5**, p. 4096, (2014), doi: [10.1038/ncomms5096](https://doi.org/10.1038/ncomms5096).
- [80] M. A. OL'SHANII, Y. B. OVCHINNIKOV, AND V. S. LETOKHOV, *Laser guiding of atoms in a hollow optical fiber*, *Optics Communications* **98**, pp. 77–79, (1993), doi: [10.1016/0030-4018\(93\)90761-S](https://doi.org/10.1016/0030-4018(93)90761-S).
- [81] B. OSTING, *Bragg structure and the first spectral gap*, *Applied Mathematics Letters* **25**, pp. 1926–1930, (2012), doi: [10.1016/j.aml.2012.03.002](https://doi.org/10.1016/j.aml.2012.03.002).
- [82] G. J. PEARCE, G. S. WIEDERHECKER, C. G. POULTON, S. BURGER, AND P. ST. J. RUSSELL, *Models for guidance in kagome-structured hollow-core photonic crystal fibres*, *Optics Express* **15**, p. 12680, (2007), doi: [10.1364/oe.15.012680](https://doi.org/10.1364/oe.15.012680).
- [83] C. PERRELLA, H. GRIESSER, P. LIGHT, R. KOSTECKI, T. STACE, H. EBENDORFF-HEIDEPRIEM, T. MONRO, A. G. WHITE, AND A. N. LUITEN, *Demonstration of an Exposed-Core Fiber Platform for Two-Photon Rubidium Spectroscopy*, *Physical Review Applied* **4**, p. 014013, (2015), doi: [10.1103/PhysRevApplied.4.014013](https://doi.org/10.1103/PhysRevApplied.4.014013).
- [84] C. PERRELLA, P. LIGHT, T. M. STACE, F. BENABID, AND A. N. LUITEN, *High-resolution optical spectroscopy in a hollow-core photonic crystal fiber*, *Physical Review A - Atomic, Molecular, and Optical Physics* **85**, pp. 1–5, (2012), doi: [10.1103/PhysRevA.85.012518](https://doi.org/10.1103/PhysRevA.85.012518).
- [85] C. PERRELLA, P. S. LIGHT, J. D. ANSTIE, F. BENABID, T. M. STACE, A. G. WHITE, AND A. N. LUITEN, *High-efficiency cross-phase modulation in a gas-filled waveguide*, *Physical Review A* **88**, p. 013819, (2013), doi: [10.1103/PhysRevA.88.013819](https://doi.org/10.1103/PhysRevA.88.013819).
- [86] C. PERRELLA, P. S. LIGHT, S. A. VAHID, F. BENABID, AND A. N. LUITEN, *Engineering Photon-Photon Interactions within Rubidium-Filled Waveguides*, *Physical Review Applied* **9**, p. 44001, (2018), doi: [10.1103/PhysRevApplied.9.044001](https://doi.org/10.1103/PhysRevApplied.9.044001).

- [87] T. PETERS, T.-P. WANG, A. NEUMANN, L. S. SIMEONOV, AND T. HALFMANN, *Stopped and stationary light at the single-photon level inside a hollow-core fiber*, (2019), Pre-print available at [ArXiv: 1906.05771](https://arxiv.org/abs/1906.05771).
- [88] T. PEYRONEL, M. BAJCSY, S. HOFFERBERTH, V. BALIC, M. HAFEZI, Q. LIANG, A. ZIBROV, V. VULETIC, AND M. D. LUKIN, *Switching and counting with atomic vapors in photonic-crystal fibers*, *IEEE Journal on Selected Topics in Quantum Electronics* **18**, pp. 1747–1753, (2012), doi: [10.1109/JSTQE.2012.2196414](https://doi.org/10.1109/JSTQE.2012.2196414).
- [89] W. D. PHILLIPS, *Nobel Lecture: Laser cooling and trapping of neutral atoms*, *Reviews of Modern Physics* **70**, pp. 721–741, (1998), doi: [10.1103/RevModPhys.70.721](https://doi.org/10.1103/RevModPhys.70.721).
- [90] W. D. PHILLIPS AND H. METCALF, *Laser Deceleration of an Atomic Beam*, *Physical Review Letters* **48**, pp. 596–599, (1982), doi: [10.1103/PhysRevLett.48.596](https://doi.org/10.1103/PhysRevLett.48.596).
- [91] W. D. PHILLIPS, J. V. PRODAN, AND H. J. METCALF, *Laser cooling and electromagnetic trapping of neutral atoms*, *Journal of the Optical Society of America B* **2**, p. 1751, (1985), doi: [10.1364/JOSAB.2.001751](https://doi.org/10.1364/JOSAB.2.001751).
- [92] F. POLETTI, M. N. PETROVICH, D. J. RICHARDSON, AND M. J. LI, *Hollow-core photonic bandgap fibers: Technology and applications*, *Nanophotonics* **2**, pp. 315–340, (2013), doi: [10.1515/nanoph-2013-0042](https://doi.org/10.1515/nanoph-2013-0042).
- [93] J. V. PRODAN, W. D. PHILLIPS, AND H. METCALF, *Laser production of a very slow monoenergetic atomic beam*, *Physical Review Letters* **49**, pp. 1149–1153, (1982), doi: [10.1103/PhysRevLett.49.1149](https://doi.org/10.1103/PhysRevLett.49.1149).
- [94] E. L. RAAB, M. PRENTISS, A. CABLE, S. CHU, AND D. E. PRITCHARD, *Trapping of Neutral Sodium Atoms with Radiation Pressure*, *Physical Review Letters* **59**, pp. 2631–2634, (1987), doi: [10.1103/PhysRevLett.59.2631](https://doi.org/10.1103/PhysRevLett.59.2631).
- [95] S. RAMACHANDRAN AND P. KRISTENSEN, *Optical vortices in fiber*, *Nanophotonics* **2**, pp. 455–474, (2013), doi: [10.1515/nanoph-2013-0047](https://doi.org/10.1515/nanoph-2013-0047).
- [96] J. K. RANKA, R. S. WINDELER, AND A. J. STENTZ, *Visible continuum generation in air-silica microstructure optical fibers with anomalous dispersion at 800 nm*, *Optics Letters* **25**, p. 25, (2000), doi: [10.1364/ol.25.000025](https://doi.org/10.1364/ol.25.000025).
- [97] U. D. RAPOL, A. WASAN, AND V. NATARAJAN, *Loading of a Rb magneto-optic trap from a getter source*, *Physical Review A* **64**, p. 023402, (2001), doi: [10.1103/PhysRevA.64.023402](https://doi.org/10.1103/PhysRevA.64.023402).

- [98] M. J. RENN, E. A. DONLEY, E. A. CORNELL, C. E. WIEMAN, AND D. Z. ANDERSON, *Evanescent-wave guiding of atoms in hollow optical fibers*, Physical Review A **53**, pp. R648–R651, (1996), doi: [10.1103/PhysRevA.53.R648](https://doi.org/10.1103/PhysRevA.53.R648).
- [99] M. J. RENN, D. MONTGOMERY, O. VDOVIN, D. Z. ANDERSON, C. E. WIEMAN, AND E. A. CORNELL, *Laser-Guided Atoms in Hollow-Core Optical Fibers*, Physical Review Letters **75**, pp. 3253–3256, (1995), doi: [10.1103/PhysRevLett.75.3253](https://doi.org/10.1103/PhysRevLett.75.3253).
- [100] M. J. RENN, A. A. ZOZULYA, E. A. DONLEY, E. A. CORNELL, AND D. Z. ANDERSON, *Optical-dipole-force fiber guiding and heating of atoms*, Physical Review A **55**, pp. 3684–3696, (1997), doi: [10.1103/PhysRevA.55.3684](https://doi.org/10.1103/PhysRevA.55.3684).
- [101] P. J. ROBERTS, F. COUNY, H. SABERT, B. J. MANGAN, D. P. WILLIAMS, L. FARR, M. W. MASON, A. TOMLINSON, T. A. BIRKS, J. C. KNIGHT, AND P. ST. J. RUSSELL, *Ultimate low loss of hollow-core photonic crystal fibres*, Optics Express **13**, p. 236, (2005), doi: [10.1364/opex.13.000236](https://doi.org/10.1364/opex.13.000236).
- [102] S. ROOF, K. KEMP, M. HAVEY, I. M. SOKOLOV, AND D. V. KUPRIYANOV, *Microscopic lensing by a dense, cold atomic sample*, Optics Letters **40**, p. 1137, (2015), doi: [10.1364/OL.40.001137](https://doi.org/10.1364/OL.40.001137).
- [103] P. RUGELAND, C. STERNER, AND W. MARGULIS, *Visible light guidance in silica capillaries by antiresonant reflection*, Optics Express **21**, p. 29217, (2013), doi: [10.1364/oe.21.029217](https://doi.org/10.1364/oe.21.029217).
- [104] P. ST. J. RUSSELL, *Photonic Crystal Fibers*, Science **299**, pp. 358–362, (2003), doi: [10.1126/science.1079280](https://doi.org/10.1126/science.1079280).
- [105] ———, *Photonic-Crystal Fibers*, Journal of Lightwave Technology **24**, pp. 4729–4749, (2006), doi: [10.1109/JLT.2006.885258](https://doi.org/10.1109/JLT.2006.885258).
- [106] P. ST. J. RUSSELL, R. BERAVAT, AND G. K. L. WONG, *Helically twisted photonic crystal fibres*, Philosophical Transactions of the Royal Society A: Mathematical, Physical and Engineering Sciences **375**, p. 20150440, (2017), doi: [10.1098/rsta.2015.0440](https://doi.org/10.1098/rsta.2015.0440).
- [107] C. M. SAVAGE, S. MARKSTEINER, AND P. ZOLLER, *Atomic waveguides and cavities from hollow optical fibers*, in Fundamentals of Quantum Optics III, Springer Berlin Heidelberg, Berlin, Heidelberg, pp. 60–74, (1993), doi: [10.1007/BFb0113556](https://doi.org/10.1007/BFb0113556).

- [108] C. SAYRIN, C. CLAUSEN, B. ALBRECHT, P. SCHNEEWEISS, AND A. RAUSCHENBEUTEL, *Storage of fiber-guided light in a nanofiber-trapped ensemble of cold atoms*, *Optica* **2**, p. 353, (2015), doi: [10.1364/OPTICA.2.000353](https://doi.org/10.1364/OPTICA.2.000353).
- [109] A. D. SLEPKOV, A. R. BHAGWAT, V. VENKATARAMAN, P. LONDERO, AND A. L. GAETA, *Generation of large alkali vapor densities inside bare hollow-core photonic band-gap fibers*, *Optics Express* **16**, p. 18976, (2008), doi: [10.1364/oe.16.018976](https://doi.org/10.1364/oe.16.018976).
- [110] ———, *Spectroscopy of Rb atoms in hollow-core fibers*, *Physical Review A* **81**, p. 053825, (2010), doi: [10.1103/PhysRevA.81.053825](https://doi.org/10.1103/PhysRevA.81.053825).
- [111] C. M. SMITH, N. VENKATARAMAN, AND M. T. GALLAGHER, *Low-loss hollow-core silica / air photonic bandgap fibre*, *Nature* **424**, pp. 657–659, (2003), doi: [10.1038/nature01797.1](https://doi.org/10.1038/nature01797.1).
- [112] M. R. SPRAGUE, D. G. ENGLAND, A. ABDOLVAND, J. NUNN, X. M. JIN, W. STEVEN KOLTHAMMER, M. BARBIERI, B. RIGAL, P. S. MICHELBERGER, T. F. CHAMPION, P. ST. J. RUSSELL, AND I. A. WALMSLEY, *Efficient optical pumping and high optical depth in a hollow-core photonic-crystal fibre for a broadband quantum memory*, *New Journal of Physics* **15**, (2013), doi: [10.1088/1367-2630/15/5/055013](https://doi.org/10.1088/1367-2630/15/5/055013).
- [113] M. R. SPRAGUE, P. S. MICHELBERGER, T. F. M. CHAMPION, D. G. ENGLAND, J. NUNN, X.-M. JIN, W. S. KOLTHAMMER, A. ABDOLVAND, P. ST. J. RUSSELL, AND I. A. WALMSLEY, *Broadband single-photon-level memory in a hollow-core photonic crystal fibre*, *Nature Photonics* **8**, pp. 287–291, (2014), doi: [10.1038/nphoton.2014.45](https://doi.org/10.1038/nphoton.2014.45).
- [114] D. A. STECK, *Rubidium 85 D Line Data*.
Available online at <http://steck.us/alkalidata> (revision 2.1.6, 20 September 2013).
- [115] J. K. STOCKTON, K. TAKASE, AND M. A. KASEVICH, *Absolute Geodetic Rotation Measurement Using Atom Interferometry*, *Physical Review Letters* **107**, p. 133001, (2011), doi: [10.1103/PhysRevLett.107.133001](https://doi.org/10.1103/PhysRevLett.107.133001).
- [116] R. SULZBACH, T. PETERS, AND R. WALSER, *Optimal pulse propagation in an inhomogeneously gas-filled hollow-core fiber*, *Physical Review A* **100**, p. 013847, (2019), doi: [10.1103/PhysRevA.100.013847](https://doi.org/10.1103/PhysRevA.100.013847).

- [117] R. THAPA, K. KNABE, M. FAHEEM, A. NAWEED, O. L. WEAVER, AND K. L. CORWIN, *Saturated absorption spectroscopy of acetylene gas inside large-core photonic bandgap fiber*, *Optics Letters* **31**, p. 2489, (2006), doi: [10.1364/OL.31.002489](https://doi.org/10.1364/OL.31.002489).
- [118] G. W. TRUONG, J. D. ANSTIE, E. F. MAY, T. M. STACE, AND A. N. LUITEN, *Accurate lineshape spectroscopy and the Boltzmann constant*, *Nature Communications* **6**, (2015), doi: [10.1038/ncomms9345](https://doi.org/10.1038/ncomms9345).
- [119] V. VENKATARAMAN, P. LONDERO, A. R. BHAGWAT, A. D. SLEPKOV, AND A. L. GAETA, *All-optical modulation of four-wave mixing in an Rb-filled photonic bandgap fiber*, *Optics Letters* **35**, p. 2287, (2010), doi: [10.1364/ol.35.002287](https://doi.org/10.1364/ol.35.002287).
- [120] V. VENKATARAMAN, K. SAHA, AND A. L. GAETA, *Phase modulation at the few-photon level for weak-nonlinearity-based quantum computing*, *Nature Photonics* **7**, pp. 138–141, (2013), doi: [10.1038/nphoton.2012.283](https://doi.org/10.1038/nphoton.2012.283).
- [121] V. VENKATARAMAN, K. SAHA, P. LONDERO, AND A. L. GAETA, *Few-Photon All-Optical Modulation in a Photonic Band-Gap Fiber*, *Physical Review Letters* **107**, p. 193902, (2011), doi: [10.1103/PhysRevLett.107.193902](https://doi.org/10.1103/PhysRevLett.107.193902).
- [122] S. VORRATH, S. A. MÖLLER, P. WINDPASSINGER, K. BONGS, AND K. SENGSTOCK, *Efficient guiding of cold atoms through a photonic band gap fiber*, *New Journal of Physics* **12**, p. 123015, (2010), doi: [10.1088/1367-2630/12/12/123015](https://doi.org/10.1088/1367-2630/12/12/123015).
- [123] C. WANG, N. V. WHEELER, C. FOURCADE-DUTIN, M. GROGAN, T. D. BRADLEY, B. R. WASHBURN, F. BENABID, AND K. L. CORWIN, *Acetylene frequency references in gas-filled hollow optical fiber and photonic microcells*, *Applied Optics* **52**, p. 5430, (2013), doi: [10.1364/ao.52.005430](https://doi.org/10.1364/ao.52.005430).
- [124] Y. Y. WANG, N. V. WHEELER, F. COUNY, P. J. ROBERTS, AND F. BENABID, *Low loss broadband transmission in hypocycloid-core Kagome hollow-core photonic crystal fiber*, *Optics Letters* **36**, p. 669, (2011), doi: [10.1364/ol.36.000669](https://doi.org/10.1364/ol.36.000669).
- [125] C. WEI, R. JOSEPH WEIBLEN, C. R. MENYUK, AND J. HU, *Negative curvature fibers*, *Advances in Optics and Photonics* **9**, p. 504, (2017), doi: [10.1364/AOP.9.000504](https://doi.org/10.1364/AOP.9.000504).
- [126] N. V. WHEELER, T. D. BRADLEY, J. R. HAYES, M. A. GOUVEIA, S. LIANG, Y. CHEN, S. R. SANDOGHCHI, S. M. ABOKHAMIS MOUSAVI, F. POLETTI, M. N. PETROVICH, AND D. J. RICHARDSON, *Low-loss Kagome hollow-core fibers operating from the near- to the mid-IR*, *Optics Letters* **42**, p. 2571, (2017), doi: [10.1364/OL.42.002571](https://doi.org/10.1364/OL.42.002571).

- [127] P. B. WIGLEY, P. J. EVERITT, A. VAN DEN HENGEL, J. W. BASTIAN, M. A. SOORIYABANDARA, G. D. McDONALD, K. S. HARDMAN, C. D. QUINLIVAN, P. MANJU, C. C. N. KUHN, I. R. PETERSEN, A. N. LUITEN, J. J. HOPE, N. P. ROBINS, AND M. R. HUSH, *Fast machine-learning online optimization of ultra-cold-atom experiments*, Scientific Reports **6**, p. 25890, (2016), doi: [10.1038/srep25890](https://doi.org/10.1038/srep25890).
- [128] D. WINELAND AND D. DEHMELT, *Proposed $10^{-14} \Delta\nu/\nu$ Laser Fluorescence Spectroscopy on $Tl + Mono\text{-}Ion$ Oscillator*, Bulletin of the American Physical Society **20**, p. 637, (1975).
- [129] D. J. WINELAND AND W. M. ITANO, *Laser cooling of atoms*, Physical Review A **20**, pp. 1521–1540, (1979), doi: [10.1103/PhysRevA.20.1521](https://doi.org/10.1103/PhysRevA.20.1521).
- [130] G. WOKURKA, J. KEUPP, K. SENGSTOCK, AND W. ERTMER, *Guiding of Lasercooled Atoms in Hollow Core Optical Fibres*, in Technical Digest. 1998 EQEC. European Quantum Electronics Conference (Cat. No.98TH8326), IEEE, pp. 41–41, (1998), doi: [10.1109/EQEC.1998.714726](https://doi.org/10.1109/EQEC.1998.714726).
- [131] G. WORKURKA, J. KEUPP, AND K. SENGSTOCK, *Guiding of metastable neon atoms in hollow-core optical fibers*, in Summaries of Papers Presented at the International Quantum Electronics Conference. Conference Edition. 1998 Technical Digest Series, Vol.7 (IEEE Cat. No.98CH36236), Opt. Soc. America, pp. 235–236, (1998), doi: [10.1109/IQEC.1998.680492](https://doi.org/10.1109/IQEC.1998.680492).
- [132] M. XIN, W. S. LEONG, Z. CHEN, AND S.-Y. LAN, *An atom interferometer inside a hollow-core photonic crystal fiber*, Science Advances **4**, p. e1701723, (2018), doi: [10.1126/sciadv.1701723](https://doi.org/10.1126/sciadv.1701723).
- [133] W.-J. XU, M.-K. ZHOU, M.-M. ZHAO, K. ZHANG, AND Z.-K. HU, *Quantum tilt-meter with atom interferometry*, Physical Review A **96**, p. 063606, (2017), doi: [10.1103/PhysRevA.96.063606](https://doi.org/10.1103/PhysRevA.96.063606).
- [134] J. YE, H. J. KIMBLE, AND H. KATORI, *Quantum State Engineering and Precision Metrology Using State-Insensitive Light Traps*, Science **320**, pp. 1734–1738, (2008), doi: [10.1126/science.1148259](https://doi.org/10.1126/science.1148259).
- [135] T. YOON AND M. BAJCSY, *Laser-cooled cesium atoms confined with a magic-wavelength dipole trap inside a hollow-core photonic-bandgap fiber*, Physical Review A **99**, p. 023415, (2019), doi: [10.1103/PhysRevA.99.023415](https://doi.org/10.1103/PhysRevA.99.023415).

- [136] T. YOON, Z. DING, J. FLANNERY, F. RAJABI, AND M. BAJCSY, *Monitoring Raman emission through state population in cold atoms confined inside a hollow-core fiber*, *Optics Express* **27**, p. 17592, (2019), doi: [10.1364/OE.27.017592](https://doi.org/10.1364/OE.27.017592).
- [137] X. ZHANG AND J. YE, *Precision measurement and frequency metrology with ultra-cold atoms*, *National Science Review* **3**, pp. 189–200, (2016), doi: [10.1093/NSR/NWW013](https://doi.org/10.1093/NSR/NWW013).

